Hybrid Electromagnetic Forming of Aluminum Alloy Sheet

by

José Miguel Segundo Imbert Boyd

A thesis
presented to the University of Waterloo
in fulfilment of the
thesis requirement for the degree of
Doctor of Philosophy
in
Mechanical Engineering

Waterloo, Ontario, Canada, 2010

© José Miguel Segundo Imbert Boyd 2010

I hereby declare that I am the sole author of this thesis. This is a true copy of the thesis, including any required final revisions, as accepted by my examiners.

I understand that my thesis may be made electronically available to the public.

ABSTRACT

Electromagnetic (EM) forming is a high-speed forming process that uses the forces induced on a conductive workpiece by a transient high frequency current to form the workpiece into a desired shape. This thesis presents the results of an experimental and numerical study carried out to determine whether an EM forming process could be used to sharpen the radius of part pre-formed using a stamping process. Two processes were studied; a single step EM forming operation and a "hybrid forming" operation consisting of a conventional pre-forming step and an EM corner fill, both considering aluminum alloy AA 5754. The single step EM process proved unable to form acceptable samples due to excessive sample distortion, but was used to gain insight into the EM forming process. The hybrid operation consisted of pre-forming 1 mm AA 5754 sheet into a v-shape with a 20 mm outer radius using a conventional stamping operation and then reducing or "sharpening" the radius to 5 mm using EM forming. Sharpening the radius to 5 mm using conventional stamping was not achievable. The hybrid operation proved successful in forming the 5 mm radius, thus demonstrating that the material could be formed beyond its conventional formability limit using the hybrid operation. Numerical models were used to gain insight into the processes and the challenges involved in their numerical simulation. The numerical simulations showed that EM corner fill operation produces very high strain rates (10,000- 100,000 s^{-1}) and complex three dimensional stress and strain states. The effect of the high strain rates could not be properly assessed, since no constitutive data was available for such high strain rates. The predicted stress states show that the process was not plane stress and that large through-thickness compressive stresses are produced that are favorable to damage suppression and through-thickness shear strains that increase ductility. The high strain rates and the complex stress and strain states are considered the likely causes for the observed increase in formability. The models provided valuable insight, but did not predict the final shape exactly and the possible reasons behind this are analyzed. The research indicates that features that are not achievable using traditional stamping techniques can be obtained with the hybrid EM forming process.

ACKNOWLEDGEMENTS

This thesis would not have been possible without the help, guidance, support and friendship of many. First and foremost I would like to thank my supervisor Prof. Michael Worswick for providing me with the opportunity to do research on such an interesting topic. Throughout this work he has been a constant source of guidance, ideas and support. Also, I would like to commend his belief in research simply for the sake of knowledge, which is sometimes lacking in many researchers in engineering areas that are closely associated with industry.

The experimental portion of this work required the development, manufacture, procurement and installation of specialized equipment. I owe many thanks to Tom Gawel who was always willing and able to help. I am very grateful to Andy Barber who literally kept the current flowing. This work benefited greatly from the ideas and excellent work of the Engineering Machine Shop, so special thanks to John Boldt and his staff, especially Rick Forgett, Rob Kraemer, Jason Benninger and Charlie Boyle. I am also grateful to Doug Hirst and Richard Morrison, who kindly made available an apparatus from the Civil Engineering Department, as well of providing help and advice. Special thanks to Dr. Sooky Winkler for her help and guidance, which made possible the metallographic section of this work.

The numerical work in this thesis benefited immensely from the help and advice provided by Dr. Pierre L'Eplattenier of LSTC. Dr. L'Eplattenier made available a "beta" version of an EM capable LS-DYNA, which made possible the numerical effort of this research. I am very grateful for all his help and advice.

Keeping a project moving forward at this distinguished institution requires dealing with a byzantine administrative system that may be considered less than ideal. Laurie Wilfong has been a patient and knowledgeable guide through this system and I thank her for all her help. I am grateful to Lynn Crema, Marlene Dolson, Jennifer Nicholson and the rest of the MME administration staff.

The research presented was possible due to the generous funding of the Ontario Research Fund and the National Science and Engineering Research Council. Their support is gratefully acknowledged.

I have been privileged to work with an exceptional group of people throughout my time at the University of Waterloo, who provided friendship, support and a wealth of technical knowledge and expertise. Some of these great people left the group as time went on, but I will never forget their contributions. I am very grateful to Blake Hodgins, dear friend of old, who provided a great deal of modeling knowledge and much needed distractions. Chris Salisbury, who selflessly went above and beyond to keep the clusters running and who was always willing to share his knowledge; I thank for this and for his friendship. I thank Dr. Hari Sima for interesting discussions, his friendship and his unselfish sharing of knowledge. To Alex Bardelcik, the last of the old guard, I thank for his friendship, help and epicurean advice. To Dino Oliveira, Rafal Smerd, Rassin Grantab and the other past members of the Worswick group, my sincere thanks.

Although included last, the people who have supported me in my personal life have been just as important in helping me complete this work. I am extremely lucky to have excellent friends, some I've had for a lifetime others for months, but their friendships have made me enjoy the good times and helped me through the bad, and to them I will be eternally grateful. I am immensely fortunate to have a wonderful extended family, to which I am grateful for their love and support. I thank my dear Nataliya, who has provided incredible encouragement and support throughout the critical parts of this work. I do not have the words to express the love and gratitude I owe my brother, grandmother, father and mother.

For my mother, father and grandma Batty

TABLE OF CONTENTS

Author's declaration……II
ABSTRACT……. III
ACKNOWLEDGEMENTS IV
Dedication…… VI
TABLE OF CONTENTS VII
LIST OF FIGURES X
LIST OF TABLES XXIII
1 INTRODUCTION 1
1.1 FORMABILITY OF ALUMINUM ALLOY SHEET-CONVENTIONAL FORMING 2
1.2 THE EMF PROCESS 8
1.3 EM FORMING OF SHEET METAL 9
1.4 FACTORS THAT INFLUENCE FORMABILITY IN HIGH VELOCITY FORMING 11
1.4.1 Constitutive Effects - High Strain Rate Behaviour of Aluminum Alloys 11
1.4.2 Inertial Effects 13
1.5 TOOL/SHEET INTERACTION EFFECTS 13
1.5.1 Effects of Compressive Stresses on Formability 16
1.6 STRAIN PATH EFFECTS..... 19
1.7 ELECTROMAGNETIC BASICS OF THE EM FORMING PROCESSES..... 19
1.7.1 Maxwell's Equations 24
1.7.2 Lorentz's Forces 25
1.7.3 Workpiece Geometric Effects 26
1.8 NUMERICAL SIMULATION OF EM FORMING 27
1.9 HYBRID FORMING IN THE LITERATURE..... 28
1.10 PRESENT WORK..... 30
2 EXPERIMENTAL METHODS AND PROCEDURES 34
2.1 EM FORMING LABORATORY 35
2.2 MATERIAL AND SAMPLE PREPARATION 35

2.2.1 Material Properties 35
2.2.2 Sample Size 36
2.2.3 Strain Measurements 36
2.2.4 Sheet Pre-Straining 38
2.3 SINGLE STEP EM FORMING OPERATION 42
2.4 HYBRID FORMING OPERATION 44
2.5 TOOLING FOR THE CONVENTIONAL PRE-FORM 45
2.6 EM CORNER FILL APPARATUS 47
2.6.1 Coil Used for the EM Corner Fill 47
2.7 PRELIMINARY COIL DESIGNS 53
2.8 FIELD SHAPERS OR COLLECTORS 58
2.9 METALLOGRAPHY 62
3 NUMERICAL METHODS AND PROCEDURES 65
3.1 SINGLE STEP EM PROCESS MODELS 67
3.2 HYBRID PROCESS MODELS 69
3.2.1 Conventional Pre-form 70
3.2.2 EM Corner Fill 71
4 EXPERIMENTAL RESULTS 73
4.1 SINGLE STEP EM FORMING RESULTS 73
4.1.1 Effect of Force Distribution 74
4.1.2 Rebound of the Sheet 76
4.2 HYBRID FORMING RESULTS 77
4.2.1 Conventional Pre-Form Results 77
4.2.2 EM Corner Fill 82
4.2.3 Results for the As-Received Sheet 83
4.2.4 Results for the 5% Pre-Strained Sheet 88
4.2.5 Results for the 10% Pre-Strained Sheet 92
4.2.6 Results for the 15% Pre-Strained Sheet 96
4.3 CONVENTIONAL (STAMPING) CORNER FILL EXPERIMENTS 102
4.4 RESULTS FROM THE METALLOGRAPHIC ANALYSIS 104
5 NUMERICAL RESULTS 111

5.1 SINGLE STEP EM FORMING 111
5.2 CONVENTIONAL PRE-FORMING RESULTS 118
5.3 EM CORNER FILL RESULTS 123
5.3.1 Stress and Strain Histories from the Corner Fill Operation 127
5.3.2 Strain Rates 139
5.4 POSSIBLE CAUSES OF THE DEVIATION OF THE PREDICTED FINAL SHAPE FROM THE EXPERIMENTALLY OBSERVED PROFILE 141
5.4.1 Effect of the Material Flow Stress 142
5.4.2 Current Profile Effects 146
5.4.3 Effects of Reducing the Amount of Energy 149
5.4.4 Possible Damping Effects 150
5.5 PRE-STRAINED SHEET SIMULATIONS 152
5.6 EFFICIENCY OF THE CORNER FILL PROCESS 158
6 DISCUSSION 160
7 CONCLUSIONS AND FUTURE WORK 167
7.1 CONCLUSIONS 167
7.2 FUTURE WORK 168
REFERENCES 170

LIST OF FIGURES

Figure 1: Schematic of a simple hybrid process. A conventional tool forms the sheet in a) and b), then an EM coil is introduced c) to sharpen the corner radius d) of the pre-formed sheet. 2

Figure 2: Door panel formed with a) draw quality steel and b) the same door panel formed with 6011 T4 Aluminum alloy. The parts were formed with the same die with some allowances being made for the aluminum part. The difference in formability can be gauged by comparing the areas in the dashed rectangles, where sharp features can be seen in a) that are not present in b) []. 3

Figure 3: License plate and door-handle pockets are potential applications of EM hybrid forming [,]. 3

Figure 4: Forming limit diagram showing FLC's for a common automotive steel and three aluminum alloys [1]. 4

Figure 5: Rectangular draw showing areas were forming corresponds to bending and drawing. Note the grid pattern which illustrates the deformation strains of the material. 5

Figure 6: Schematic representation of a cup deep-drawing [9]. 5

Figure 7: Definition of "r- value". 6

Figure 8: Relation between LDR and r-values [9], where $\overline{r}$ s the average of r-values measured in several orientations relative to the rolling direction. 6

Figure 9: Stress distribution during bending. Image adapted from Schey [9]. 7

Figure 10: Schematic of EM forming. 8

Figure 11: Schematic representations of a) flat sheet forming and b) feature sharpening or corner fill. 9

Figure 12: Types of flat or pancake coils with approximate resulting pressure distributions along indicated sections [11,15]. 9

Figure 13: Formability data for electrohydraulically formed AA 6061 [19,20]. 10

Figure 14: Formability data for AA6111-T4 EM formed into a V-die (taken from Golovashchenko *et al.* [21]). Forming limit curve (FLC) provided by ALCAN International []. 10

Figure 15: Strain rate dependence of several aluminum alloys compiled by Lindholm *et al.* [27]. 12
Figure 16: Stress versus Strain at high strain rates for AA 5754 [28]. 12
Figure 17: Inertial force neck retardation effect as proposed by Balanethiram and Daehn [19]. 13
Figure 18: Formability data for free-formed a) AA 5754 and b) AA 6111 samples. The curves are conventional FLCs for the respective materials [17]. 14
Figure 19: Formability data for conical a) AA 5754 and b) AA 6111 samples. The curves are conventional FLCs for the respective materials [17] 14
Figure 20: Schematic diagram illustrating the inertial ironing effect [20]. 15
Figure 21: Effective plastic strain distribution as the sheet is formed into the die. Contours are effective plastic strain [17]. 16
Figure 22: Aluminum-Copper alloy deformed at a) ambient pressure and b) and c) with a hydrostatic pressure of 300 MPa. Images b and c show views of the neck of the same specimen at 90º from each other [51]. 17
Figure 23: Triaxiality histories for a typical location in a free-formed and conical sample [17]. 17
Figure 24: Comparison of quasi static (QS), high strain rate ($1500s^{-1}$) and EMF failure of AA 5754 sheet. * taken from [] and EMF from [17]. 18
Figure 25: Simplified EM forming circuit. C= capacitance, L= inductance and R= resistance. The magnetic mutual induction is represented by M. 20
Figure 26: Circuit for the EMF apparatus. 21
Figure 27: Current profile produced by equation 1-8 with the R, L and C values for the MPG generator of the University of Waterloo. 22
Figure 28: Current profiles for an EM forming experiment performed for this work. The MPG used was the same one whose properties were used to generate the curve shown in Figure 27. Note that peak current and frequency are lower, which is due to the inductance from the coil and the effect of the workpiece. 24
Figure 29: Results of corner fill study with an inner door panel [6]. 28
Figure 30: Schematic of an EM assisted forming operation [77]. 29
Figure 31: Corner fill experimental tooling from Psyk *et al.* [81]. 29

Figure 32: Schematic of the single step EM process. 31
Figure 33: Cross section of the experimental geometries in the 20 mm radius pre-form and nominal 5 mm outer radius final shape. 32
Figure 34: Schematic of the EM corner fill step of the hybrid process. 32
Figure 35: Chart outlining the experimental program for this research 34
Figure 36: Experimental apparatus showing the MPG and hydraulic press used. 35
Figure 37: True stress-strain curves for AA 5754 [25]. 36
Figure 38: Grid measurement system. 37
Figure 39: Location of the grids used to measure strain in the a) un-deformed sheet, b) drawn sheet and c) EM corner filled sheet. 38
Figure 40: Apparatus used to pre-strain sheets of aluminum a) without and b) with sheet. A close-up of the grips with a sheet sample is shown in c). 39
Figure 41: Images showing a) 203 x 356 mm (8 x 14") sheet cut from as-received material prior to stretching, and stretched to b) 5%, c) 10 %, and d) 15 %. 39
Figure 42: Measured strains for samples pre-strained to 5%. 40
Figure 43: Measured strains for samples pre-strained to 10%. 41
Figure 44: Measured strains for samples pre-strained to 15%. 41
Figure 45: V-Channel dies with idealized pressure distributions for the centre of the coil. 42
Figure 46: Tooling used for the experiment a) coil and die and b) tooling with a formed part and insulating sheet. 43
Figure 47: Schematic showing the insulation for the experiments with the double pancake coil. 43
Figure 48: Coil and die assembly as installed in the hydraulic press. 44
Figure 49: Schematic of the hybrid forming operation which consists of a) conventional forming to produce b) a pre-formed blank with a radius of 20 mm that is then subjected to c) an EM corner fill operation to produce d) the final sample shape. 45
Figure 50: Exploded schematic view of the conventional forming tool used to pre-form the sheet to a 20 mm outer radius. 46
Figure 51: Actual tool used for the conventional forming operations. 46
Figure 52: Corner-fill coil used shown a) without and with b) a sample. The connectors and supports used are not shown. 48

Figure 53: Detailed drawing of the corner-fill coil. All dimensions in mm. 48
Figure 54: Top a) and bottom b) view of the coil showing the types of joints used. The material that can be seen inside the coil in a) is a polycarbonate rod. 49
Figure 55: Coil preparation for use. The coil and supporting rod are shown individually in a) and assembled in b). The first vinyl insulation layer is shown in c) and the Kapton® layer in d). The coil with the final vinyl layer and ready for use is shown in e). 50
Figure 56: Schematic of the corner fill operation of the hybrid process. 51
Figure 57: EM corner fill apparatus. 51
Figure 58: Photographs showing a) the PVC base of the connector and b) shows the base with the coil in place. 52
Figure 59: The connection of the coil with the connector to the MPG is shown in a) and the same connection with the plasticine applied is shown in b). 52
Figure 60: Placement of the pre-formed sample on the corner fill apparatus. A pre-formed sample with the tape used to affix it to the die is also shown. 53
Figure 61: Front view of the apparatus with a sample in position in the a)open and b) closed configurations. 53
Figure 62: Coil design that led to the successful coil. 54
Figure 63: Simplified induced force distribution for a) the unsuccessful and b) successful coil design. 54
Figure 64: Aluminum U coil. 55
Figure 65: Copper U coil after four of tests. 55
Figure 66: Wound coil with details of the soldered connections. The coil with the connecting cables is shown on the top right-hand corner. 56
Figure 67: Idealized wound coil with the current direction for half of the wires. The connectors have been removed for clarity. 56
Figure 68: Simulation of a helical coil with a workpiece. Contours are of current density. ... 57
Figure 69: Basic collector layout for the corner fill application. 58
Figure 70: Simulation of a simple collector for a corner fill application, showing the relatively large predicted deformation that was likely the result of numerical over-prediction. 59
Figure 71: “L” collector. 60
Figure 72: Square collector. 60

Figure 73: Double pancake coil a) and collectors placed on coil b). The brown sheets that can be seen on b) are sheets of Kapton® for insulation. The cables seen on the collectors were used to try and detect if current was passing through that section of the collector. . 61
Figure 74: Predicted current density on a square collector excited by a flat spiral coil like the one used for the experimental work. 62
Figure 75: Samples of a) drawn sample and b) corner filled sample showing where the samples for the metallographic analysis were taken. 63
Figure 76: Original (top) and re-touched (bottom) tiled image. The white scale bar is 500 μm long. 64
Figure 77: Diagram illustrating the processes modeled numerically for this research. 65
Figure 78: Illustration of the differences between a Finite Element-only solution for an EM forming problem versus a combined Boundary Element and Finite Element approach. .. 66
Figure 79: Coil and sheet meshes for the single step EM process. 68
Figure 80: Die and binder meshes for the single step EM process. The binder and the die are used to clamp the sheet in place. Neither the die or binder meshes are included in the EM calculations. 69
Figure 81: Mesh used for the model of the conventional pre-form operation..... 70
Figure 82: Blank mesh after conventional pre-forming. 71
Figure 83: Meshes used for the electromagnetic corner fill calculations. 72
Figure 84: Current used as the input for the electromagnetic simulation. The values were taken from experimental measurements. 72
Figure 85: Part formed using the double pancake coil and a charge energy of 6.75 kJ, a)oblique view, b) front view (magnified) and c) side view. The blue markings in a) indicate where the sheet made contact with the die. Note the difference between the part and the nominal V-channel shape..... 74
Figure 86: Predicted force distribution on the side of the sheet exposed to the coil. Fringe levels are of Lorentz force in μN. The solid black lines indicate the approximate location of the die cavity. 75
Figure 87: : Part formed using a charging energy of 2.4 kJ and the double pancake coil, a) view from above and b) front view. 76
Figure 88: Typical 20 mm radius pre-formed sample. 77

Figure 89: Measured strains for the pre-formed samples formed with the sheet in the as-received condition in the longitudinal direction. 78
Figure 90: Measured strains for the pre-formed samples formed with the sheet in the as-received condition in the transverse direction. 78
Figure 91: Measured strains for the pre-formed samples formed with 5% pre-strained sheet in the longitudinal direction. 79
Figure 92: Measured strains for the pre-formed samples formed with 5% pre-strained sheet in the transverse direction. 79
Figure 93: Measured strains for the pre-formed samples formed with 10% pre-strained sheet in the longitudinal direction. 80
Figure 94: Measured strains for the pre-formed samples formed with 10% pre-strained sheet in the transverse direction. 80
Figure 95: Measured strains for pre-formed samples formed with 15% pre-strained sheet in the left to right direction. 81
Figure 96: Measured strains for the pre-formed samples formed with 15% pre-strained sheet in the transverse direction. 81
Figure 97: Sample formed into the 5 mm die by a Hybrid EM corner fill. The height legends refer to the height measurements in Table 4. The area enclosed in the dashed line in b) us where the highest strains were observed. 82
Figure 98: Samples formed from the pre-formed samples formed with as-received sheet. 84
Figure 99: Close up of the centre region of the samples formed from the as-received sheet with a 5 mm radius gauge. 84
Figure 100: Close up of one the edges of the samples formed from the as-received sheet with a 8 mm radius gauge 85
Figure 101: Experimental current versus for the samples formed from the as-received sheet. 86
Figure 102: Measured strains for samples formed from the sheet in the as-received condition in the longitudinal direction 87
Figure 103: Measured strains for samples formed from the sheet in the as-received condition in the transverse direction. 87

Figure 104: Forming limit diagram containing the largest strains measured on the final corner filled samples and the samples in the pre-formed state formed from sheet in the as-received condition. 88
Figure 105: Samples formed from the 5% pre-strained sheet. 89
Figure 106: Close up of the centre region of the samples formed from the 5% pre-strained sheet with a 5 mm radius gauge. 89
Figure 107: Close up of one the edges of the samples formed from the 5% pre-strained sheet with a 8 mm radius gauge. 89
Figure 108: Experimental current versus for the samples formed from the sheet with 5% pre-strain. Due to an equipment malfunction the data for the other samples was lost. 90
Figure 109: Measured strains for samples formed from 5% pre-strained sheet in the longitudinal direction. 91
Figure 110: Measured strains for samples formed from 5% pre-strained sheet in the transverse direction. 91
Figure 111: Forming limit diagram containing the largest strains measured on the final corner filled samples and the samples in the pre-formed state formed with the sheet pre-strained to 5%. Also shown are the strains measured on the pre-strained sheets. 92
Figure 112: Samples formed from the 5% pre-strained sheet. 92
Figure 113: Close up of the centre region of the samples formed from the 10% pre-strained sheet with a 5 mm radius gauge. 93
Figure 114: Close up of one the edges of the samples formed from the 10% pre-strained sheet with a 8 mm radius gauge. 93
Figure 115: Experimental current versus for the samples formed from the sheet with the 10% pre-strain. 94
Figure 116: Measured strains for samples formed from 10% pre-strained sheet in the longitudinal direction. 95
Figure 117: Measured strains for samples formed with 10% pre-strained sheet in the transverse direction. 95
Figure 118: Forming limit diagram containing the largest strains measured on the final corner filled samples and the samples in the pre-formed state formed with the sheet pre-strained to 10%. Also shown are the strains measured on the pre-strained sheets. 96

Figure 119: Samples formed from the 5% pre-strained sheet. 97
Figure 120: Close up of the centre region of the samples formed from the 15% pre-strained sheet with a 5 mm radius gauge. 97
Figure 121: Close up of one the edges of the samples formed from the 15% pre-strained sheet with a 8 mm radius gauge. 97
Figure 122: Experimental current versus for the samples formed from the the sheet with the 15% pre-strain. 98
Figure 123: Measured strains for samples formed from 15% pre-strained sheet in the longitudinal direction. 99
Figure 124: Measured strains for samples formed from 15% pre-strained sheet in the transverse direction. 99
Figure 125: Forming limit diagram containing the largest strains measured on the final corner filled samples and the samples in the pre-formed state formed with the sheet pre-strained to 15%. Also shown are the strains measured on the pre-strained sheets. 100
Figure 126: Forming limit diagram showing the highest strains measured on the corner filled samples formed with the sheet in all of the conditions studied. 101
Figure 127: Overlay of all the measured current profiles. 102
Figure 128: Pre-formed samples that were formed with a conventional stamping tool to fill the 5 mm corner radius. Most samples failed in the same manner as a). Some samples were arrested prior to complete fracture by stopping the punch, as in b). Some of pre-strain samples failed as shown in c) in an area where the emery paper used for draw-in control produced additional thinning. 103
Figure 129: Close-up of the two type of failures observed in the conventional corner fill experiments. The most common failure mode is shown on a), which corresponds to the sample shown in Figure 128-b. The failure that occurred near the area of the lock beads with the emery paper is shown in b), which corresponds to Figure 128-c. 103
Figure 130: Heights of pre-formed samples that were formed with a conventional tool to try to achieve a 5 mm radius. All samples failed. Samples marked with an * failed in the manner shown in Figure 128-c. 104

Figure 131: Micrograph from a corner filled sample formed with sheet that was pre-strained to 15%. Second phase particles and voids are indicated. The damage values were obtained by measuring the voids. 105
Figure 132: Tiled images used for damage measurements on flat sheet for the a) as-received, b) 5% pre-strained, c) 10% pre-strain and d) 15% pre-strained conditions. 106
Figure 133: Tiled images used for damage measurements on the pre-formed samples drawn to a 20 mm outer radius for the a) as-received, b) 5% pre-strained, c) 10% pre-strain and d) 15% pre-strained conditions. 107
Figure 134: Tiled micrographs for the corner filled sample formed with as-received sheet.. 108
Figure 135: Tiled micrographs for the corner filled sample formed with the 5% pre-strained sheet. 108
Figure 136: Tiled micrographs for the corner filled sample formed with the 10% pre-strained sheet. 109
Figure 137: Tiled micrographs for the corner filled sample formed with the 15% pre-strained sheet. 109
Figure 138: Void volume fractions for the samples measured. Key: ar = as received, 5= 5% pre-strain, 10 = 10% pre-strain, 15 = 15% pre-strain, s = flat sheet, d = drawn to 20 mm outer radius and cf = corner filled. The tip, l and r indicate whether the measurement was made on the tip, or to the left (l) or right (r) of the tip, as shown on the inset. 110
Figure 139: Experimental and numerical currents for a discharge through the coil with no workpiece. 112
Figure 140: Experimental and numerical current profiles for 3000 and 5000 charging volt cases. The steps in the predicted values are a consequence of the time steps for the EM calculations and the movement of the sheet. 113
Figure 141: Experimental land numerical sample heights for a) the 40° conical samples from [17], b) single step EM samples with no die contact and c) single step EM samples with die contact. 114
Figure 142: Final predicted v-channel shape for a sample that makes no contact with the die (3000 V charging voltage). The general trends in the height are predicted by the model. 115
Figure 143: Comparison of the final predicted shape with the experimental sample. 115

Figure 144: Final predicted v-channel shape for sample with rebound present (5000 V charging voltage). The edge effect is present but is not as pronounced as in the lower voltage case. 116
Figure 145: Comparison between the experimental shape of the sample and the predicted final shape. The experimental shape resembles more the predicted shape just prior to impact. The difference between the predicted final shape and the actual one are due to the excessive rebound predicted. 117
Figure 146: Predicted pre-formed shape. Contours are of effective plastic strain. 118
Figure 147: Predicted and measured engineering strains for the longitudinal direction for the pre-form model with the sheet in the as-received condition. 119
Figure 148: Predicted and measured engineering strains for the transverse direction for the pre-form model with the sheet in the as-received condition. 119
Figure 149: Predicted and measured engineering strains for the longitudinal direction for the pre-form model with the sheet pre-strained by 5%. 120
Figure 150: Predicted and measured engineering strains for the transverse direction for the pre-form model with the sheet pre-strained by 5%. 120
Figure 151: Predicted and measured engineering strains for the longitudinal direction for the pre-form model with the sheet pre-strained by10%. 121
Figure 152: Predicted and measured engineering strains for the transverse direction for the pre-form model with the sheet pre-strained by10%. 121
Figure 153: Predicted and measured engineering strains for the longitudinal direction for the pre-form model with the sheet pre-strained by15%. 122
Figure 154: Predicted and measured engineering strains for the transverse direction for the pre-form model with the sheet pre-strained by15%. 122
Figure 155: Predicted final shape using the experimental quasi-static flow curve. Strains are of effective plastic strain. 123
Figure 156: Comparison between experimental and predicted final shapes. 124
Figure 157: Cross-section at the centre of the part a) before forming, b) just prior to impact at the top of the die, c) when the material impacts the top of the die and d) final shape. The shape at b) is entirely due to the force distribution. At c) the part has been shaped by both

the force distribution and impact with the die. The final shape at d) is the result of the rebound. 125
Figure 158: Lorentz force distribution at a) the centre of the sample and b) at one of the edges. Bothe are images are from the same time in the simulation. The contours and vectors are of Lorentz force in μN. 125
Figure 159: Segment from a sample formed with the as-received sheet cut from the centre of the sample. The dashed lines are added to highlight the shape of the cross section. 126
Figure 160: Predicted and measured engineering strains for the longitudinal direction. 126
Figure 161: Predicted and measured engineering strains for the transverse direction. 127
Figure 162: The three zones that were chosen for stress/strain history analysis. The impact of zone 3 is presented in a), of zone 2 in b) and of zone 1 in c). Image d) shows the sample after it has rebounded. 128
Figure 163: Normal stress directions and designations for the stresses presented in the stress histories..... 129
Figure 164: Shear stress directions and designations for the stresses presented in the stress histories..... 129
Figure 165: Normal stress histories for zone 1 elements. 130
Figure 166: Normal stress histories for zone 2 elements. 130
Figure 167: Normal stress histories for zone 3 elements. 131
Figure 168: Shear stress histories for zone 1 elements..... 132
Figure 169: Shear stress histories for zone 2 elements..... 133
Figure 170: Shear stress histories for zone 3 elements..... 133
Figure 171: Triaxiality histories for the elements of all three zones. 134
Figure 172: Normal strain histories for zone 1 elements. 135
Figure 173: Normal strain histories for zone 2 elements. 136
Figure 174: Normal strain histories for zone 3 elements. 136
Figure 175: Shear strain histories for zone 1 elements..... 137
Figure 176: Shear strain histories for zone 2 elements..... 138
Figure 177: Shear strain histories for zone 3 elements..... 138
Figure 178: Effective plastic strain histories. Inset indicates the locations of the zones. 139

Figure 179: Instantaneous strain rates calculated for the inner and outer elements of zone's 1, 2 and 3. 140
Figure 180: Flow stresses used for the numerical study. 143
Figure 181: Predicted final shapes of the centre of the sample using flow curves scaled to 120, 130 and 140% as shown in Figure 180. 143
Figure 182: Predicted final shape using a flow stress scaled up by 140% together with a picture of an experimental sample. Note the closer agreement to the actual sample shape. 144
Figure 183: Predicted and measured engineering strains for the longitudinal direction for the model with the flow stress scaled by 140%. 145
Figure 184: Predicted and measured engineering strains for the transverse direction for the model with the flow stress scaled by 140%. 146
Figure 185: Current profile used to test the effects of additional EM pulses on the workpiece. 147
Figure 186: Section of the experimental sample compared to the numerical prediction using the current profile shown in Figure 185. 147
Figure 187: Deformation history of the sample with the multiple peak current pulse show in Figure 185. The forces induced by the second pulse can be seen on e). The contours are of Lorentz's forces in μN. 148
Figure 188: Image showing where the forces are induced on the second by the second current pulse. The contours are of μN. 149
Figure 189: Current versus time profile used for the reduced energy simulations. 150
Figure 190: Section of an experimental sample compared to the numerical prediction using half the current profile shown in Figure 84. 150
Figure 191: Allowed displacement of die used to simulate damping due to a moving tool. 151
Figure 192: Effect of allowed die velocity on the final predicted shape. 151
Figure 193: Flow stress used to simulate the effect of the pre-straining on the sheet. 153
Figure 194: Cross sections of the predicted final shapes for t he original (0% pre-strain), 5, 10 and 15% pre-strain models, compared to a sections of the actual corresponding samples. 154

Figure 195: Predicted and measured engineering strains for the longitudinal direction for the model with the sheet pre-strained by 5%. 155
Figure 196: Predicted and measured engineering strains for the transverse direction for the model with the sheet pre-strained by 5%. 155
Figure 197: Predicted and measured engineering strains for the longitudinal direction for the model with the sheet pre-strained by 10%. 156
Figure 198: Predicted and measured engineering strains for the transverse direction for the model with the sheet pre-strained by 10%. 156
Figure 199: Predicted and measured engineering strains for the longitudinal direction for the model with the sheet pre-strained by 15%. 157
Figure 200: Predicted and measured engineering strains for the transverse direction for the model with the sheet pre-strained by 15%. 157
Figure 201: Illustration of the quantities used in equation 5-3. 159
Figure 202: Forming limit diagram containing the largest strains measured on the final corner filled samples and the samples in the pre-formed state formed with the sheet pre-strained to 15%. Also shown are the strains measured on the pre-strained sheets. 160
Figure 203: Figure showing the predicted hydrostatic stress, strain and instantaneous strain rate for the inside element of zone 1. 161
Figure 204: Figure showing the predicted hydrostatic stress, strain and instantaneous strain rate for the outside element of zone 1. 162
Figure 205: Figure showing the predicted hydrostatic stress, strain and instantaneous strain rate for the inside element of zone 2. 162
Figure 206: Figure showing the predicted hydrostatic stress, strain and instantaneous strain rate for the outside element of zone 2. 163
Figure 207: Figure showing the predicted hydrostatic stress, strain and instantaneous strain rate for the inside element of zone 3. 163
Figure 208: Figure showing the predicted hydrostatic stress, strain and instantaneous strain rate for the outside element of zone 3. 164

LIST OF TABLES

Table 1: Nominal composition (wt%) of AA 5754 [] aluminum alloy. 35
Table 2: Samples used for the metallographic analysis. The d_, 5_, 10_ and 15_ designations refer to the as-received, 5%, 19% and 15% pre-strained samples respectively, with the subsequent number indicating the specific sample. 63
Table 3: Forming conditions for the corner fill samples. AR = as received, 5% = 5% pre-strain, 10% = 10% pre-strain, 15% = 15% pre-strain and NA = not available due to technical problems. 83
Table 4: Heights of selected corner filled samples. The values of h_1, h_2 and h_3 are as described in Figure 97. All dimensions in mm. 83
Table 5: The three highest strain rates and the elements where they where predicted. 141
Table 6: Strain rates calculated from the time of the first change in strain of the element to the time of impact. 141

1 INTRODUCTION

Interest in Electromagnetic (EM) forming of sheet metal for automotive applications has been growing in recent years, due to its potential as a means of forming aluminum and other low formability materials. Forming of aluminum has been the main focus, due to its inferior forming characteristics relative to mild steel [1,2,3] and its potential to reduce automobile weight.

Despite having been in use since the early 1960's [4,5], there is not yet a complete understanding of EM forming and how it affects the formability of the material. Progress has been made in recent years in the understanding of the behaviour of the material in the process; however, there is still not sufficient knowledge of this process to be able to properly design industrial applications.

Although it has been established that EM forming can increase the formability of materials in some applications, the reasons behind the increase and the effect of tool geometry, magnetic force distribution, material properties and surface conditions (e.g. lubrication) have not been systematically studied.

This thesis presents the results of a study on using EM forming to achieve sharp features in a commercial aluminum alloy sheet, AA 5754. Low formability materials often exhibit insufficient ductility and tend to tear at sharp corners during forming. Aluminum alloys, like AA 5754, suffer from this problem. To try to overcome this limitation, two forming processes were studied: an EM forming process and a hybrid forming process that combines conventional forming (stamping) with EM forming. The former did not achieve the desired result, while the hybrid process showed that it could be used to achieve formed aluminum parts with sharp features. Figure 1 illustrates a process with a simple corner fill operation, in which a sheet is formed with a conventional tool comprising a die and a punch and then an EMF operation is used to shape or "fill" the corner.

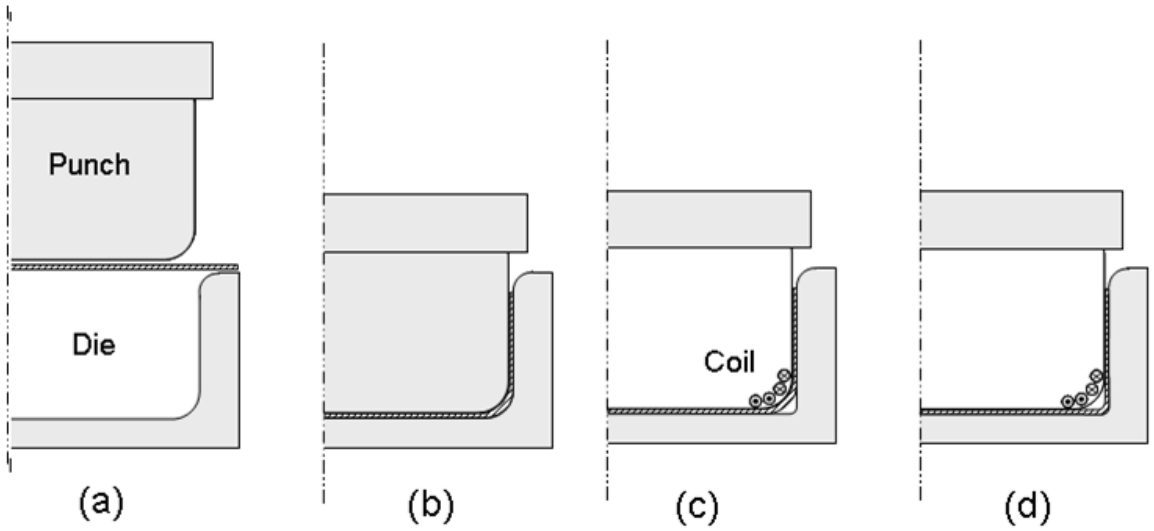

Figure 1: Schematic of a simple hybrid process. A conventional tool forms the sheet in a) and b), then an EM coil is introduced c) to sharpen the corner radius d) of the pre-formed sheet.

Hybrid operations in which EM forming is used to shape corners could have significant practical potential in the automotive, aerospace, and appliance industries, provided that the possible benefits can be demonstrated and can be obtained in commercially viable operations. Hybrid forming may allow features with radii smaller than those that can be obtained from conventional forming to be economically achieved in a production environment. This performance gain could make low formability alloys, such as aluminum alloys and even high strength steels, viable in many applications for which they are currently unable to be used.

The remainder of this section presents a review of previous work done in EM forming. This review starts with an outline of some basic concepts behind sheet metal forming, after which previous research in EM forming is presented. Finally, the current research is introduced.

1.1 Formability of Aluminum Alloy Sheet-Conventional Forming

Aluminum alloy sheet has relatively poor formability when compared to mild steel, the most commonly used sheet metal in the automotive industry and considered the benchmark for formability. A comparison of two door panels formed with steel and aluminum using the same stamping die is shown in Figure 2. The difference in the achievable final part can be seen by comparing the areas surrounded by the dashed lines, where sharp features can be seen in the steel part but not in the aluminum one. One approach that could be used to obtain the sharp

features would be to use a subsequent operation to form or to "fill" the sharp corner regions; often referred to as a "Corner Fill" operation. For low formability alloys, this can not always be done economically or effectively. Several techniques exist that can be used to form sharp features in lower formability alloys at the expense of more complex dies and often increased scrap rates. Even worse, the properties of some alloys make some features economically unattainable.

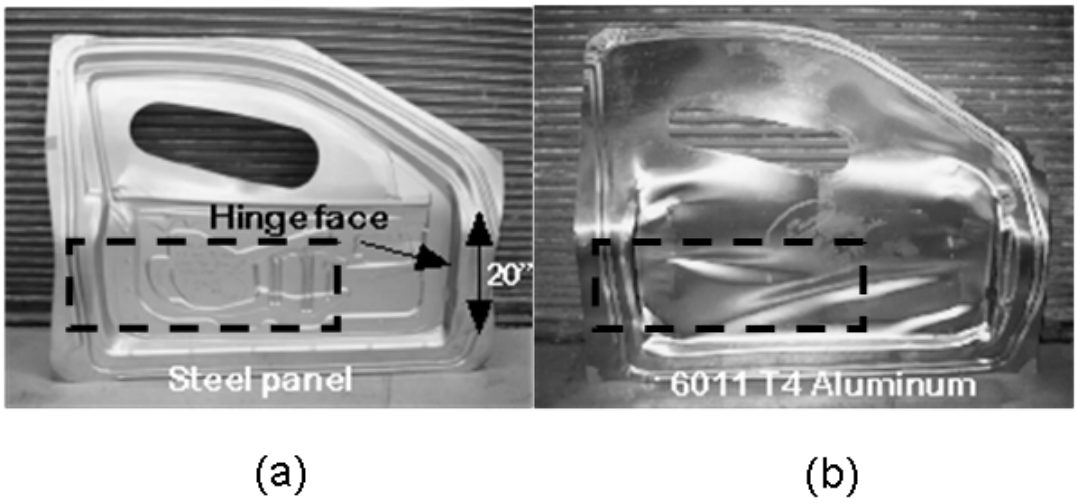

Figure 2: Door panel formed with a) draw quality steel and b) the same door panel formed with 6011 T4 Aluminum alloy. The parts were formed with the same die with some allowances being made for the aluminum part. The difference in formability can be gauged by comparing the areas in the dashed rectangles, where sharp features can be seen in a) that are not present in b) [6].

The door panel in Figure 2 is one possible application where an additional corner fill process could be used. Other target applications include license plate and door handle pockets (Figure 3). Although of simpler geometry than a door panel, these pockets have similar limitations in terms of formability as the door panel shown above.

Figure 3: License plate and door-handle pockets are potential applications of EM hybrid forming [7,8].

The Forming Limit Diagram (FLD) is the standard tool used to measure the formability of sheet metal [9]. The diagram consists of one or more Forming Limit Curves (FLCs) plotted in a Cartesian coordinate system where the axes represent the two principal in-plane strains encountered in sheet metal forming. Figure 4 shows an FLD with FLC's for mild steel and three aluminum alloys. The higher the curves, the more formable the material is; thus, the higher formability of the steel compared to the aluminum alloys is readily apparent.

To use tan FLD, the measured or predicted strains are plotted on the diagram. If the strains are below the curve, the process is considered safe. If the strains fall at or above the curve, the material is expected to localize (neck) and fail. In an FLD, the area to the right of the vertical axes represents biaxial stretching and the area to the left a drawing process. In biaxial stretching, the sheet is deformed in such a way that it will elongate in both the principal directions. Drawing involves elongation in one direction and compression in the other, resulting in the negative values shown in the FLD. Note that for the FLD analysis it is assumed that there are no through-thickness stresses; that is, that there is a plane stress condition. In a typical sheet metal forming operation, the material undergoes both stretching and drawing, as well as bending, which will be described below.

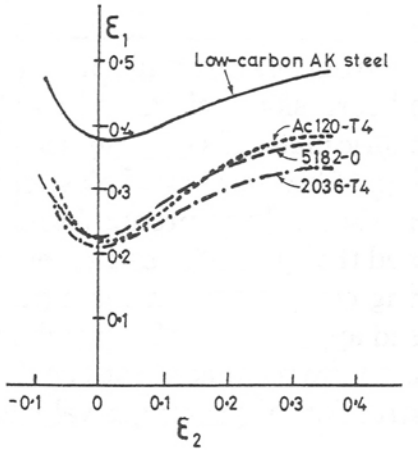

Figure 4: Forming limit diagram showing FLC's for a common automotive steel and three aluminum alloys [1].

In the applications of interest for this investigation (such as the parts in Figure 2 and Figure 3) the critical forming process is drawing. There is no such thing as "pure" drawing since the material will also undergo some stretching and bending. A simple formed part is shown in Figure 5. This part is a simplified version of the pockets shown in Figure 3. The

areas where the part undergoes mostly drawing and bending are illustrated. Figure 6 shows a schematic view of a simple draw with the basic dimensions labeled.

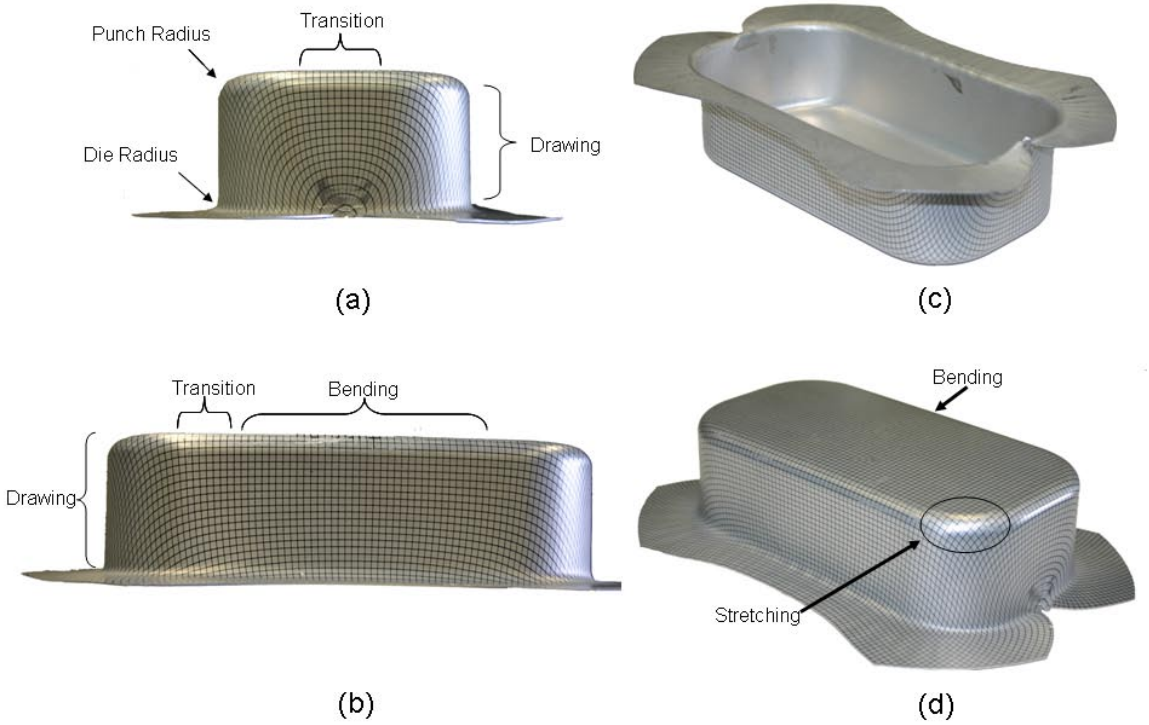

Figure 5: Rectangular draw showing areas were forming corresponds to bending and drawing. Note the grid pattern which illustrates the deformation strains of the material.

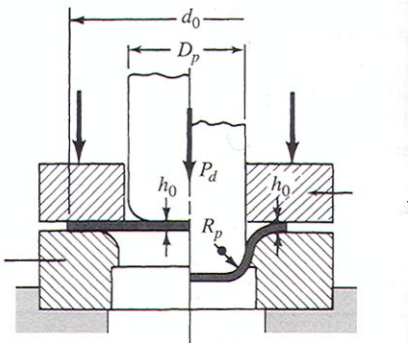

Figure 6: Schematic representation of a cup deep-drawing [9].

For drawing the two most important material parameters are the rate of the work hardening or "n-value" and the ratio of thinning to reduction in width in a tensile test, termed the "r-value" and which is illustrated in Figure 7 [9]. Both parameters in aluminum alloys are inferior for drawing when compared to mild steels. Aluminum alloys in general have r-values

less than unity which means that they thin more rapidly. Drawability is measured by the Limiting Draw Ratio (LDR) which is a ratio of the original blank diameter to the punch diameter (d_o and D_p respectively in Figure 6) that can be formed successfully without necking or wrinkling. Figure 8 shows how the r-value affects LDR. It can be seen from Figure 8 that aluminum alloys generally exhibit lower LDR's than steel. Reduced r-values also affect the stretching behaviour, again due to the proportionally higher thinning, which results in more rapid localization.

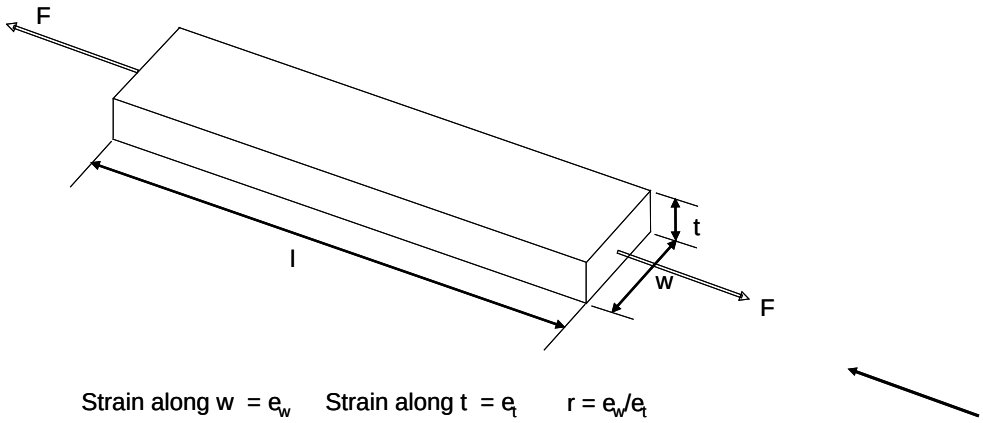

Figure 7: Definition of "r- value".

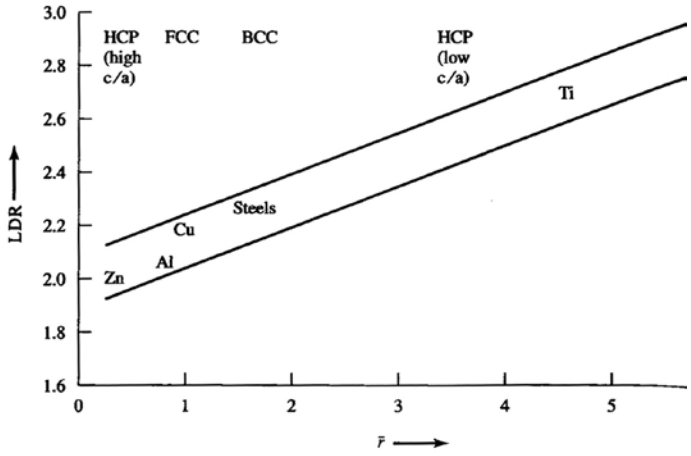

Figure 8: Relation between LDR and r-values [9], where $\bar{r}$ s the average of r-values measured in several orientations relative to the rolling direction.

In terms of the corners of deep pockets, the formability of the aluminum alloys is limited since small punch corner radii result in increased local stretching of the material around the corner. This increased stretching results in proportionally higher thinning and

eventual failure. Thus, punch radii are usually limited to 8 -10 times the sheet thickness [10]. This corner radius limitation can be minimized with some techniques such as blank holder pressure control and die features such as draw beads, draw walls and draw bars [10]. However, these techniques increase the complexity and cost of the dies and result in a lot of scrap material, which is a more significant problem with aluminum since it is of higher cost than steel.

During a typical sheet forming operation, at least part of the material will undergo bending (Figure 9). In bending, the material on the outside of the bend will be in tension and the material on the inside will be in compression. Fracture is the limiting factor in bending [9]. Failure typically occurs on the outside of the bend due to the high tensile stresses present [9]. The formability of aluminum alloys is inferior to that of steel in bending. Many steels can be bent to a bend angle (α_b in Figure 9) of 180 degrees with a near zero bend radius; this performance cannot be achieved with typical commercial aluminum alloys.

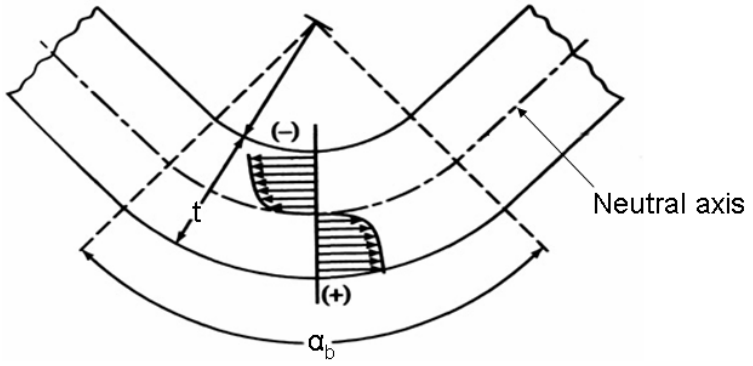

Figure 9: Stress distribution during bending. Image adapted from Schey [9].

Electromagnetic forming has been proposed as a way to obtain deep-drawn parts from aluminum that are comparable to those obtained with mild steel [6]. In principle, the parts would be formed to radii large enough to avoid the use of complicated dies using conventional forming tools like the one shown in Figure 6 and then an EM process would be used to reduce the radii or “sharpen the corner”. An overview of the EM forming (EMF) process is presented in the next sections.

1.2 The EMF Process

The electromagnetic forming process uses the energy stored in a capacitor bank to deform a workpiece, be it a tube or sheet metal. To transfer the energy, the process takes advantage of the repelling force that is produced between two opposing transient magnetic fields. A schematic of the EMF process is shown in Figure 10. The process begins by charging a capacitor bank to the energy required for the specific operation and then discharging it through a coil. A current pulse flows through the coil, generating a transient magnetic field. This magnetic field in turn generates a time varying current in the conductive workpiece, which generates a magnetic field that opposes the field of the coil. The magnetic fields repel one another, generating a body force called the Lorentz force on the workpiece that propels it away from the coil. This force is typically referred to as the "magnetic pressure" [4,5,11,12,13], although strictly speaking this is a body force rather than a surface traction. Given the characteristics of the EMF process (see Section 1.7), the repelling body force behaves as if it was applied on the surface of the workpiece, hence the term "magnetic pressure".

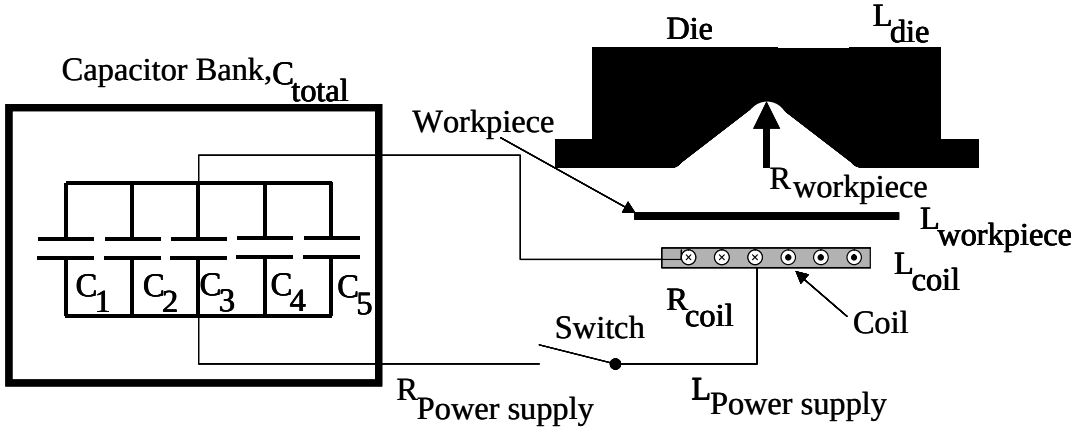

Figure 10: Schematic of EM forming.

Electromagnetic forming can be divided in two major categories: forming of axi-symmetric workpieces (*e.g.* tube) and forming of sheet. EM forming of axisymmetric workpieces has been a niche manufacturing technique for many years. This process uses solenoidal or ring-shaped coils that produce a nearly uniform magnetic field to expand or contract tube. It is mainly used in industry to produce mechanical joints (crimping) [13].

Since this proposal is concerned with sheet metal, forming of axi-symmetric workpieces will not be discussed in detail; the reader is referred to [12,13,14] for further information.

1.3 EM Forming Of Sheet Metal

EMF can be used to form parts from flat sheet, or to sharpen features of pre-formed workpieces (Figure 11) in hybrid operations as previously described. Often, sheet metal workpieces do not deform uniformly under EM loading, as do tubes for example, leading to additional complications in the design and implementation of the process.

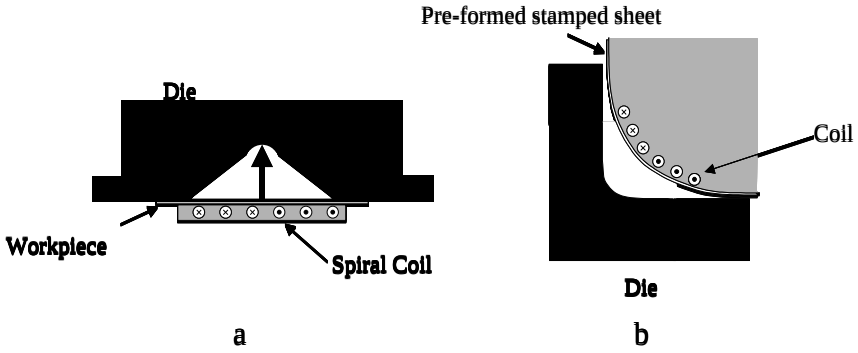

Figure 11: Schematic representations of a) flat sheet forming and b) feature sharpening or corner fill.

Flat or "pancake" coils are generally used to form parts from sheet metal (Figure 12). These coils do not produce uniform magnetic fields and often have dead spots where the magnetic field, and thus the induced forces are zero [11, 15]. These non-uniform magnetic fields lead to non-uniform force distributions that can cause significant problems when forming sheet metal and must be taken into account when designing the processes. Uniform pressure coils (or actuators, as they are called by their developers) have been proposed to solve these issues in some applications [16].

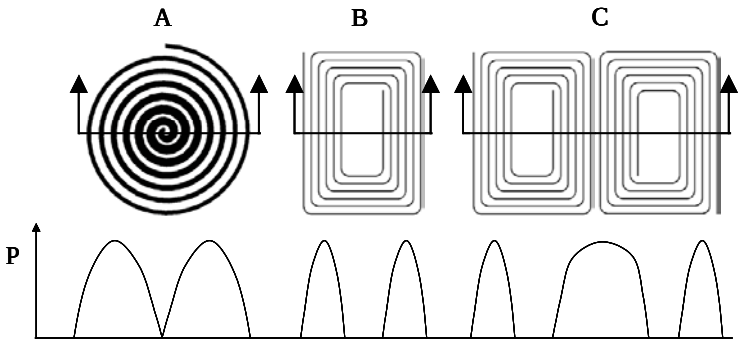

Figure 12: Types of flat or pancake coils with approximate resulting pressure distributions along indicated sections [11,15].

EMF of sheet has become the focus of numerous investigations due to the possibility of increasing the formability of aluminum alloys. Several studies have indicated that the formability of aluminum increases when it is formed using high-speed processes like EMF or electrohydraulic forming [17,18,19,20,21,22,23,24]. Significant increases in formability have been observed in electro-hydraulically formed AA 6061 (Figure 13) [19,20] and EM formed AA 6111 (Figure 14) [21]. Both figures show a significant increase in formability when compared to the conventional forming limit diagram (FLD). Previous work by the author [17] has also demonstrated increases in formability for AA 5754 and AA 6111 formed into conical cavity dies

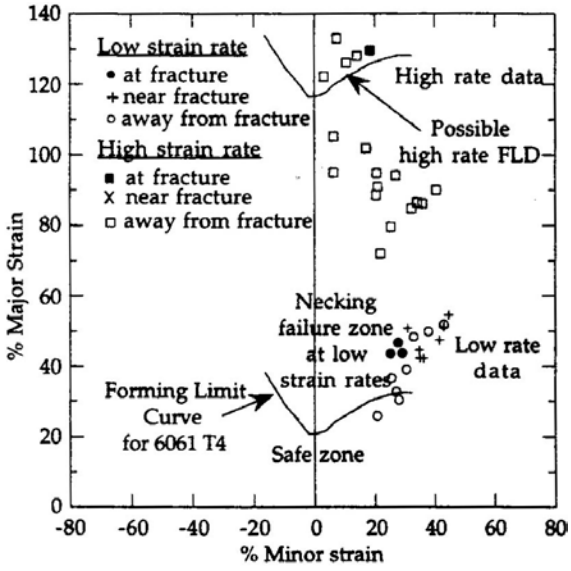

Figure 13: Formability data for electrohydraulically formed AA 6061 [19,20].

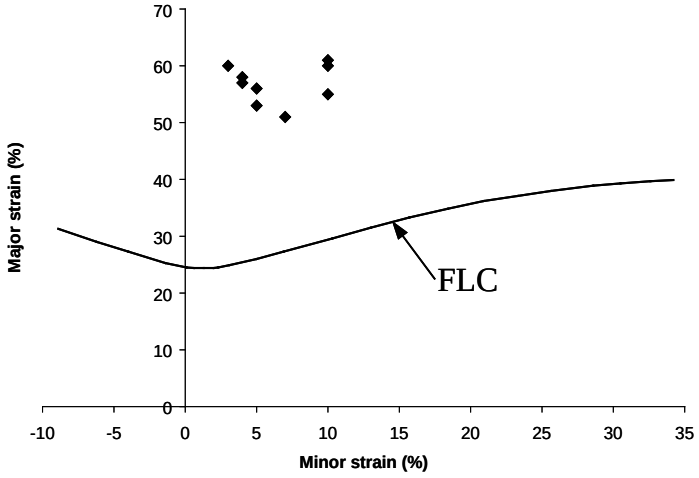

Figure 14: Formability data for AA6111-T4 EM formed into a V-die (taken from Golovashchenko *et al.* [21]). Forming limit curve (FLC) provided by ALCAN International [25].

1.4 Factors that Influence Formability in High Velocity Forming

The increases in formability observed in high speed forming have been attributed to constitutive and inertial effects. Constitutive effects are introduced by so-called high strain rate behaviour of materials, while inertial effects encompass the effects caused by velocity gradients within the parts being formed and the rapid decelerations during contact (impact) with rigid tooling.

1.4.1 Constitutive Effects - High Strain Rate Behaviour of Aluminum Alloys

At high strain rates, some materials exhibit an increase in flow stress and ductility [26]. Although aluminum alloys typically show hardly any strain rate sensitivity for the strain rates and temperatures involved in conventional forming operations, at high strain rates and temperatures, some aluminum alloys show strain rate dependence. The increased formability observed in high velocity forming processes has been attributed in part to strain rate effects. The available information indicates that the flow stress of most aluminum alloys is only mildly strain rate dependant, but that the composition of the alloys plays an important role in how elevated strain rates affect properties.

Figure 15 shows the strain rate sensitivity of pure aluminum and aluminum alloys, as compiled by Lindholm *et al.* [27]. A “strain rate sensitivity parameter” was used that is equal to the derivative of the flow stress with respect to the logarithm of the strain rate, normalized by the yield stress. It can be seen from the figure that the strain rate sensitivity decreases with decreasing purity and increasing alloy strength.

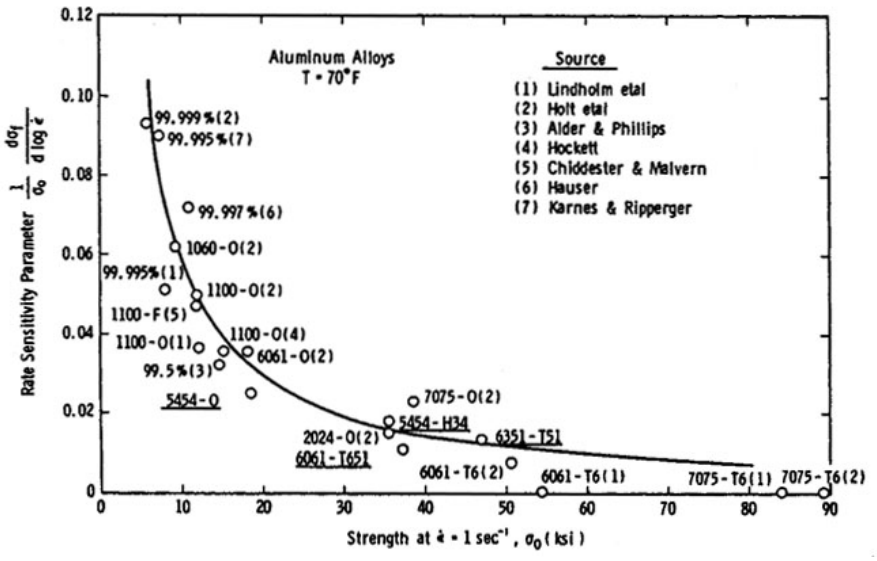

Figure 15: Strain rate dependence of several aluminum alloys compiled by Lindholm *et al.* [27].

Smerd *et al.* [28] studied the strain rate sensitivity of AA 5754 and AA 5182. They found that AA 5754 exhibits some strain-rate sensitivity, while AA 5182 showed little or no rate sensitivity. Figure 16 shows results for AA 5754 tested under quasi-static conditions and at strain rates of 600, 1100 and 1500 s^{-1}. Note that the end of the high strain-rate curves does not represent failure, but rather the strain at which the loading terminated during the test at which point the specimen unloaded elastically. This data cannot be directly compared to the data presented in Figure 15; however, the rate sensitivity parameter for both materials is close to zero.

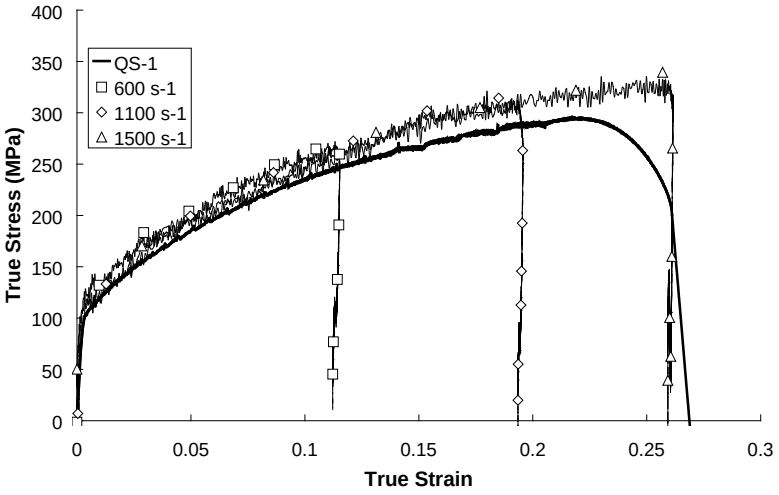

Figure 16: Stress versus Strain at high strain rates for AA 5754 [28].

Tanaka and Nojima [29], Mukai *et al.* [30], Higashi *et al.* [31] and Oosterkamp *et al.* [32] have also studied similar alloys and have reported little or no strain rate sensitivity at room temperature.

1.4.2 Inertial Effects

It has been reported that inertial effects increase ductility [19,20,33,34,35,36,37,38,39]. These effects occur in addition to any rate sensitivity of the material. The reasons for this increase in ductility are not yet completely understood; however, several theories have been proposed. Ragazzoni *et al.* [35] proposed that the increase in elongation was caused by an unloading front, which results in an extra amount of deformation in the non-localized region of the part.

Another theory proposes that necking is retarded by the inertial forces caused by the difference in velocity within the part [19,20,36-39]. At high speeds, the difference can be substantial enough to produce an inertial force opposite to the applied force. Several researchers [19,20,36-39] have argued that this inertial force reduces the net load on the part, retarding necking (Figure 17).

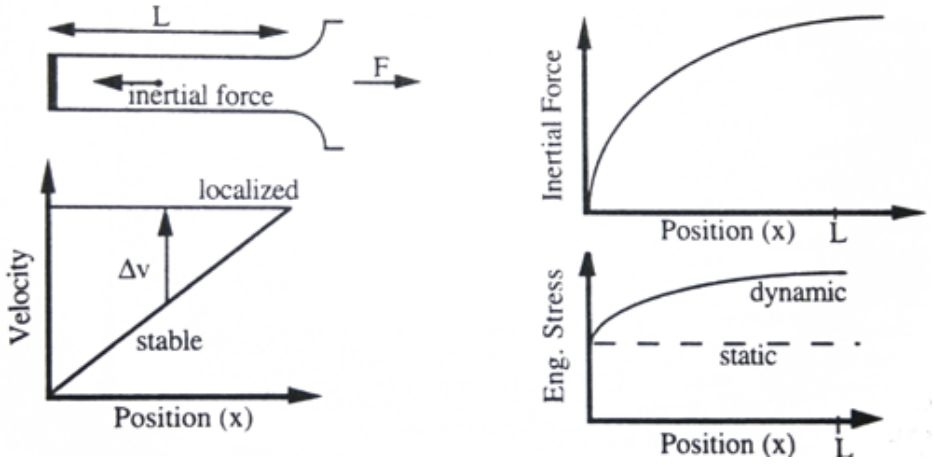

Figure 17: Inertial force neck retardation effect as proposed by Balanethiram and Daehn [19].

1.5 Tool/Sheet Interaction Effects

The interaction between the tool and the sheet as it impacts the die, makes the EM forming process significantly different from standard sheet forming operations. Recent work

by Imbert [17] suggests that this interaction produces the increased formability observed. This conclusion was reached by comparing the formability of sheet that was free-formed (*i.e.* for which no contact is made with a die) by EM forming to that of sheet formed into a conical cavity die. Figure 18 shows the formability results for free formed samples made from AA 5754 and AA 6111. No significant increases in formability are observed when compared to a standard forming limit curve (FLC). In contrast, when the sheet is formed into a conical die, the formability increases substantially, as is shown in Figure 19.

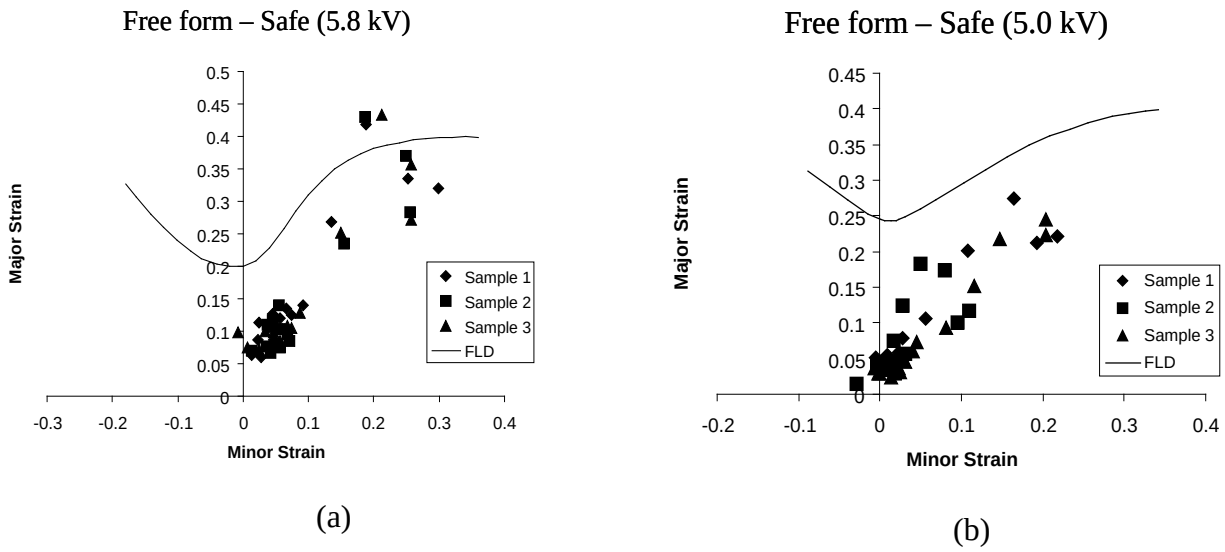

Figure 18: Formability data for free-formed a) AA 5754 and b) AA 6111 samples. The curves are conventional FLCs for the respective materials [17].

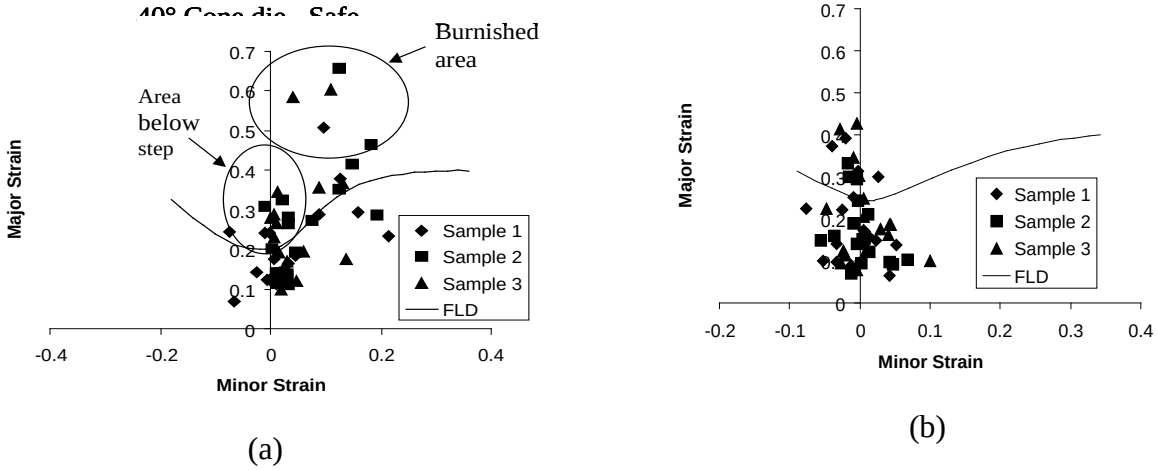

Figure 19: Formability data for conical a) AA 5754 and b) AA 6111 samples. The curves are conventional FLCs for the respective materials [17]

The first analysis of the tool/sheet interaction was presented by Balanetherian [20], who proposed that when a sheet of material impacts a die at high velocities, a compressive through-thickness stress is generated (Figure 20). Balanetheriam [20] suggested that the compressive forces "contribute to stretching of the sheet metal instead of localization", in a form of "inertial ironing". The behavior at impact was simplified for this analysis; however, it predicts the presence of large through-thickness compressive stresses, which are an important feature of the interaction.

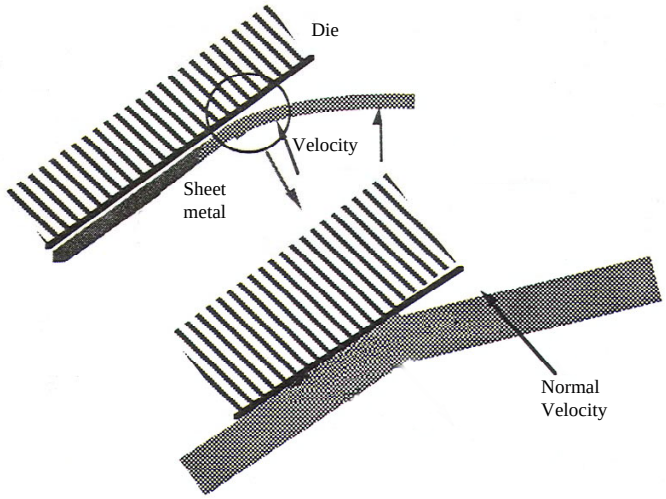

Figure 20: Schematic diagram illustrating the inertial ironing effect [20].

Golovashchenko [40] studied the effect of impact on EM tube forming numerically and reported compressive stresses on the order of the yield strength. Fenton and Daehn [41] have also studied the impact pressures created by sheet forming, and found that they peaked at approximately three times the yield stress of the material.

Imbert [17] modeled EM forming of sheet metal into a conical die using LS-Dyna [42] and a Gurson-Tvergaard-Needleman (GTN) constitutive model, [43,44,45,46] and found that the process produces an unusual forming history for a sheet metal operation, which results in a complex stress state, very high strain rates and non-linear strain paths. Figure 21 presents a detailed view of the tool/sheet interaction for an area close to the tip of the conical die. The tool/sheet interaction can be divided into regions A, B and C, corresponding to the periods prior to, during and after impact with the die.

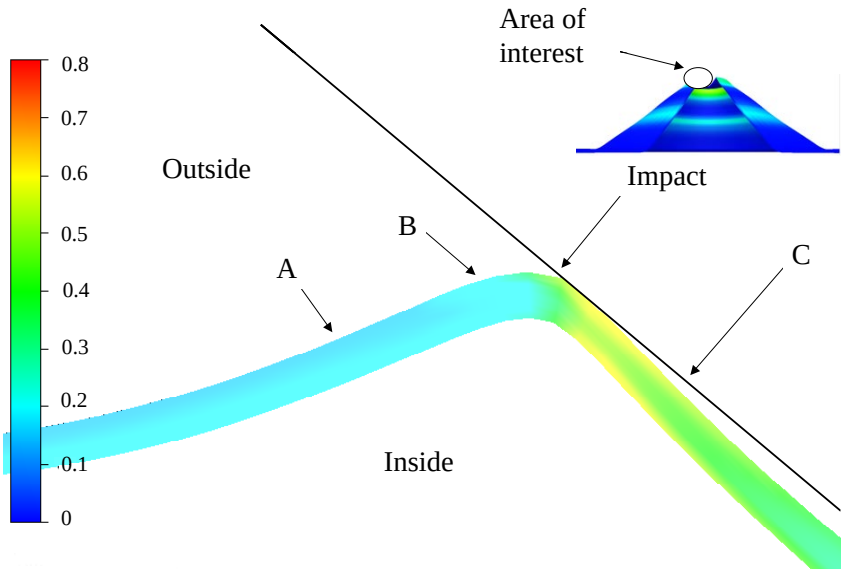

Figure 21: Effective plastic strain distribution as the sheet is formed into the die. Contours are effective plastic strain [17].

Substantial through-thickness stresses were predicted to occur at the time of impact in [17], which is consistent with the inertial ironing proposed by Balanethiram and Daehn [19,20]; however, the predictions of [17] indicate that the through-thickness stresses are not uniform throughout the thickness. The tool/sheet interaction also results in shear stresses and strains that likely contribute to the increased formability by introducing a shear deformation mode that is not typically encountered in conventional sheet metal forming, for which the stress state is nearly plane stress [17].

The predicted strain rates reported in [17] for the free-formed samples were on the order of 3000 s^{-1} compared to 10,000 s^{-1} for the conical elements at the time of impact. These rates are very high and characterization of the stress-strain behaviour for sheet aluminum alloys at these rates is not readily available.

1.5.1 Effects of Compressive Stresses on Formability

Negative hydrostatic stresses (hydrostatic pressure) will retard or even suppress void damage. This effect has been demonstrated in numerous studies [47,48,49,50,51]. Materials deformed under hydrostatic pressure have shown an increase in ductility and a change in failure mode from ductile fracture to plastic collapse or even brittle fracture [49-51] (Figure 22). The predicted hydrostatic stresses for both free-formed and conical formed parts from [17] are shown in Figure 23. It can be seen that very large negative stresses are produced at

impact for the conical part, while for the free formed parts, positive hydrostatic stresses are present for most of the forming process. A comprehensive review of the literature on the effects of hydrostatic stress on ductility and failure modes is given by Lewandowski and Lowhaphandu [47].

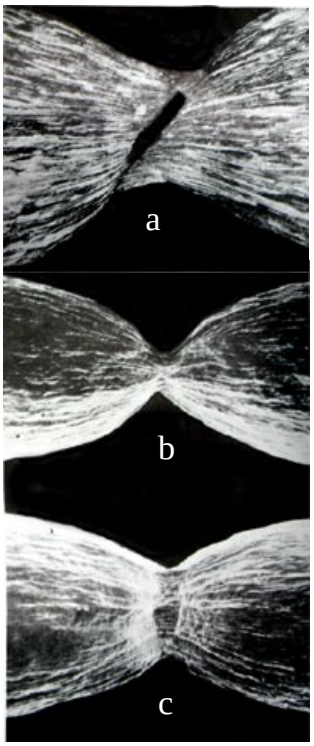

Figure 22: Aluminum-Copper alloy deformed at a) ambient pressure and b) and c) with a hydrostatic pressure of 300 MPa. Images b and c show views of the neck of the same specimen at 90º from each other [51].

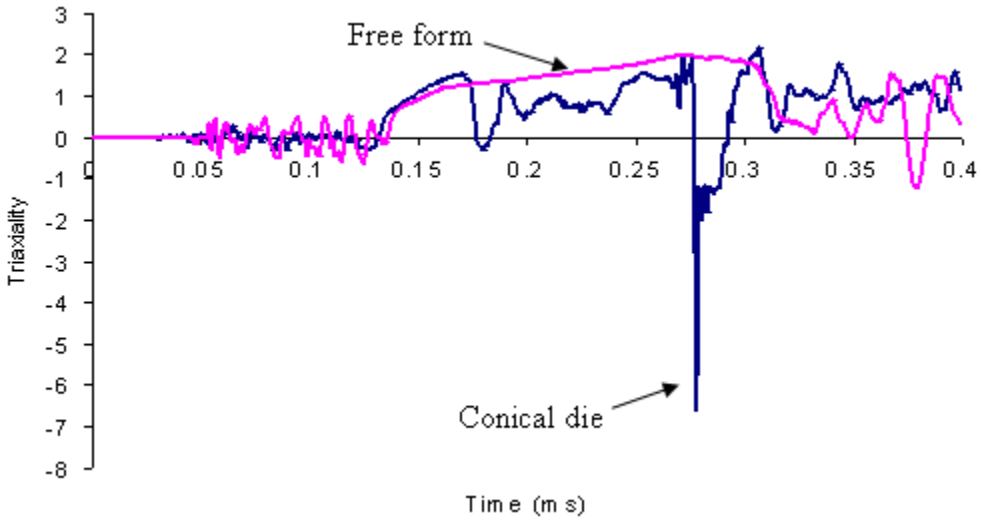

Figure 23: Triaxiality histories for a typical location in a free-formed and conical sample [17].

Evidence of the presence of compressive hydrostatic stresses can be found by examining the failure modes and measuring the damage in the materials. Metallographic and scanning electron microscopy (SEM) analysis of the fracture surfaces for AA 5754 and AA 6111 have shown evidence of a change in failure mode during EM forming [17]. Figure 24 shows a comparison of the fracture of AA 5754 sheet for quasi static, high strain rate and EM formed conditions. The amount of thinning observed in the EM sample is larger than that observed in the other two cases. This thinning is similar to the thinning reported in [51] and shown in Figure 22 b) and c) which indicates that large compressive hydrostatic stresses were present.

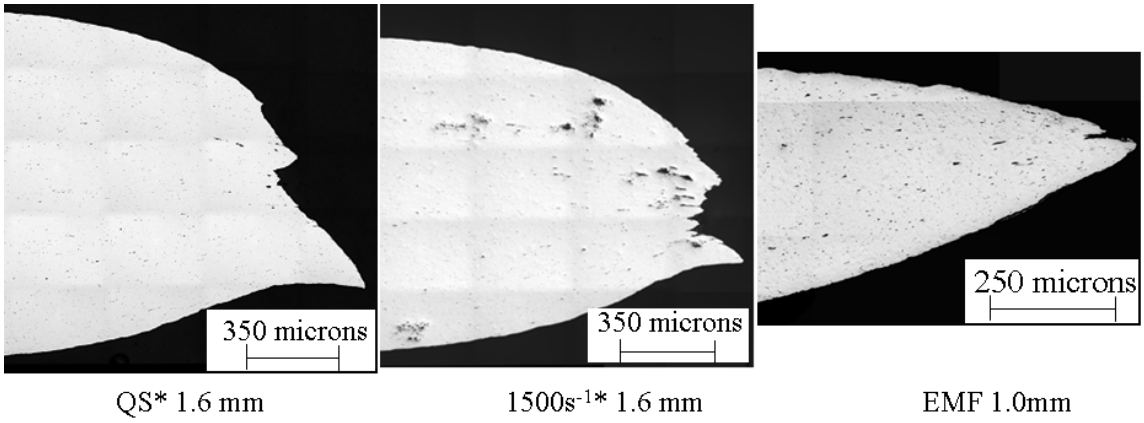

Figure 24: Comparison of quasi static (QS), high strain rate ($1500s^{-1}$) and EMF failure of AA 5754 sheet. * taken from [52] and EMF from [17].

SEM analysis of the fracture surfaces of AA 5754 samples formed under quasi static, free-forming EM and conical die forming conditions have shown that there are significant differences between the fracture surfaces of EM formed material and those formed using quasi-static forming [17]. These differences could be the result of compressive stresses or material rate sensitivity at the very high strain rates generated. Changes in failure mode were also observed in AA 6111 [17].

Another indication of the presence of hydrostatic stresses is the suppression of micro-damage. Damage measurements form EM formed samples have shown relatively small increases in damage relative to the damage increase expected in quasi-static forming, which indicated that damage suppression could be taking place [17].

1.6 Strain Path Effects

Strain paths are very important when dealing with sheet formability [53,54,55]. The conventional FLD approach assumes that deformation occurs in a linear path in strain space. If the strain path varies during forming, the formability of the material will be affected [53]. Predicted strain paths from [17] were shown to be highly non-linear, especially when the sheet is interacting with tool. Some forms of pre-straining can improve formability; however, biaxial pre-strain has been shown to decrease formability in AA6111 [53]. No data was found for pre-straining effects on AA 5754, but work on AA 5052 has shown that biaxial tensile deformation followed by uniaxial deformation increased formability when the sheet was formed under near plane strain condition [55].

1.7 Electromagnetic Basics of the EM Forming Processes

A detailed analysis of the electromagnetic theory that explains the physics of the EM forming process is beyond the scope of this work. This section is intended to provide the reader with a basic understanding of the physics that are at play in EM forming. A rigorous analysis of EM forming theory is offered by Belyy *et al.* [56] and an in-depth analysis of the interactions of magnetic fields with solids is presented by Moon [57]. Electromagnetic phenomena permeate, literally, our daily lives. Most of us are familiar with the ability of electromagnetic waves to transmit information, be it through radio, television or the myriad of the now ubiquitous wireless devices available. Another commonly used electromagnetic phenomenon is the ability of transient magnetic fields to generate current in a conductors and the ability of transient currents to generate magnetic fields. It is this phenomenon that is exploited in EM forming, since it can be used to transform electrical energy into mechanical energy.

In EM forming, the energy required to deform the sheet metal is transferred to the sheet by interacting magnetic fields that are generated as a high frequency transient current passes through a coil that is in close proximity to the workpiece. This current generates a magnetic field which induces currents on the workpiece. Since these induced currents are also transient, they will generate a magnetic field. The two magnetic fields interact resulting in body forces on the workpiece. It is these forces that produce the deformation on the workpiece.

Despite the complexity of the electromagnetic interactions that occur, the EM forming process can be represented by a relatively simple electrical circuit like the one shown on Figure 25 [4-12]. In the schematic the workpiece, be it sheet or tube, is represented by circuit with an induction and a resistance. The EMF apparatus consists of a magnetic pulse generator (MPG) and a coil that is in close proximity to the workpiece. A typical MPG consists of a capacitor bank and the electrical busses and connections that are needed to connect them to the electrical power supply and to the coil. A real MPG has a resistance and induction associated with it, that are represented in the basic circuit shown.

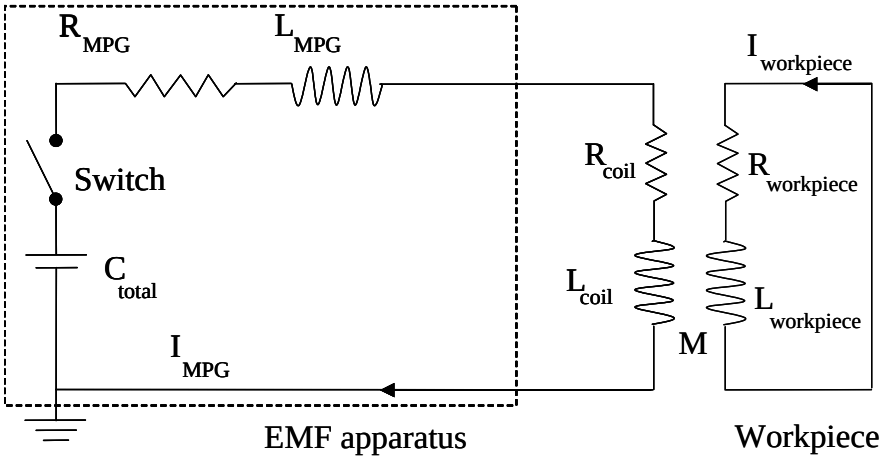

Figure 25: Simplified EM forming circuit. C= capacitance, L= inductance and R= resistance. The magnetic mutual induction is represented by M.

To begin the analysis, consider the EMF apparatus part of the circuit (Figure 26). The MPG section of the apparatus is used to store the energy and to create a transient current, which when it passes through the coil will generate a transient magnetic field that will be the means of transferring the energy from the capacitor bank to the workpiece. The energy is stored by the capacitors and the maximum energy that can be stored is given by

$$E = \frac{1}{2} C V_0^2 \qquad \textbf{Equation 1-1}$$

where V_0 is the charging voltage applied to the capacitors.

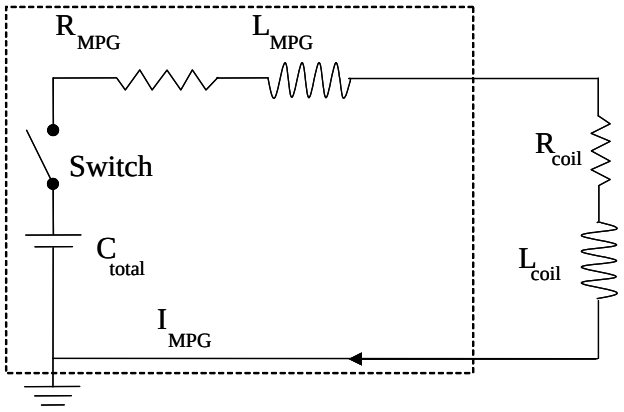

Figure 26: Circuit for the EMF apparatus.

The EMF apparatus can be analyzed using the well known RLC circuit analysis. The circuit can be simplified by obtaining an equivalent resistance and inductance using,

$$R_a = R_{coil} + R_{MPG}$$ **Equation 1-2**

and;

$$L_a = L_{coil} + L_{MPG}$$ **Equation 1-3**

Using conservation of energy, an expression for the energy of the circuit can be obtained, which is given by [58];

$$L_a I(t)\frac{dI(t)}{dt} + \frac{Q}{C_{total}}\frac{dQ}{dt} + I^2(t)R_a = 0$$ **Equation 1-4**

Where, I is the current, Q the charge in the capacitor, C_{total} is the capacitance. The first term represents the magnetic energy stored, the second the electrical energy stored in the capacitor and the third the energy dissipated in the form of heat by the resistance of the circuit. To obtain a profile of the circuit, the time derivative is taken to obtain a power equation. Taking the derivative and realizing that $\frac{dQ}{dt} = I(t)$, one obtains;

$$\frac{d^2 I(t)}{dt^2} + 2\xi\omega\frac{dI(t)}{dt} + \omega^2 I(t) = 0$$ **Equation 1-5**

where

$$\xi = \frac{1}{2}R_a\sqrt{\frac{C}{L_a}}$$ **Equation 1-6**

and

$$\omega = \sqrt{\frac{1}{L_a C}} = 2\pi f \qquad \textbf{Equation 1-7}$$

where f = frequency in Hz. Solving for the current yields the following equation;

$$I(t) = \frac{V_0 \sqrt{\frac{C}{L_a}}}{\sqrt{1-\xi^2}} e^{-\xi\omega t} \sin(\omega t) \qquad \textbf{Equation 1-8}$$

which is the equation of a damped sinusoid. The maximum current is given by;

$$I_{\max} = V_0 \sqrt{\frac{C}{L_a}} \qquad \textbf{Equation 1-9}$$

The damping is the result of the energy dissipation due to the resistance of the circuit. A sample current profile obtained by using the parameters of the University of Waterloo's MPG is shown on Figure 27.

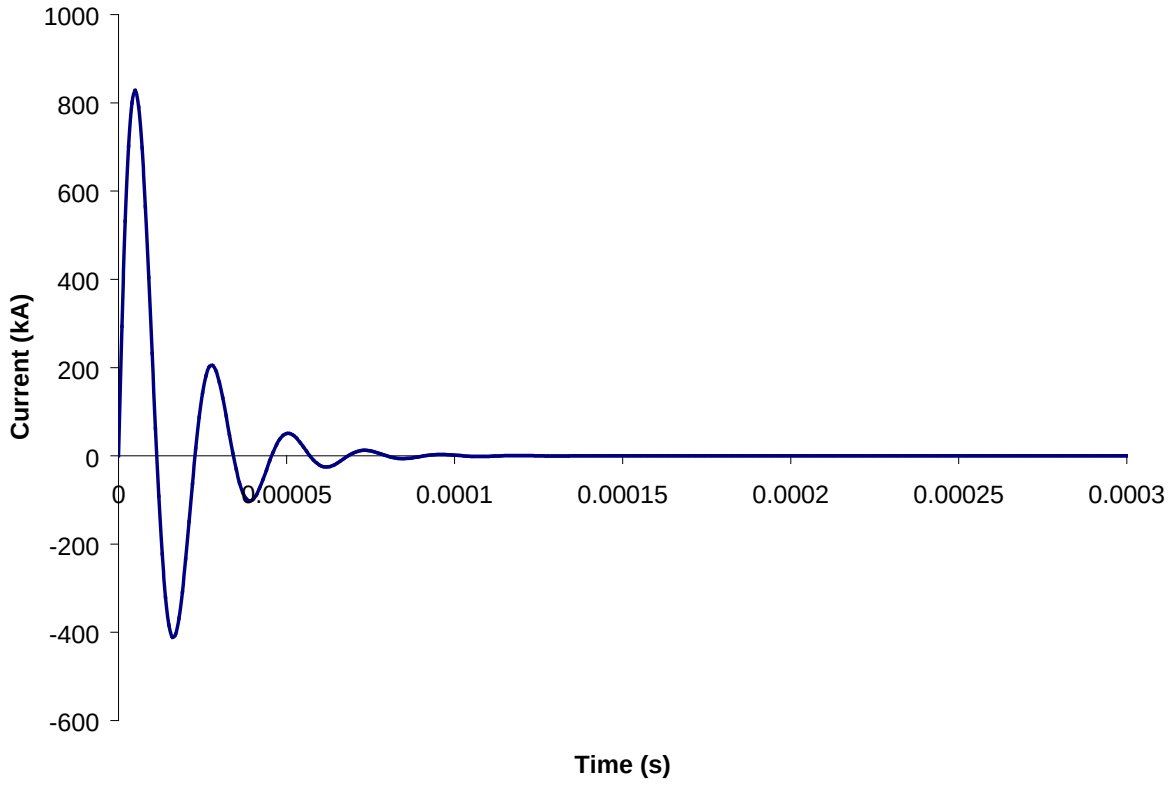

Figure 27: Current profile produced by equation 1-8 with the R, L and C values for the MPG generator of the University of Waterloo.

The transient nature of the current results in a transient magnetic field at all points of the circuit were current is flowing. The coils are designed to generate a magnetic field close to the workpiece that will result in forces being induced on the workpiece, which will result in the workpiece deformation. With the workpiece as part of the process the electrical circuit is now back to the one that is shown in Figure 25. Following Al-Hassani *et a.* [59], the energy equation for such a circuit is given by;

$$L_e I(t)\frac{dI(t)}{dt} + \frac{Q}{C_{total}}\frac{dQ}{dt} + I(t)^2 R_e + \dot{w} = 0 \qquad \textbf{Equation 1-10}$$

where L_ϵ is the equivalent induction of the circuit, R_ϵ the equivalent resistance and $\dot{w}$ the rate of doing mechanical work in the form of changes in geometry of the circuit. Ideally, the only mechanical work done by the circuit would be in the deformation of the workpiece; however, in practice work can be done in the displacement of the coil, connector cables and bus bars of the apparatus.

Although equation 1-10 appears to be relatively simple, the determination of the equivalent inductance and resistance at any given time during the discharge and, in particular, the rate of doing mechanical work can be very difficult. An analysis of tube EM tube expansion using a solenoid coil is presented in [12,59] and an analytical solution for forming sheet metal using a spiral coil is presented in [15]. General analytical solutions for EM forming of sheet metal are not available and numerical methods are typically used. To illustrate the effect of adding a coil and deforming sheet metal to an EM forming apparatus compare Figure 27 and Figure 28. The former is an ideal current profile calculated for a capacitor bank without a coil and with the properties of the University of Waterloo's MPG; the latter is an actual experimental current profile produced while forming a sample using the MPG in question. Note that in Figure 28 the peak current and the frequency of the current pulse are lower than for the ideal case, with the peak current and frequency being 823 kA and 44 kHz for the ideal case compared to 282 kA and 12 kHz for the actual case. The differences are the result of the addition of the coil and workpiece in the circuit.

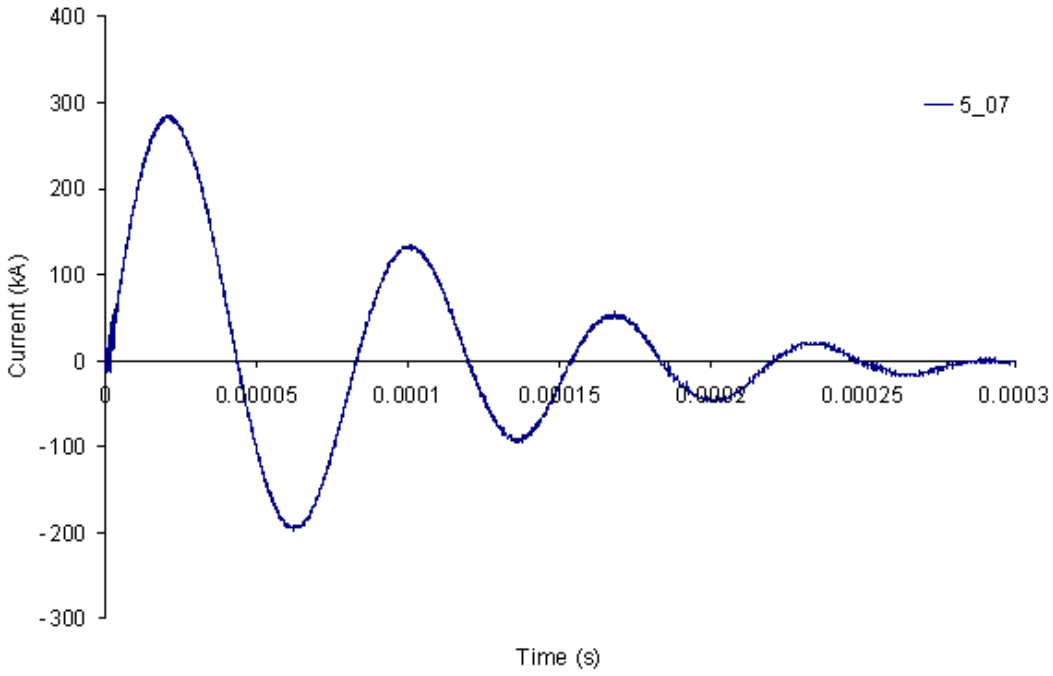

Figure 28: Current profiles for an EM forming experiment performed for this work. The MPG used was the same one whose properties were used to generate the curve shown in Figure 27. Note that peak current and frequency are lower, which is due to the inductance from the coil and the effect of the workpiece.

1.7.1 Maxwell's Equations

The induction of currents within the workpiece, like all electromagnetic phenomena, are governed by Maxwell's equations. There are several formulations of these powerful equations, the one presented below is the low frequency or "eddy current" approximation for good conductors with low frequency varying fields such that $\varepsilon \frac{\partial \vec{E}}{\partial t} \prec\prec \sigma \vec{E}$. This formulation is used since it is the one solved by the simulation software used in the current research and the assumptions are held in EM forming processes [60].

$$\vec{\nabla} \times \vec{E} = -\frac{\partial \vec{B}}{\partial t} \qquad \textbf{Equation 1-11}$$

$$\vec{\nabla} \times \frac{\vec{B}}{\mu} = \vec{j} \qquad \textbf{Equation 1-12}$$

$$\nabla \bullet \vec{B} = 0 \qquad \textbf{Equation 1-13}$$

$$\nabla \bullet \varepsilon \vec{E} = 0 \qquad \textbf{Equation 1-14}$$

where $\vec{E}$ is the electric field, $\vec{B}$ the magnetic flux density, $\vec{j}$ the total current density, μ the permeability, and ε is the permittivity. To solve the equations for EM forming analysis, additional constraints are required which are given by;

$$\nabla \bullet \vec{j} = 0 \qquad \textbf{Equation 1-15}$$

$$\vec{j} = \sigma\vec{E} + \vec{j}_S \qquad \textbf{Equation 1-16}$$

$\vec{j}_S$ is the divergence free source current density and σ the conductivity.

Electric and magnetic fields are intrinsically linked by equation 1-11. The relation between current and a changing magnetic field is given by 1-12. To analyze an EM forming process these equations must be solved and the effects of the material deformation must be taken into account.

This formulation of the equations does not take into account the fact that the workpiece is moving, which is a justified simplification since in the numerical models the process is broken into steps and at each step the sheet is considered to be stationary. Formulations of Maxwell's equations that take into account velocity effects have been developed, the first of these are known as the Maxwell-Minkowski equations, which are described by Tai [61], who also describes other formulations for moving media. A complete analysis of the deformation of moving media under the effect of magnetic fields incorporating velocity effects is presented by Pao and Hutter [62]. A more detailed discussion of these formulations was considered beyond the scope of this work.

1.7.2 Lorentz's Forces

The interaction of the magnetic fields from the coil and the workpiece creates body forces on both the workpiece and the coil. Lorentz's law governs the generation of these forces:

$$F = \vec{j} \times B \qquad \textbf{Equation 1-17}$$

where F is the Lorentz force. For a body with constant current density and magnetic flux and a simple geometry equation 1-17 can be solved relatively easily (e.g. tube expansion with a solenoidal coil). However, in EM sheet forming operations the current density can vary significantly in the workpiece, the magnetic flux on the workpice will be non uniform and the

geometry can be complex and rapidly changing, which will affect the current density and the magnetic flux. The ensuing complexity leads to the need for numerical models for these problems.

1.7.3 Workpiece Geometric Effects

This section describes three characteristics of transient currents in EM forming that are related to the geometry of the coil/workpiece combination and are of significant practical importance for the process. A detailed explanation of the causes will not be provided. The first of these properties is the tendency of a flowing current to take the path of least resistance, which results in currents taking the shortest path along a coil [57]. For example, in a wound helical coil the current will tend to flow on the inside, since the circumference will be smaller than on the outside.

Currents induced on a conductor will tend to flow in the part of the conductor that is closest to the coil that is inducing the current [57]. For example, the current induced in a sheet of aluminum by a spiral coil will flow on the area of the sheet that is closest to the coil. Also, the current on the coil will tend to flow on the surface of the coil that is closest to the workpiece.

Transient magnetic fields will penetrate metals to a certain depth and this effect is called the "Skin Effect". The depth of penetration is given by [11]:

$$\delta = \sqrt{\frac{2}{\mu_0 \sigma \omega}} \qquad \textbf{Equation 1-18}$$

where σ is the conductivity, ω the ringing frequency (2π x frequency) in Hertz and μ_0 the permeability of free space.

Magnetic field frequencies within a certain range will cause the skin penetration to be greater than the thickness of the sheet, leading the field to "leak" through the workpiece, thus reducing the efficiency of the forming operation [11,63]. Therefore, an optimal skin depth exists for EM forming processes [11,63].

1.8 Numerical Simulation of EM Forming

Like conventional forming operations, numerical methods can be used to simulate EM forming processes. The time-varying magnetic fields produced make the modeling of EMF more complex. Three numerical approaches have been used to model the EMF process:

- Use of a structural code with an analytical pressure distribution;
- Use of an EM code to calculate the pressure distribution, which is then used in a structural code ;
- Simultaneous solution of the EM and structural equations.

Applying an analytical pressure distribution to the workpiece in a structural code is the simplest way to model the process, since it does not require time consuming and expensive EM computations. Accuracy is sacrificed for speed of simulation and computational economy. This approach has been used to model tube forming processes [64,65] and sheet forming [17,66] with good agreement with relatively simple experiments.

The second approach uses an EM code to calculate the pressure distribution and this information is then passed to a structural code. This operation can be done once at the beginning of the simulation, or it can be repeated at discrete intervals throughout the duration of the simulation, leading to what is referred to as a "loosely coupled" code [11,67,68,69]. This process can capture the variation of the pressure distribution caused by the deformation of the workpiece [11,67,70]. This approach has the advantage of using proven codes that can handle complex 3-D structural and EM calculations; however, it is computationally expensive since two codes must solve the respective problems and communicate with each other while doing so.

Codes that can simultaneously solve the EM and structural equations are called "coupled" or "fully coupled" codes. They provide the best available simulation of the time varying pressure distribution, but at substantial computational cost [71]. Another draw back is that they are not widely available, which forces investigators to develop their own codes [40,41,72,73,72,73,74,75,76]. Recently, a fully coupled solver has been added to the commercially available finite element code LS-Dyna [42]. The basic principles of this solver will be described in the numerical section (Chapter 3) of this thesis.

For a detailed review of electromagnetic theory and the modeling of coupled electromagnetic and structural problems the reader is referred to Oliveira [11] and El-Azab *et al.* [71].

1.9 Hybrid Forming in the Literature

Despite the interest shown on this subject by researchers in both academia and industry, there have been very few works published on the subject of hybrid forming. Daehn *et al* [6] attempted to form the sharp features of the aluminum panel shown in Figure 2 using EMF and found that the process was feasible. Figure 29 shows the results of the corner fill operation. Unfortunately, the work did not go beyond a feasibility study.

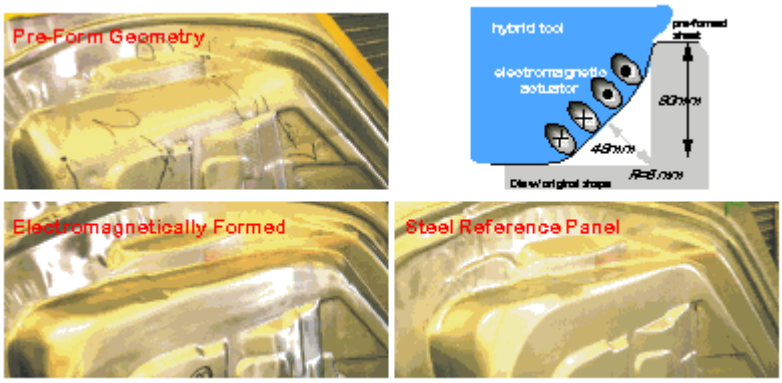

Figure 29: Results of corner fill study with an inner door panel [6].

Oliveira [11] studied corner fill numerically and analyzed the effect of pressure distributions, for an axi-symmetric geometry. The induced force distribution was found to have a significant effect on the final shape of the material in the corner. It was reported that the dead spots produced by certain coil designs were very significant in determining the final shape of the material. Shang [77] developed a hybrid forming method to aid in the drawing of deep parts. In these processes EMF is not used to form sharp features, but rather to aid in deep-drawing by applying energy to specific areas to help feed the material into die. Significant increases in drawing depth were reported. A novel approach to eliminate spring back was proposed by Woodward *et al.* [78], which consisted of using a current pulse to vaporize a thin sheet of metal in the area of a pre-formed part where spring back was an issue. The technique shows promise for low volume application.

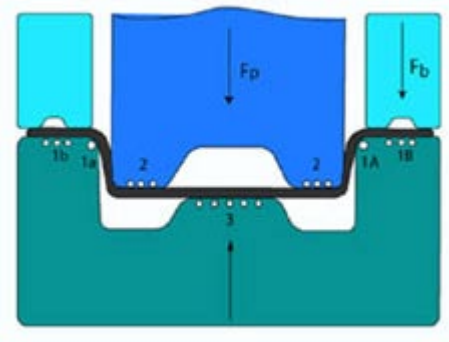

Figure 30: Schematic of an EM assisted forming operation [77].

EM forming has also been proposed as a pre-forming step for hydroforming operations by Psyk *et al.* [79]. Psyk *et al.* [80,81] studied sharpening of a feature on a representative full-scale automotive stamping similar to that studied in [6]. Their experimental tooling is shown in Figure 31. Their work showed that the process was feasible; unfortunately, they reported deviations from the desired final geometry of the part. The deviations were reportedly caused by the rebound that was allowed to occur within the necessary clearance between the sheet and the die.

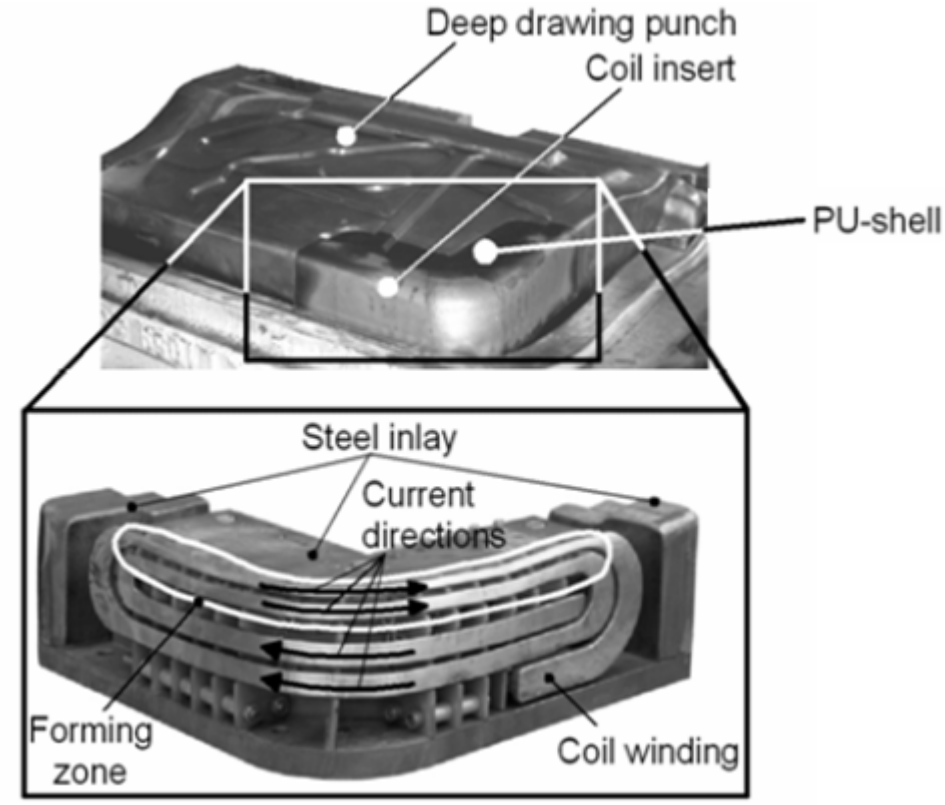

Figure 31: Corner fill experimental tooling from Psyk *et al.* [81].

Liu *et al.* [82] showed that EM forming was a feasible process for sharpening corners on axisymmetric deep drawn parts. This work focused on a deep drawn cup similar to the ones used in LDR tests.

Golovashchenko [83] studied both electromagnetic and electrohydraulic forming as a means to achieve sharp radii on a representative automotive production part. The part consisted of a deep pocket with relatively sharp corners that could not be formed conventionally. The process consisted of pre-forming the blank and then using EM and electrohydraulic corners to sharpen the corner. It was reported that EM forming could be used to form two dimensional radii, but not three-dimensional ones, where electrohydraulic forming was required.

1.10 Present Work

The available literature indicates that EM forming can improve the formability of aluminum alloys under certain conditions. However, the work that has been published so far is limited to samples with relatively simple geometries often formed with pancake coils. Practical applications, such as forming of interior door panels and license plate pockets, require forming of complex geometries, likely using custom designed coils and collectors. There is sufficient evidence to indicate that the stress states created by the tool/sheet interaction play a prominent role. However, the process is not understood to the point where clear design guidelines can be confidently proposed and more work is needed to address this issue. Investigation of more geometries and driving pressure distributions are needed to gain a better understanding of the tool sheet interaction. Also, the strain rates predicted for the process are far in excess of the data available for most materials in the literature. Information about the behaviour of materials at these high strain rates is needed to determine whether or not constitutive effects are important.

The goal of the current work was to determine whether EM forming could be used to form sharp features in aluminum alloy AA 5754 1 mm sheet that could not be formed using conventional forming and to determine what factors were important in such an operation. To this end, experimental and numerical studies were carried out. Two types of EM operations were studied in this work; a single step EM forming operation and a hybrid forming operation that combined conventional pre-forming using a stamping operation with an EM corner fill.

The single step EM process is illustrated schematically in Figure 32. This process did not prove successful for corner fill, but provided valuable insight into EM forming processes.

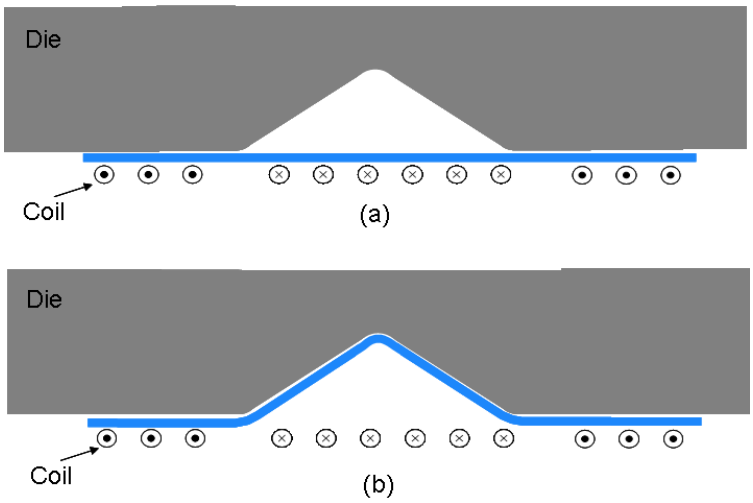

Figure 32: Schematic of the single step EM process.

The hybrid operation chosen for study consisted of pre-forming the material using a v-channel tool to an outside radius of 20 mm while allowing draw-in and then reducing the radius to 5 mm using EM forming without draw-in. Figure 33 shows the nominal pre-formed and final sample shapes used for this work. A schematic of the EM corner fill operation is shown in Figure 34. This geometry was chosen for the current work becasue the pre-formed part could not be formed to a 5 mm outer radius using a conventional stamping operation if the material was not allowed to draw into the die. Thus it was important to ascertain whether the hybrid EM process could successfully perform this corner fill operation. This experiment serves to represent a multi-step forming process in which the material within a larger part is constrained from drawing-in to sharpen a corner feature, in which case an EM forming step could provide a means to sharpen corner radii.

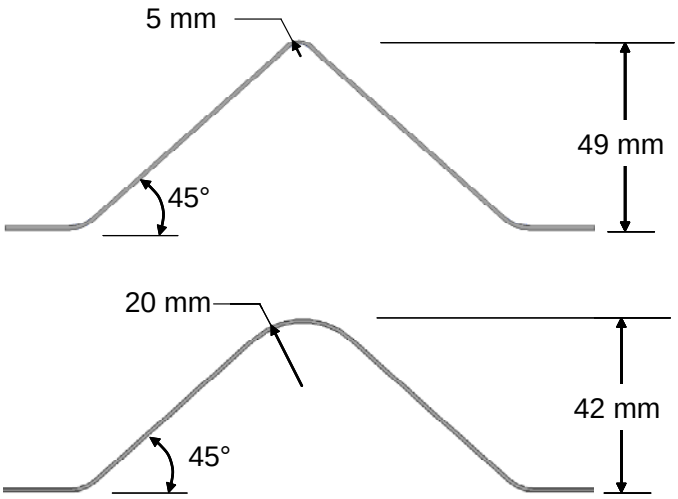

Figure 33: Cross section of the experimental geometries in the 20 mm radius pre-form and nominal 5 mm outer radius final shape.

Figure 34: Schematic of the EM corner fill step of the hybrid process.

For the hybrid forming experiments, the sheets were tested in the as-received condition and in a pre-strained condition with nominal pre-strains of 5, 10 and 15%. The strains within the samples were measured and compared to traditional forming limit curves. Metallographic analysis was also performed to quantify the micro-damage. Numerical analysis was carried out with a commercially available code to gain insight into the process. Due to the high speed of the process and the tooling used, it is difficult to record the process as it happens. This made the simulations an important tool in the analysis of the process, despite the inherent limitations of the software.

In the remainder of this thesis will outline the methods and procedures used, followed by a presentation and discussion of the results obtained. First, the experimental and numerical methods and procedures will be described. Then, the results of the experiments will be presented and discussed. The results of the numerical analysis will be presented and

discussed, with comparisons made to the experimental results when possible. Finally, the conclusions reached will be outlined together with recommendations for future work.

2 EXPERIMENTAL METHODS AND PROCEDURES

The experiments performed as part of this research consisted of conventional forming (stamping), single step EM forming, and hybrid forming operations on AA 5754 1 mm sheet, carried out in the University of Waterloo Electromagnetic Forming Laboratory. The sheets were tested in the as-received condition and after pre-straining to 5, 10 and 15% strain. The experimental program is outlined in Figure 35. The conventional forming operations were stamping operations used to pre-form samples for the EM corner fill and to test if the pre-formed samples could be sharpened to a 5 mm outer radius via conventional stamping.

The single step EM forming experiments were an attempt to form the samples from flat sheet into a final part using a single EM discharge. Such an operation was determined to be unlikely to produce a successful part since excessive rebound resulted in shapes that were significantly different than the desired one. The single step process was not used on the pre-strained sheet.

The majority of the experimental effort focused on the hybrid process that consisted of a conventional pre-forming stage followed by an electromagnetic stage for the corner fill. The experimental methods and apparatus used are described in the following sections.

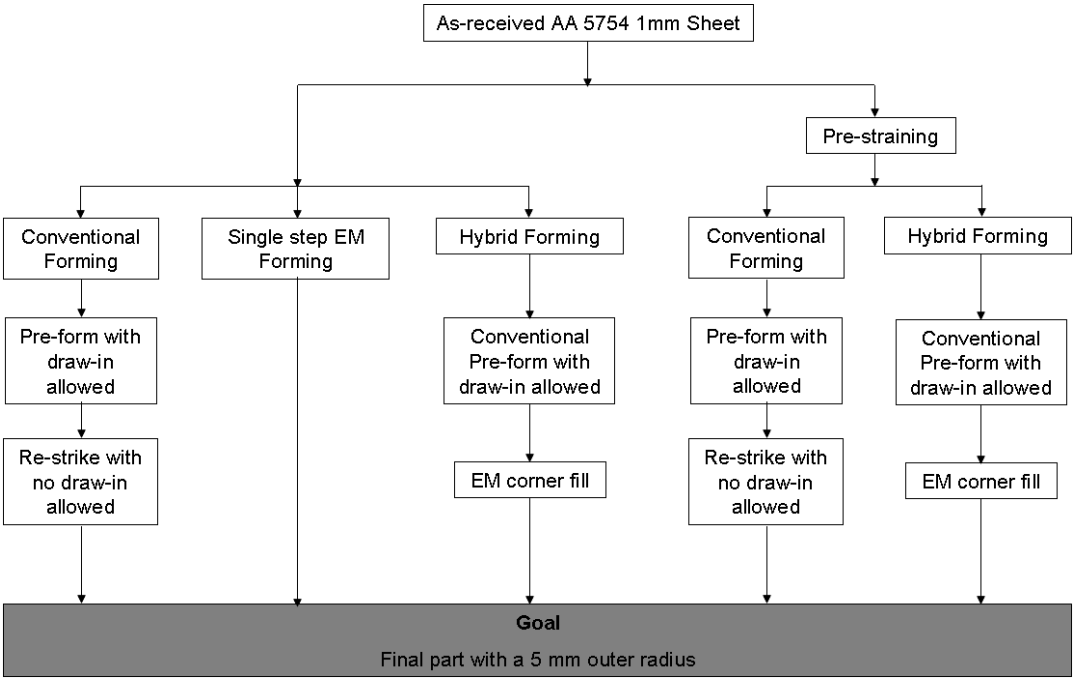

Figure 35: Chart outlining the experimental program for this research

2.1 EM Forming Laboratory

The laboratory consisted of a Pulsar MPW 20 Research Edition Magnetic Pulse Generator (MPG) used in conjunction with a 75 ton hydraulic press. The apparatus is shown in Figure 36. The MPG consists of a capacitor bank and a power supply to deliver the current to the capacitors at the required specifications. The MPG has a nominal maximum energy capacity of 20 kJ and a maximum charging voltage of 9,000 volts. The machine capacitance is 539.7 μF, inductance is 24.35 nH, and resistance is 2.98 mΩ. The nominal discharge frequency using a shorting bar across the output terminals of the capacitor bank was 24.51 kHz (all specifications provided by the manufacturer [84]).

Figure 36: Experimental apparatus showing the MPG and hydraulic press used.

2.2 Material and Sample Preparation

2.2.1 Material Properties

The aluminum alloy AA 5754 in the O temper was used in this work, since it is in relatively wide spread use in the automotive industry. The composition of the alloy is shown in Table 1.

Table 1: Nominal composition (wt%) of AA 5754 [85] aluminum alloy.

Alloy	Mg	Mn	Fe	Si	Zn	Cu	Cr	Ti
AA 5754	3.2	0.2	0.3	0.06	-	-	-	0.01

The quasi-static true stress-strain curve for the AA 5754 alloy is shown in Figure 37. The yield stress was 97.0 MPa [25]. The limited high strain rate data available for this alloy

indicates that the strain rate sensitivity is low (Figure 16) at least for strain rates up to 10^3 s^{-1} [28]. Thus the quasi static stress strain curve provided by the manufacturer (Figure 37) was used.

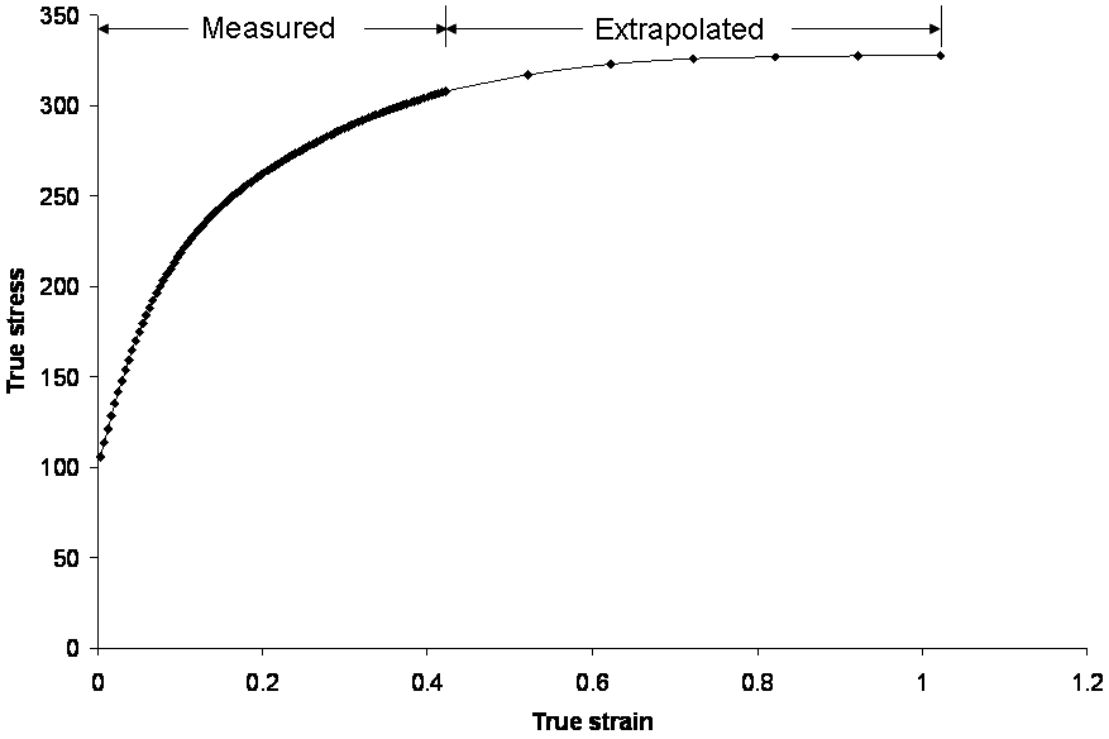

Figure 37: True stress-strain curves for AA 5754 [25].

2.2.2 Sample Size

The material was cut into 197 x 305 mm (8 x 12 in) blanks for the single step EM forming experiments and 152 x 250 mm (6 x10 in) blanks for the conventional and hybrid forming experiments. The specimens were cut with the rolling direction oriented along the longest dimension. No surface treatments were applied, other than the circle gird etching that will be described in the next section.

2.2.3 Strain Measurements

Circle grid analysis was used to measure the strains within the samples. Samples were electrochemically etched with 2.5 mm diameter circles. After deformation, the major and minor diameters of the ellipses resulting from the deformed circle grids on the sample were

measured using a digital image analysis system with a micro-CCD camera (see Figure 38). The strains were measured by taking a digital image of the grid in question and then picking five points on the outside edge of the grids, from which the program calculated an ellipse. The major and minor axes of the ellipse are compared with an average of the diameter of the grids to determine the engineering strain. To determine the average original diameter, at least five grids are measured in an undeformed state. The final strain is the average of three measurements. The accuracy of these strain measurements has been estimated to be ± 3% strain [11]; however, in the current work it was observed that the error could be closer to ± 5%.

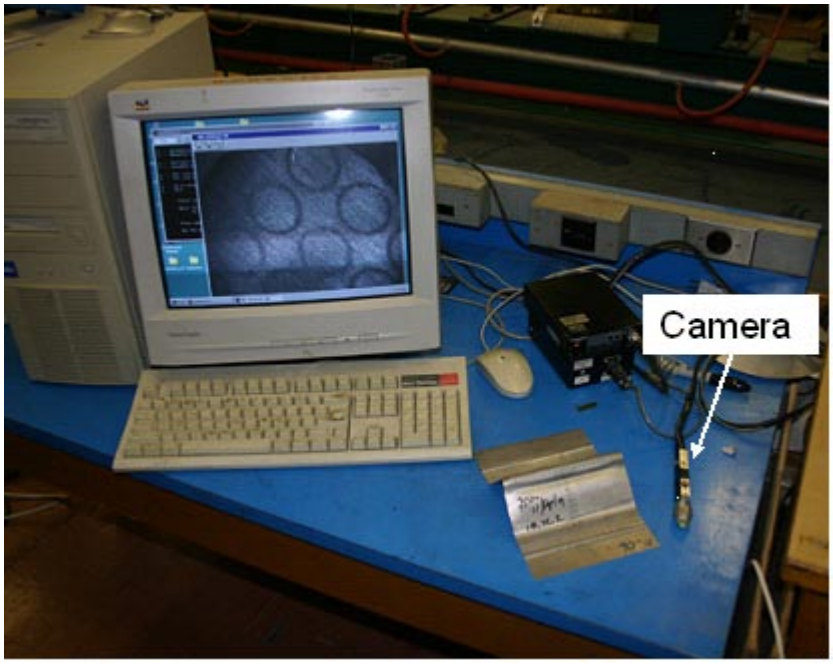

Figure 38: Grid measurement system.

Strain distributions were measured in two directions, transverse and longitudinal, which are illustrated in Figure 39. The grids on the transverse path were the ones that were located at the top of the samples after deformation. The curvature in that area leads to some additional error. Five additional grids were measured in the final corner filled samples in the area were the largest ellipses were observed; strain measurements from these grids were used to generated Forming Limit data.

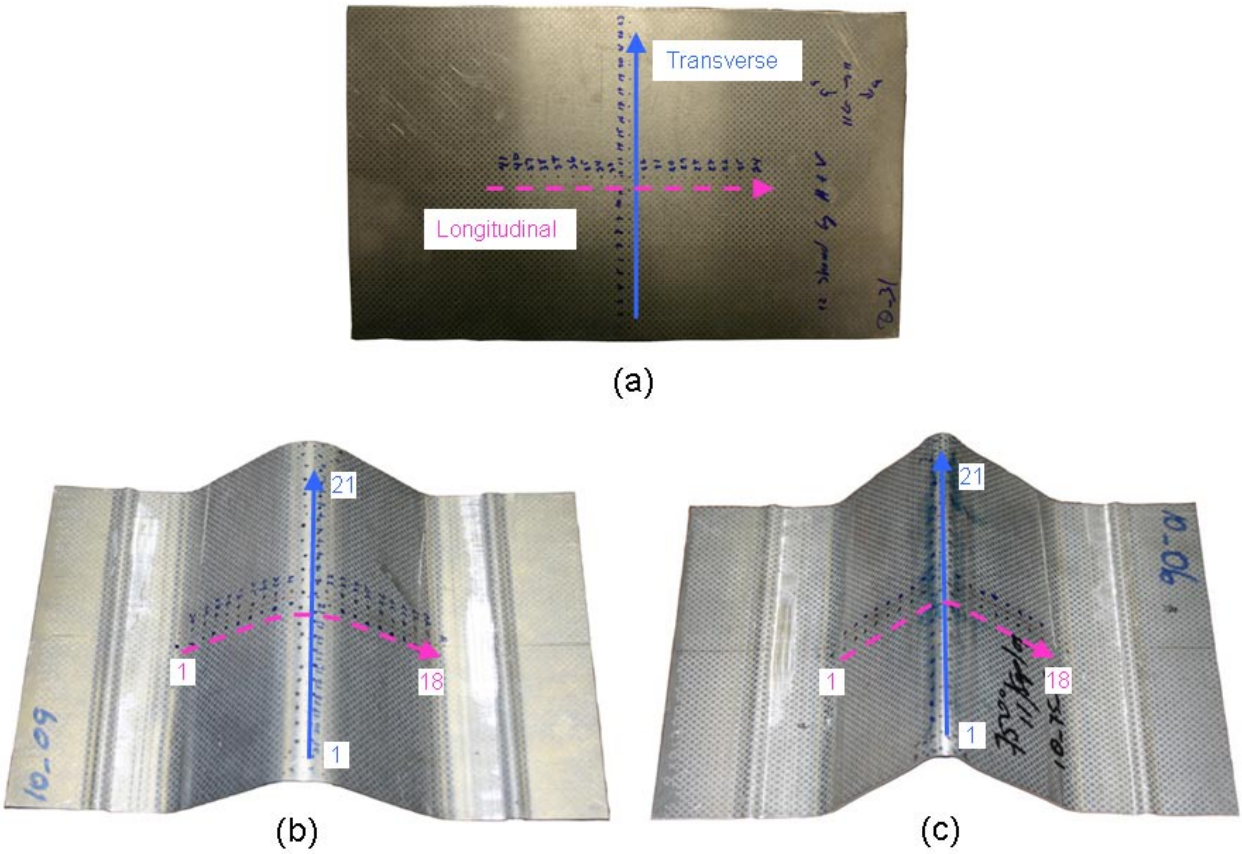

Figure 39: Location of the grids used to measure strain in the a) un-deformed sheet, b) drawn sheet and c) EM corner filled sheet.

2.2.4 Sheet Pre-Straining

Some samples were made from sheet that was pre-strained prior to the EM corner fill operation. The sheets were pre strained by stretching them using a MTS 810 Material Test System (Figure 40). Special grips were manufactured so that relatively large sheet samples could be pre-strained (Figure 40-b).

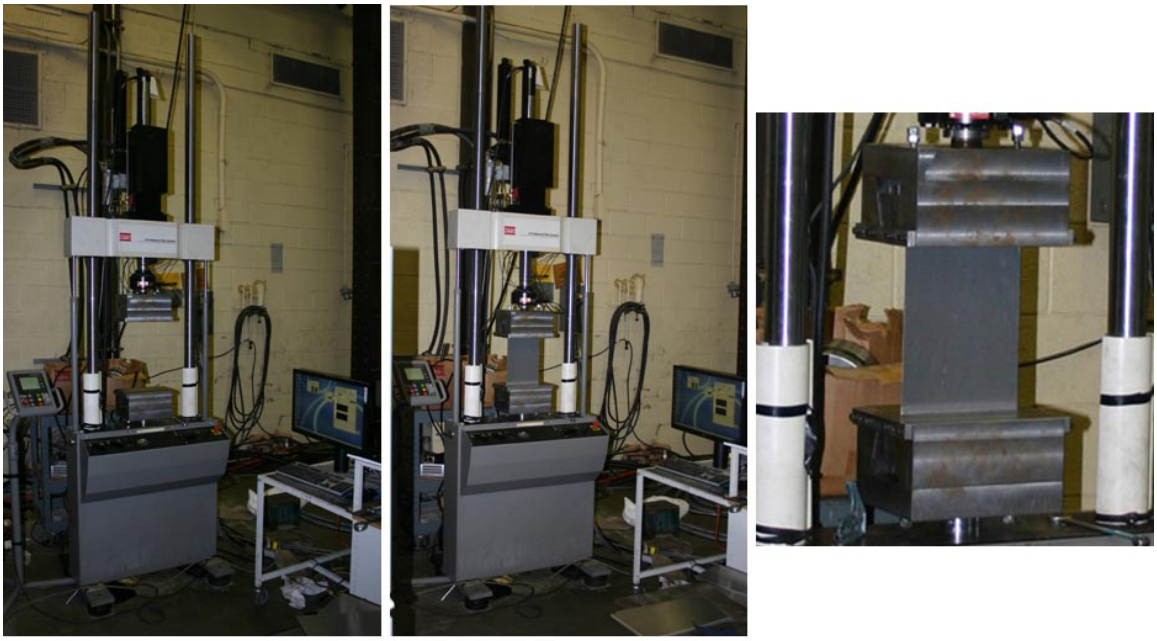

Figure 40: Apparatus used to pre-strain sheets of aluminum a) without and b) with sheet. A close-up of the grips with a sheet sample is shown in c).

Samples of dimensions 203 x 356 mm (8 x 14") were stretched along the 356 mm length, which corresponded to the rolling direction of the sheet. Each grip acted on approximately 53 mm of the sample material on the top and the bottom leaving a 250 mm gauge length. The samples were then stretched until the gauge lengths were increased by 5% (12.5 mm), 10% (25.0 mm) and 15% (38.0 mm). Figure 41 shows deformed samples corresponding to each condition.

Figure 41: Images showing a) 203 x 356 mm (8 x 14") sheet cut from as-received material prior to stretching, and stretched to b) 5%, c) 10 %, and d) 15 %.

Strain measurements from ten samples for the 5% and 10% pre-strained sheets and seven 15% pre-strained sheets were taken to measure the actual strains and determine how much strain had occurred in the direction perpendicular to the stretch. The strains are shown in Figure 42, Figure 43 and Figure 44. All of the strains recorded were lower than the nominal 5, 10 or 15% strain value, but given the ± 3% strain error, the measurements are close to the nominal values. The strains for the 15% pre-strained sheet are biased towards the negative side of the FLD, which are consistent with the reduction in width that is expected due to Poisson's effect as the sheet is stretched. The same effect is present for the other two pre-strain cases, but the strain measurements were not sensitive enough to capture the effect.

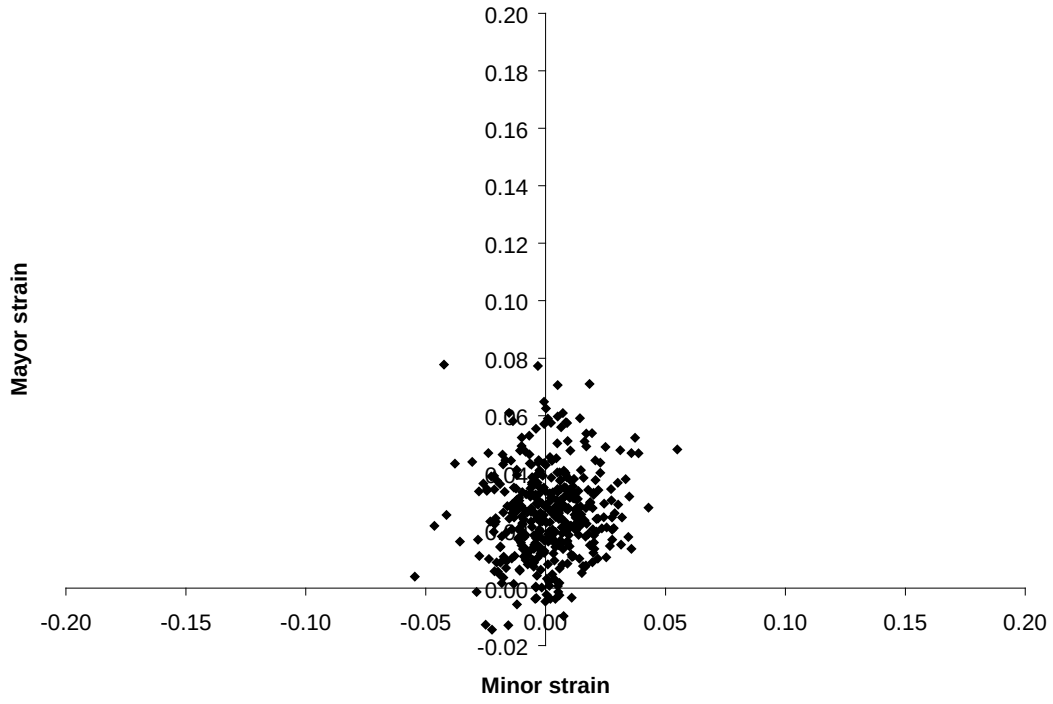

Figure 42: Measured strains for samples pre-strained to 5%.

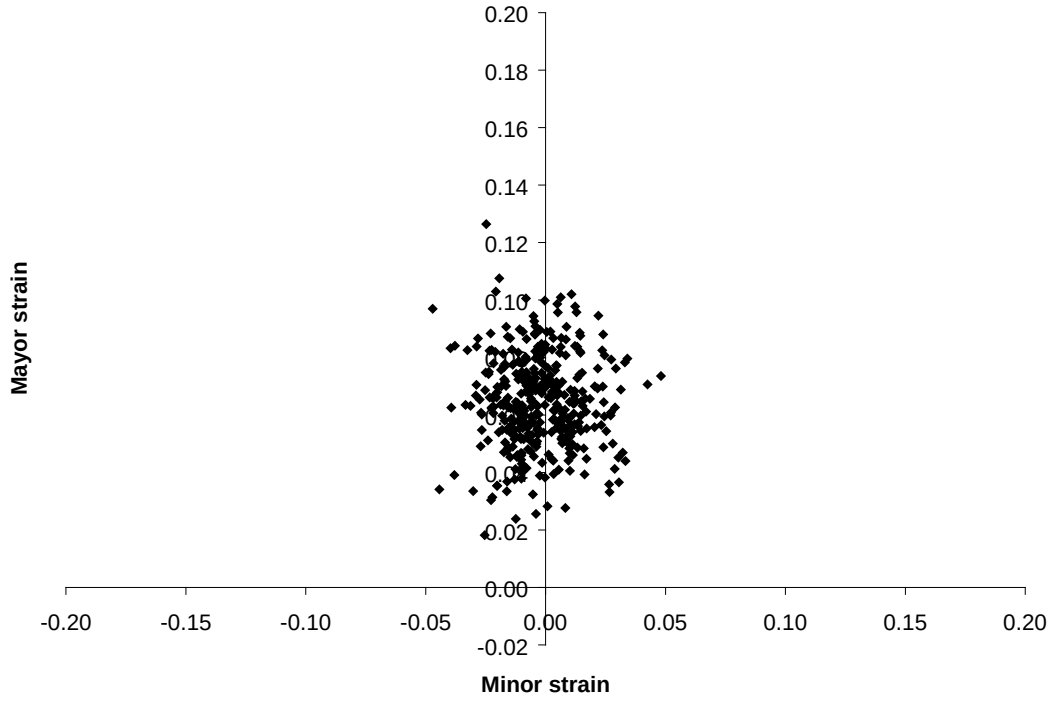

Figure 43: Measured strains for samples pre-strained to 10%.

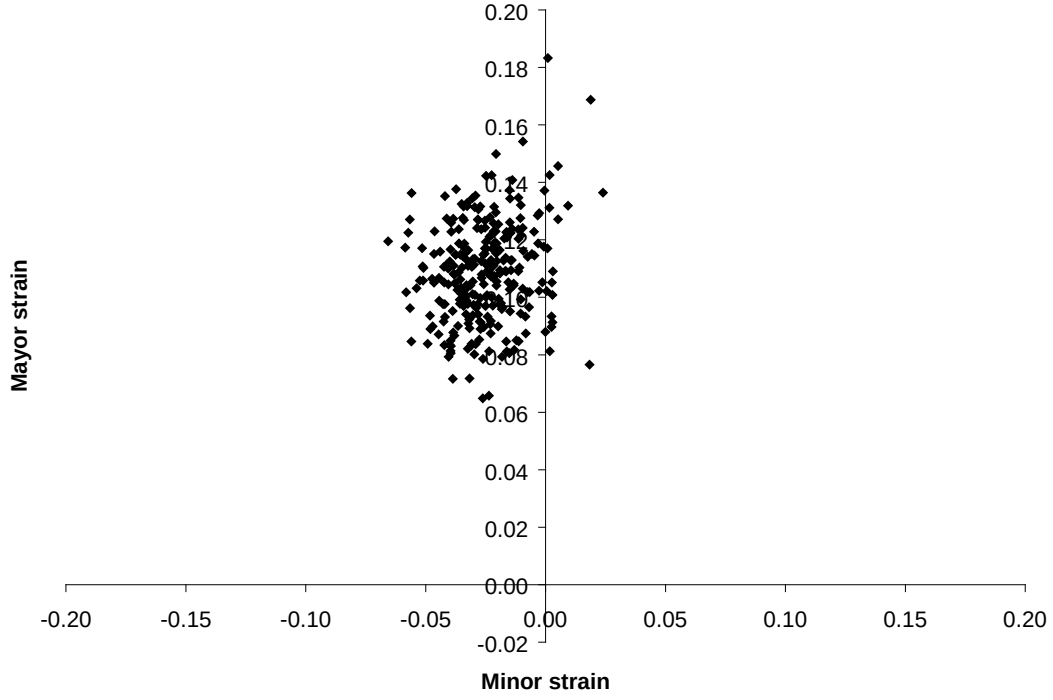

Figure 44: Measured strains for samples pre-strained to 15%.

2.3 Single Step EM Forming Operation

The single step EM forming corner fill was attempted with a v-channel shaped die and a “double-pancake” coil. A schematic of the operation is shown in Figure 45. The v-channel had a side angle of 40° with a 30.5 mm height and a corner radius of 10 mm. A “double pancake” coil was used to create a somewhat uniform pressure distribution on the forming area (Figure 46). The coil was the same one used by Oliveira and it is described in detail in [11]. The die and coil were mounted in the hydraulic press, with the die attached to the hydraulic actuator so that it could be moved up and down. The coil was fixed to the base (Figure 46). The coil was insulated from the sheet by a layer of epoxy that was part of the coil mounting and by Kapton® polymeric sheets, to form an insulating layer of approximately 1 mm thickness (Figure 47). The entire coil and die assembly, as installed in the hydraulic press, is shown in Figure 48.

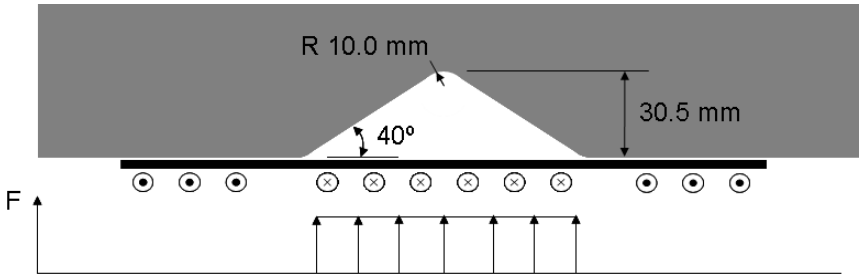

Figure 45: V-Channel dies with idealized pressure distributions for the centre of the coil.

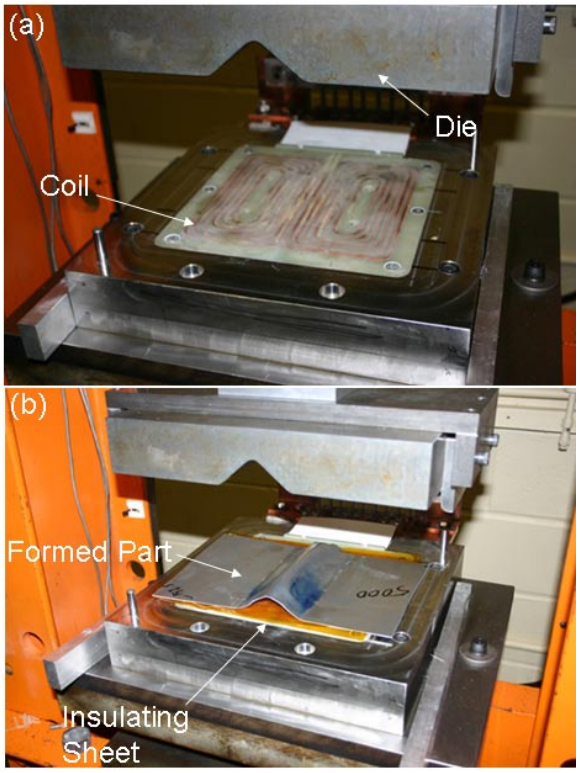

Figure 46: Tooling used for the experiment a) coil and die and b) tooling with a formed part and insulating sheet.

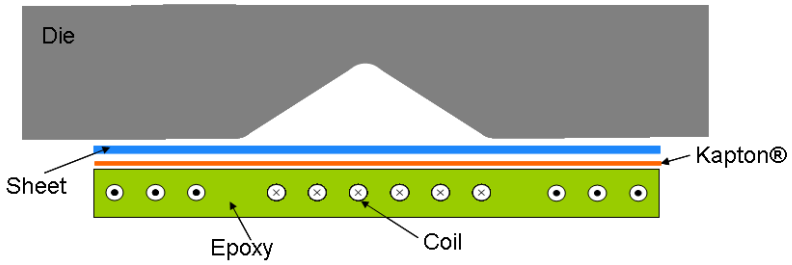

Figure 47: Schematic showing the insulation for the experiments with the double pancake coil.

Figure 48: Coil and die assembly as installed in the hydraulic press.

To form a sample, the sheet was placed over the insulated coil and the die was brought down to hold the sheet in place. Once the sheet was secure, the capacitor bank was charged and then discharged into the coil. With this apparatus, a charge voltage of 5000 V resulted in the sheet making impact with the top of the die. Several voltages were tested before this value was determined. To determine whether the material had made contact with the die, blue ink was placed on the surface. This was necessary because the final parts did not conform to the shape of the die due to rebound and the process was too fast to allow visual determination of whether contact had occurred.

2.4 Hybrid Forming Operation

The hybrid process consisted on pre-forming blanks using a conventional metal forming operation to an outside radius of 20 mm and then reducing the radius to 5 mm using an EM corner fill operation. The process is illustrated in Figure 49. This process was used on samples made from the as-received and pre-strained sheets. The conventional metal forming tooling and the EM corner fill apparatus will be described in detail below.

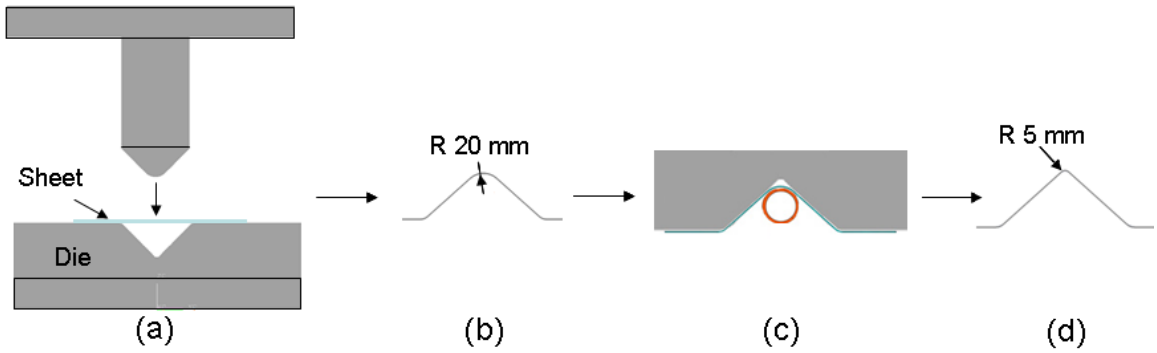

Figure 49: Schematic of the hybrid forming operation which consists of a) conventional forming to produce b) a pre-formed blank with a radius of 20 mm that is then subjected to c) an EM corner fill operation to produce d) the final sample shape.

2.5 Tooling for the Conventional Pre-Form

The stamping tool used for the pre-forming operation consists of a punch, binder and die mounted in a hydraulic press. A schematic of the tool is shown in Figure 50 and a photograph of the actual tool on Figure 51. The tool could be equipped with either draw or lock-beads to achieve forming operations with and without draw-in. Pre-formed parts with a 20 mm outer radius were formed for use in the EM corner fill operation. The tool could also be equipped with a punch for forming parts with outside radii of 5 mm, which was used to test whether a 5 mm outer radius could be formed using a conventional stamping operation. The tool was equipped with four springs that provided a compressive load on the binder that was used to help hold the sheet place.

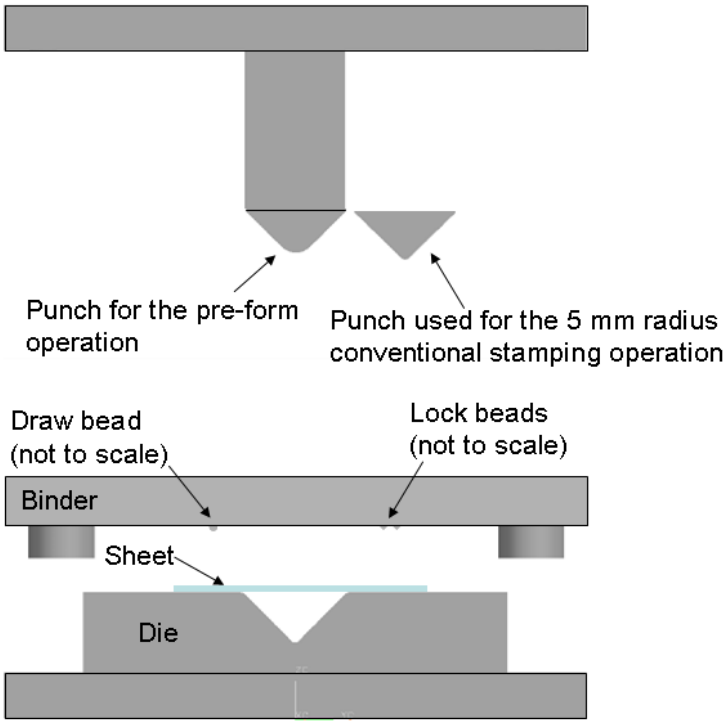

Figure 50: Exploded schematic view of the conventional forming tool used to pre-form the sheet to a 20 mm outer radius.

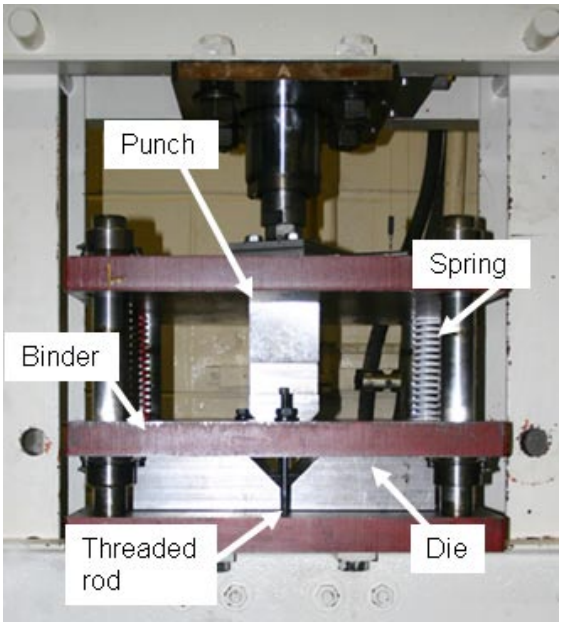

Figure 51: Actual tool used for the conventional forming operations.

Conventional forming operations consisted of placing the sheet on the die and then lowering the binder and punch until the springs reached the highest compression without the punch touching the sheet. Then, threaded rods were inserted and the binder was tightened with

nuts using a torque wrench to prevent the binder from rising during forming. Once the binder was secured, the punch was brought down until the part was completely formed or until fracture occurred. For the pre-formed samples, the draw beads were used and a combination of emery paper and tape was applied to the samples in the bead region to prevent excessive draw-in.

To attempt to form a 5 mm radius with no draw-in, lock beads were used to prevent draw-in in combination with strips of emery paper that were applied to the die. The threaded rods were used as described above and for this forming operation they also helped lock the sample in place.

In order to detect failure, cracks were detected audibly and the maximum forming depth was judged by sight with the aid of marks placed on the tool. The system proved more than adequate for the task.

2.6 EM Corner Fill Apparatus

The EM corner fill apparatus consisted on a coil connected to the MPG and a die, which were mounted on a hydraulic press. The coil is the most important component of the EM corner fill apparatus and a detailed description of the coil and how it was prepared for operation will be presented. A description of the complete EM corner fill apparatus follows.

2.6.1 Coil Used for the EM Corner Fill

The coil for the EM corner fill operation is a critical part of the apparatus. Coil design is one of the most significant problems in EM forming and the coil design for this process was no exception. For this operation the coil had to deliver as much energy as possible to the area that was to be formed and do so while maintaining its structural integrity. Due to the energy capacity of the MPG, the coil had to be as efficient as possible, which for this application required a very low impedance, to obtain a high peak current. Finally, the coil had to fit within the geometric constraints imposed by the pre-formed samples and the connectors for the MPG. Here, the coil design used for the experiments and the complete corner fill apparatus will be described in detail. For completeness, a description of the rejected coil designs, with a brief description of the reasons for their rejection will be presented in a subsequent section.

An illustration of the coil used for the corner fill experiments is shown in Figure 52 with and without a pre-formed specimen. A detailed drawing of the coil is shown in Figure 53. The coil is essentially in the form of a U, with the section that is closest to the part narrowed to increase the current density. The simplicity of the shape was chosen not only for its current flow characteristics, but also because it had significant structural strength once it was assembled for use with the connectors and an internal support.

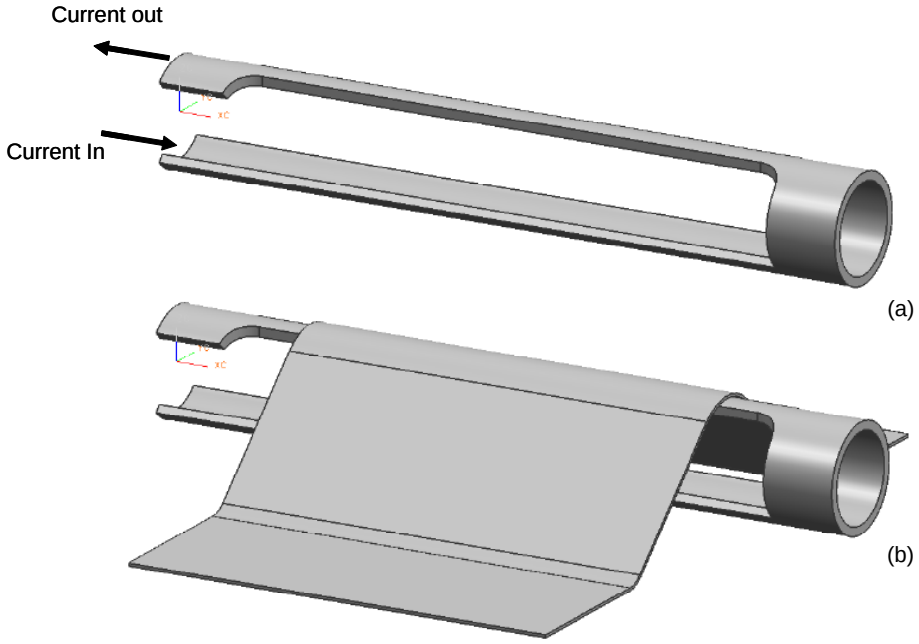

Figure 52: Corner-fill coil used shown a) without and with b) a sample. The connectors and supports used are not shown.

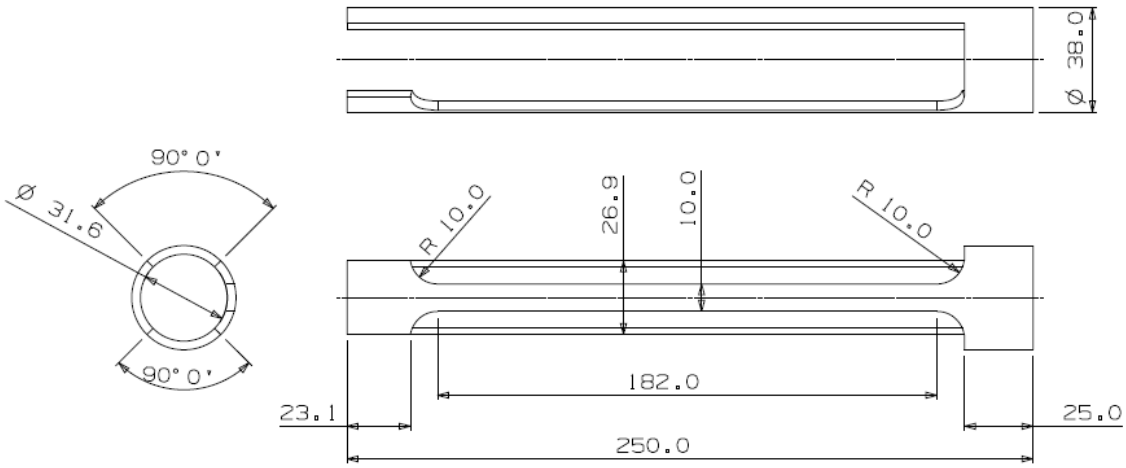

Figure 53: Detailed drawing of the corner-fill coil. All dimensions in mm.

Solid copper rods were used to connect the coil to the connectors of the MPG in order to increase the structural integrity of the coil. Cables were tried first but during each pulse the cables were accelerated resulting in dynamic loads on the soldered joints that caused their failure. The rods were stiffer than the cables and they could be welded to the coil using a TIG welding process, which resulted in a much stronger connection. The space within the coil was filled with a polycarbonate rod for structural support. Figure 54 shows the coil with the connectors and the polycarbonate rod.

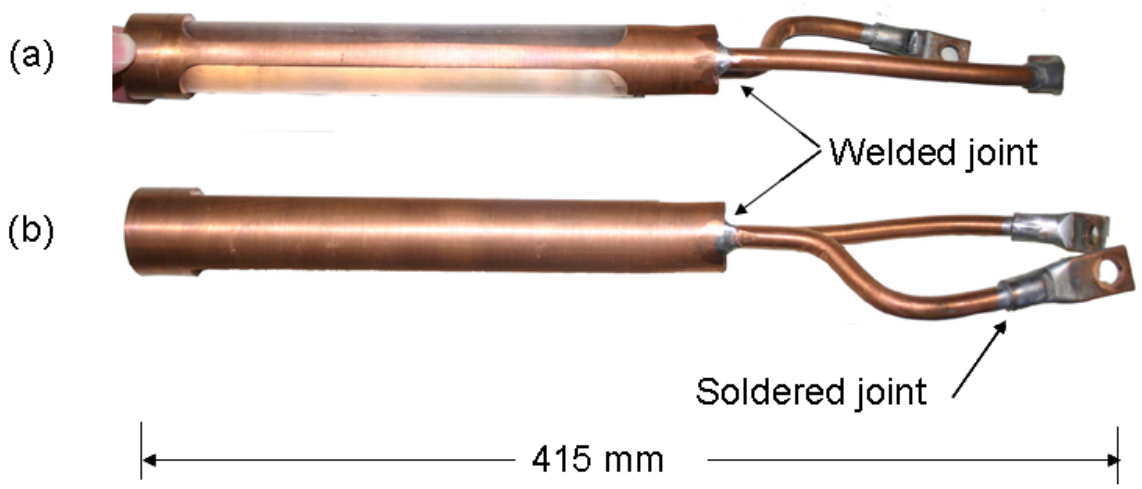

Figure 54: Top a) and bottom b) view of the coil showing the types of joints used. The material that can be seen inside the coil in a) is a polycarbonate rod.

The whole coil assembly had to be insulated from the sheet and from the rest of the apparatus. If the workpiece and coil touch, current would flow from the coil to the sheet and no induced currents and magnetic fields would be created. Also, in practice, if the sheet and coil touched, arcing would result that could result in damage to both the coil and the workpiece. To insulate the coil, it was wrapped in two layers of vinyl tape with a layer of polyamid Kapton® in between. The total thickness of the insulation was approximately 1 mm. The connecting rods were wrapped in vinyl tape to prevent arcing between the rods and the metal in the MPG connector and the die. Figure 55 shows the coil assembly in different stages of preparation for use. Note that the pictures were taken after the coil was used and that the top rod was originally straight. The curvature visible on the top rod was caused by the forces induced on it during the current pulses.

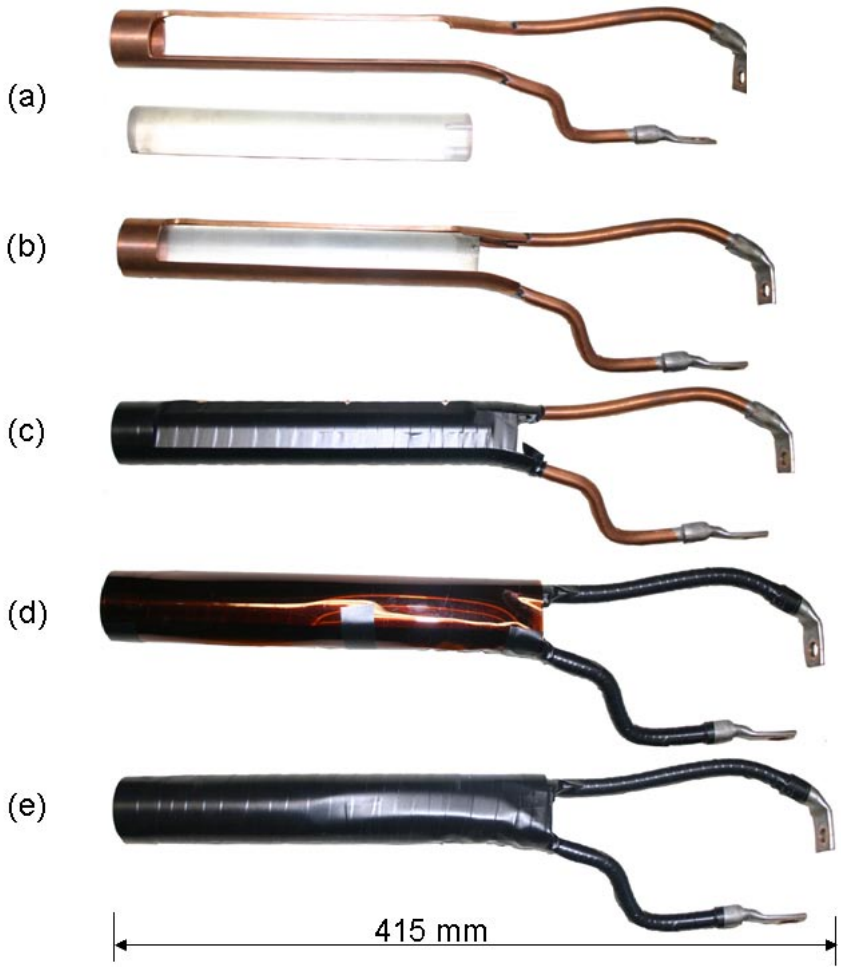

Figure 55: Coil preparation for use. The coil and supporting rod are shown individually in a) and assembled in b). The first vinyl insulation layer is shown in c) and the Kapton® layer in d). The coil with the final vinyl layer and ready for use is shown in e).

This coil met the requirements of the forming operation and did not fail. Improvements can be made to the design, for example by providing a stronger polymer base that could support the lateral loads on the part of the coil that is interacting with the workpiece. The impedance of the connectors could possibly be reduced by having a form of concentric connector, analogous to low impedance cables. Also, although not strictly part of the coil design, the connector cables could be eliminated and the coil connected directly to the capacitor bank.

2.6.1.1 EM Corner Fill Apparatus

The complete corner fill apparatus was installed on a hydraulic press, where the coil was mounted on a PVC base and connected to the MPG on the base of the press and where a

v-channel die was connected to the press cylinder. A schematic of the corner fill process is shown in Figure 56. Figure 57 shows the complete apparatus with the die open. Two stops were used to ensure that the die was at the correct height for each experiment.

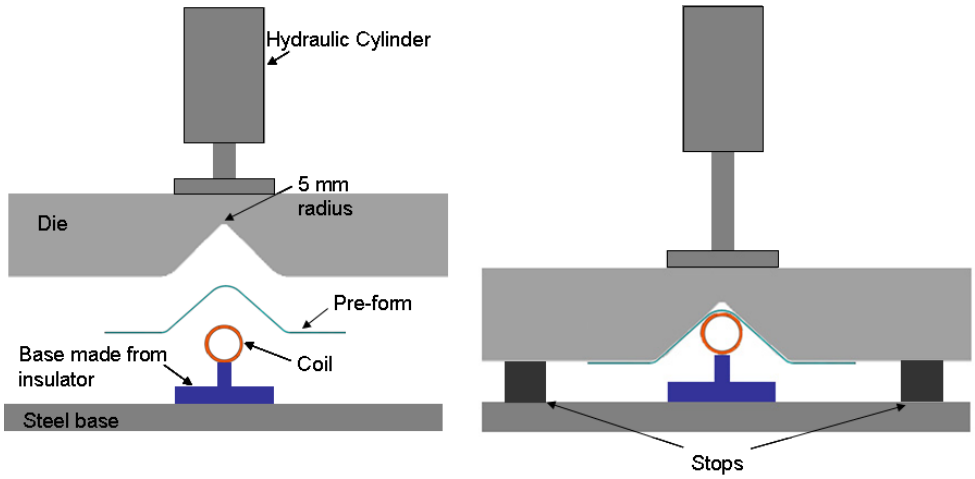

Figure 56: Schematic of the corner fill operation of the hybrid process.

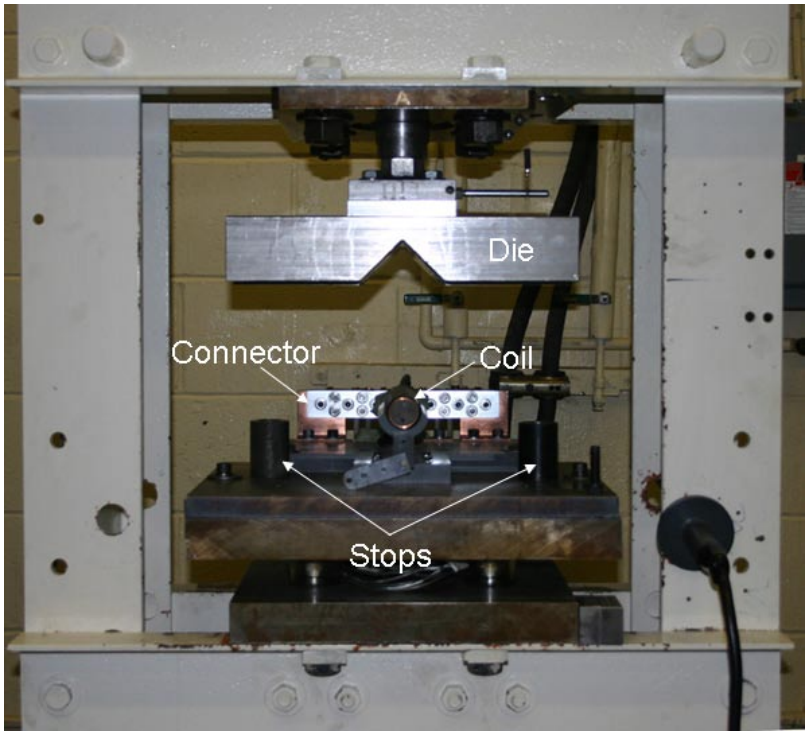

Figure 57: EM corner fill apparatus.

The coil was mounted on a PVC base that isolated it electrically from the press and did not affect the electromagnetic fields produced by the coil/workpiece system (Figure 58). The

coil was connected to the MPG by bolting the ends of the rods to the connector. A flat lead with a hole was soldered to the end of the rods to facilitate the connection. Plasticine was used to cover the area of the connector where the coil was attached to prevent arcing (Figure 59).

(a) (b)

Figure 58: Photographs showing a) the PVC base of the connector and b) shows the base with the coil in place.

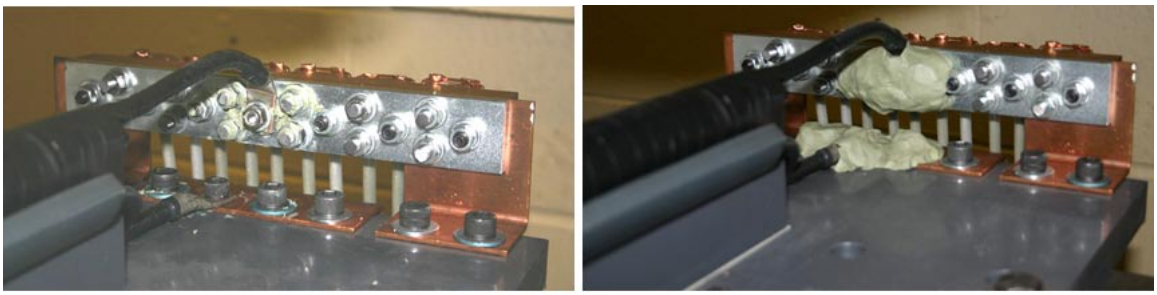

(a) (b)

Figure 59: The connection of the coil with the connector to the MPG is shown in a) and the same connection with the plasticine applied is shown in b).

The pre-formed blanks were held in position in the die using vinyl tape (Figure 60) prior to die closure. The blank was located using grooves and stops to ensure that all specimens would be in the same nominal position. However, small variations caused by the pre-forming process caused the samples to differ in position slightly. To correct this, the coil was used as the final locating device. Figure 60 shows a sample in position for the corner fill operation with the die in the open position. Figure 61 shows the tool in the open and closed position. To determine if the samples experienced any draw-in, their position within the die was determined and their length was measured after the corner fill process.

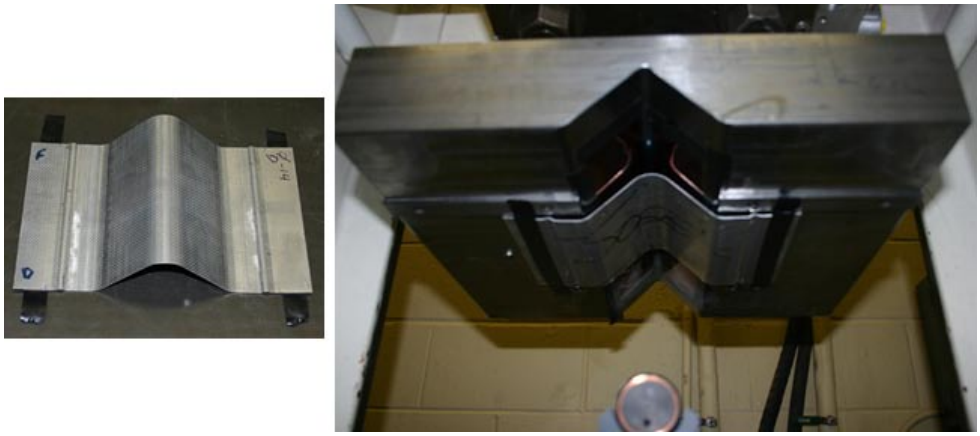

Figure 60: Placement of the pre-formed sample on the corner fill apparatus. A pre-formed sample with the tape used to affix it to the die is also shown.

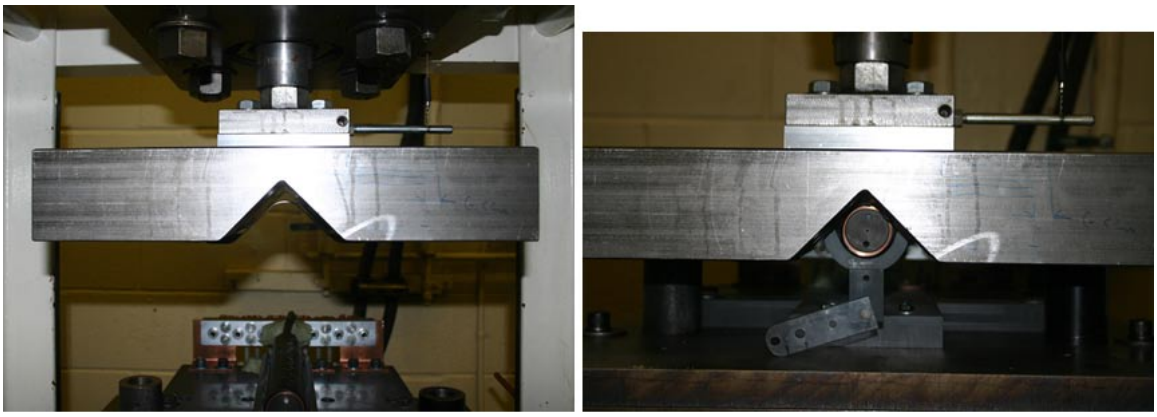

Figure 61: Front view of the apparatus with a sample in position in the a)open and b) closed configurations.

2.7 Preliminary Coil Designs

Four other coil designs were tested that proved inadequate for the task. They are presented here in reverse chronological order of development. The coil design that led to the final working coil is shown in Figure 62 and is very similar to the final design. The main difference is that the both the top and bottom of the coil are the same width. This resulted in a lower current density on the side of the coil that interacts with the workpiece when compared with the final design. Also, part of the induced forces acted directly against material that was supported by the die and produced no deformation, as illustrated in Figure 63. A less obvious,

but very important, difference was that the connectors for this coil were soldered to the coil and not welded. This resulted in a significantly weaker joint that failed during testing.

Figure 62: Coil design that led to the successful coil.

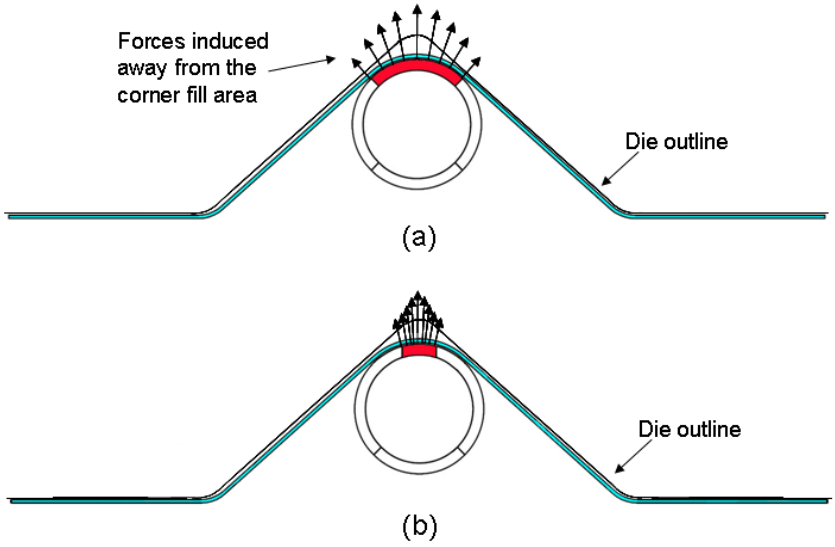

Figure 63: Simplified induced force distribution for a) the unsuccessful and b) successful coil design.

Another single piece coil design was tested that consisted of a half cylinder with a slot cut into it. The first prototype of this coil was made from aluminum and is shown in Figure 64. The slot provided a U-shaped path for the current; due to this, the coil was referred to as the U coil. The coil was mounted on a polycarbonate rod for structural support. The connectors for the aluminum U coil were soldered to the ends. The coil was wrapped in vinyl tape for insulation.

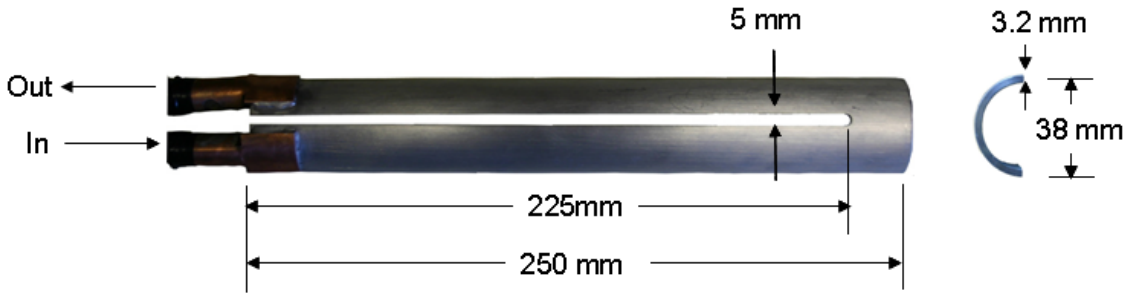

Figure 64: Aluminum U coil.

The aluminum coil provided enough energy to produce significant deformation on a sample sheet and a copper version was made to try and improve the conductivity and thus the induced forces generated. The copper U coil is shown in Figure 65. The connectors for this coil were welded to increase structural strength. Vinyl tape was wrapped around the coil for insulation. After four tests it was found that the forces induced on the coil had plastically deformed it. The extent of the deformation can be seen in Figure 65, where the 9 mm maximum width of the deformed is shown. The slot was originally 5 mm as shown in Figure 64. Re-enforcements for the coil were designed and partly built, but not implemented since the final corner fill coil proved to be a better design.

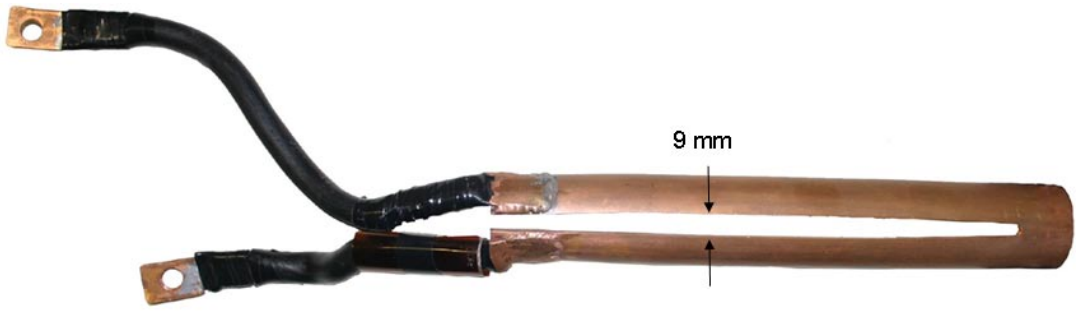

Figure 65: Copper U coil after four of tests.

A coil made from wound copper wire was designed and tested (Figure 66). The coil was based on an axi-symmetric design presented by Oliveira [11] that provided an area of relative uniform current distribution on the workpiece by moving the dead-spot away from the area to be formed. To achieve this result in a coil for a linear corner fill, copper wires were shaped in the form of concentric U shapes so that all the wires at the top of the coil would have

current flowing in the same direction. The current would flow back on the side of the coils, thus moving the dead spot away from the workpiece. Figure 67 shows an idealized coil with the current directions.

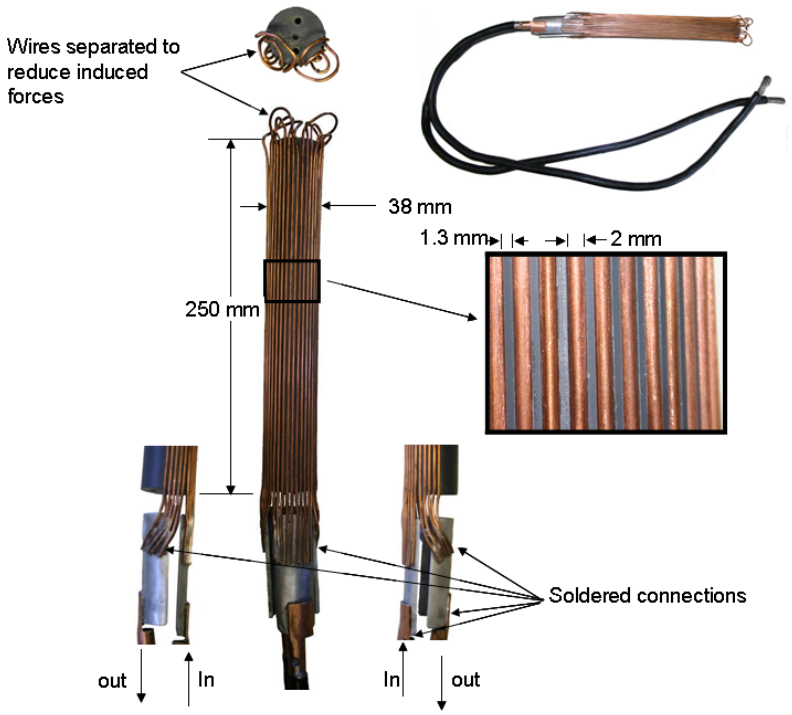

Figure 66: Wound coil with details of the soldered connections. The coil with the connecting cables is shown on the top right-hand corner.

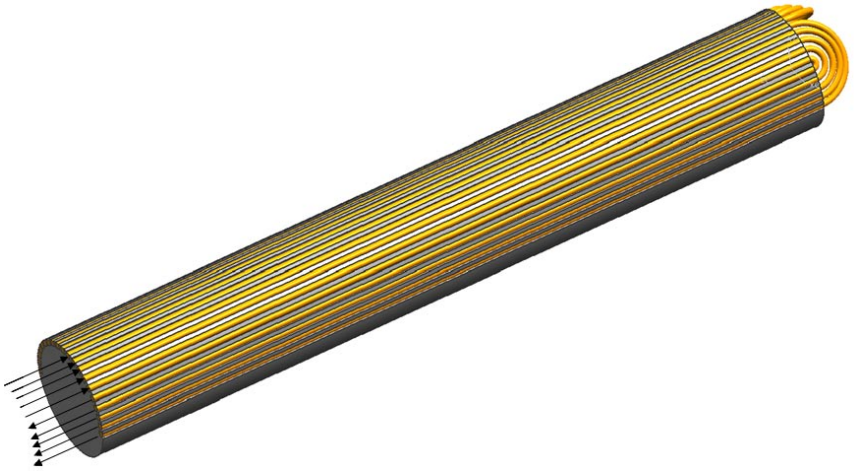

Figure 67: Idealized wound coil with the current direction for half of the wires. The connectors have been removed for clarity.

The wires were wound on a PVC cylinder with groves cut into it to support the wires and prevent any lateral movement. The segments of the wire that were bent were separated from each other as much as possible to reduce the induced forces that they would generate on each other. To connect the coil to the MPG, the ends of the wires were soldered to an aluminum bus for the input and output wires and to each of these buses a cable was in turn soldered that connected the coil to the MPG connector. For insulation, vinyl tape was wrapped around the coil. These soldered connections proved to be the weak point of this design, which was not successful due mainly to structural weakness. The soldered wire joints could not resist the loads generated and failed typically with one pulse. This design was also very hard to realize with significant amounts of time being required to form and install the wires and to solder them to the connectors.

A helical coil, made from wound 0.5 in cable, was also tried with no success since the sample sheets did not show any deformation. A simulation of such a coil illustrates one reason why the design was not successful (Figure 68). The current flows on the inside of the coil, since it is the shortest path it can take, thus taking it away from the workpiece and reducing the induced forces.

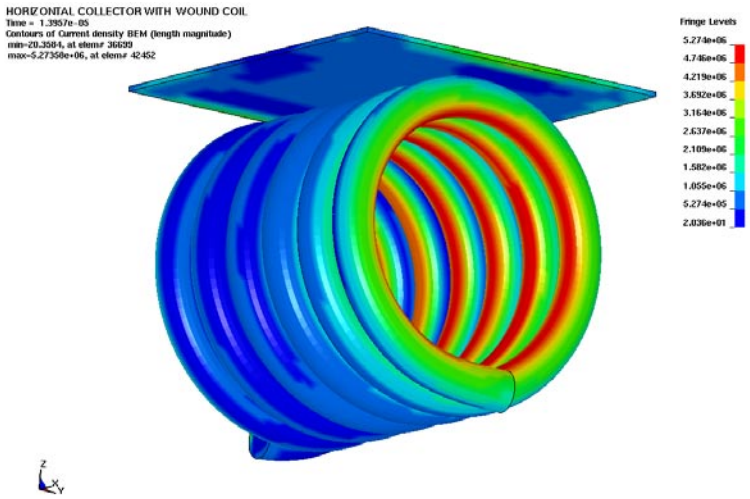

Figure 68: Simulation of a helical coil with a workpiece. Contours are of current density.

2.8 Field Shapers or Collectors

In the early stages of the project which led to this thesis, field shapers or collectors (they will be referred to as collectors henceforth) were considered as a means of delivering the energy to the area of interest of the workpiece. The use of collectors for this type of application was first proposed by Golovashchenko [86]. A basic collector layout is shown in Figure 69. One of the possible advantages of using a collector are that a flat coil could be used to generate the primary magnetic field, thus combining the strength and efficiency of a flat coil with the ability to deliver energy to a narrow area where the coil could not reach.

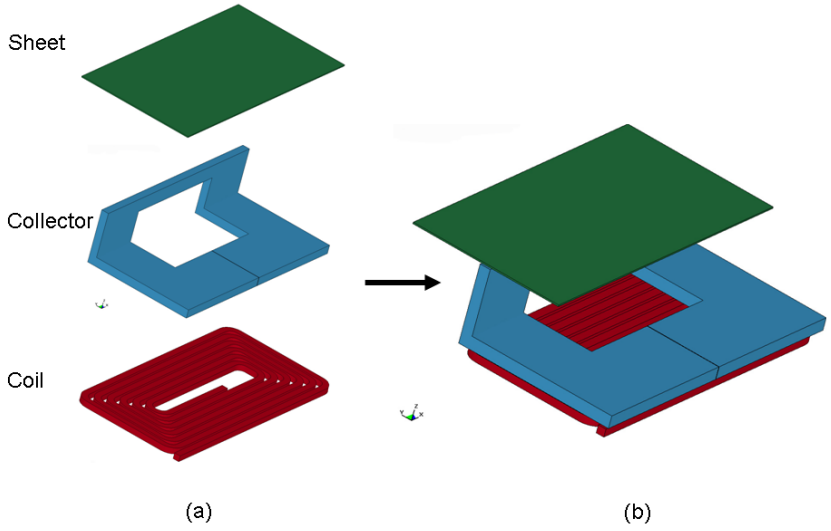

Figure 69: Basic collector layout for the corner fill application.

Numerical simulations were carried out to study the feasibility of this method and the results indicated that the collectors could work. Figure 70 shows the results of the models and the deformation induced on the sheet can be clearly seen. The models used a simplified geometry with sharp corners. It was known that such corners would cause artificially high current concentrations, but the effects of these were under estimated. Based on the numerical simulations and the published work on the subject, it was decided to try and use collectors for the corner fill project.

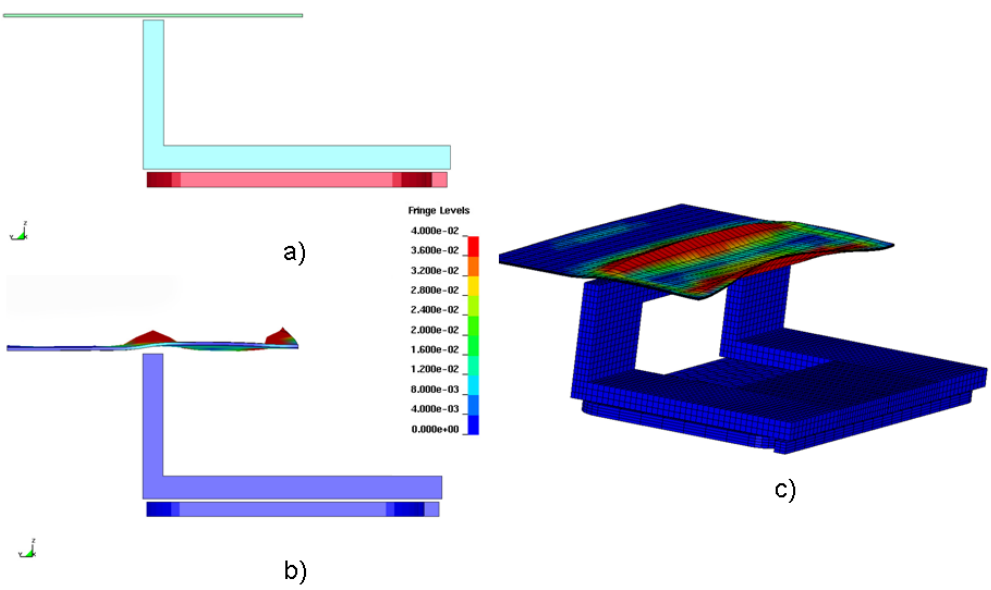

Figure 70: Simulation of a simple collector for a corner fill application, showing the relatively large predicted deformation that was likely the result of numerical over-prediction.

Two collector shapes were tried, which are shown in Figure 71 and Figure 72. The coil shown in Figure 71 was called the "L" collector and the one in Figure 72 the "Square" collector. Both collectors were made from aluminum. To test the collectors a new double pancake coil was made to replace the one used in the single step corner fill experiments (Figure 73-a). The coil was similar in design as the previous one, but made from 12.5 mm (½ in) copper plate instead of copper wire, to increase its strength. Figure 73 shows the coil and the collectors placed on it. To hold the collectors in place, rubber and polymer plates were placed on top of them and the v-channel die was clamped against the coil using the press to provide a restraining force.

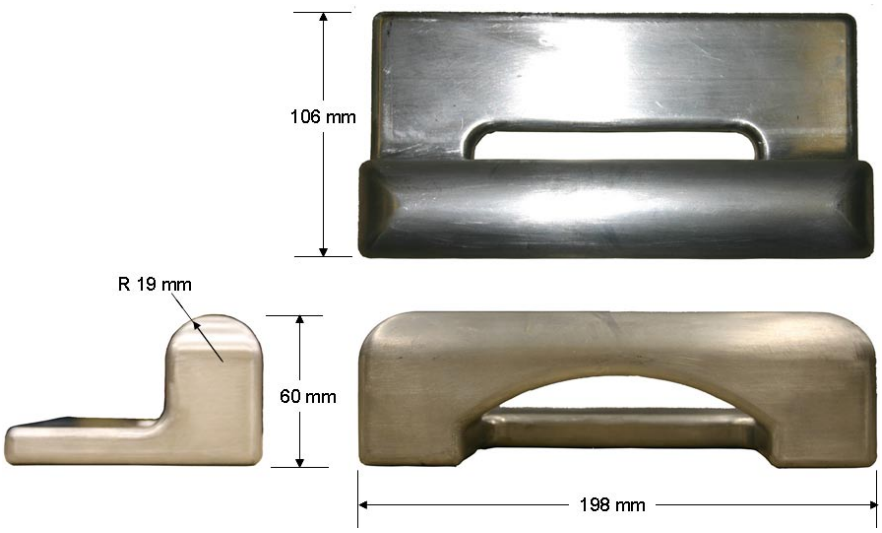

Figure 71: "L" collector.

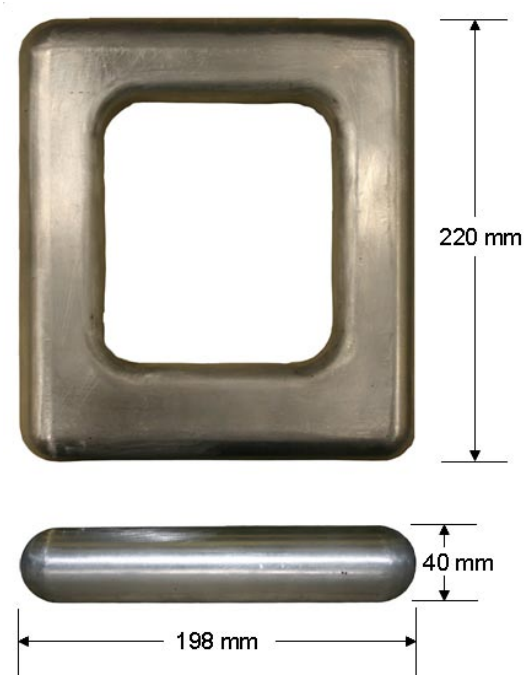

Figure 72: Square collector.

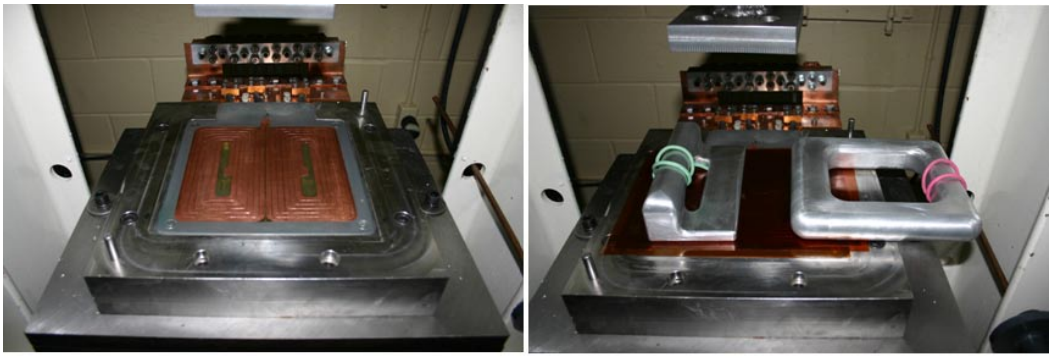

Figure 73: Double pancake coil a) and collectors placed on coil b). The brown sheets that can be seen on b) are sheets of Kapton® for insulation. The cables seen on the collectors were used to try and detect if current was passing through that section of the collector.

An insufficient level of current was conducted to the area of the collectors that would interact with the workpiece and due to this the collectors were not considered further. Currents were induced in the collectors as evidenced by the loads induced on them, which were detectable by the displacement of the whole cylinder assembly during tests. Wires (as shown in Figure 73) and aluminum sheets were placed in close proximity to the collectors to see if enough force was induced on them to cause displacement. Since neither the wires nor sheets moved during the tests, the induced forces were judged to be too small. A numerical model of the square coil was developed to try and analyze the process and it indicated that very little of the induced flowed in the forming areas. The only areas with sufficient current density were the ones just over the coil. Although it was thought possible that a collector could be designed for the task, the time and effort involved were estimated as being considerable and corner fill coils were seen as the best solution to the problem. Since a coil that was able to do the task was developed, the collector approach was abandoned.

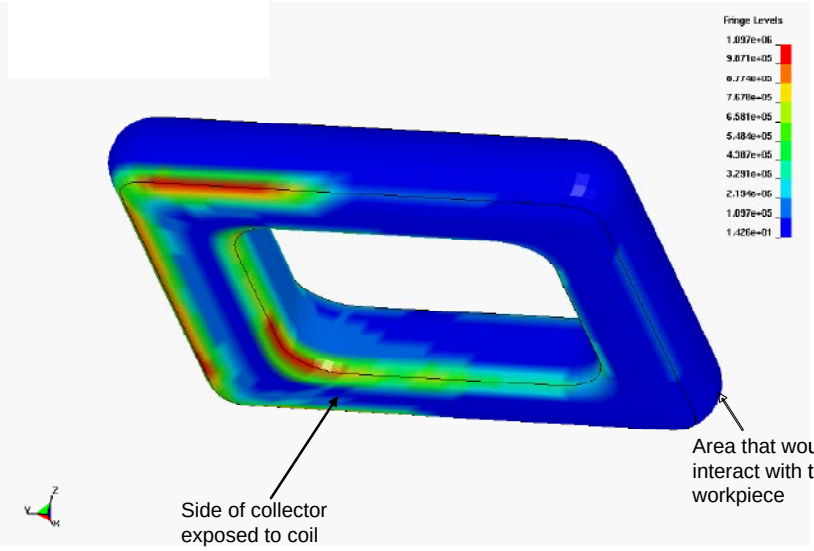

Figure 74: Predicted current density on a square collector excited by a flat spiral coil like the one used for the experimental work.

2.9 Metallography

Metallographic analysis was carried out to quantify the amount of micro-damage generated by each forming step. One sample was measured from each of the sheets in the as-received, 5, 10 and 15% pre-strained conditions. Also, measurements were taken from pre-formed samples and corner filled samples made from the as-received, 5, 10 and 15% pre-strained sheet. For the pre-formed and corner filled samples, segments from the middle of the samples (Figure 75) were sectioned carefully to avoid additional damage and to avoid excess heating of the part. This process was accomplished by first using a grinder to cut segments of the formed parts. The specimens were then mounted with epoxy resin, to avoid any excessive heating, and cut with a high precision metallographical circular saw to remove any parts of the specimen that may have been affected by the heat of the grinding. The specimens were wet ground using 500, 1200 and 4000 grit SiC paper. Final polishing was carried out using 3 μm and 1 μm diamond paste, and 0.05 μm colloidal silica suspension. Table 2 lists the samples used for each condition.

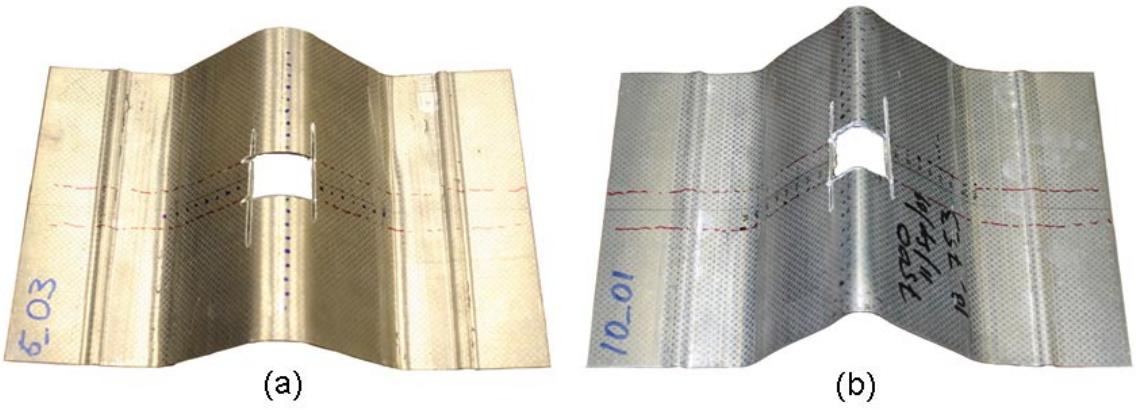

Figure 75: Samples of a) drawn sample and b) corner filled sample showing where the samples for the metallographic analysis were taken.

Table 2: Samples used for the metallographic analysis. The d_, 5_, 10_ and 15_ designations refer to the as-received, 5%, 19% and 15% pre-strained samples respectively, with the subsequent number indicating the specific sample.

Condition	Sheet	Pre-formed	Corner filled
as-received	d_2	d_5	d_8
5% pre-strain	5_10	5_5	5_8
10% pre-strain	10_10	10_2	10_1
15% pre-strain	15_7	15_5	15_2

The micrographs used for analysis were obtained with an Olympus BX61 optical microscope equipped with a Q Imaging MicroPublisher 5.0 RTV 5.0 megapixel digital camera [87]. A 20x objective lens with an additional 2x increment with a white light was used, giving an image resolution where of 0.17 μm/pixel. Each micrograph was $435x10^{-3}$ mm x 236 $x10^{-3}$ mm (2560 x 1920 pixels). The images obtained were analyzed using the Image-Pro Plus 5.1 software from Media Cybernetics [88].

The images analyzed were composed of 18 or 24 individual images tiled together, which gave areas of analysis on the order of 0.7 mm x 2.6 mm. Before the micrographs were taken, the samples were cleaned by immersing them in a vibration bath, then rinsing with water and alcohol and finally air dried with compressed air. Despite the cleaning procedure, some foreign particles were present in the micrographs, which, together with some scratches, could have led to some inaccuracies in the damage measurements. Each tiled image was digitally re-touched to eliminate any foreign particle or scratch whose colour was dark enough

to interfere with the damage measurements. Figure 76 shows a tiled image in its original form and the re-touched version.

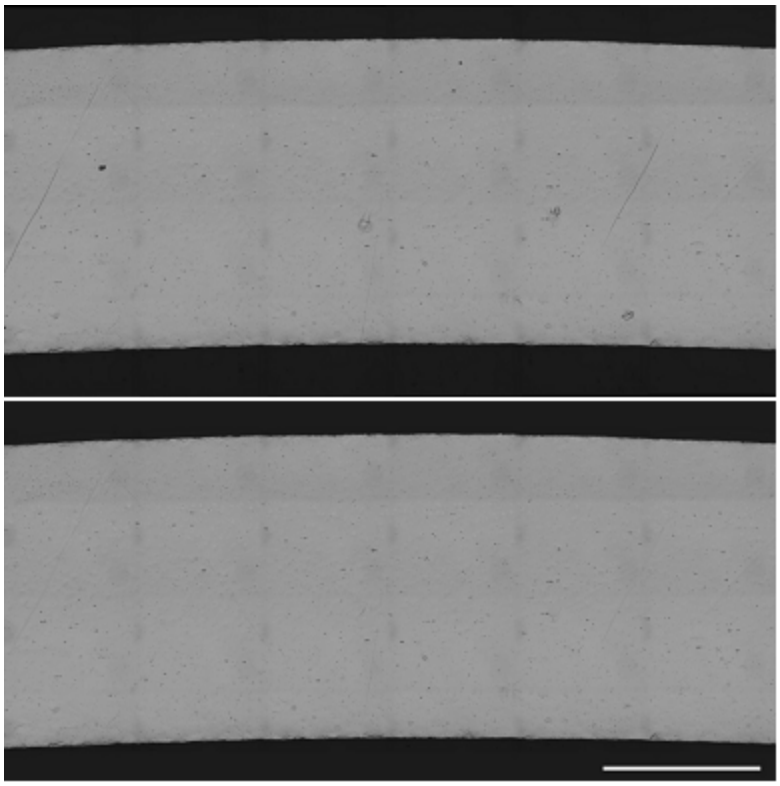

Figure 76: Original (top) and re-touched (bottom) tiled image. The white scale bar is 500 μm long.

3 NUMERICAL METHODS AND PROCEDURES

The single step EM and hybrid processes were modeled in order to gain further insight into these processes. As with the experiments, the numerical work concentrated on the hybrid forming operation. Figure 77 shows a chart of the experimental processes modeled. The single step EM process was only modeled for the as-received sheet and provided data on the effects of force distribution and rebound, as well as helping with the validation of the model. The hybrid process was modeled for both the as-received and pre-strained sheet. From the models of the hybrid process, strain and stress histories were obtained. Also, numerical experiments were performed to determine the effects of flow stress and current-time history on the final part shape.

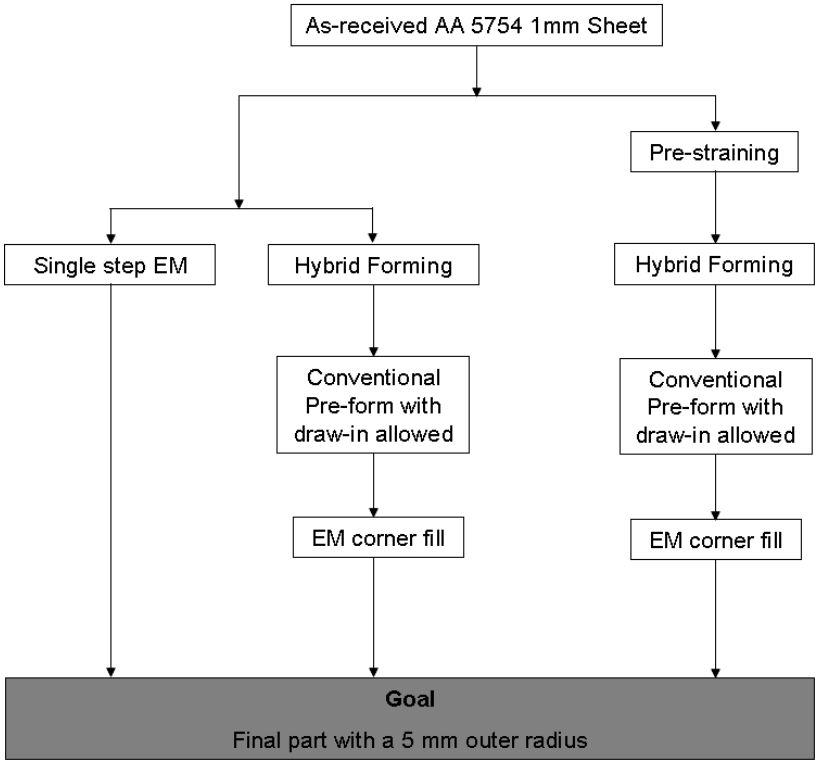

Figure 77: Diagram illustrating the processes modeled numerically for this research.

The numerical effort for this work was undertaken with LS-DYNA, a well established and tested explicit dynamic finite element code which is described in [42]. The software has an extensive track record in modeling high rate processes such as EM forming. A version of the

software that can model the electromagnetic phenomena present in EM forming used. A detailed description of the numerical methods used by the software is not included for the sake of brevity.

The software combines Finite Element Analysis (FEA) with Boundary Element Methods (BEMs) to perform the electromagnetic analysis by solving Maxwell's equations. The BEM is used to model the air, so that it does not have to be meshed. The electromagnetic equations in the coil and workpiece are solved using FEA (Figure 78). Using BEM for the air has the advantage of eliminating the mesh and the small elements and element distortion that are associated with the air in EM forming problems. This distortion arises from the small gaps between the coil and the workpiece and the large deformation of the air elements as the workpiece deforms. The major drawback of the BEM is that it is memory and processor time intensive, due to the heavily populated matrices required by the method. In contrast, in an FEM solution matrices are large but sparsely populated.

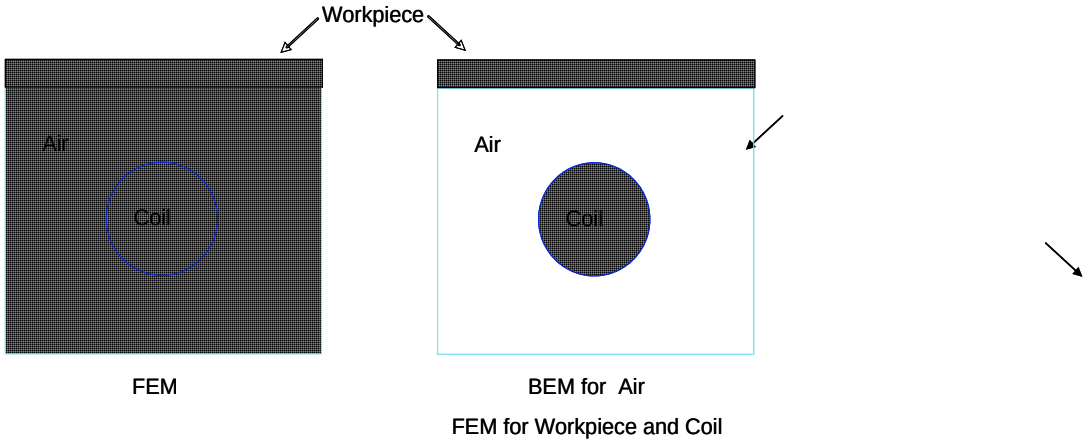

Figure 78: Illustration of the differences between a Finite Element-only solution for an EM forming problem versus a combined Boundary Element and Finite Element approach.

L'Eplattenier *et al.* [60] provide a detailed description of the BEMs used and the software. The software solves the low frequency or "eddy current" approximation of Maxwell's equations that were presented in Section 1.7.1 in differential form. The equations are transformed using Green's identities in order to be used in the BEM [60]. A BEM approach would generate fully dense matrices, which would lead to significant memory requirements. The software uses a low rank approximation technique to reduce the size of the matrices produced [60]. Despite this technique the memory requirements are significantly higher than those for a structural FEM application. The memory requirements were such that

the RAM usage for the electromagnetic models used for this work ranged from 4 to 8 Gbytes, this is in stark contrast to the 160 Mbytes of RAM that the conventional models for this work consumed.

Solid elements were required for the workpiece for both the electromagnetic and structural calculations. These are necessary for the EM solver in order to calculate the induced currents in the workpiece and the currents in the coil. Solid elements were also needed to capture the through-thickness normal and shear stresses that are generated on the sheet during forming, which were reported in [17] and were also predicted in this research, as will be discussed later. The need for solid elements adds to the already high computational cost.

The models were run using 2.0 GHz AMD 64 processors which form part of one of the clusters at the University of Waterloo. The conventional forming model took approximately seven days to run, while the EM corner fill model took approximately three days. The memory requirements for the conventional model were 320 Mbytes, versus the 4.2 GBytes for the EMF calculation. The time and memory requirements made a proper mesh refinement study impossible and this has likely lead to a non-optimum mesh for the problem. However, since the main goal of the modelling was gaining insight and due to the fact that the model results agree reasonably well with the experiments, the meshes used were deemed acceptable.

3.1 Single Step EM Process Models

The coil and workpiece were modeled using eight node hexahedral solid elements. The meshes used are shown in Figure 79 and Figure 80. The sheet was meshed using 28,800 elements and the coil with 5,952. The sheet had four elements through-thickness, with the smallest element size being 0.25 x 2.47 x 2.42 mm. Utilizing more elements likely would have resulted in more accurate results; however, the memory limits of the computers being used at the time was exceeded when more elements were used. The sheet was modeled with an elastic-plastic piece-wise-linear plasticity model that is incorporated into LS-DYNA [42] using the quasi-static stress-strain flow curve shown in Figure 37. The model was isotropic and did not consider material rate effects. The coils were modeled as elastic materials. Tooling components were modeled as rigid bodies and their surfaces were discretized using shell elements for the structural calculation. The tool elements were ignored for the electromagnetic calculation.

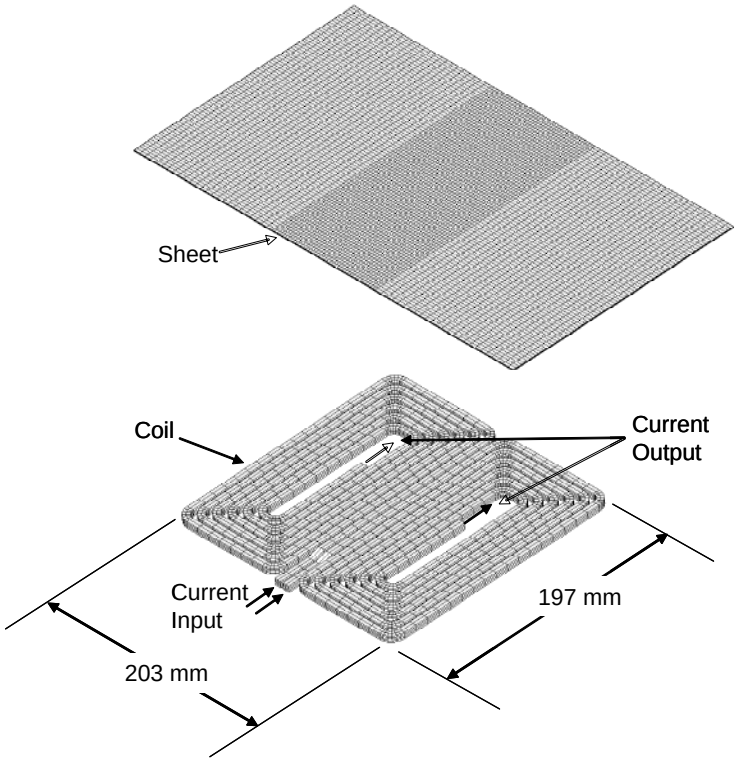

Figure 79: Coil and sheet meshes for the single step EM process.

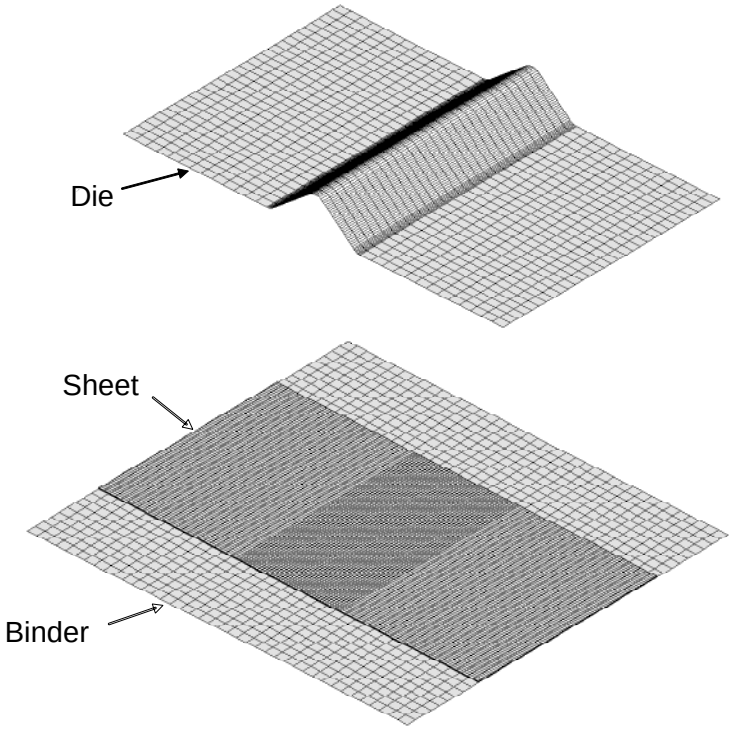

Figure 80: Die and binder meshes for the single step EM process. The binder and the die are used to clamp the sheet in place. Neither the die or binder meshes are included in the EM calculations.

The coils were modeled as a part of an RLC circuit, with the coils treated as parallel inductors. The electrical properties used for the model were adjusted to account for the parallel coil installation and comprised a system resistance of 5.96 mΩ, capacitance of 270 μF and inductance of 48.7 nH. The desired voltage was an input of the simulation. The conductivity of AA 5182 of 1.799 x 10^7 $\Omega^{-1}m^{-1}$ was used as provided by the ASM Handbook-Volume 2, since no value was available for AA 5754. For the coil, the conductivity of C10100 of 5.75 x10^7 $\Omega^{-1}m^{-1}$, as given by the ASM Handbook, was used [89].

To reduce run times the EM part of the solver was not active for the whole simulation and was deactivated after the induced forces became negligible. The total run time was 400 μs, with the EM module turned off after 50 μs.

3.2 Hybrid Process Models

The hybrid process was modeled in two stages: first the conventional forming operation was modeled with all the EM features inactive and then the EM corner fill was modeled using the deformed sheet from the predictions of the first model. This two-stage

approach was adapted because the version of the code used at the time of writing always had the EM solver active, which consumed an impractical amount time for the during the pre-form stage (it was estimated that the complete solution could take months). Using the adopted approach, the geometry, stresses and strains were transferred from the conventional step to the EM step of the model. This approach still required long simulation times, since the brick elements required for the EM calculations were needed in the pre-forming operation rather than the shell elements normally used for simulation of sheet stamping processes.

3.2.1 Conventional Pre-form

The mesh for the conventional pre-form model is shown in Figure 81. The sheet was modeled with solid hexahedral elements, which were required for the EM calculations and to resolve the through-thickness compressive and shear stresses that can be generated when the sheet makes impact with die [17]. The punch, binder and die were discretized with shell elements and treated as rigid bodies.

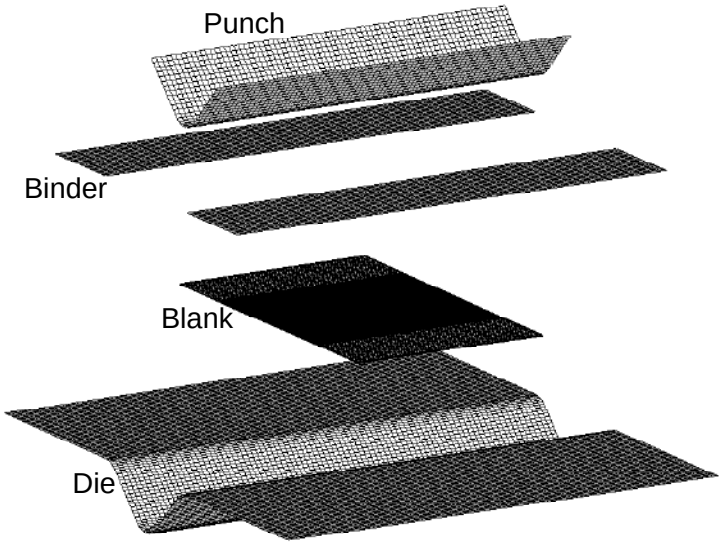

Figure 81: Mesh used for the model of the conventional pre-form operation.

For the blank, 78,280 elements were used, with five elements being used through the thickness. Figure 82 shows the mesh after conventional forming. It can be seen that the element distribution is not uniform. The area with the highest element density corresponds to the part of the sheet where the radii are formed. For the electromagnetic calculation, only the elements in the area of the radius were considered. This area had the highest density of

elements and consisted of 25,840 elements of size 0.2 x 0.5 x 2.0 mm. The same piece-wise linear plasticity model previously described was used to model the sheet.

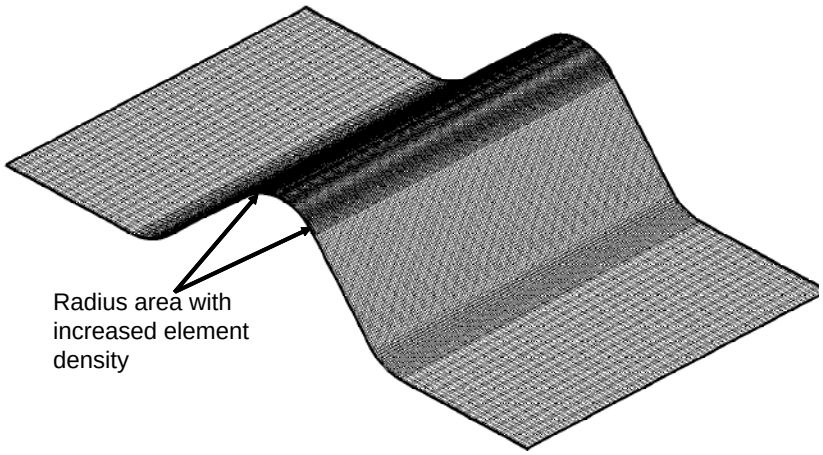

Figure 82: Blank mesh after conventional pre-forming.

3.2.2 EM Corner Fill

The mesh for the EM corner fill calculation is shown in Figure 83. The coil was discretized using the same eight node hexahedral solid elements as the sheet. Shell elements were used for the die. The coil was modeled as an elastic material. The conductivity of AA 5182 of 1.799 x 10^7 $\Omega^{-1}m^{-1}$ was used as provided by the ASM Handbook-Volume 2, since no value was available for AA 5754. For the coil, the conductivity of C10100 of 5.75 x10^7 $\Omega^{-1}m^{-1}$ as given by the ASM Handbook, was used [89]. The partial current profile obtained from experimental measurements, shown in Figure 84, was used as the current input for most of the simulations. The units used for the figures are the ones used in the model for consistency. Additional current profiles based on the experimentally recorded profiles were also used and they will be presented in the sections that discuss the results of those particular models. Several conditions were modeled with modified stress-strain curves which will be described in the relevant results sections.

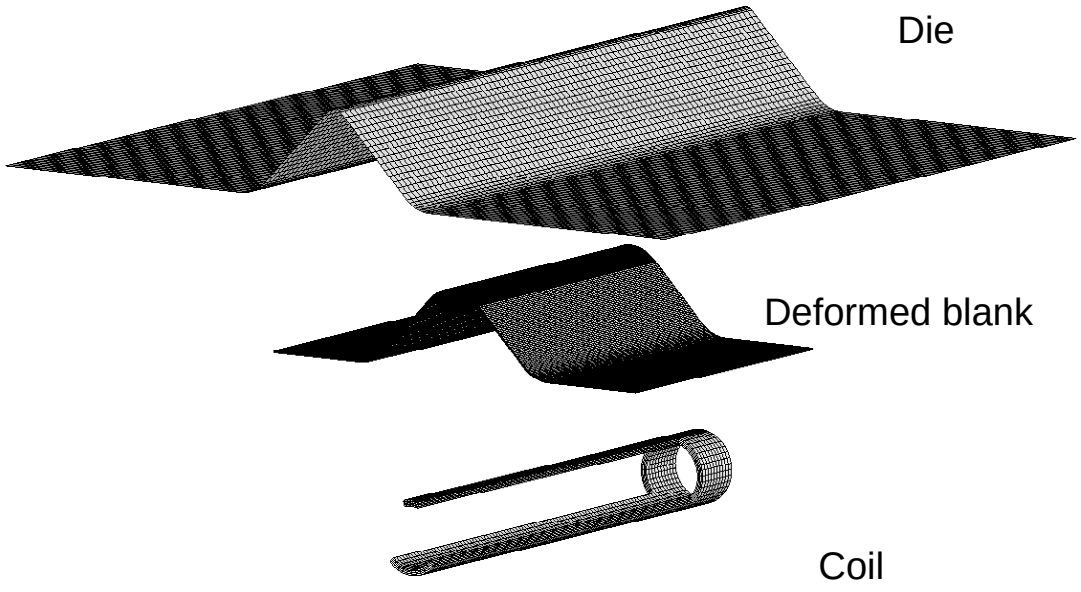

Figure 83: Meshes used for the electromagnetic corner fill calculations.

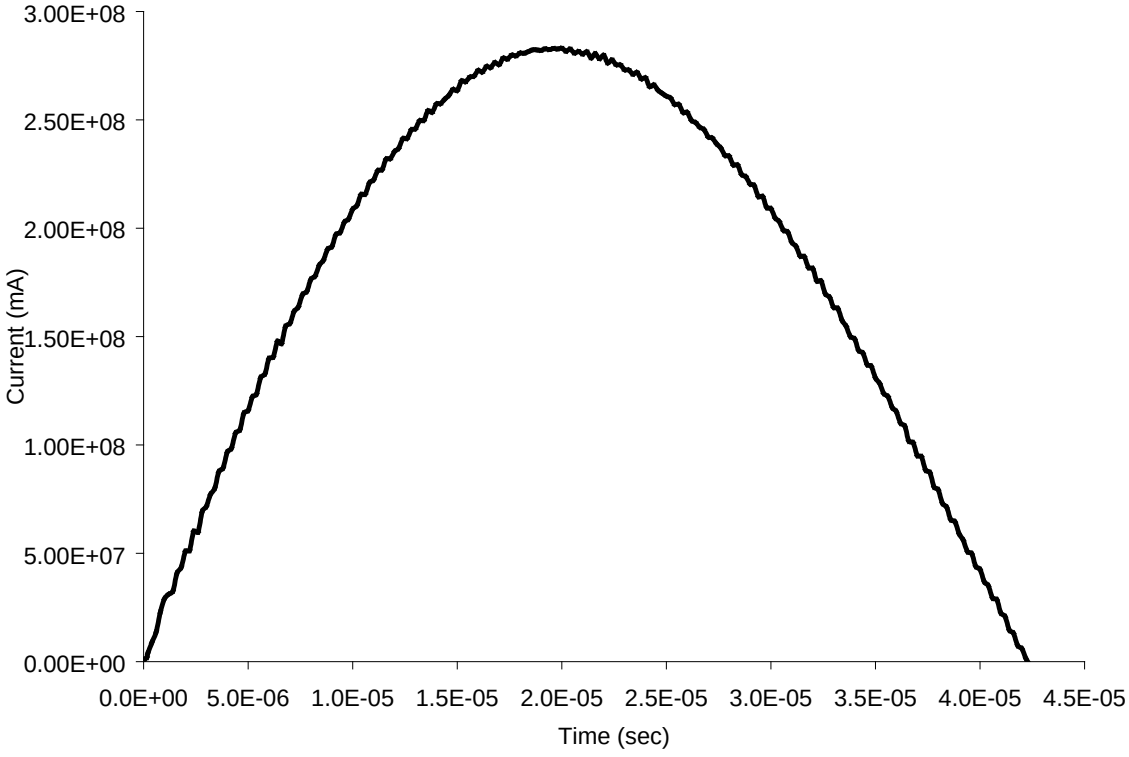

Figure 84: Current used as the input for the electromagnetic simulation. The values were taken from experimental measurements.

4 EXPERIMENTAL RESULTS

The following sections will present the results obtained from the experimental portion of this work. First, the single step EM forming results will be presented. This process did not result in proper corner fill, but did provide valuable insight into the effects of the force distribution and the rebound of the sheet. Also, the results were used to help validate the numerical models. The results for the hybrid corner fill experiments are described next; this represents the major component of the experimental results from this research. The final shapes, formability and metallographic data for the samples formed from the as-received sheet and from sheet pre-strained to 5, 10 and 15% will be presented.

4.1 Single Step EM Forming Results

A representative sample formed with the single step EM process is shown in Figure 85. These v-channel experiments were originally intended to test the feasibility of filling a corner with a single EM discharge. It was determined that the part could not be formed as a single step using the available apparatus since the final sample shapes produced were very different from the desired ones (Figure 85). This approach was not pursued further as a means of obtaining a sharp feature. However, these experiments were used to gain valuable insight into the effects of force distribution and rebound. Also, the results were used to validate the computer models and are presented in that context in Chapter 5.

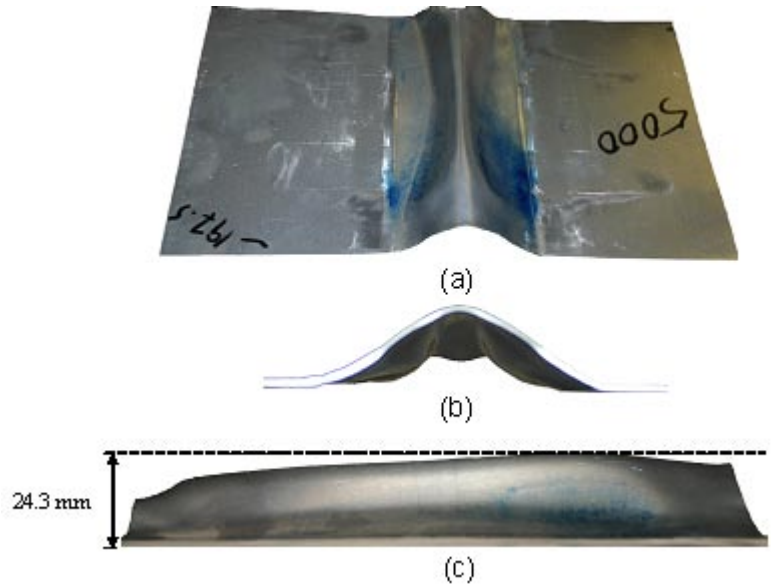

Figure 85: Part formed using the double pancake coil and a charge energy of 6.75 kJ, a)oblique view, b) front view (magnified) and c) side view. The blue markings in a) indicate where the sheet made contact with the die. Note the difference between the part and the nominal V-channel shape.

4.1.1 Effect of Force Distribution

In EMF, the force on the sample is the result of the repelling magnetic fields of the coil and those of the induced eddy currents in the sheet [57]. Since the path of the eddy currents will be opposite to the path of the current flowing through the coil, the eddy currents and the force distribution on the sample will be dictated by the shape of the coil. Practical limitations such as the provision of an adequate current path, ease of manufacture, structural strength and magnetic properties result in coil shapes that may not produce the optimal force distributions. Also, the sharp edges of the blank can add current concentrations that will locally increase the induced force on the sample. The net result is a force distribution that may not be ideal for a particular forming process. Figure 86 shows the predicted force distribution induced on a sheet using a double pancake coil. The distribution is noticeably non-uniform, although the force distribution is somewhat uniform in the area near the centre of the sheet.

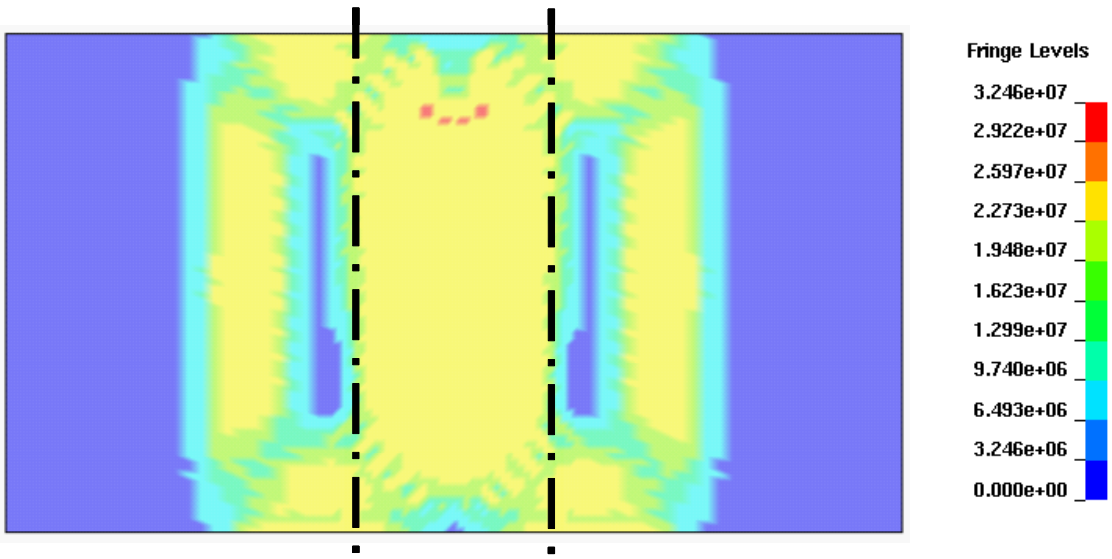

Figure 86: Predicted force distribution on the side of the sheet exposed to the coil. Fringe levels are of Lorentz force in μN. The solid black lines indicate the approximate location of the die cavity.

A number of samples were formed using a lower charging energy of 2.4 kJ in order to avoid contact with the die cavity. These experiments were performed to isolate the effects of the force distribution from the effects of the impact of the sheet with the die. A representative sample formed is shown in Figure 87. It can be clearly seen that the part does not have a uniform height. The final shape is the result of the non-uniform force distribution produced by the coil. It can be seen that the height varies along the length of the part, with the centre of the part being the highest point. The average height for three experimental samples was 13.8 mm. This height distribution is consistent with the predicted force distribution shown in Figure 86. One side of the sample is higher than the other, due to higher forces acting on that side of the sheet, which are the result of irregularities in the coil due to manufacturing flaws. These irregularities result in the coil being slightly more separated from the sheet on the side with the lower height. Towards the ends of the part there is a reduction in height which is consistent with the geometry of the coil and the predicted force distribution which will be discussed below. At the edge of the samples the height increases slightly, this may be due to the concentration of the current produced at the edges, which results in a local increase in Lorentz forces.

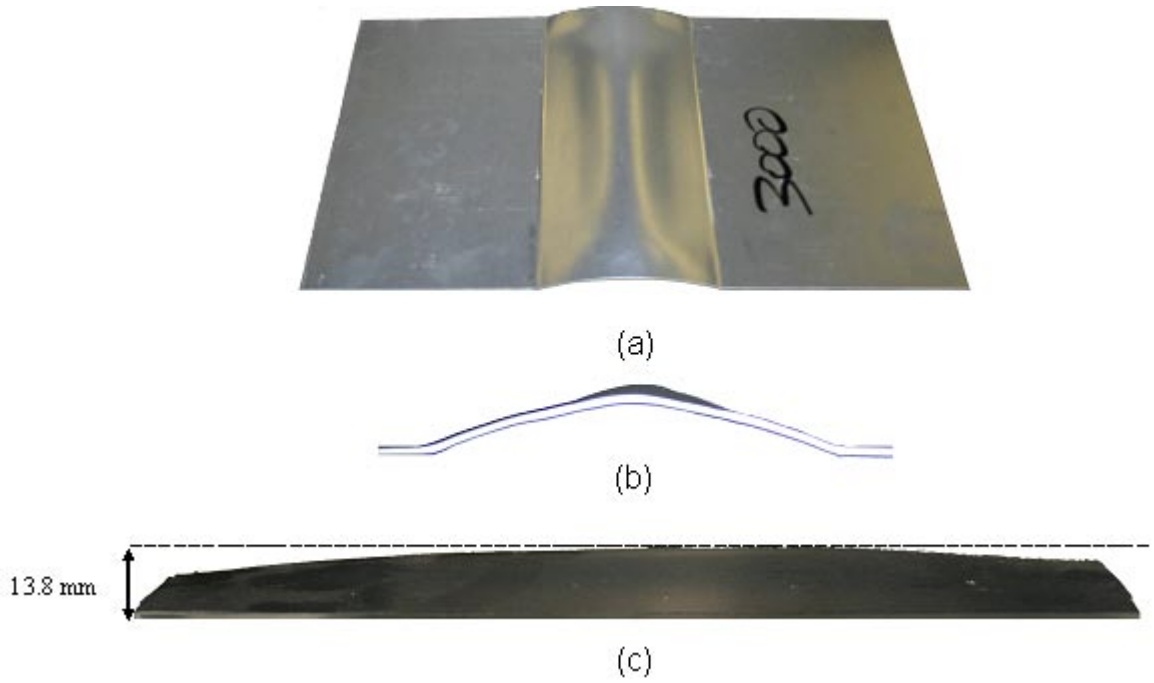

Figure 87: : Part formed using a charging energy of 2.4 kJ and the double pancake coil, a) view from above and b) front view.

4.1.2 Rebound of the Sheet

Since the sheet impacts the die, not all of the kinetic energy results in plastic deformation, some of the energy is expended by causing the sheet to rebound off the die wall. The principal effect of this rebound is that the parts do no conform to the die shape. The samples show clear evidence of this rebound. Rebound in EM forming operations has been reported in [17,69, 90].

Samples that made contact with the die were formed using a charging energy of 6.75 kJ. A representative sample is shown in Figure 85. Blue ink was applied to the surface of the die to confirm that the sheet impacted the die during the experiment. After forming, the samples showed clear indications of impact. The dark areas that can be seen on the part shown in Figure 78 are stains left by the ink from the die that indicate where the sheet contacted the tool. It is clear that after impact, the sheet rebounded from the die surface to form the final shape. This rebound was also observed on the samples formed using the hybrid process, but to a lesser extent.

4.2 Hybrid Forming Results

For the hybrid forming experiments, the material was pre-formed with a conventional v-channel tool to a 20 mm outer radius while allowing some draw-in. The corner radius was then sharpened to 5 mm using a subsequent EM corner fill operation. Hybrid forming experiments were performed on sheet material in the as-received and pre-strained condition. This section first presents the results for the pre-form operation and then for the EM corner fill. The results of for the samples formed from the as-received sheet and the three pre-strained conditions are presented.

4.2.1 Conventional Pre-Form Results

Figure 88 shows a typical drawn pre-formed sample with the 20 mm outer radius. The strains measured after pre-forming for three of the samples were recorded along the longitudinal and transverse directions (Figure 39). The measured strains after pre-forming are shown in Figure 90 to Figure 95, for the as-received, 5, 10 and 15% pre-strained samples. These “pre-formed” strain measurements will serve as a basis of comparison with the strain measurements taken from the EM corner filled samples. The strains show the expected trends, with the strains increasing with the amount of pre-strain.

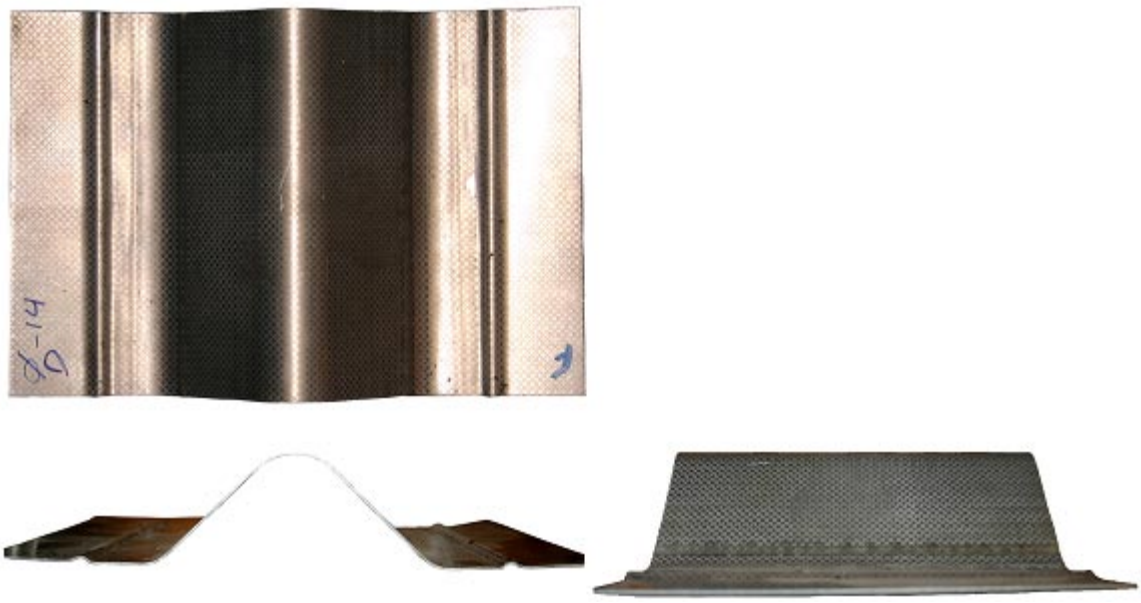

Figure 88: Typical 20 mm radius pre-formed sample.

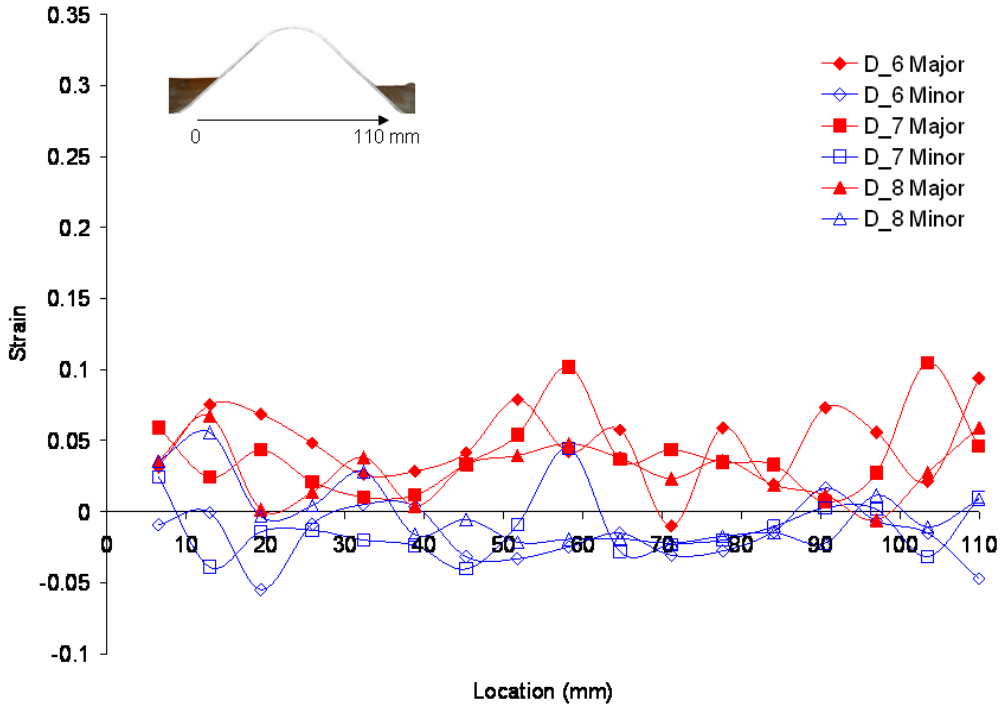

Figure 89: Measured strains for the pre-formed samples formed with the sheet in the as-received condition in the longitudinal direction.

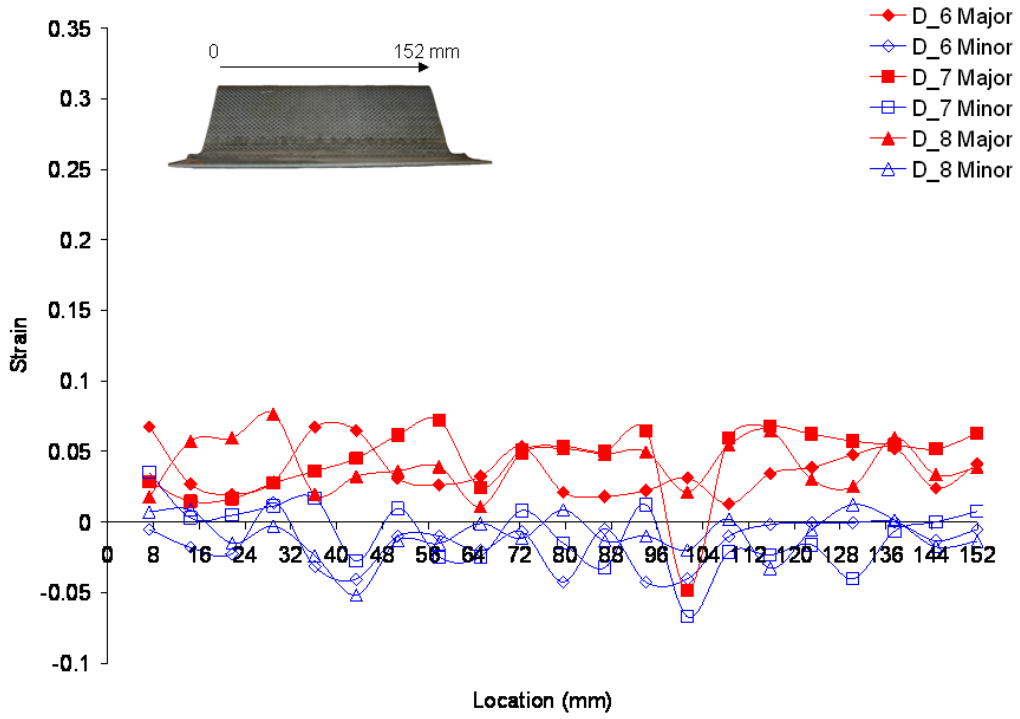

Figure 90: Measured strains for the pre-formed samples formed with the sheet in the as-received condition in the transverse direction.

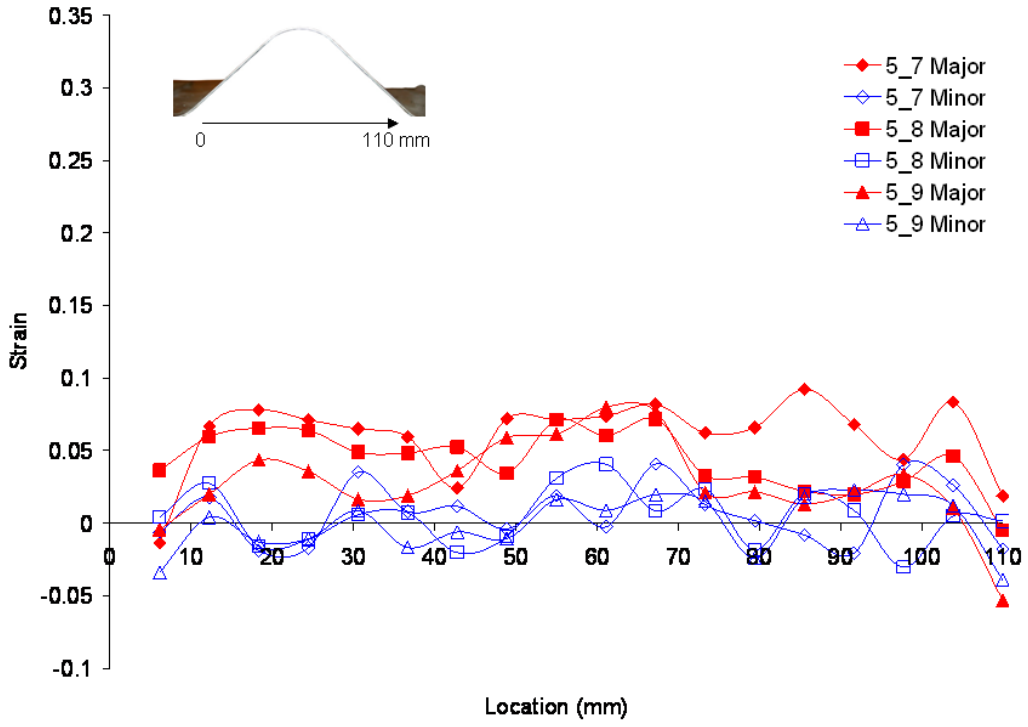

Figure 91: Measured strains for the pre-formed samples formed with 5% pre-strained sheet in the longitudinal direction.

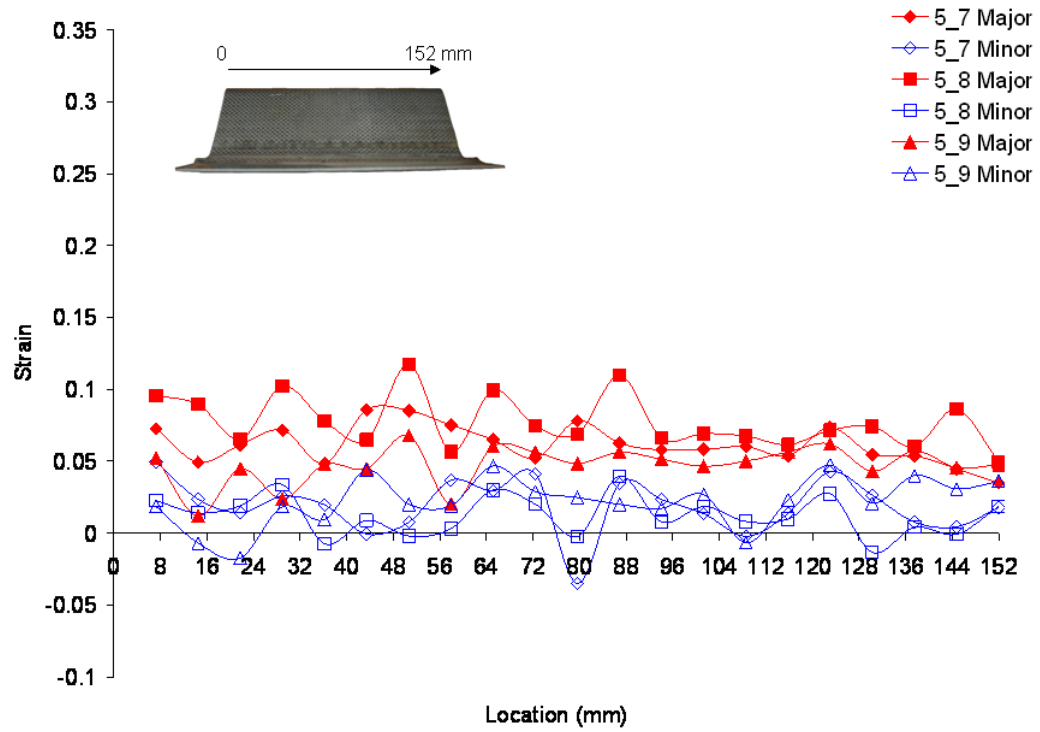

Figure 92: Measured strains for the pre-formed samples formed with 5% pre-strained sheet in the transverse direction.

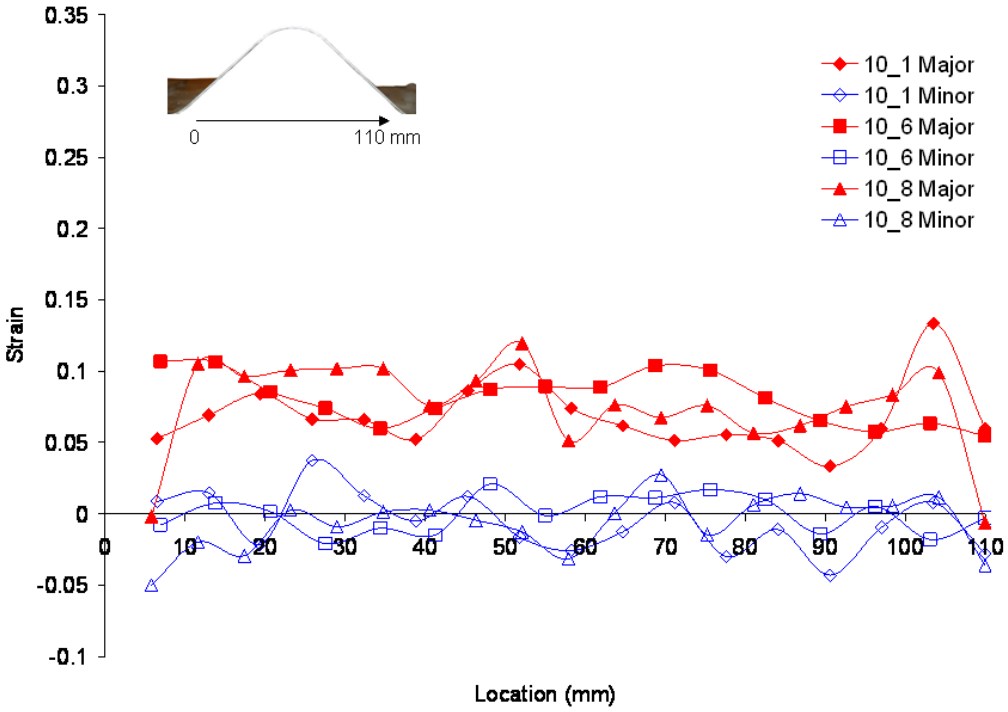

Figure 93: Measured strains for the pre-formed samples formed with 10% pre-strained sheet in the longitudinal direction.

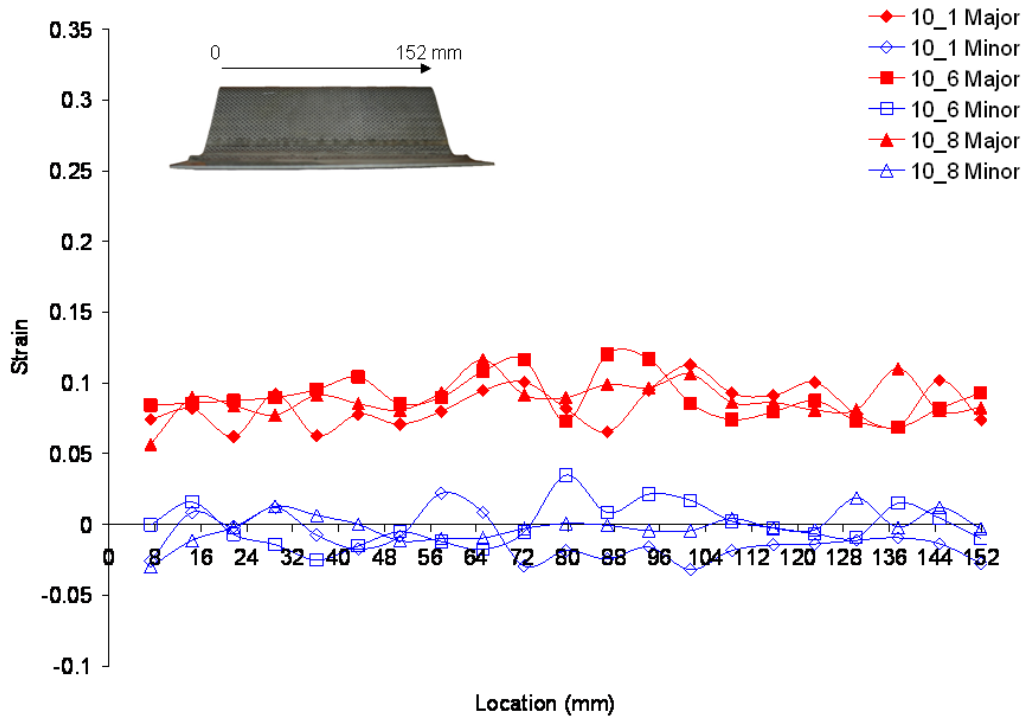

Figure 94: Measured strains for the pre-formed samples formed with 10% pre-strained sheet in the transverse direction.

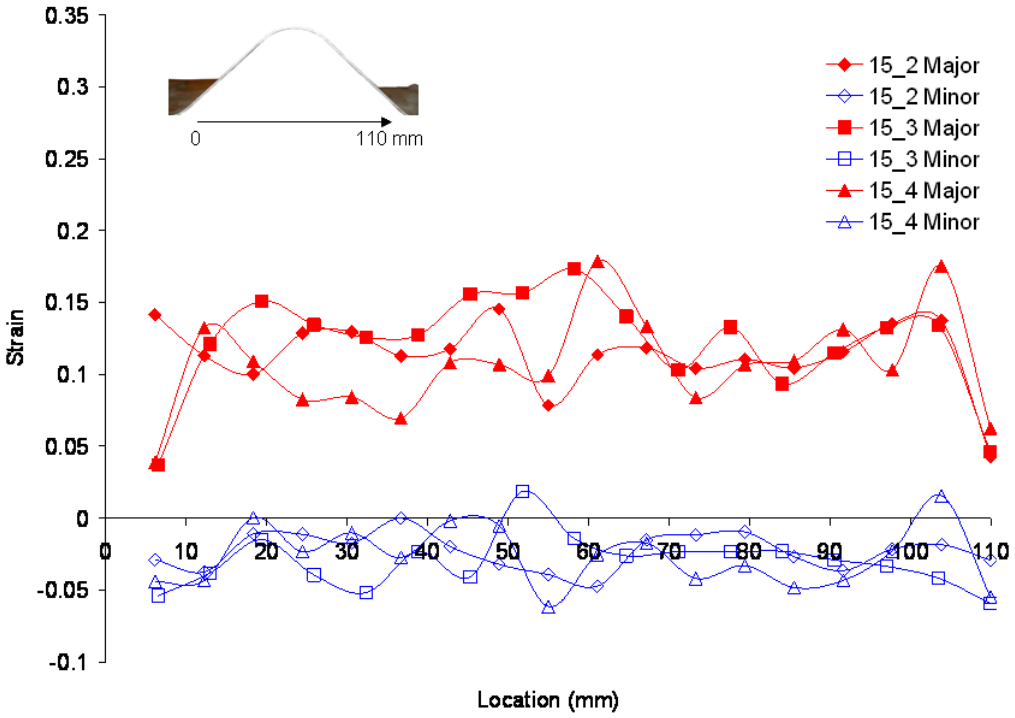

Figure 95: Measured strains for pre-formed samples formed with 15% pre-strained sheet in the left to right direction.

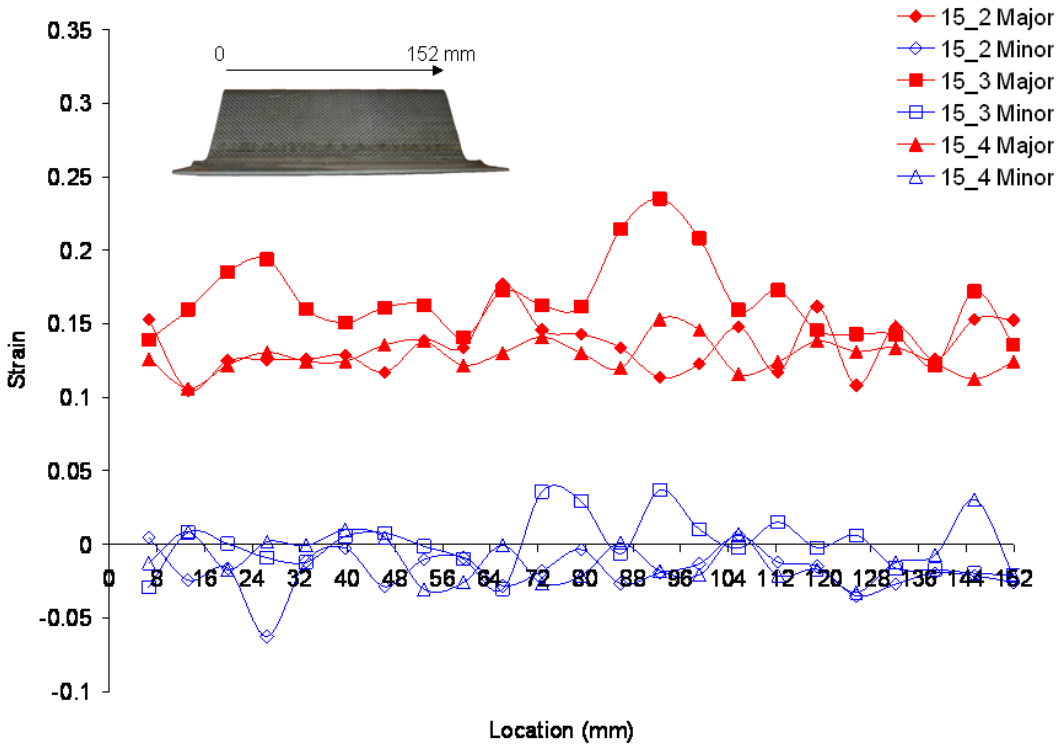

Figure 96: Measured strains for the pre-formed samples formed with 15% pre-strained sheet in the transverse direction.

4.2.2 EM Corner Fill

A representative EM corner filled sample is shown in Figure 97. All samples formed showed the same general shape regardless of the starting condition. The samples presented a relatively uniform height over most of their length, with the height dropping of at the ends (h_1 and h_2 in Figure 97). The numerical simulations indicated that the drop in height is due to the differences in the magnetic field at those locations, inducing forces on the top of the sheet that reduced the overall forming force, as will be discussed in the next chapter. Samples with the as-received, 5, 10 and 15% pre-strained sheet were formed. The charging voltage for these experiments was 7500 v, which resulted in a stored energy of 15.1 kJ. Table 3summarizes the forming conditions for the samples and Table 4 presents the height data from selected samples.

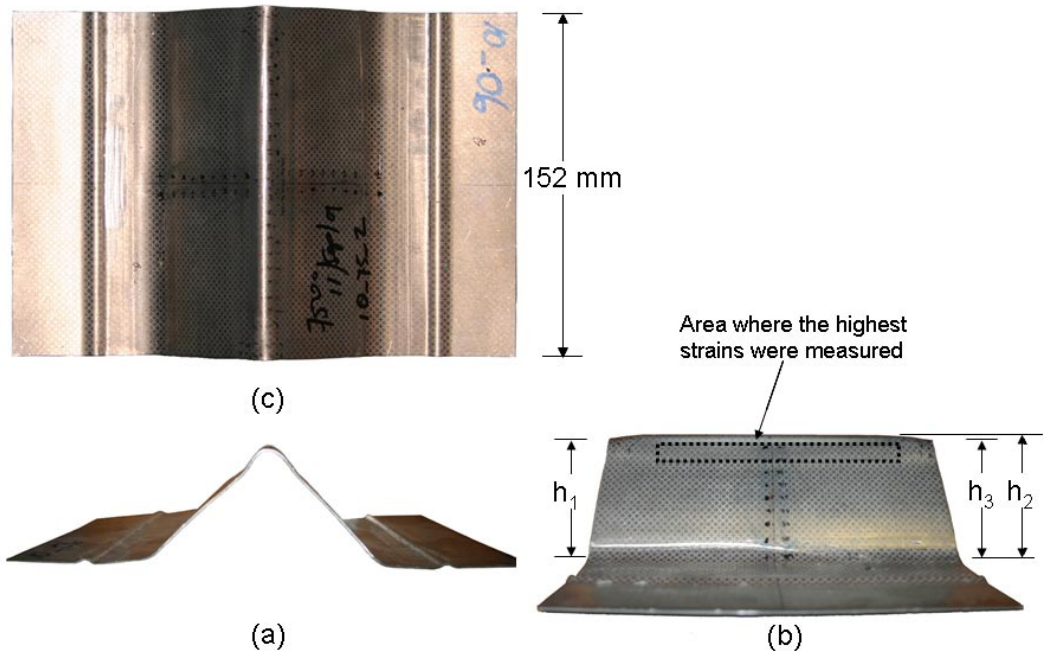

Figure 97: Sample formed into the 5 mm die by a Hybrid EM corner fill. The height legends refer to the height measurements in Table 4. The area enclosed in the dashed line in b) us where the highest strains were observed.

Table 3: Forming conditions for the corner fill samples. AR = as received, 5% = 5% pre-strain, 10% = 10% pre-strain, 15% = 15% pre-strain and NA = not available due to technical problems.

Sample	Condition	Charging Voltage (V)	Energy (kJ)	Peak Current (kA)	Frequency (kHz)
d_6	AR	7500	15.1	282	11.21
d_7	AR	7500	15.1	282	12.47
d_8	AR	7500	15.1	273	11.16
d_13	AR	7500	15.1	NA	NA
d_15	AR	7500	15.1	282	12.76
d_16	AR	7500	15.1	285	11.57
d_17	AR	7500	15.1	282	12.76
d_20	AR	7500	15.1	282	11.57
5_7	5%	7500	15.1	282	12.47
5_8	5%	7500	15.1	NA	NA
5_9	5%	7500	15.1	NA	NA
10_1	10%	7500	15.1	282	11.36
10_6	10%	7500	15.1	285	12.56
10_7	10%	7500	15.1	NA	NA
10_8	10%	7500	15.1	285	14.33
15_2	15%	7500	15.1	282	12.47
15_3	15%	7500	15.1	282	12.44
15_6	15%	7500	15.1	282	12.47

Table 4: Heights of selected corner filled samples. The values of h_1, h_2 and h_3 are as described in Figure 97. All dimensions in mm.

Sample	Condition	h_1	h_2	h_3	Average height
d_7	AR	51.1	52.8	51.0	51.6
d_20	AR	49.4	52.2	49.9	50.5
d_17	AR	48.9	51.3	48.9	49.7
d_16	AR	49.7	51.6	49.7	50.3
d_15	AR	48.8	51.5	48.7	49.7
5_09	5%	50.5	52.8	51.1	51.5
10_06	10%	49.4	51.5	49.8	50.2
10_08	10%	51.0	52.5	49.9	51.1
10_07	10%	51.2	52.9	50.6	51.6
15_6	15%	50.5	52.4	50.6	51.2
15_2	15%	49.5	52.1	49.5	50.4

4.2.3 Results for the As-Received Sheet

Figure 98 shows samples formed from the as-received sheet. The samples present some blue coloring on the top, which is a pigment that was placed on the tool to determine whether the sheet made contact with the top of the die.

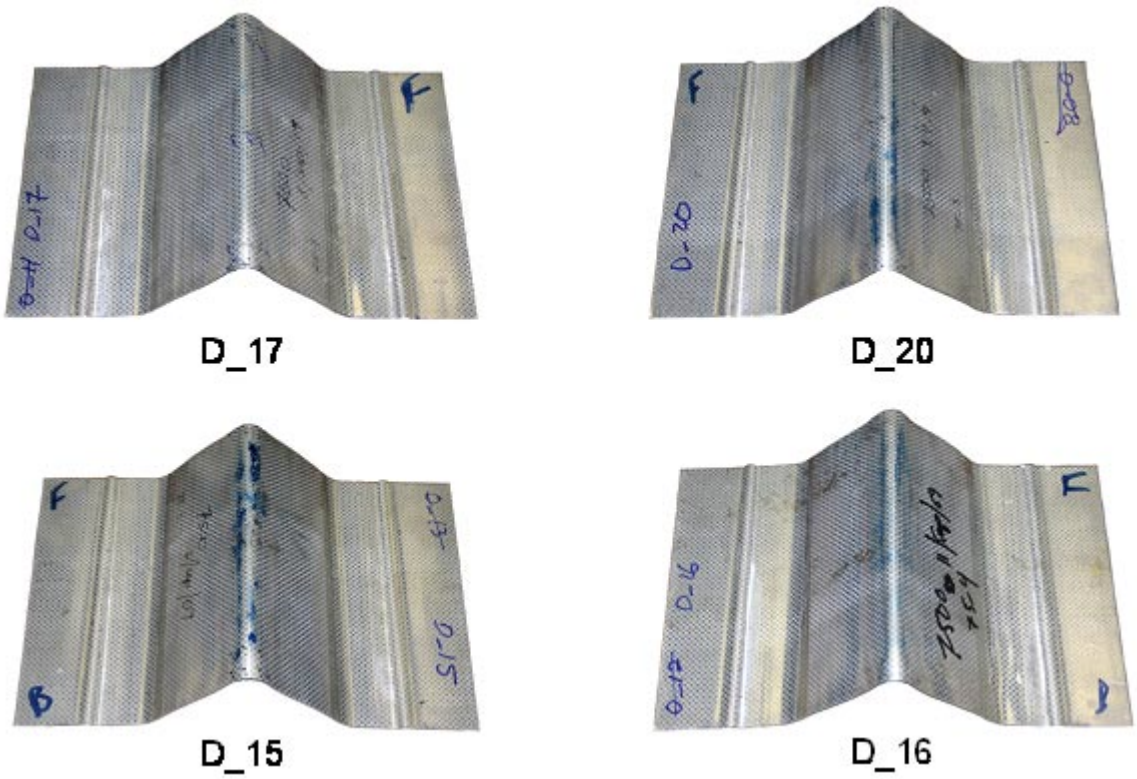

Figure 98: Samples formed from the pre-formed samples formed with as-received sheet.

Radius gauges were used to measure the radius of the as-formed corner. Figure 99 shows a 5 mm radius gauge placed on five drawn samples. The gauge is shown in a location close to the centre of the part. The radius corresponds quite closely to the gauge, despite the fact that the final shape of the sample was the result of the sheet rebounding from the die.

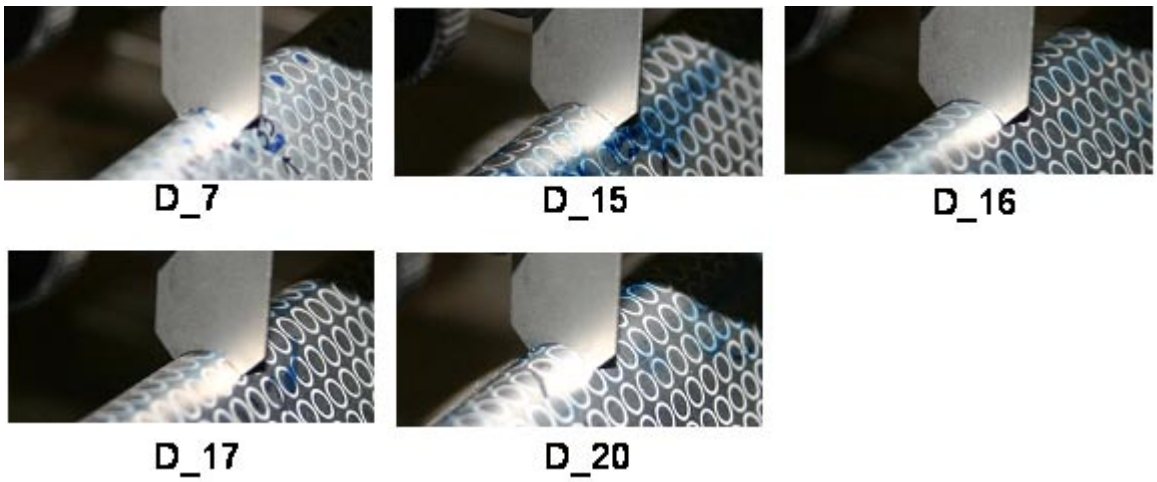

Figure 99: Close up of the centre region of the samples formed from the as-received sheet with a 5 mm radius gauge.

On the ends of the samples, the radius was larger than at the centre, which is expected due to the lower height at that point. Figure 100 shows an 8 mm gauge placed on one end of the same samples shown above. The location shown was where the largest radius was observed. At this location the shape deviates more from an arc than it does at the centre of the sample.

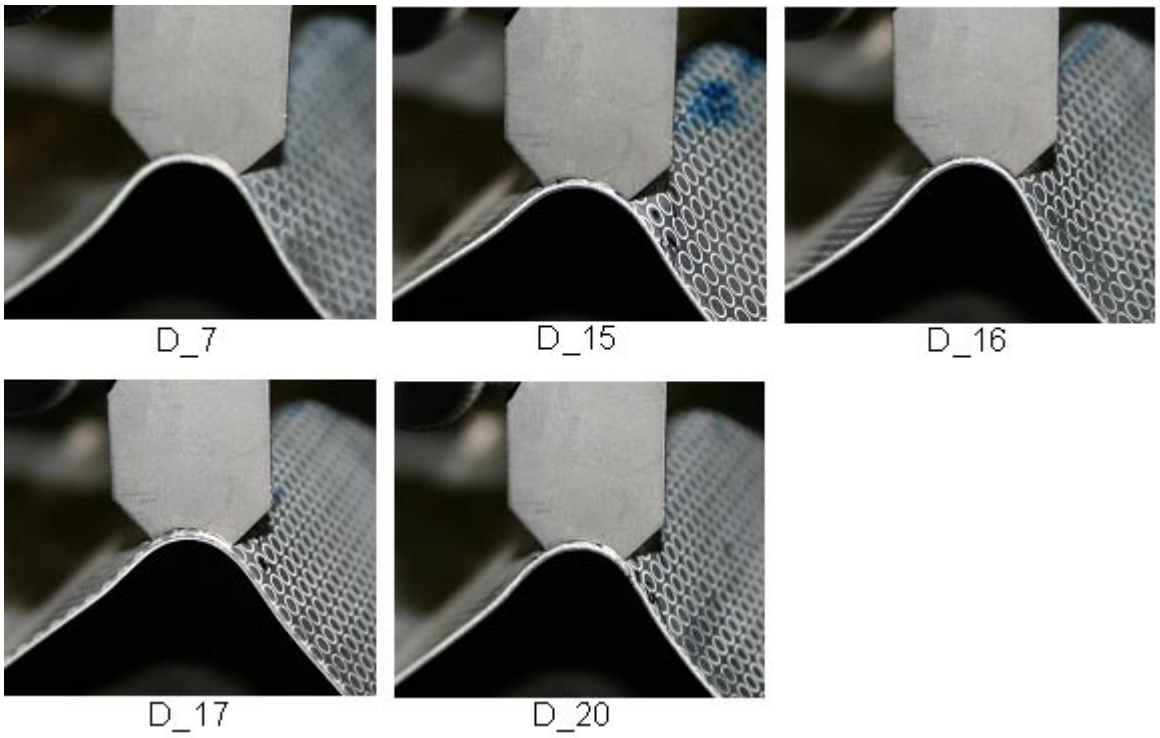

Figure 100: Close up of one the edges of the samples formed from the as-received sheet with a 8 mm radius gauge.

The measured discharge current profiles for seven samples are shown in Figure 101**.** It can be seen that the profiles are nearly identical from the start until they reach zero again at 42 μs which is a good indication of the consistency of the process. According to the simulations the samples have impacted the tool by this time. Soon after the current becomes negative, the current profiles start diverging. The reasons for this variation are not completely clear, but arcing and variations in movement of the sample are suspected causes.

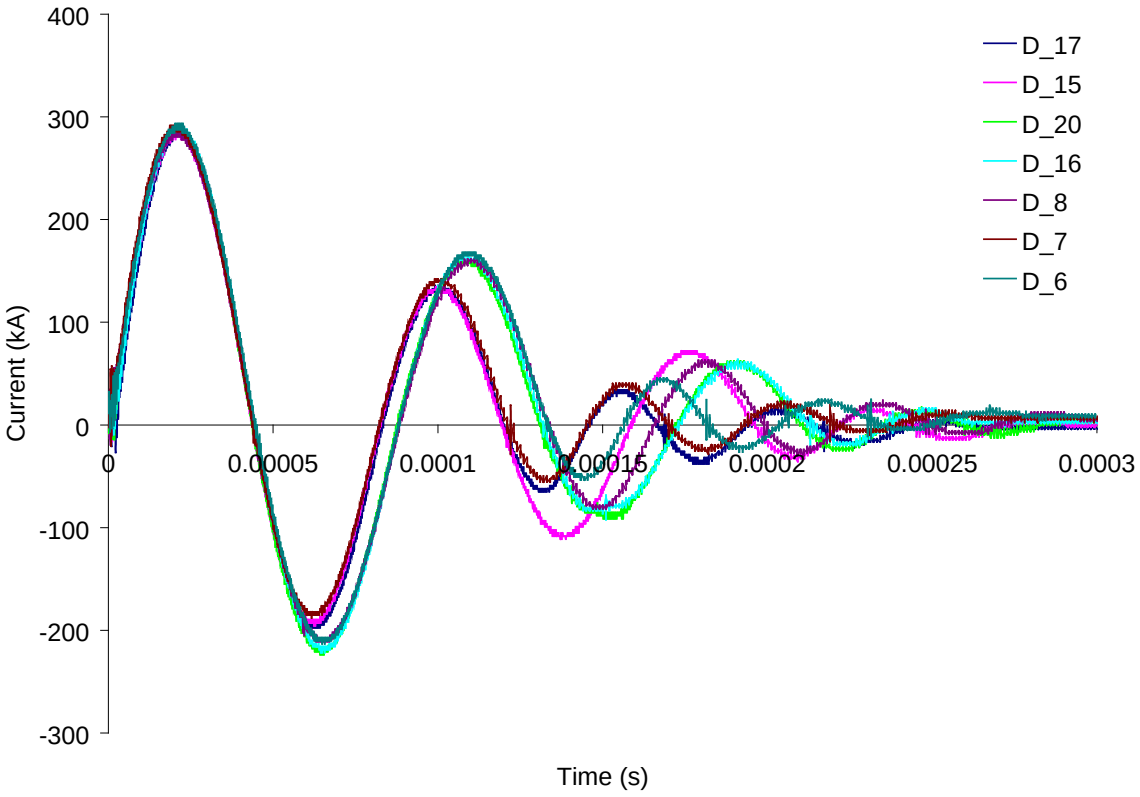

Figure 101: Experimental current versus for the samples formed from the as-received sheet.

The measured strains in the transverse and longitudinal directions for the as-received samples are shown in Figure 102 and Figure 103. The strains along the top of the samples are larger than those measured on the drawn samples (Figure 89 and Figure 90), which is consistent with the additional deformation.

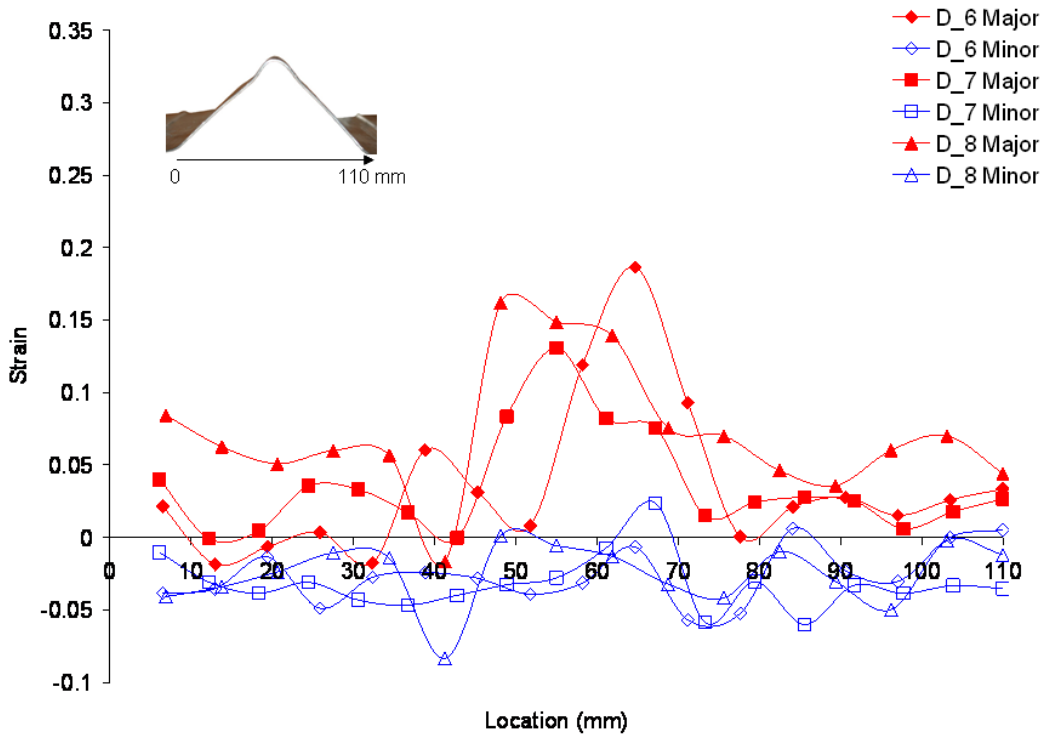

Figure 102: Measured strains for samples formed from the sheet in the as-received condition in the longitudinal direction.

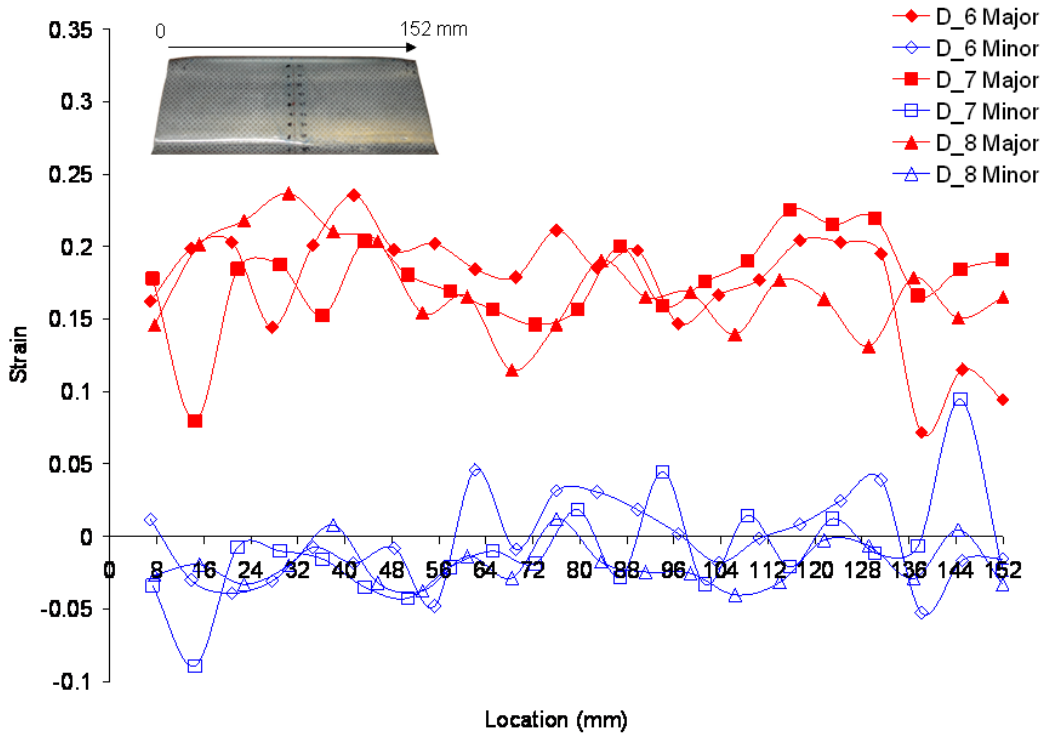

Figure 103: Measured strains for samples formed from the sheet in the as-received condition in the transverse direction.

The highest strains were observed on the side of the sample adjacent to the sharp radius, as indicated in Figure 97-b. The strains from the five grids with the highest deformation observed were measured for each sample and plotted on a forming limit diagram (FLD) along with the conventional forming limit curve (FLC) for AA 5754, (Figure 104). Also included in the figure are the highest strains measured on the samples in the pre-formed state prior to the corner fill operation. A few measurements were above the FLC, but given the measurements error, it can be said that the strains were close to the curve.

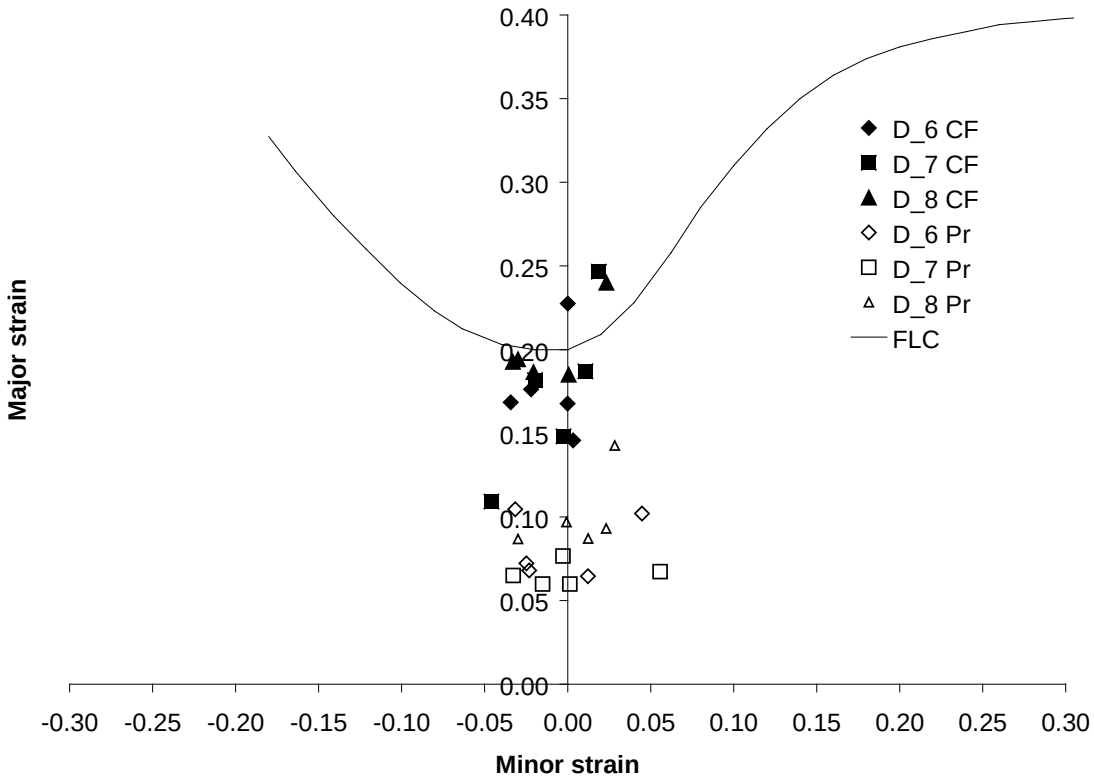

Figure 104: Forming limit diagram containing the largest strains measured on the final corner filled samples and the samples in the pre-formed state formed from sheet in the as-received condition.

4.2.4 Results for the 5% Pre-Strained Sheet

The same process and analysis was followed for the samples formed using sheet pre-trained by 5%. Figure 105 shows samples formed with the 5% pre-strained sheet, the blue ink at the top of the samples indicates that contact was made with the die. The shape of the

samples was essentially the same as for the as-received samples. The radius gauge measurements for two samples are shown in Figure 106 and Figure 107. The same trends discussed for the as-received samples were observed. Only two samples were measured with the radius gauge because the other samples were cut for metallographic analysis before the measurements could be made.

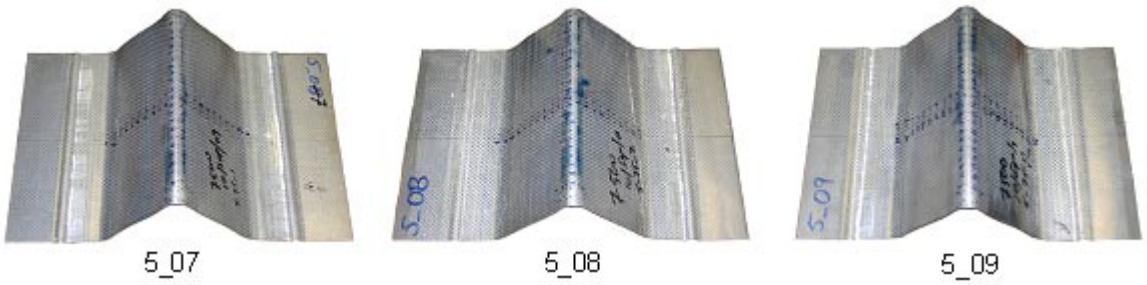

Figure 105: Samples formed from the 5% pre-strained sheet.

Figure 106: Close up of the centre region of the samples formed from the 5% pre-strained sheet with a 5 mm radius gauge.

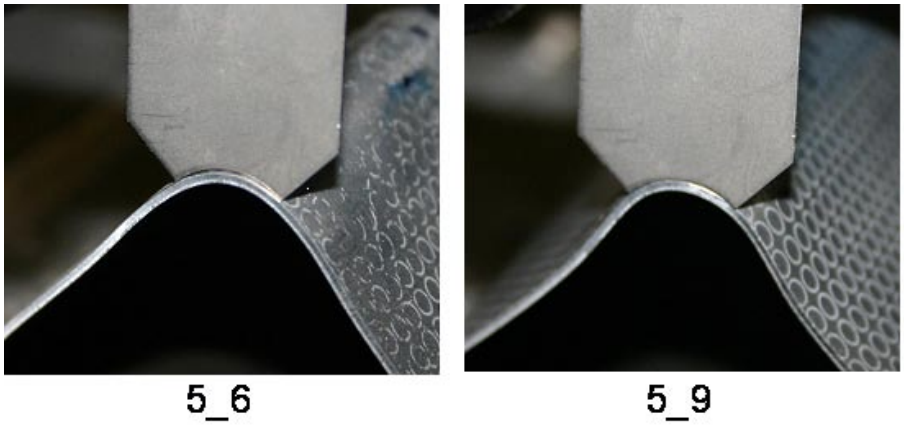

Figure 107: Close up of one the edges of the samples formed from the 5% pre-strained sheet with a 8 mm radius gauge.

The experimental current profile for a 5% pre-strained sample is shown in Figure 108. Due to a technical problem, only the current for a single test was recorded. The current pulses were checked as the experiments were being conducted and no anomaly was visually detected. The first positive part of the pulse is nearly identical to the pulses in the other tests; differences in the recorded pulses will be discussed in more detail below.

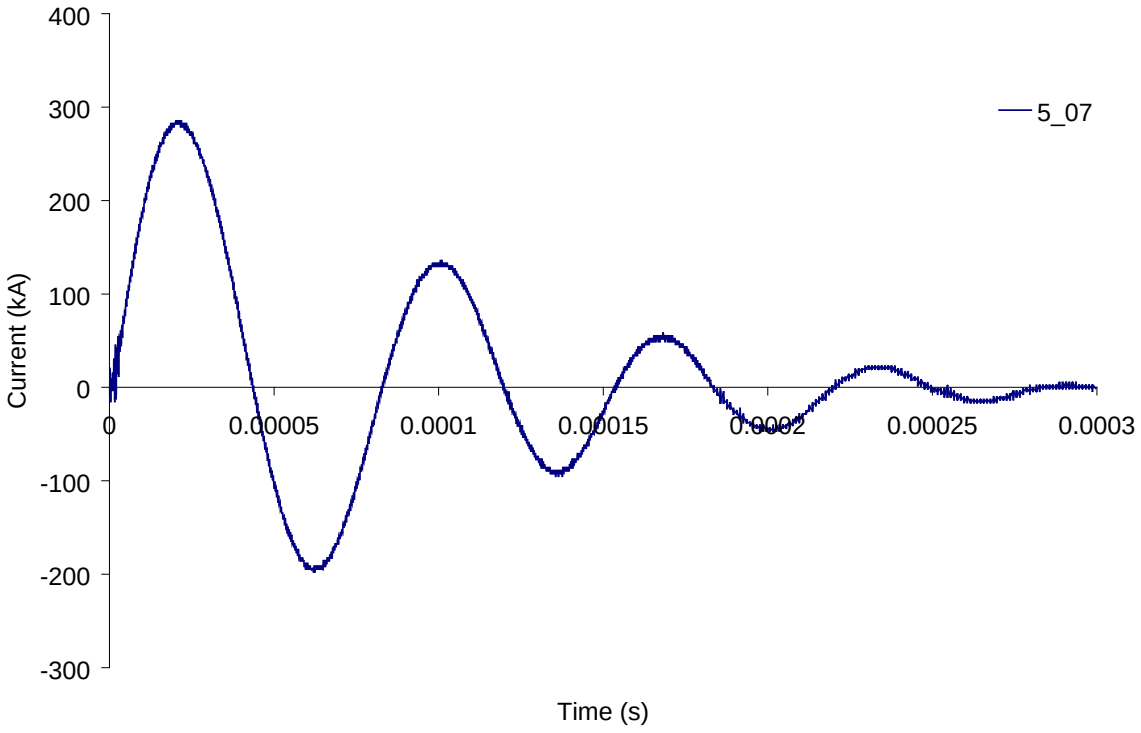

Figure 108: Experimental current versus for the samples formed from the sheet with 5% pre-strain. Due to an equipment malfunction the data for the other samples was lost.

The measured strains in the longitudinal and transverse directions for the 5% pre-strained samples are shown in Figure 109 and Figure 110. The strains for the five largest observed grids are plotted on an FLD in Figure 111, together with the strains for the samples in the pre-strained state and with the strains recorded on the sheets after the pre-straining operations. The strains for each condition increase from the pre-strained sheet, through the pre-formed and final states, as expected. As with the as-received samples the strains are near the FLC, but still on the safe area of the diagram.

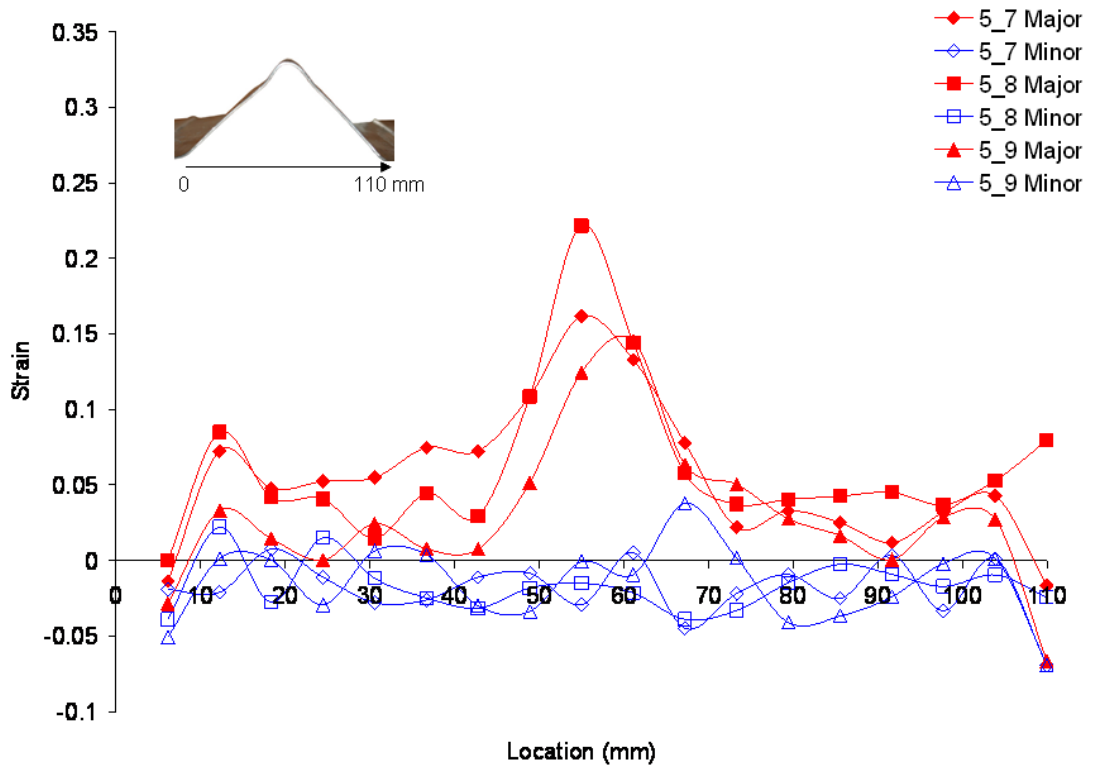

Figure 109: Measured strains for samples formed from 5% pre-strained sheet in the longitudinal direction.

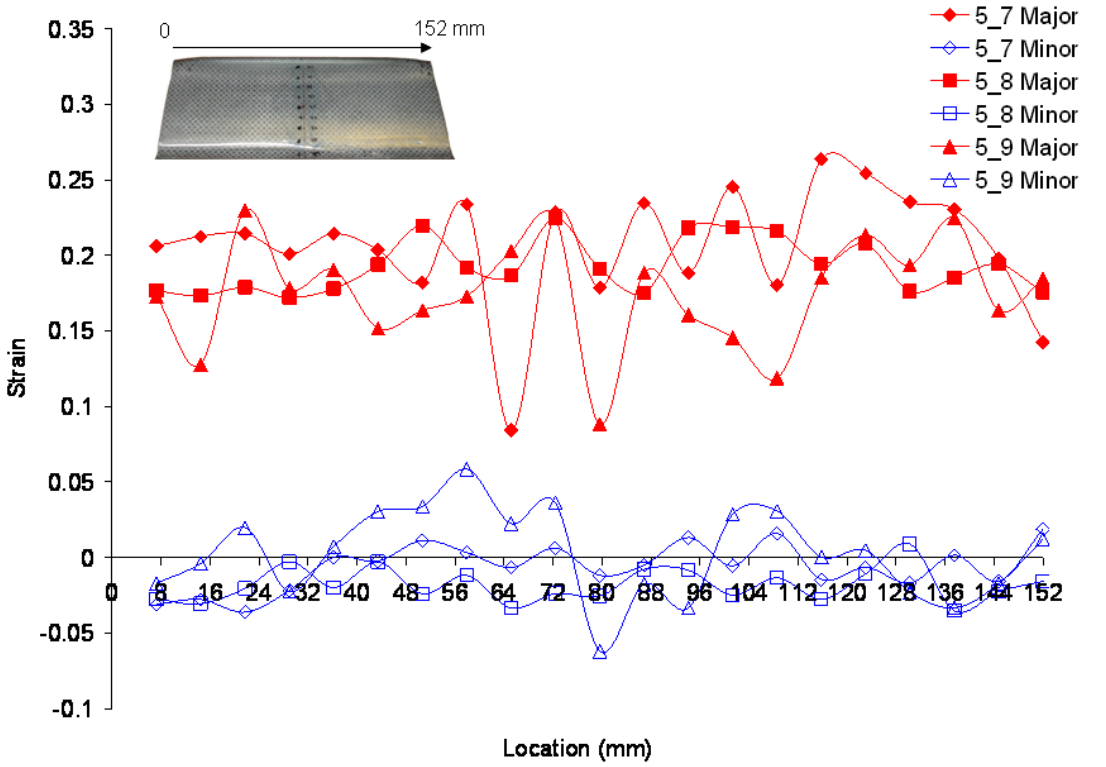

Figure 110: Measured strains for samples formed from 5% pre-strained sheet in the transverse direction.

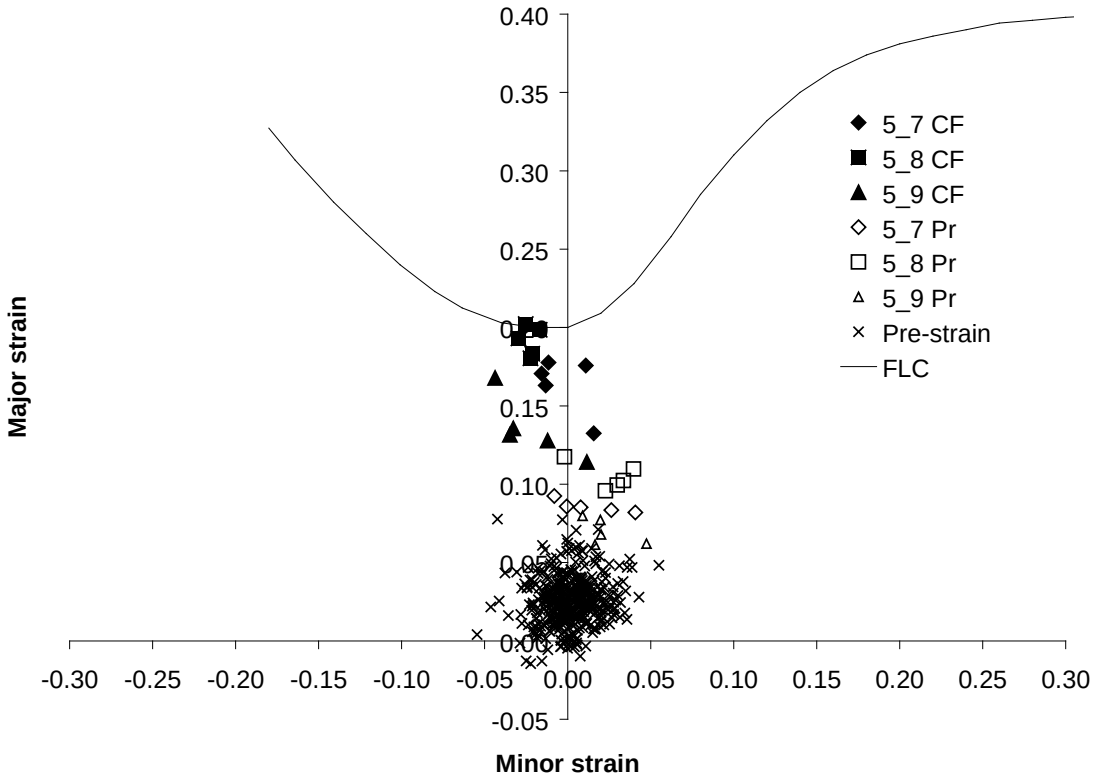

Figure 111: Forming limit diagram containing the largest strains measured on the final corner filled samples and the samples in the pre-formed state formed with the sheet pre-strained to 5%. Also shown are the strains measured on the pre-strained sheets.

4.2.5 Results for the 10% Pre-Strained Sheet

Figure 112 shows samples formed with the 10% pre-strained sheet. The radius gauge measurements are shown in Figure 113 and Figure 114. These samples presented the same shapes as those already described.

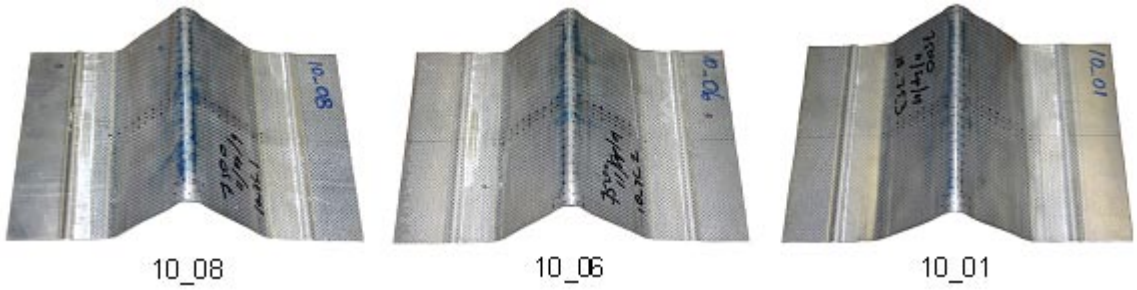

Figure 112: Samples formed from the 5% pre-strained sheet.

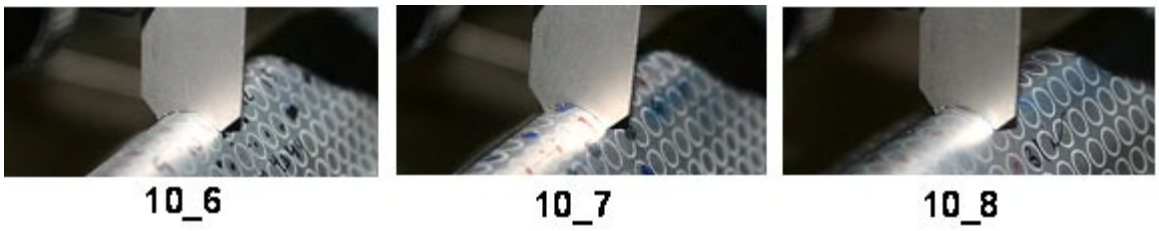

Figure 113: Close up of the centre region of the samples formed from the 10% pre-strained sheet with a 5 mm radius gauge.

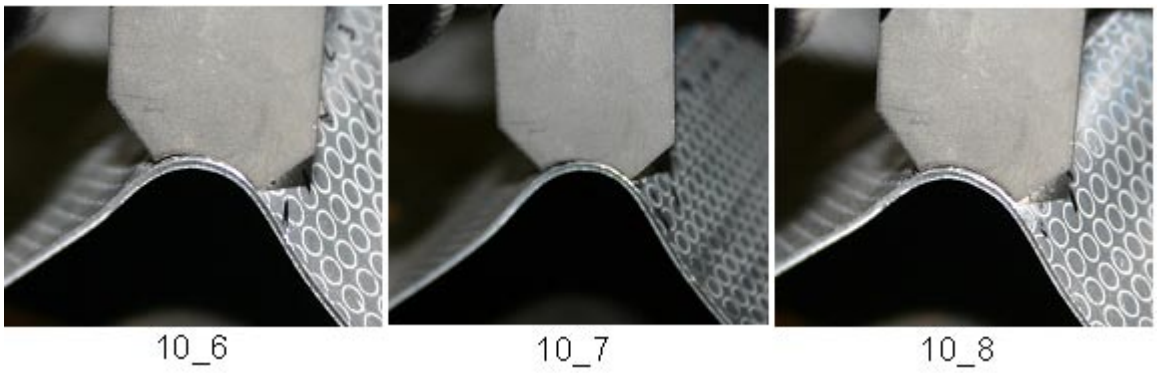

Figure 114: Close up of one the edges of the samples formed from the 10% pre-strained sheet with a 8 mm radius gauge.

The current profiles for three samples are shown in Figure 115. As with the samples formed with the as-received sheet, the pulses for all three samples are nearly identical from the beginning until after the current becomes negative.

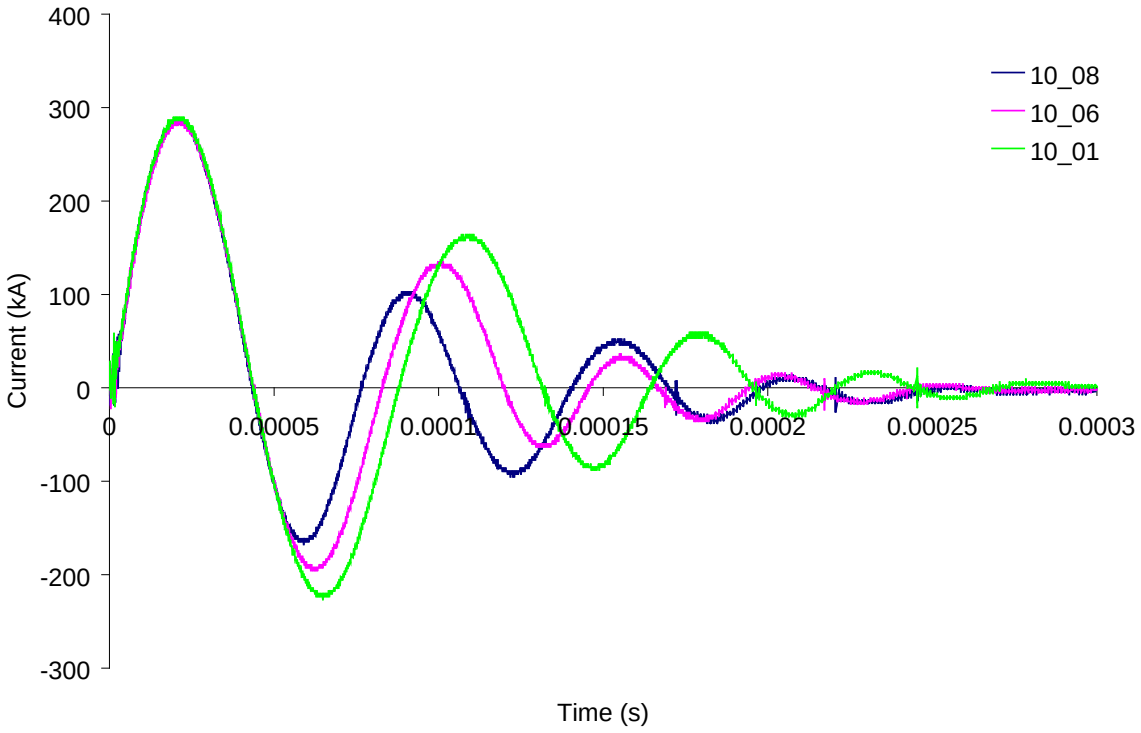

Figure 115: Experimental current versus for the samples formed from the sheet with the 10% pre-strain.

The measured strains in the transverse and longitudinal directions for the 10% pre-strained samples are shown in Figure 117 and Figure 116. The trends are similar to the one observed in the 5% and as-received samples, with the major strains being larger. The five most heavily deformed grids were measured and plotted on an FLD (Figure 118), together with the strains for the samples in the pre-strained state and with the strains recorded on the sheets after the pre-straining operations. For these samples many of the strains were above the FLC in what would be considered the failure area, even when the measurement error is considered.

.

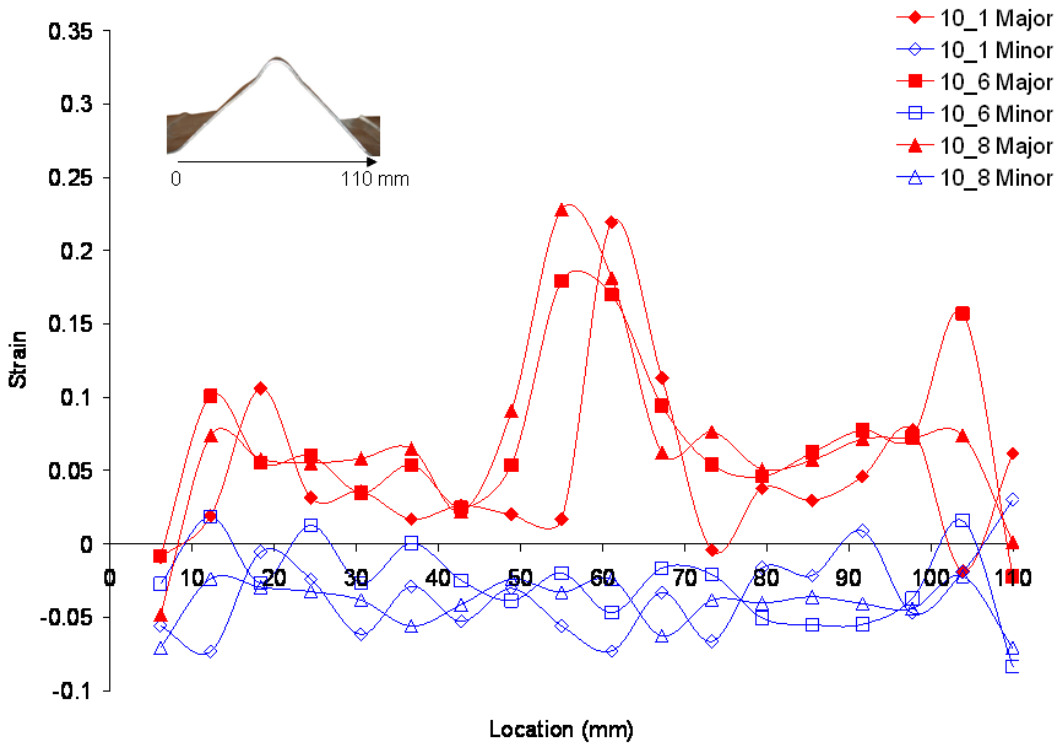

Figure 116: Measured strains for samples formed from 10% pre-strained sheet in the longitudinal direction.

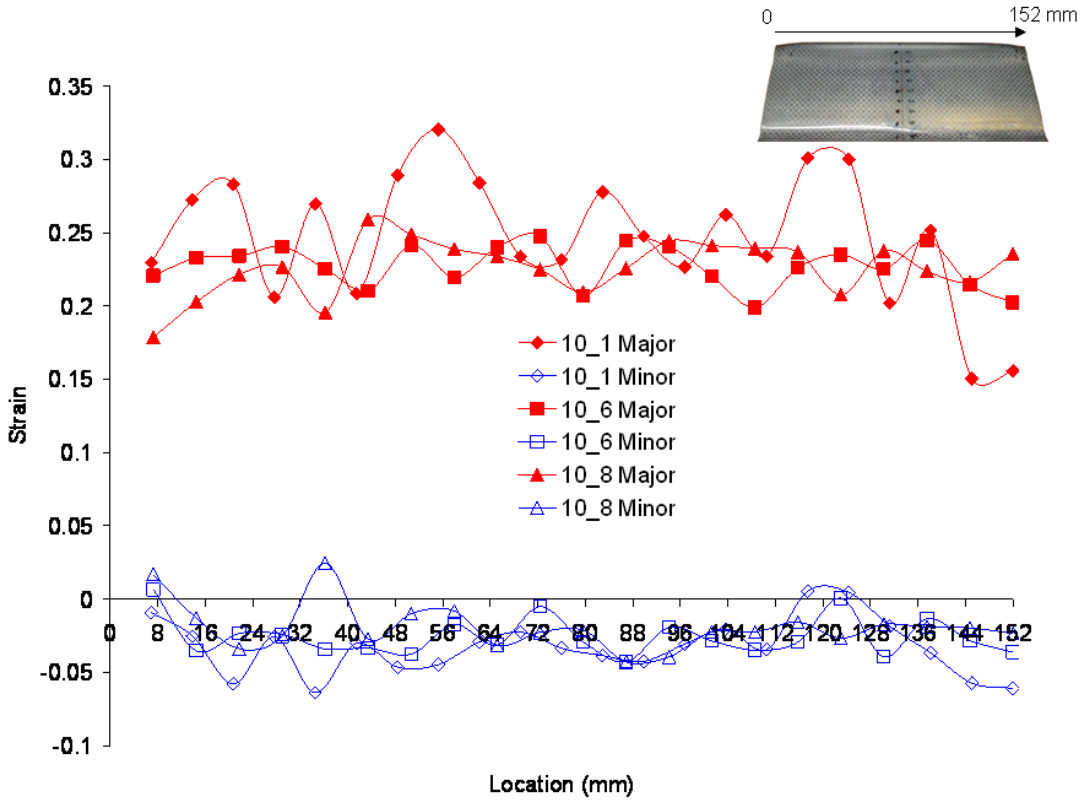

Figure 117: Measured strains for samples formed with 10% pre-strained sheet in the transverse direction.

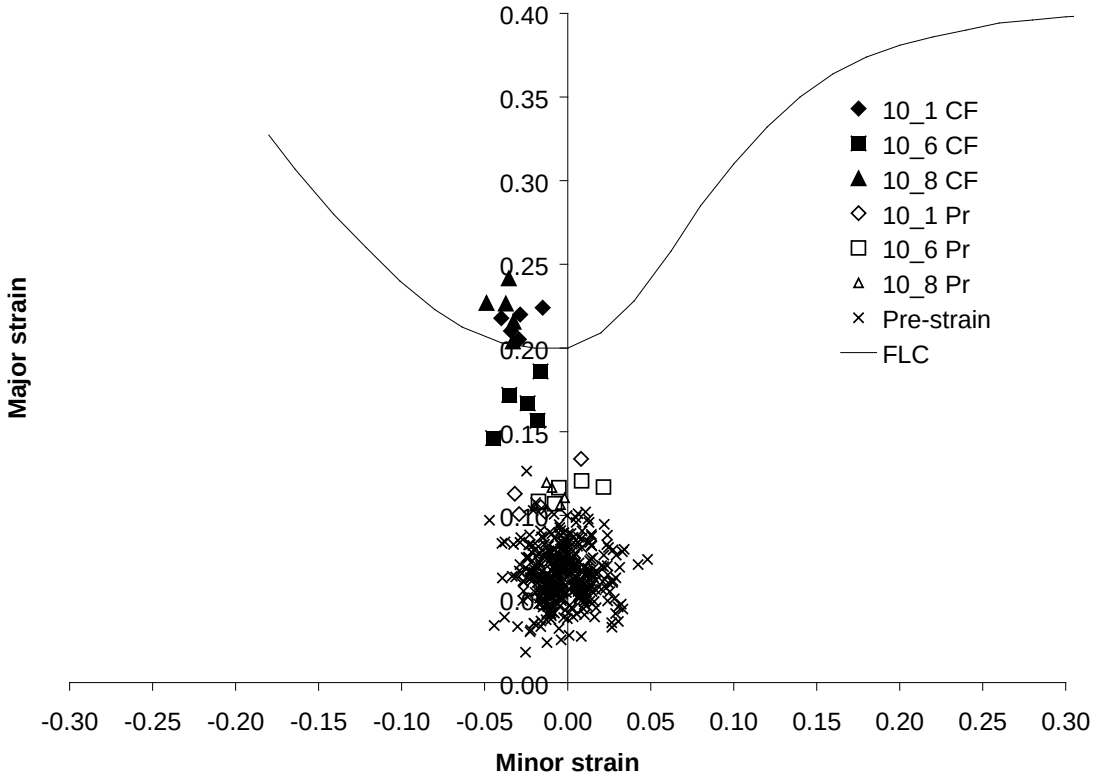

Figure 118: Forming limit diagram containing the largest strains measured on the final corner filled samples and the samples in the pre-formed state formed with the sheet pre-strained to 10%. Also shown are the strains measured on the pre-strained sheets.

4.2.6 Results for the 15% Pre-Strained Sheet

Figure 119 shows samples formed with the 15% pre-strained sheet and the radius gauge measurements are shown in Figure 120 and Figure 121. The same general shapes were observed. The ink marks left on the samples were not as dark as the ones for the as-received, 5 and 10% pre-strained samples, which may indicate that the samples did not strike the die with as much force, which could be due to the higher work hardening and flow stress of the pre-strained material.

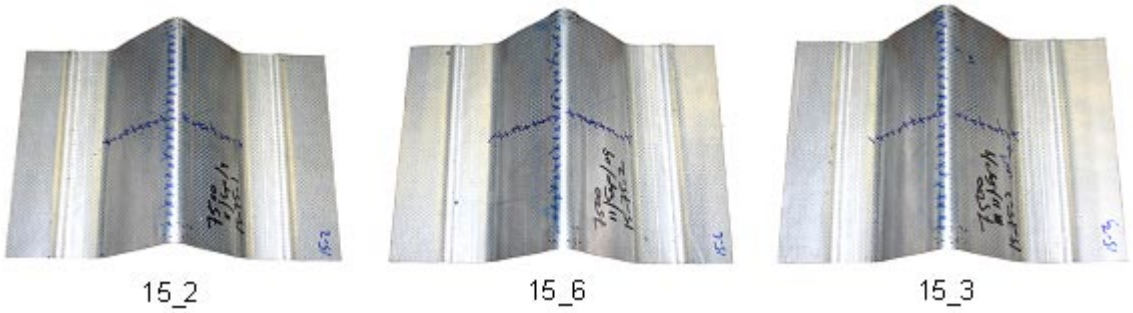

Figure 119: Samples formed from the 5% pre-strained sheet.

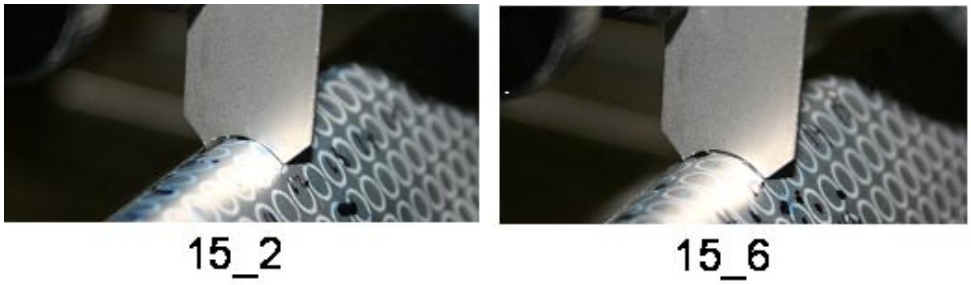

Figure 120: Close up of the centre region of the samples formed from the 15% pre-strained sheet with a 5 mm radius gauge.

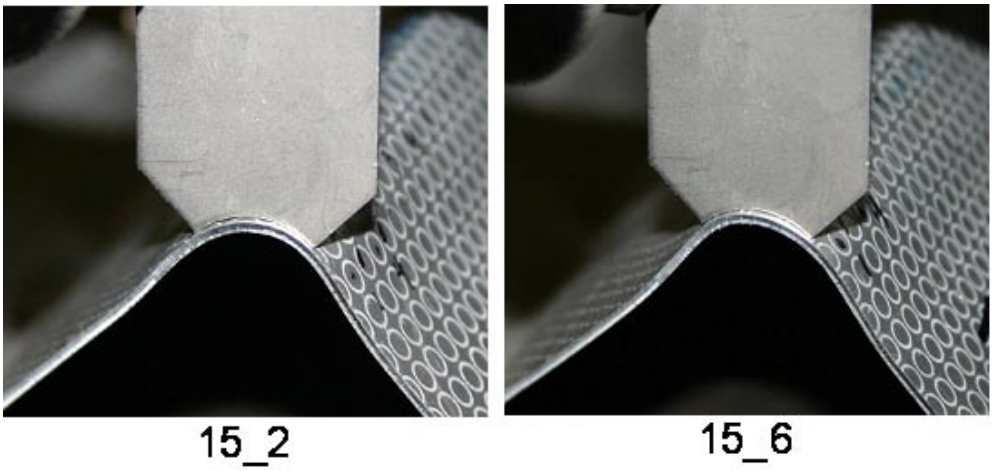

Figure 121: Close up of one the edges of the samples formed from the 15% pre-strained sheet with a 8 mm radius gauge.

The current profiles for the three tests (Figure 122) were more consistent for a longer duration than seen, for example on the as-received samples (Figure 101). This could be due to less rebound which could be the result of the sample striking the die with less energy, which could also be due to the aforementioned work hardening of the pre-strained sheet.

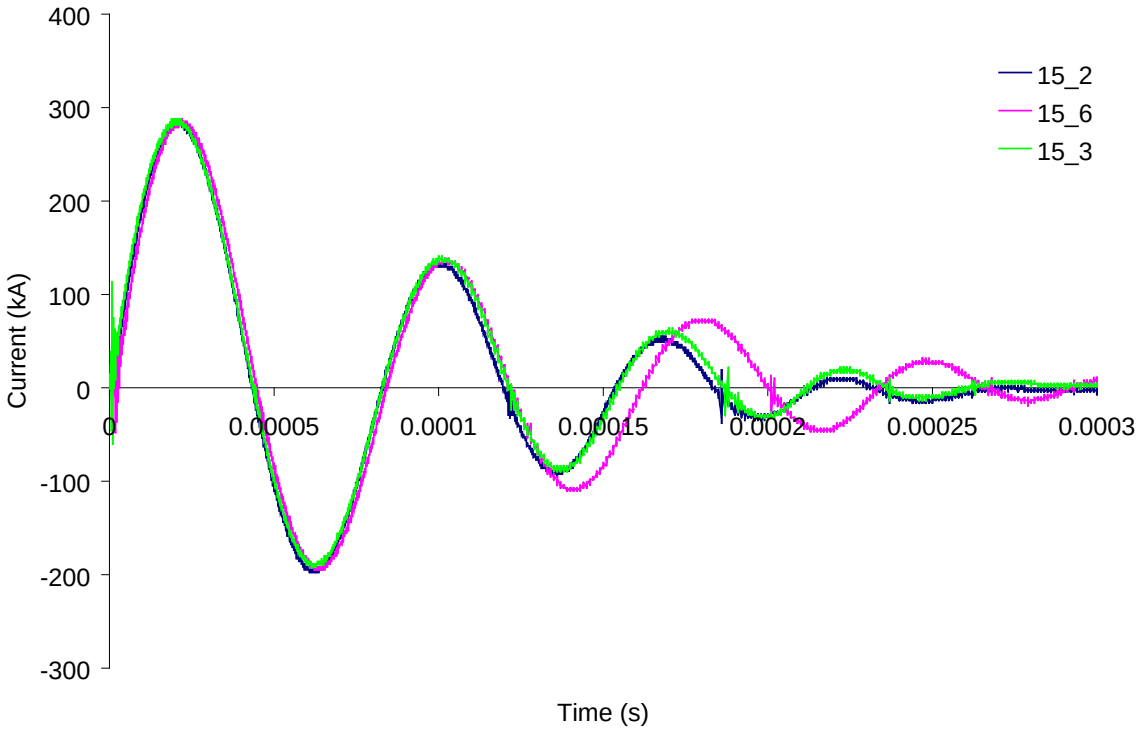

Figure 122: Experimental current versus for the samples formed from the the sheet with the 15% pre-strain.

The measured strains in the transverse and longitudinal directions for the 15% pre-strained samples are shown in Figure 123 and Figure 124. The trends are similar to the other pre-strained conditions, but with higher measured strains. The FLD for these samples is shown in Figure 125, together with the strains for the samples in the pre-strained state and with the strains recorded on the sheets after the pre-straining operations. For these samples, many strains are clearly above the FLC, indicating an increase in formability when compared to traditional forming processes. For this condition, the pre-formed samples showed strains that were close to the FLC (Figure 125) and the subsequent corner fill operation produced increased strains with no indication of failure, which is an indication that the formability of the material has been increased. Since the sheets were pre-strained, the possibility that strain path effects were altering formability was considered; however, experiments with conventional corner fill operations (presented in Section 4.3) showed that the samples pre-strained to 15% were less formable than those in the as-received condition. Furthermore, the FLD plot in Figure 125, for example, suggest that the strain paths were relatively monotonic.

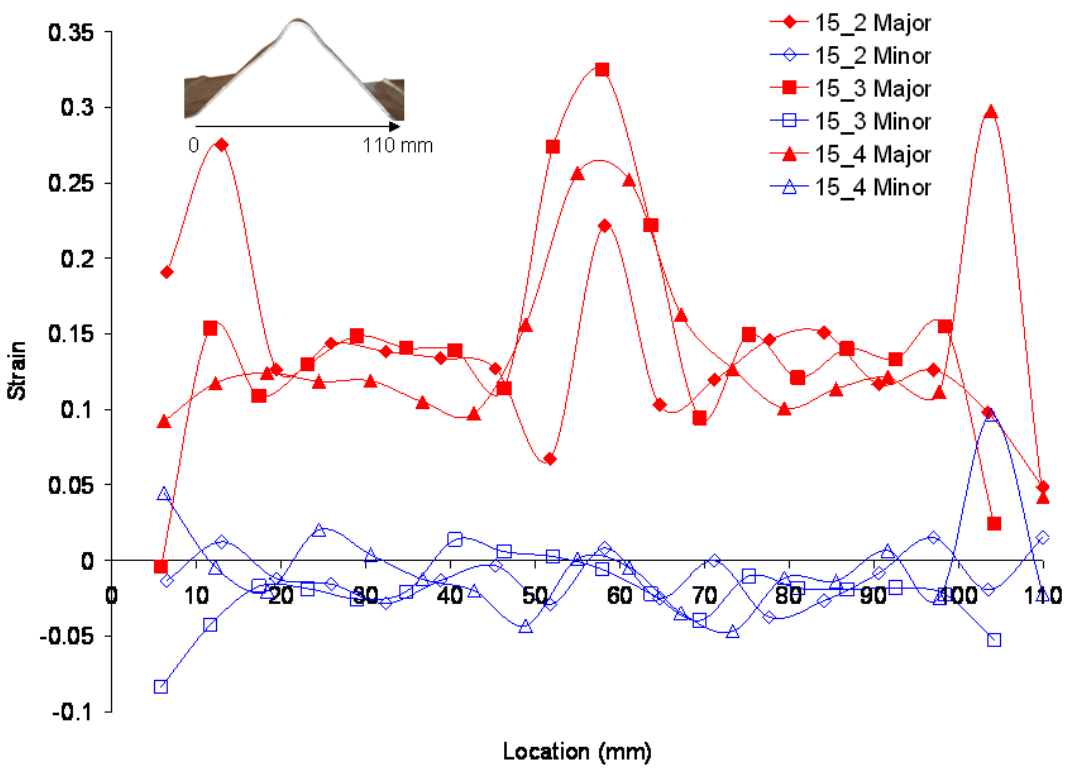

Figure 123: Measured strains for samples formed from 15% pre-strained sheet in the longitudinal direction.

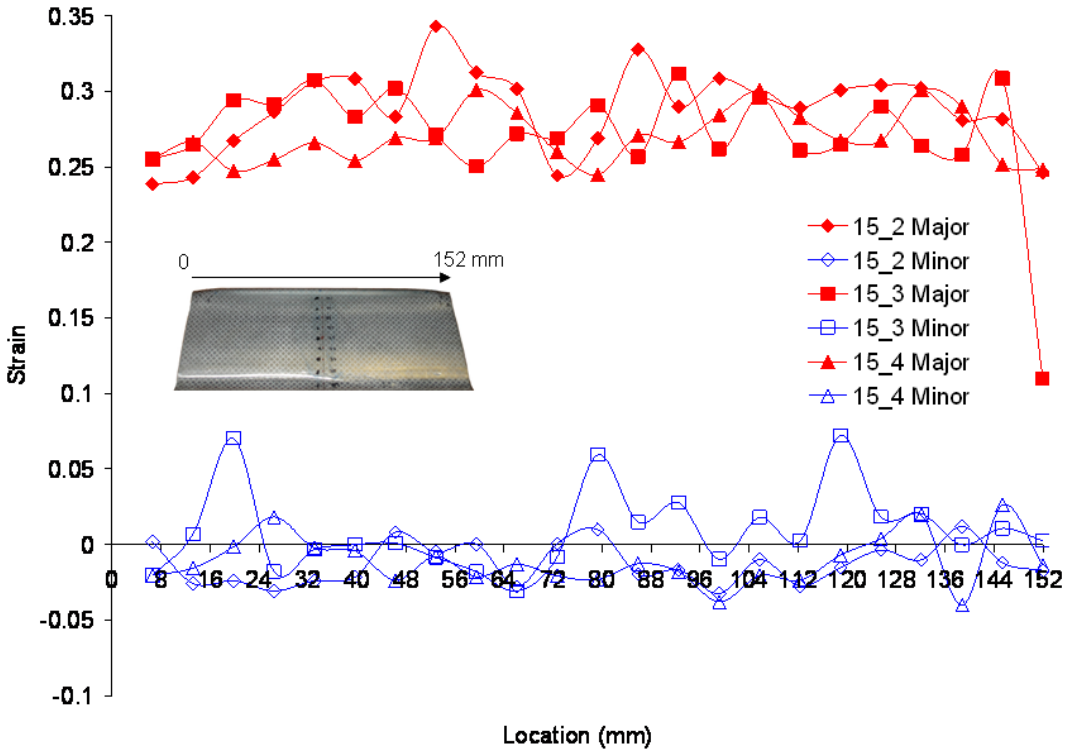

Figure 124: Measured strains for samples formed from 15% pre-strained sheet in the transverse direction.

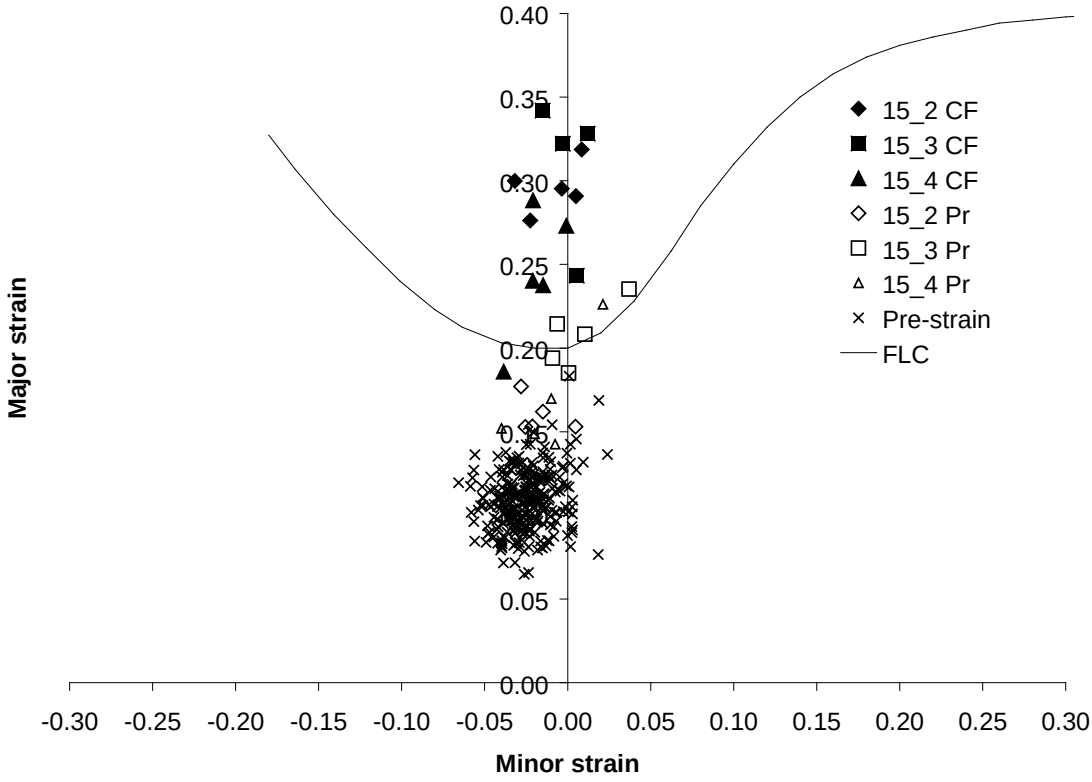

Figure 125: Forming limit diagram containing the largest strains measured on the final corner filled samples and the samples in the pre-formed state formed with the sheet pre-strained to 15%. Also shown are the strains measured on the pre-strained sheets.

An FLD with showing the strains for the final samples formed with the sheets in all the conditions is shown in Figure 126. The samples formed with the 15% pre-strained sheet show the highest strains, with the samples formed from the as-received and 5% pre-strain sheets showing similar results, which is consistent with the measurement errors. Increases in formability compared to the conventional forming limits are clearly visible for the 10 and 15% pre-strain samples.

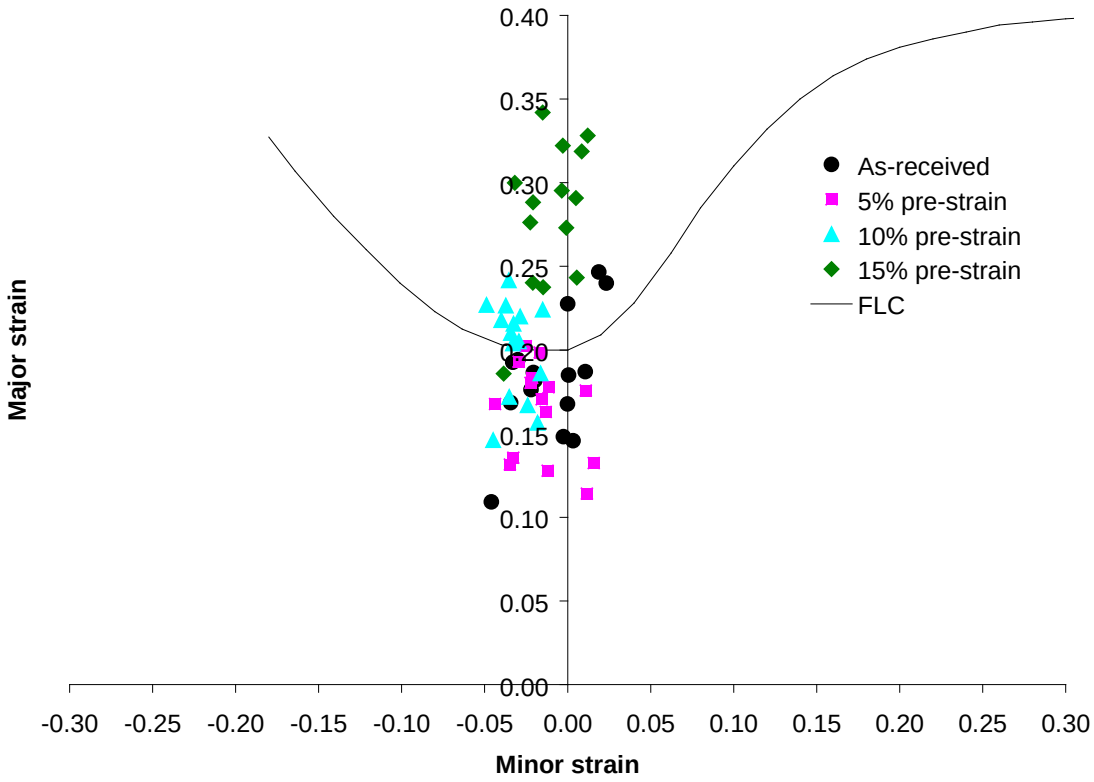

Figure 126: Forming limit diagram showing the highest strains measured on the corner filled samples formed with the sheet in all of the conditions studied.

Figure 127 shows all the measured current profiles for the samples discussed immediately above. It can be seen that for the first pulse all the profiles are nearly identical. The profiles begin to diverge near the first negative peak. The reasons for this behaviour are not completely clear, but arcing and variations in the movement of the samples are suspected causes.

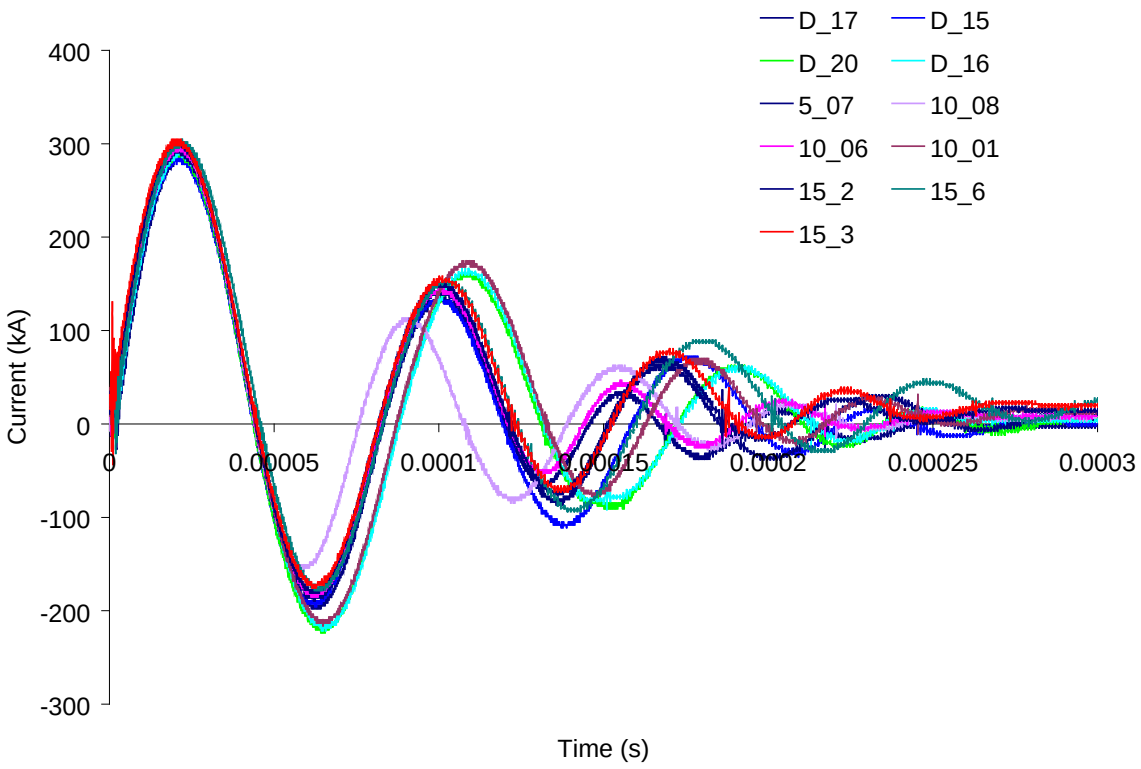

Figure 127: Overlay of all the measured current profiles.

4.3 Conventional (Stamping) Corner Fill Experiments

Experiments were performed in which 20 mm radius pre-formed samples were subsequently formed into a 5 mm radius die using a conventional stamping operation. These experiments provide a baseline formability performance for comparison to the Hybrid EM corner fill experiments. For these experiments, the pre-formed samples were clamped using double lock beads to prevent any draw-in and then stamped with the 5 mm radius punch to attempt to form the sharp corner.

Non of the samples were formed successfully, most samples failed in the punch radius region, as shown in Figure 128. Some of the samples formed with the pre-strained sheets failed as shown in Figure 128-c in an area where the emery paper used for draw-in control produced additional thinning. The same thinning was also present in samples formed from the sheet in the as-received condition, but no failure in those areas was observed. A close-up of the two failure modes is shown in Figure 129. Some of these samples also presented a neck in the area of the 5 mm radius.

Based on these forming trials, it was determined that the radius could not be sharpened to a 5 mm radius using the conventional tools if no draw-in was allowed. This is consistent with the limiting radius equal to 8-10 times the thickness of the material, as quoted in Section 1.1, since the 5 mm radius attempted was only 5 times the thickness of the sheet.

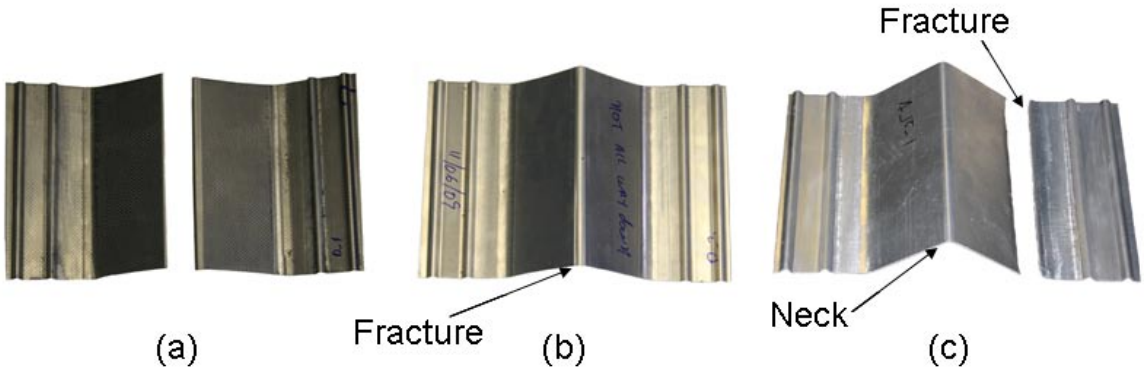

Figure 128: Pre-formed samples that were formed with a conventional stamping tool to fill the 5 mm corner radius. Most samples failed in the same manner as a). Some samples were arrested prior to complete fracture by stopping the punch, as in b). Some of pre-strain samples failed as shown in c) in an area where the emery paper used for draw-in control produced additional thinning.

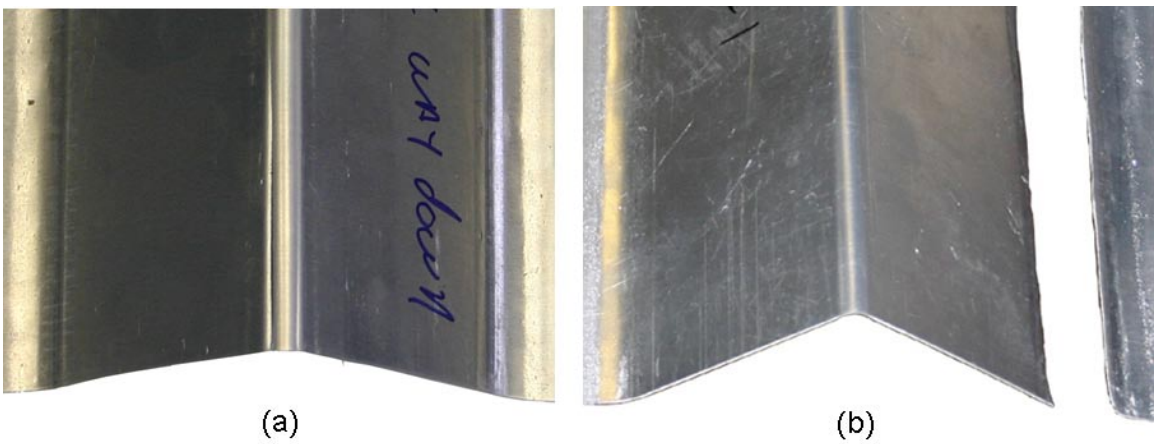

Figure 129: Close-up of the two type of failures observed in the conventional corner fill experiments. The most common failure mode is shown on a), which corresponds to the sample shown in Figure 128-b. The failure that occurred near the area of the lock beads with the emery paper is shown in b), which corresponds to Figure 128-c.

The heights of the formed samples are shown in Figure 130, where it can be seen that the greater the pre-straining the lower the failure height of the sample. This indicates that the pre-straining is reducing the formability of the parts. Only two of the samples pre-strained to 10% are shown in Figure 130, since the samples unfortunately failed in the manner show in Figure 128-c with no indication of material localization.

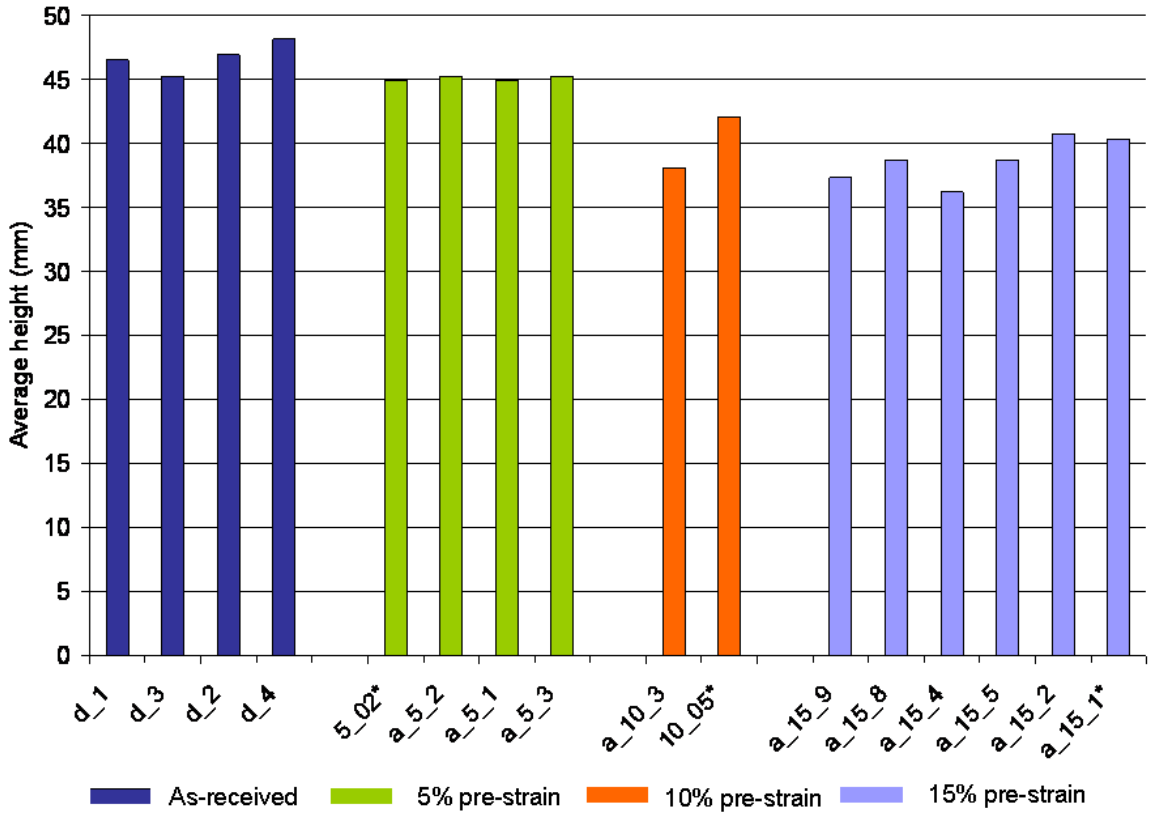

Figure 130: Heights of pre-formed samples that were formed with a conventional tool to try to achieve a 5 mm radius. All samples failed. Samples marked with an * failed in the manner shown in Figure 128-c.

4.4 Results from the Metallographic Analysis

A micrograph that shows the main features found in the microstructure of the samples formed is shown in Figure 131. This sample was used since it presented the second phase particles and voids clearly. The sample chosen for the figure was from a corner filled sample formed using the sheet that was pre-strained by 15%. The second phase particles present in this material are composed of iron and manganese [91].

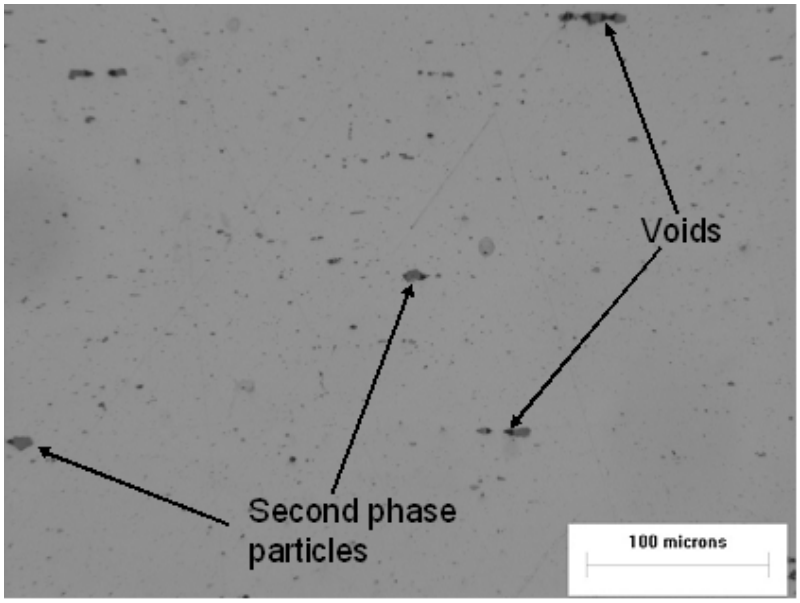

Figure 131: Micrograph from a corner filled sample formed with sheet that was pre-strained to 15%. Second phase particles and voids are indicated. The damage values were obtained by measuring the voids.

To measure the damage, the software counts pixels whose shades of gray were dark enough to be considered a void, as indicated by the operator. The software then calculated the area of the image that was covered with voids. Finally, the area covered with voids was divided by the analysis area to determine the void volume fraction. Figure 138 shows the measured void volume fractions for the samples analysed. Damage measurements were taken on the top of the sample (labeled the "tip") and on the area on either side of the tip, where the damage was expected to be the highest (Figure 138-inset). A previously undertaken study on 1.6 mm sheet of AA 5754 showed that for quasi static tensile samples the porosity near the fracture surface averaged 0.073 % [92], which is over twice the highest level measured on the corner filled samples.

Figure 132 to Figure 137 show the tiled images used for the damage calculations. The location for the tiled images used for the corner filled sample measurements are shown in the respective figures. Each of these figures is formed from either 18 or 24 images like the one shown in Figure 138.

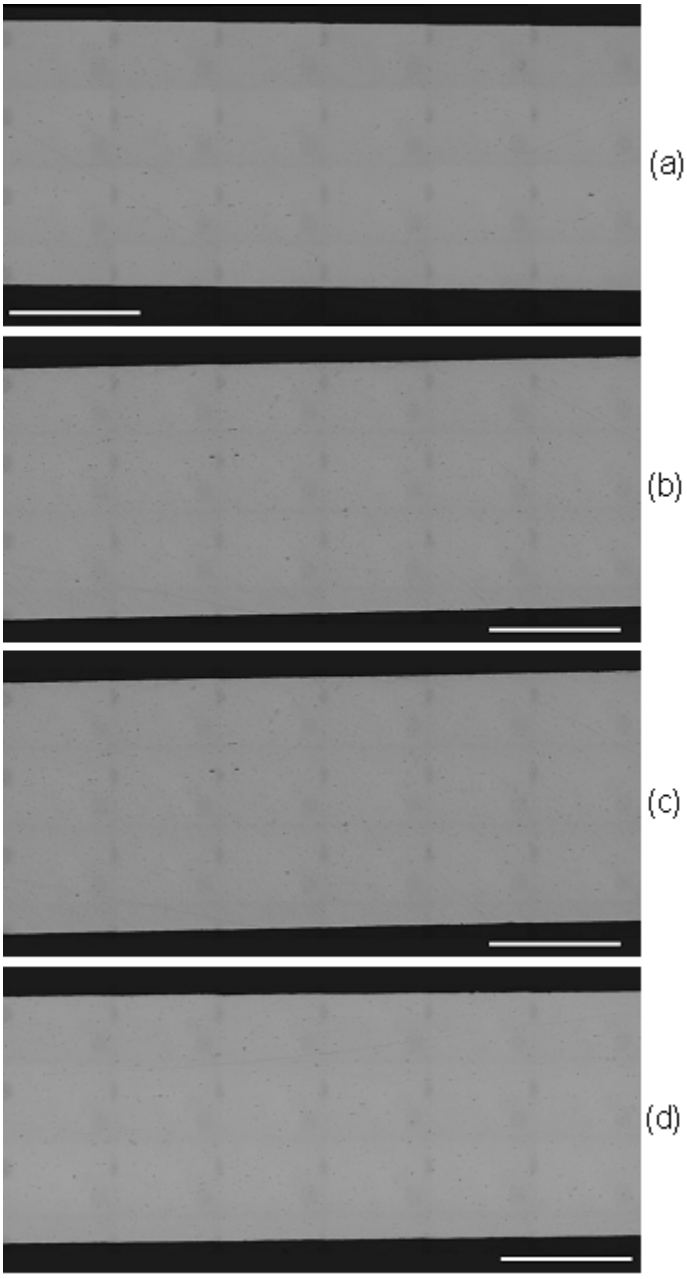

Figure 132: Tiled images used for damage measurements on flat sheet for the a) as-received, b) 5% pre-strained, c) 10% pre-strain and d) 15% pre-strained conditions.

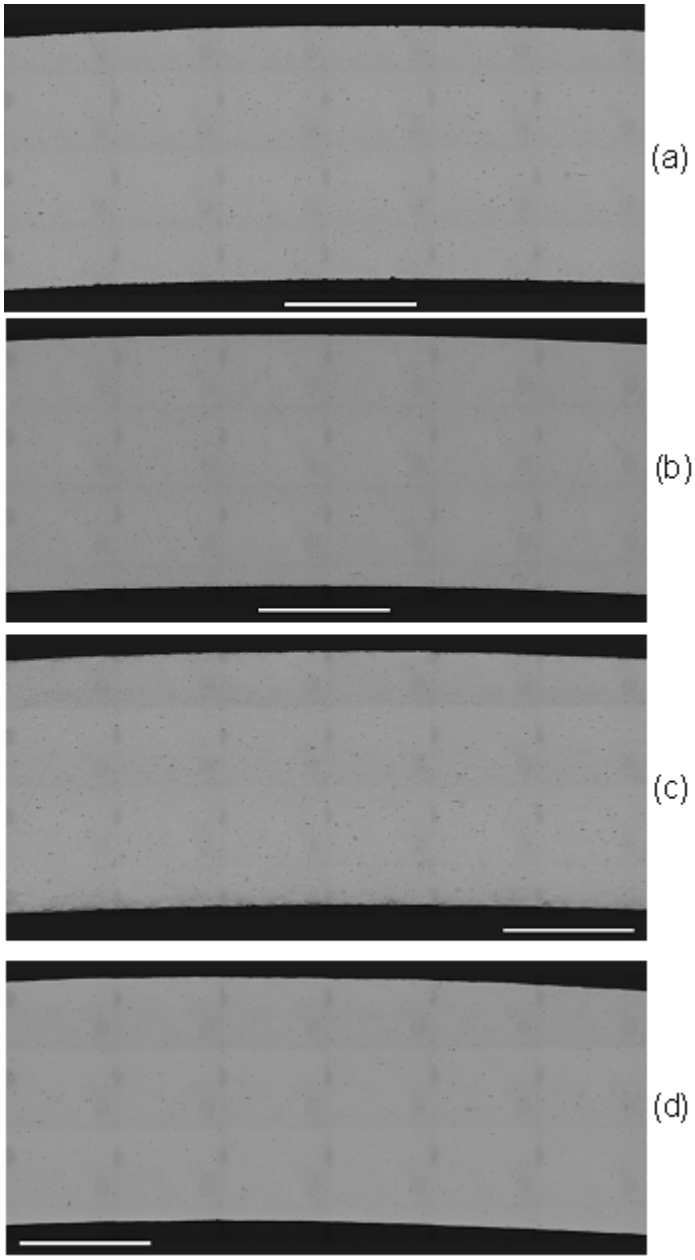

Figure 133: Tiled images used for damage measurements on the pre-formed samples drawn to a 20 mm outer radius for the a) as-received, b) 5% pre-strained, c) 10% pre-strain and d) 15% pre-strained conditions.

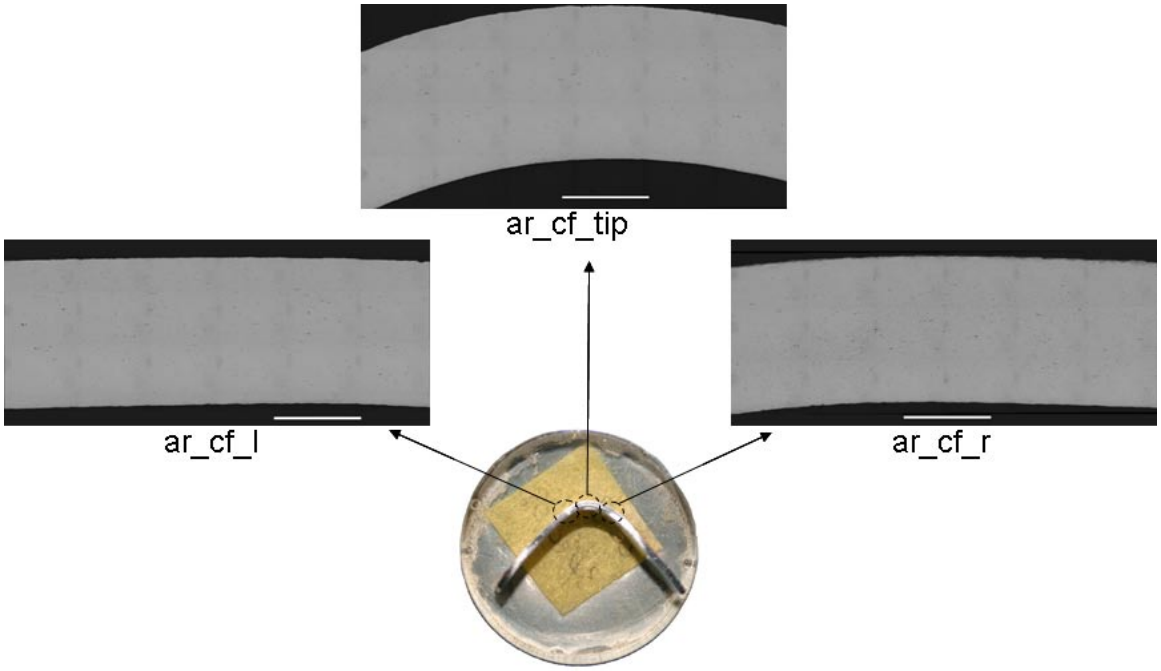

Figure 134: Tiled micrographs for the corner filled sample formed with as-received sheet.

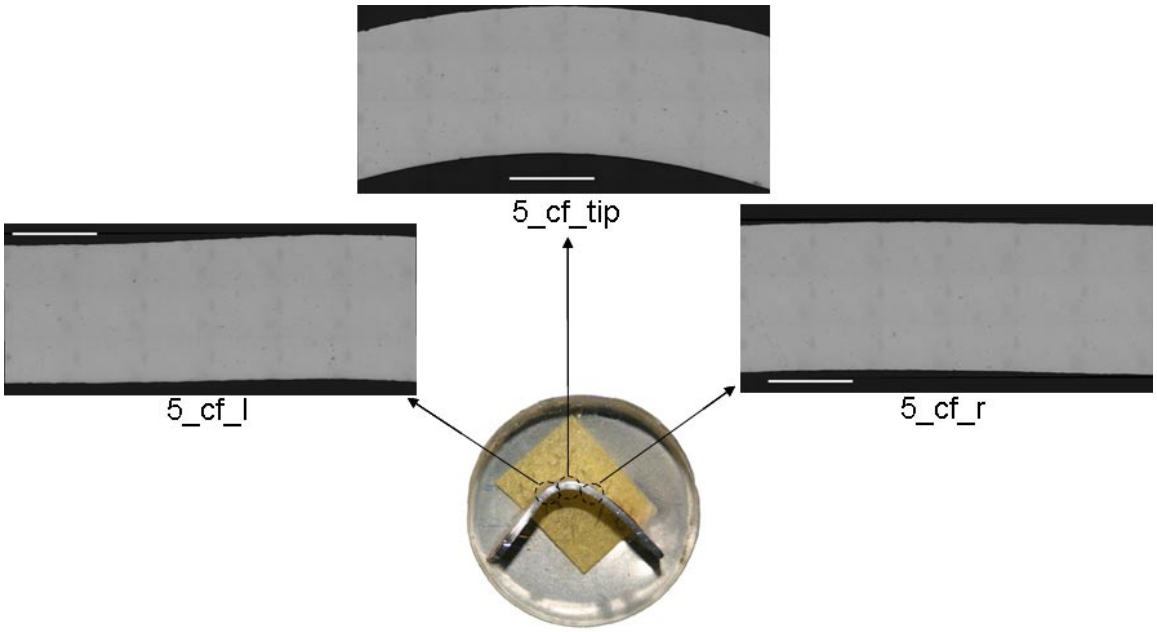

Figure 135: Tiled micrographs for the corner filled sample formed with the 5% pre-strained sheet.

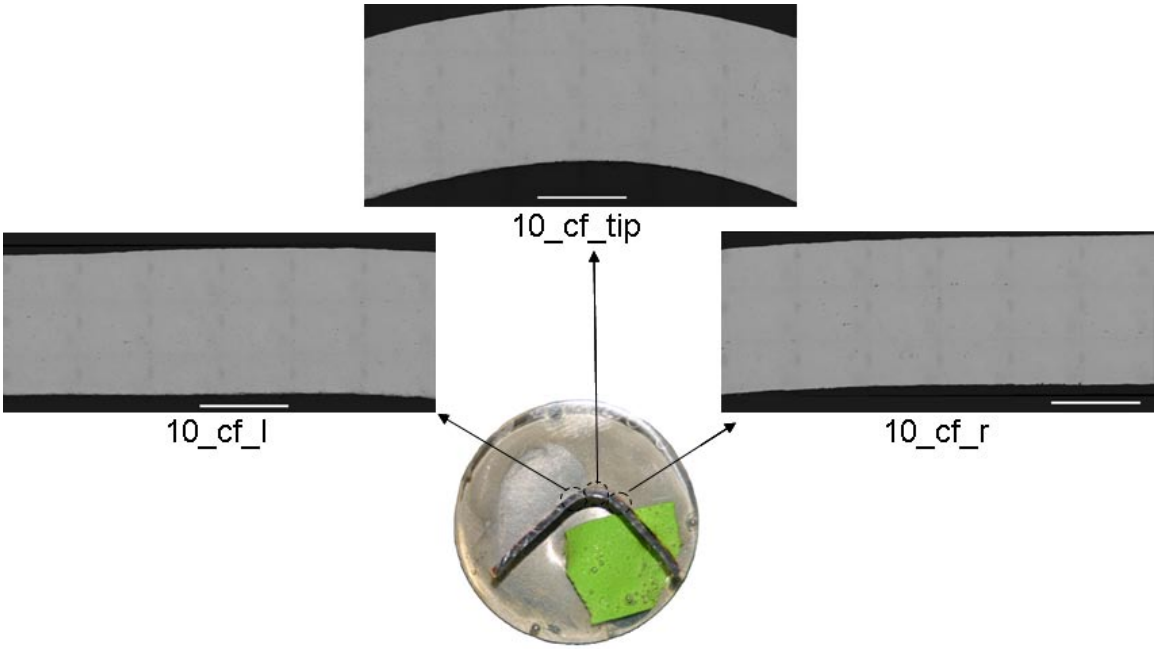

Figure 136: Tiled micrographs for the corner filled sample formed with the 10% pre-strained sheet.

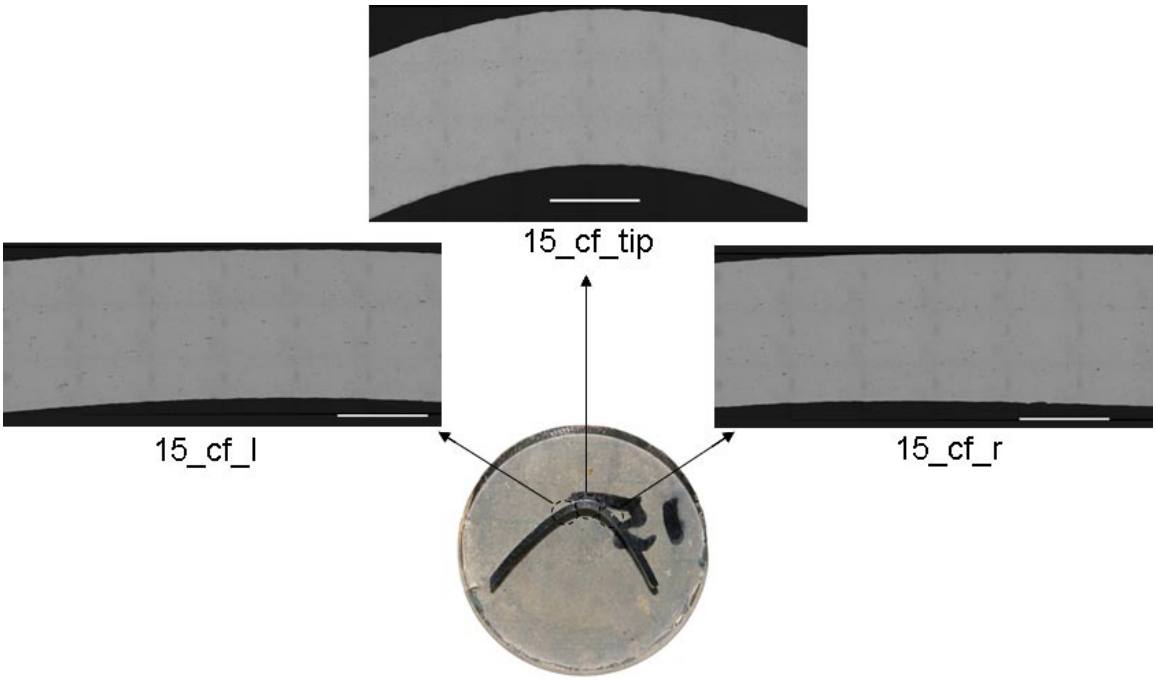

Figure 137: Tiled micrographs for the corner filled sample formed with the 15% pre-strained sheet.

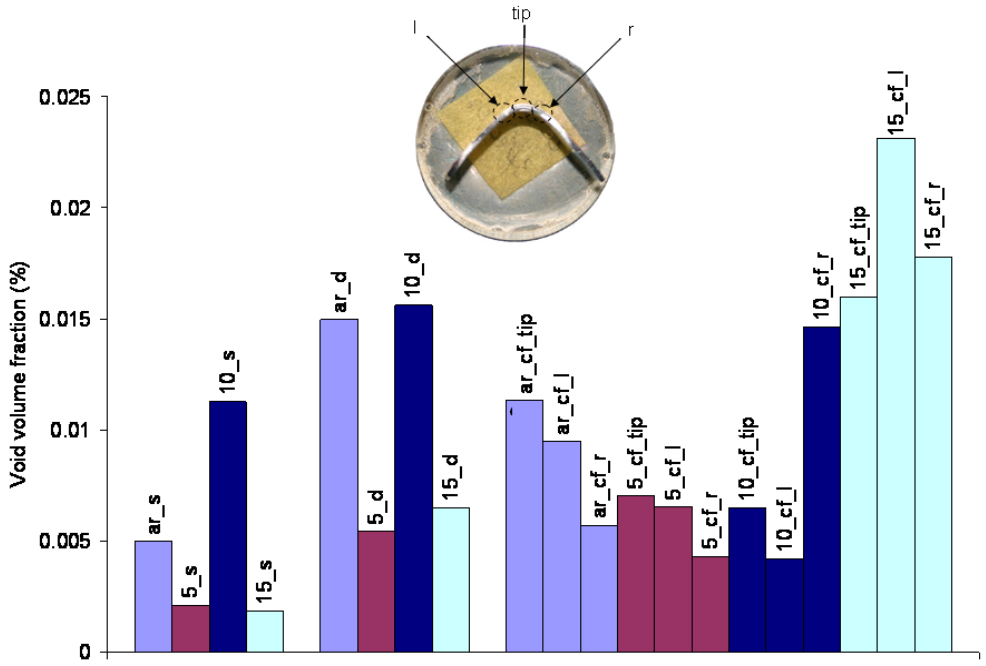

Figure 138: Void volume fractions for the samples measured. Key: ar = as received, 5= 5% pre-strain, 10 = 10% pre-strain, 15 = 15% pre-strain, s = flat sheet, d = drawn to 20 mm outer radius and cf = corner filled. The tip, l and r indicate whether the measurement was made on the tip, or to the left (l) or right (r) of the tip, as shown on the inset.

The measurements for the samples made from the 5 and 15% pre-strained sheet show increasing damage levels from the un-deformed sheet to the corner filled samples, which is the expected result. The measurements for the samples from the as-received and 10% pre-strain showed the highest damage measurements on the pre-formed part, but not on the corner filled parts where the highest damage was observed on the 15% pre-strained samples. However, it cannot be said that there is a consistent trend of increasing damage with pre-strained corner fill, which confounds the assessment of the damage results. This is not surprising given the fact that these measurements were taken on a very small area of one sample. A more detailed damage study was not possible given the time constraints of the project. What is clear is that the highest damage was observed on the corner fill samples made from 15% pre-strained sheet.

5 NUMERICAL RESULTS

In this chapter the results of the numerical simulations performed as part of this research will be presented and discussed. First, the results from the models for the single step EM operations will be shown. Then, the results for the hybrid forming operation will be presented. Results for the conventional forming step will be presented followed by the results of the EM corner fill simulations. The results for the EM corner simulations will include comparisons with measured data and an analysis of the predicted stress and strain histories. A section describing the causes of some of the limitations observed in the models is then included. The results of the models of the hybrid operation with the pre-strained sheet are presented and compared with experimental measurements. Finally, the efficiency of the process is predicted.

5.1 Single Step EM Forming

The models for the single step EM forming operation were used together with the experimental results to validate the code for this type of application. Once the model was validated, the effects of pressure distribution and rebound were studied using the models. First, the coil was modeled alone, with no sheet, as part of an RLC circuit with the properties of the magnetic pulse generator and the charging voltage as input parameters. The predicted and measured currents are shown in Figure 139. The predicted current agrees well with the measured one for the positive portion of the pulse, with a difference in peak current of approximately 4%. In the negative portion of the pulse the results deviate from the measured. This discrepancy was not a significant concern since the decaying pulse ceases to affect the sheet significantly by the time the current is reversed.

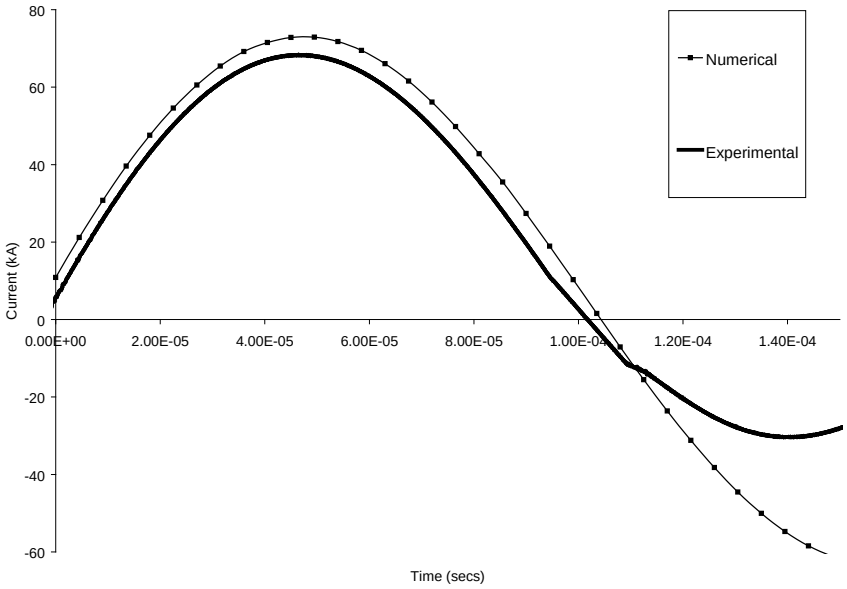

Figure 139: Experimental and numerical currents for a discharge through the coil with no workpiece.

The single step EM process was then modeled and a similar comparison was made between the predicted and measured currents as shown in Figure 140. There is less agreement than was observed for the "no sheet" case. This is likely the result of the coarseness of the sheet mesh, which affected the calculations of the coupled circuit. The discontinuities that are visible on the predicted curves shown in Figure 140 are due to the time interval between the EM calculations performed by the code. The current profiles for the hybrid operation models were not affected by this since an experimentally measured current profile was provided as input for the simulations.

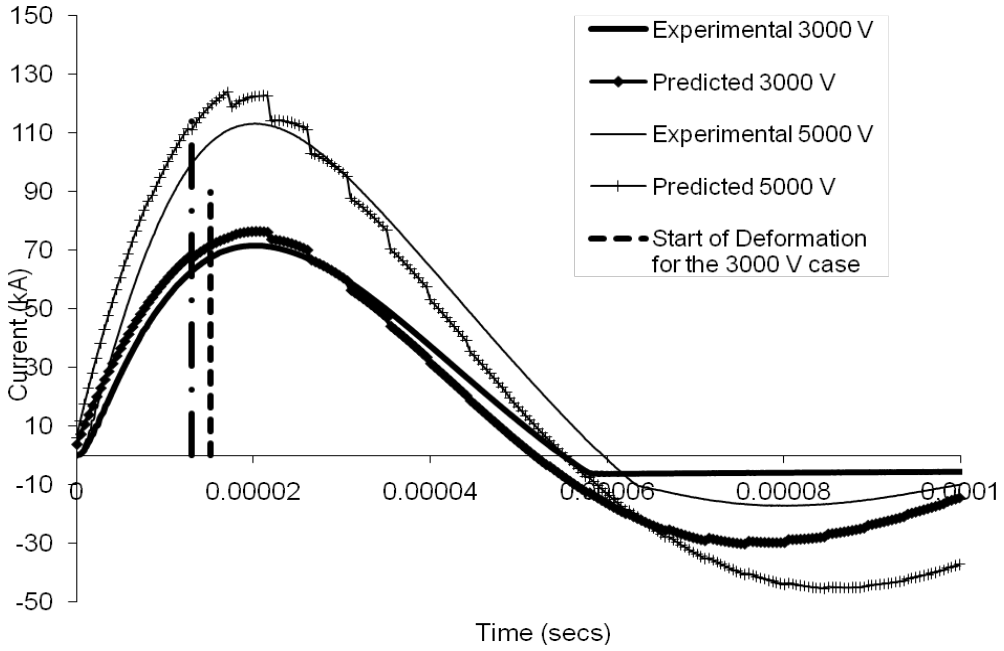

Figure 140: Experimental and numerical current profiles for 3000 and 5000 charging volt cases. The steps in the predicted values are a consequence of the time steps for the EM calculations and the movement of the sheet.

To study the effects of the induced force models were run where the sheet deformed without making contact with the die. Rebound effects were studied by using a model were the sheet contacted the die. Experimentally recorded charging voltages were used for each condition in the simulations. For the models in which the sheet did not contact the die, a charging voltage of 3,000 V was used and a voltage of 5,000 V for the case where the sheet impacts the die. The predicted heights for each case were compared with experimentally measured values as shown in Figure 141. Also, shown in Figure 141 is a comparison of the numerical predictions of forming sheet into a conical cavity die and experimental heights reported in [17] for the same process. The height agreement is much better for the conical case because the part did not exhibit rebound effects of the same magnitude as those observed in the parts studied in this work.

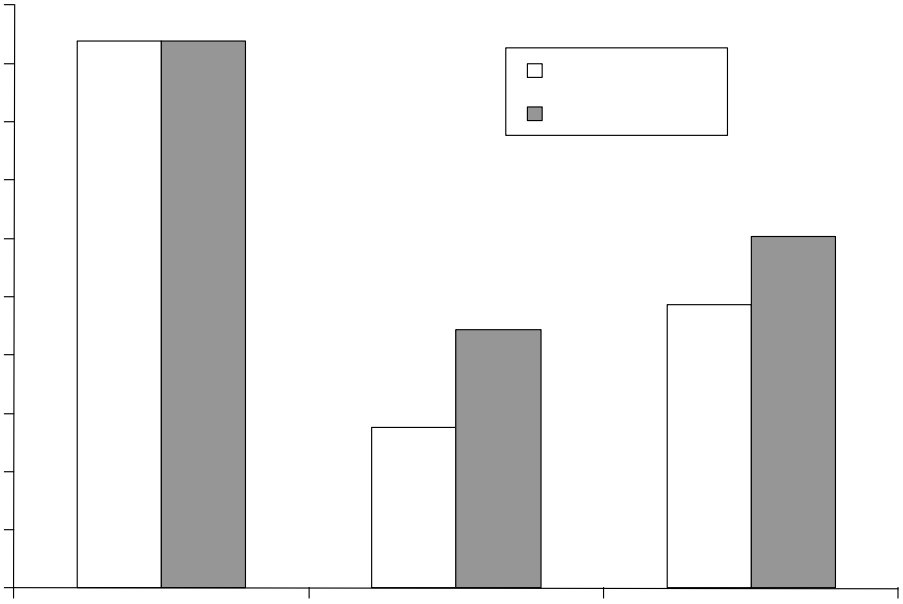

Figure 141: Experimental land numerical sample heights for a) the 40° conical samples from [17], b) single step EM samples with no die contact and c) single step EM samples with die contact.

The final predicted shapes of the samples that did not contact the die are similar to the experimental samples and show good qualitative agreement. The predicted final shape for this experiment is shown in Figure 142, which corresponds to the specimen shown in Figure 87. The predicted final shape is compared to the experimental sample in Figure 143. The maximum predicted height is 21.6 mm which is 38% higher than the actual height of the samples. This over-prediction is likely due to the material model used and to the fact that the numerical coil has an ideal shape that does not take into account the imperfections of the actual coil. Thus the coil is modeled as uniformly separated from the sheet, which results in higher induced forces when compared to the experiments. Another consequence of the ideal shape of the numerical coil is that the predicted shape is symmetric and does not show the significant difference in height from one end of the sample to the other present in the actual samples. The models predict the raised edges which are observed in the actual samples. The predicted strain distributions are non uniform, which is an expected result given the force distribution.

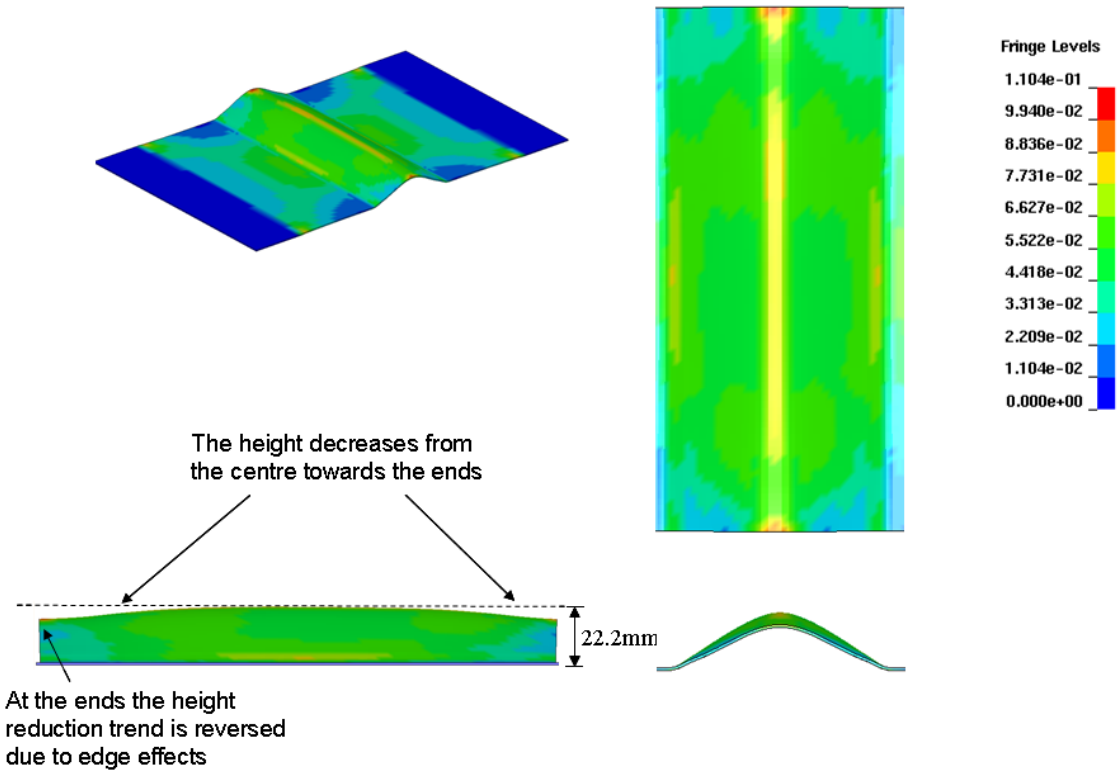

Figure 142: Final predicted v-channel shape for a sample that makes no contact with the die (3000 V charging voltage). The general trends in the height are predicted by the model.

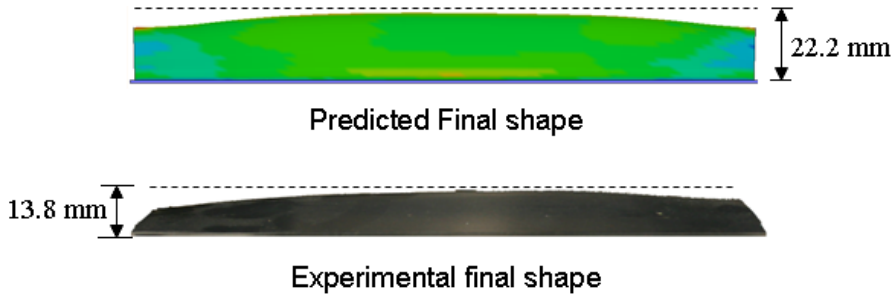

Figure 143: Comparison of the final predicted shape with the experimental sample.

The predicted final shape for the models where the sheet made contact with the die is shown in Figure 144. This model corresponds to the part shown in Figure 85. The rebound is predicted by the numerical analysis, although with less severity than is actually observed on the sides and more severity on the top of the sample. Figure 144 also shows the predicted the shape of the part just prior to impact. The effect of the EM field is negligible during the impact event, since by the time the sheet impacts the die the EM forces are not significant. In

fact, in the numerical simulations the EM solver is not active when the rebound occurs. The severity of the rebound will depend on the velocity of the sheet at impact, and thus the EM forces that were induced on the sheet during the early part of the discharge. Therefore, non-uniform force distributions will result in uneven rebound, which can be seen in the part shown in Figure 85. The model did not predict the exact height distribution seen in the samples, as can be seen in Figure 145. The final shape of the predicted samples showed an apparent reversal in the height distribution, with the highest points occurring towards the ends. This results from the sheet rebounding after impact. Figure 144 shows the sample geometry just before impact, and it can be seen that the height distribution is essentially the same as for the no-impact sample. Prior to impact, the centre of the part is not only the highest point, but also the fastest moving; therefore, when it impacts the die the rebound is greater than at the ends of the part; this effect was exaggerated in the numerical model.

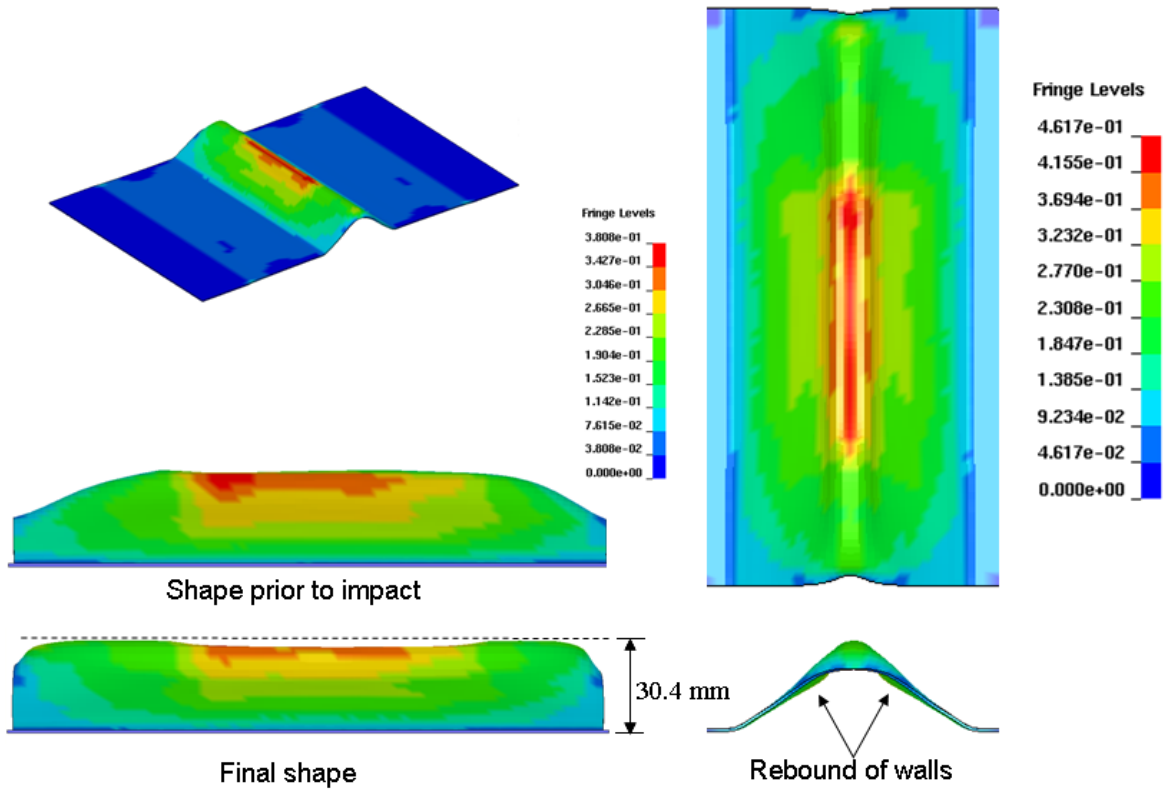

Figure 144: Final predicted v-channel shape for sample with rebound present (5000 V charging voltage). The edge effect is present but is not as pronounced as in the lower voltage case.

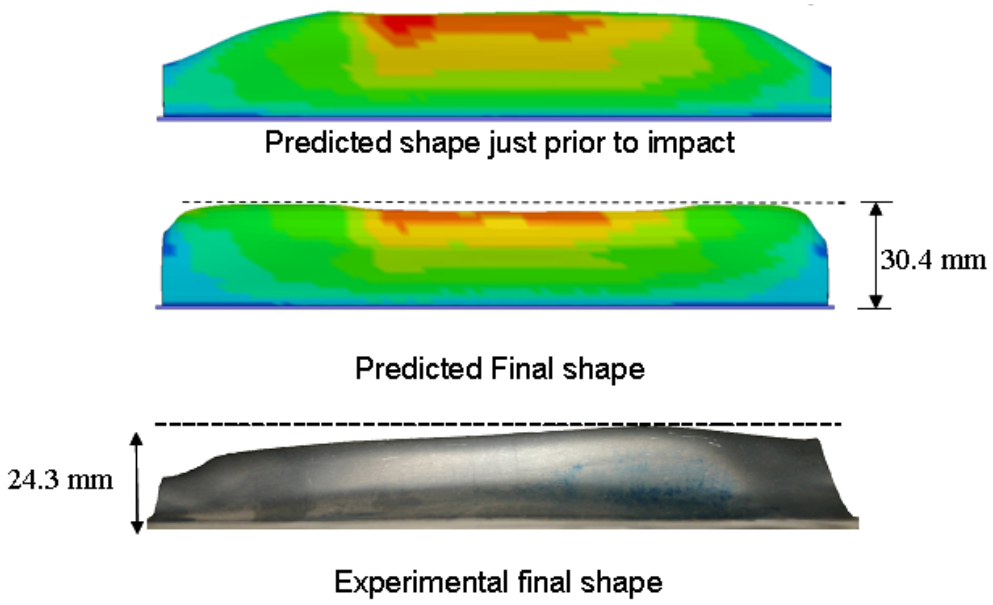

Figure 145: Comparison between the experimental shape of the sample and the predicted final shape. The experimental shape resembles more the predicted shape just prior to impact. The difference between the predicted final shape and the actual one are due to the excessive rebound predicted.

The numerical modeling of the single step process showed that the models could predict the general behaviour of an EM forming process with relatively good accuracy. Significant insight was gained from the models as to the behaviour of the sheet metal in these operations. Three likely sources of error were identified for these models: 1) the material model, 2) the coarseness of the mesh and 3) the differences between the actual coil and the ideal numerical representation of it. Other possible sources of error include the values of the inductance and resistance of the system and the conductivity of the materials.

Given the good qualitative predictions by the single step simulations, it was determined that the software was capable of providing additional insight for the analysis of the hybrid operation. Some of the sources of error identified for the single step models were addressed for the hybrid models. The discrepancy between the actual and ideal coil was reduced, since the coil used for the experiments was closer to the ideal coil used for the models than the double pancake coil used for the single step process. A current profile was provided for the model instead of having the software calculate the current. A somewhat more refined mesh was used that had five elements through-thickness. The same material model was used for the hybrid operations, since no better validated model was available. Conductivity values for copper and aluminum alloys were used for the hybrid operation model. The hybrid models were realized

in two steps, with the conventional pre-form and EM corner fill operations being done in separate simulation stages.

5.2 Conventional Pre-forming Results

To simulate the hybrid process, the pre-form operation was modeled first and the resulting geometry, stresses and strains were then used as the starting condition for the EM corner fill model. Figure 146 shows the pre-formed sheet as it was used in the EM corner fill model. The predicted engineering strain distributions are shown in Figure 147 to Figure 154 together with the measured strains. Good agreement is seen between the predicted and measured strains. Since the pre-straining of the sheet was not modeled, the average strains measured from the pre-strained sheets were added to the numerical results to facilitate comparison. As was previously explained, the models of the pre-form operation were solved with the EM version of LS-Dyna, but with the EM features deactivated for the pre-form step.

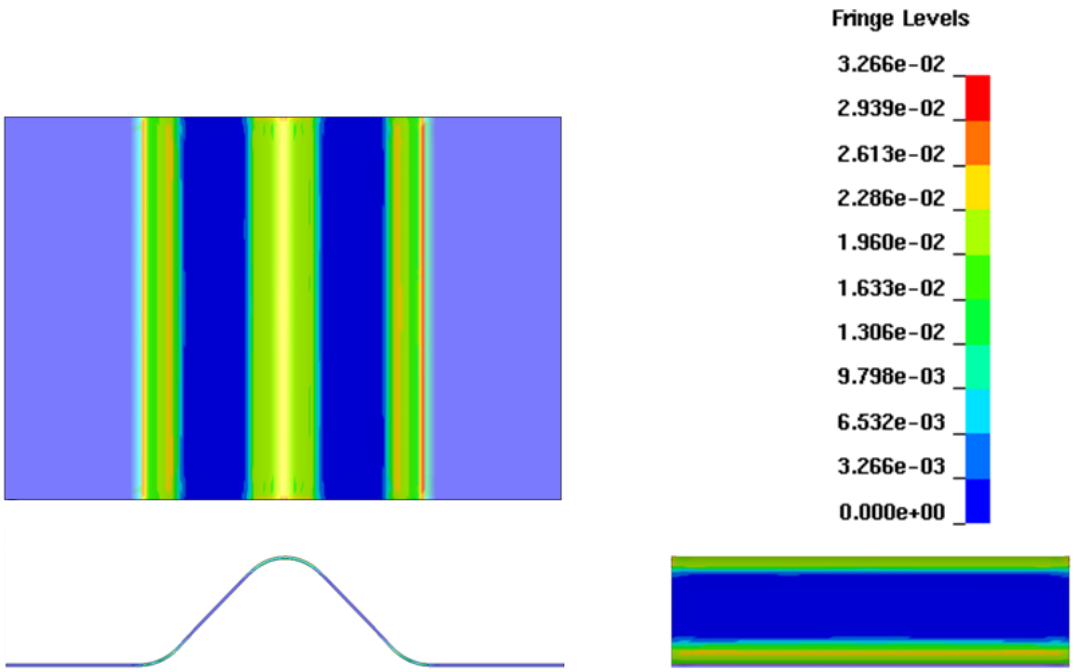

Figure 146: Predicted pre-formed shape. Contours are of effective plastic strain.

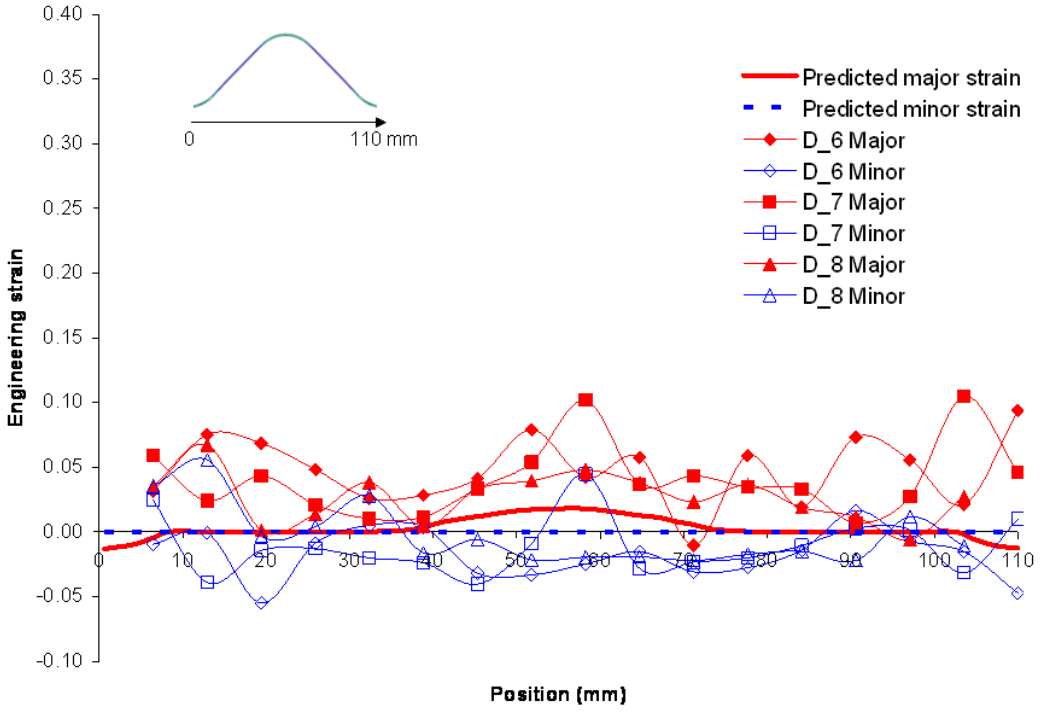

Figure 147: Predicted and measured engineering strains for the longitudinal direction for the pre-form model with the sheet in the as-received condition.

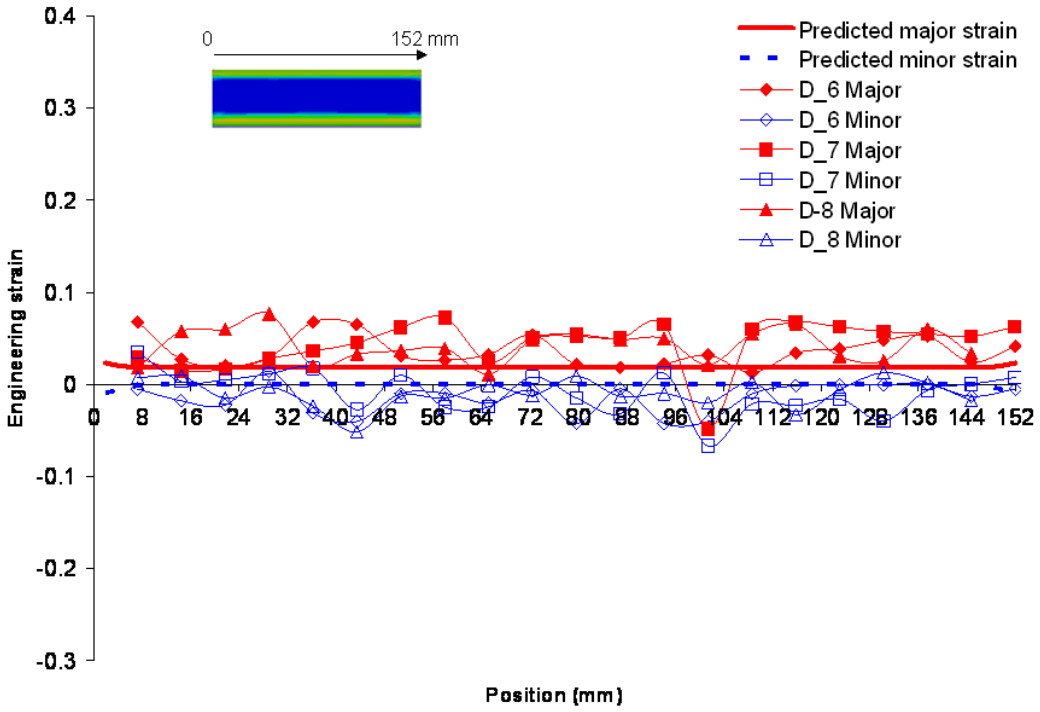

Figure 148: Predicted and measured engineering strains for the transverse direction for the pre-form model with the sheet in the as-received condition.

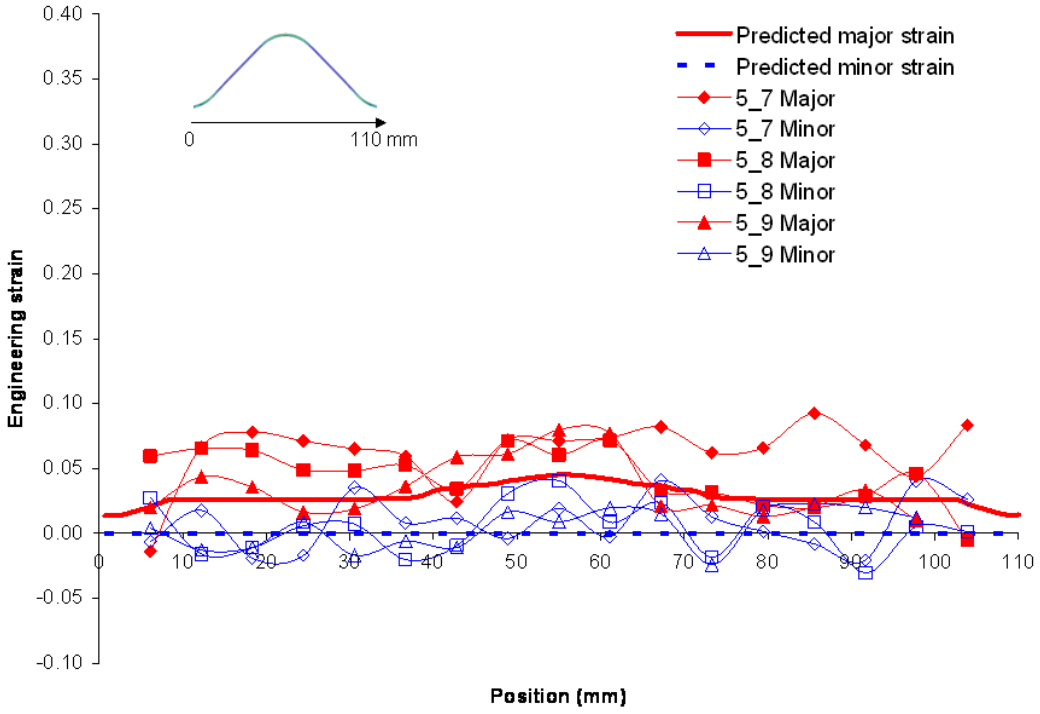

Figure 149: Predicted and measured engineering strains for the longitudinal direction for the pre-form model with the sheet pre-strained by 5%.

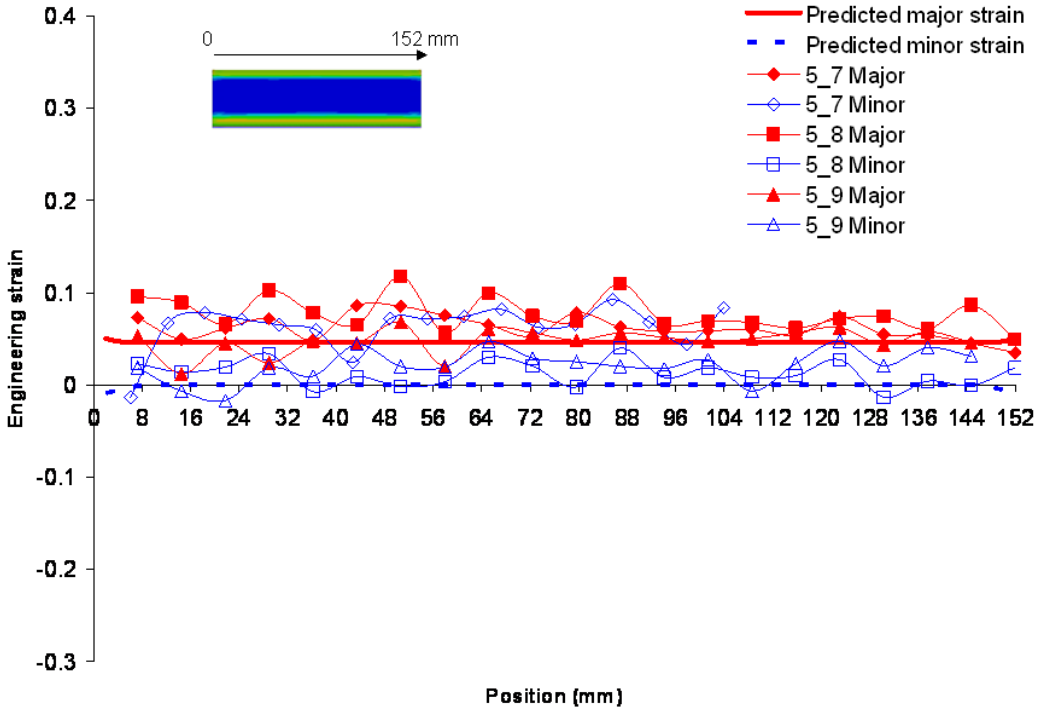

Figure 150: Predicted and measured engineering strains for the transverse direction for the pre-form model with the sheet pre-strained by 5%.

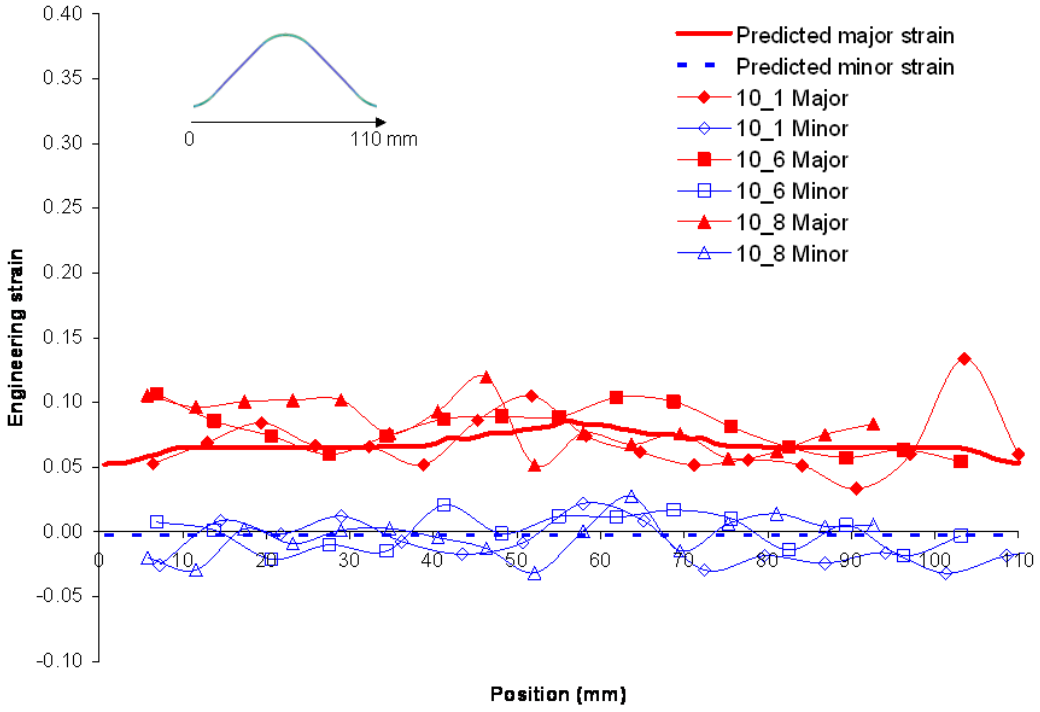

Figure 151: Predicted and measured engineering strains for the longitudinal direction for the pre-form model with the sheet pre-strained by10%.

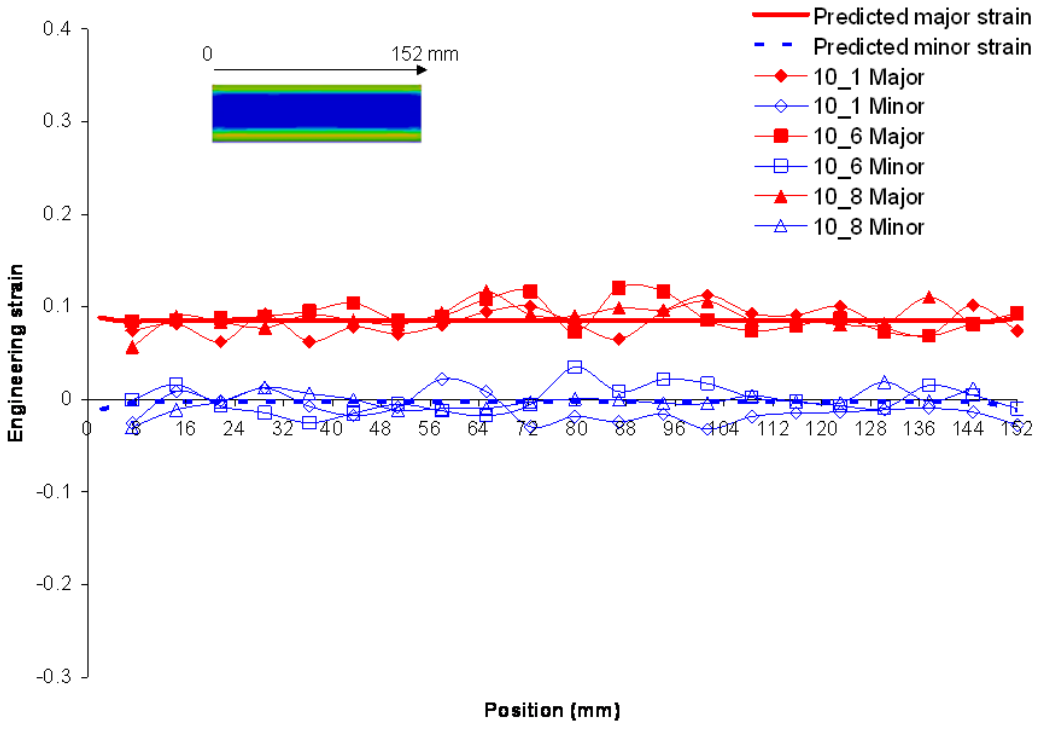

Figure 152: Predicted and measured engineering strains for the transverse direction for the pre-form model with the sheet pre-strained by10%.

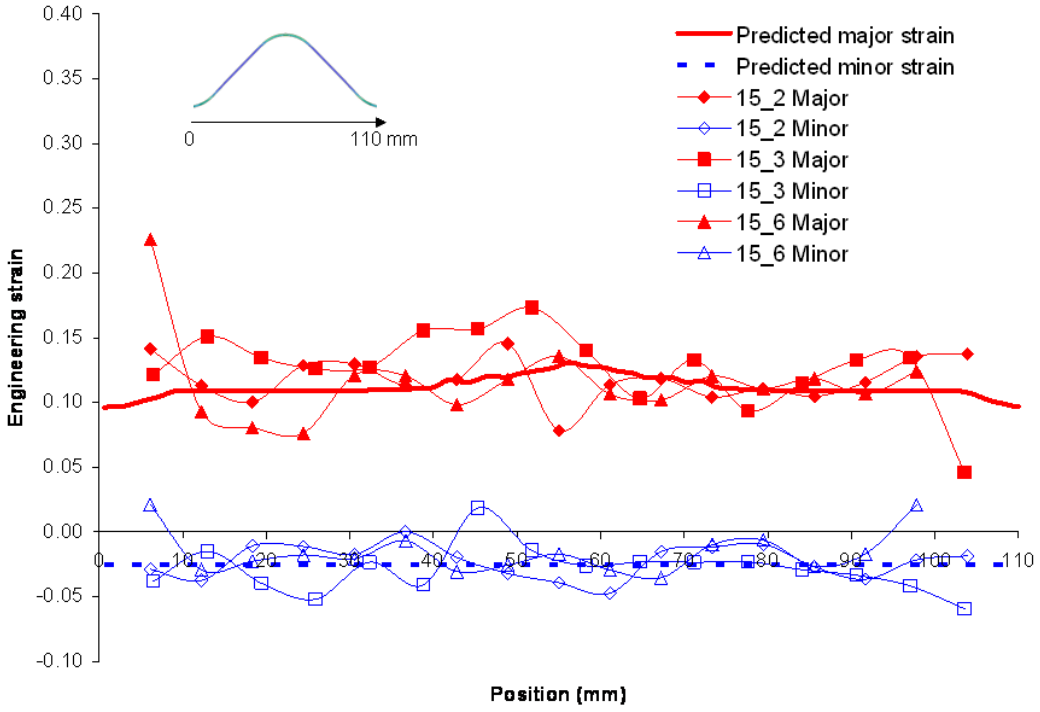

Figure 153: Predicted and measured engineering strains for the longitudinal direction for the pre-form model with the sheet pre-strained by15%.

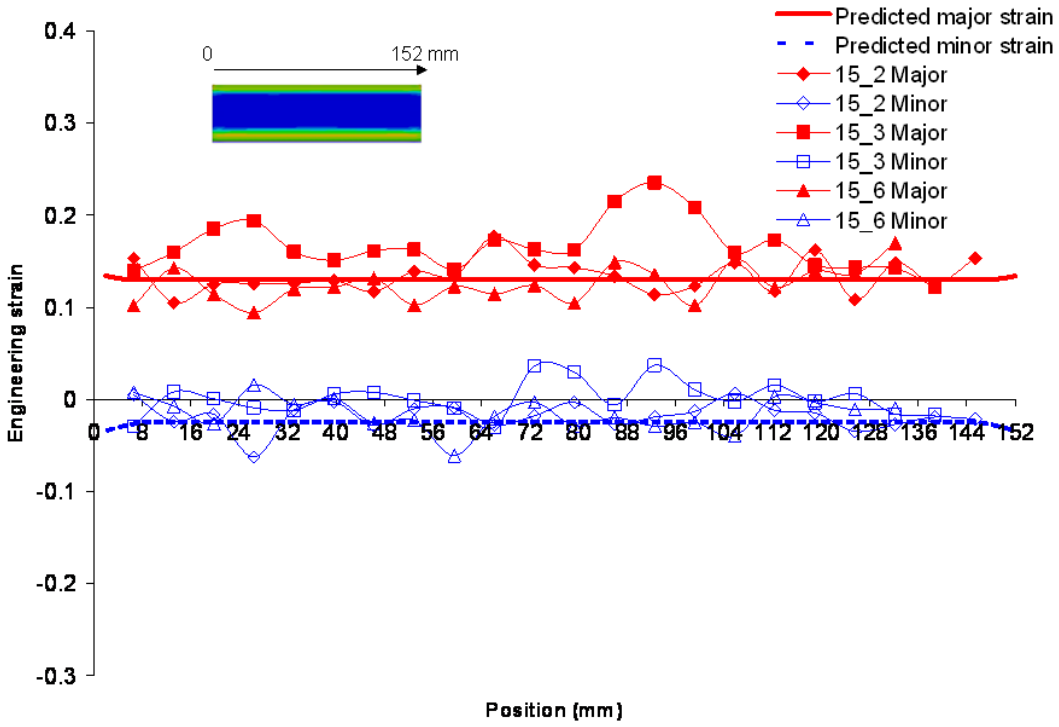

Figure 154: Predicted and measured engineering strains for the transverse direction for the pre-form model with the sheet pre-strained by15%.

5.3 EM Corner Fill Results

The predicted final shape of the zero pre-strain hybrid corner fill sample is shown in Figure 155. The general shape of the part is similar to the actual sample shown in Figure 97. The main difference between the prediction and the actual part can be seen in Figure 156. The predicted final shape has a depression on the top that results in height h_2 being lower than the measured heights and relatively lower than h_1 and h_3 (h_2, h_1 and h_3 from Figure 97-b). The height at the centre of the experimental samples (h2) was approximately 52.0 mm (Table 4), while the predicted height is 47.4 mm. The possible causes of the difference between the predicted and experimental shapes will be described in detail in Section 5.4.

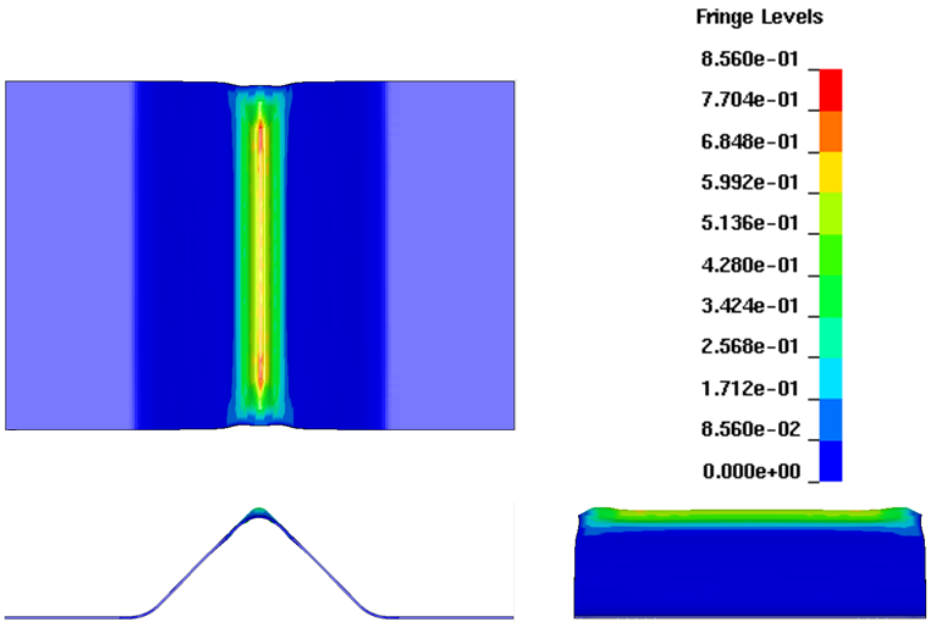

Figure 155: Predicted final shape using the experimental quasi-static flow curve. Strains are of effective plastic strain.

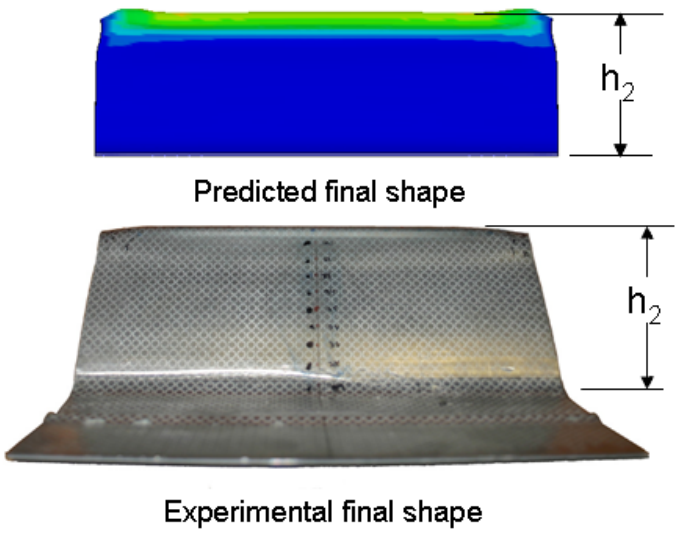

Figure 156: Comparison between experimental and predicted final shapes.

The final shape of the sample is not only the result of the die shape, but also the force distribution and rebound of the material after it impacts the die. Figure 157 shows the predicted cross-section of the part at the centre at various stages of deformation. It can be seen that even prior to any impact (Figure 157-b) the deformation is not uniform. The force distribution is also responsible for the shape at the ends of the sample. Figure 158 shows the predicted forces for a segment at the centre of the part and one at the end. It can be seen that neither distribution is uniform and that the force distribution for the edge has some regions in which the force acts opposite to the direction of motion, which results in the reduction in part height at the ends of the samples observed in the experiments. These forces are caused by the magnetic field interacting with the upper surface of the sheet, thus producing forces that oppose the deformation. By the time the material contacts the top of the die, the sides of the sample have already impacted and begun to rebound off the die surface (Figure 157–c) producing a shape that differs from that of the die. The final shape of the part (Figure 157–d) results after the sheet bounces back from the die. The actual cross section of a formed sample is shown in Figure 159 and shows some of the rebound effects predicted in the model, but to a much lower extent. This reasons for this will be discussed in Section 5.4.

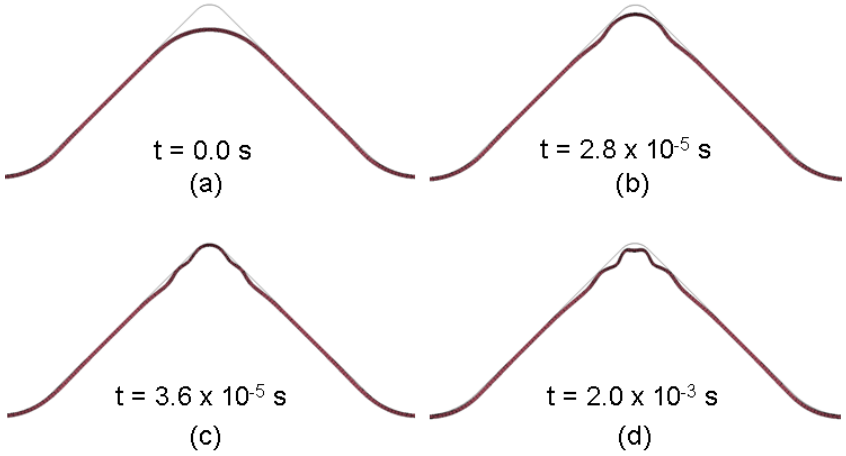

Figure 157: Cross-section at the centre of the part a) before forming, b) just prior to impact at the top of the die, c) when the material impacts the top of the die and d) final shape. The shape at b) is entirely due to the force distribution. At c) the part has been shaped by both the force distribution and impact with the die. The final shape at d) is the result of the rebound.

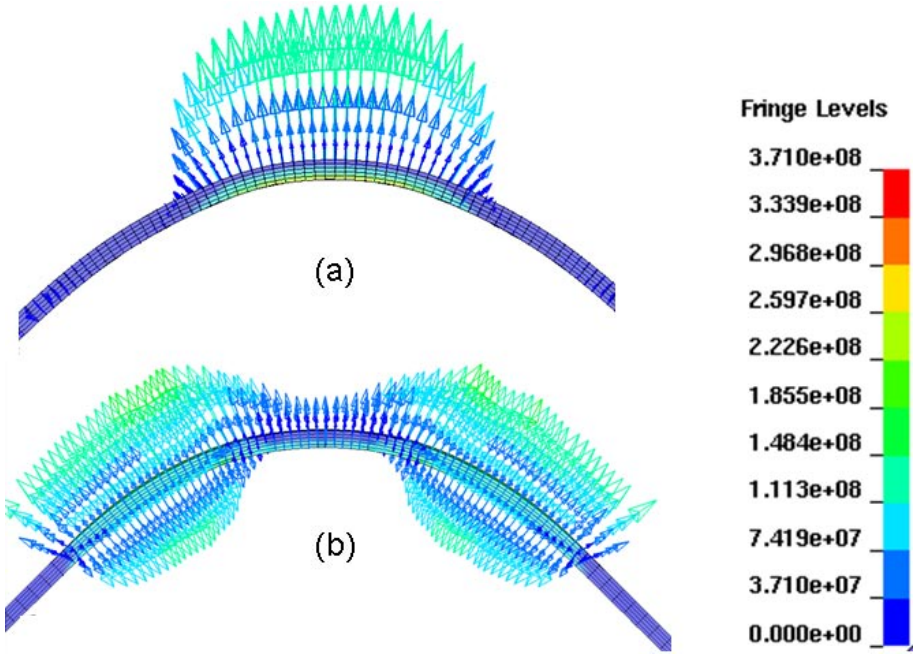

Figure 158: Lorentz force distribution at a) the centre of the sample and b) at one of the edges. Bothe are images are from the same time in the simulation. The contours and vectors are of Lorentz force in μN.

The predicted strains show the effects of this rebound. Figure 160 and Figure 161 show the predicted strains on the surface of the samples, together with the measured strains. The positive and negative peaks of the predicted major strains in Figure 160 are due to the bending that is produced by the rebound and, to a lesser extent, the force distribution (Figure 157). The peaks are labeled and the locations where they occur are indicated on the inset included in Figure 160. The negative strains on A and B correspond to areas of the sample that

are in compression due to bending. In contrast, points C and D are in tension. Point E is on the compressive side of a shallow bend, but the bending was not severe enough to result in negative strains. The model is over predicting the rebound which results in the peaks discussed. The actual samples also present areas of bending caused by the rebound (Figure 159), but the circles grids used to measure the strain were not small enough to resolve the strain variations caused by these areas of bending.

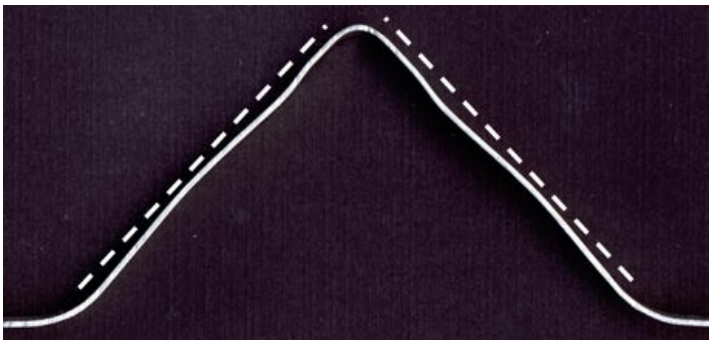

Figure 159: Segment from a sample formed with the as-received sheet cut from the centre of the sample. The dashed lines are added to highlight the shape of the cross section.

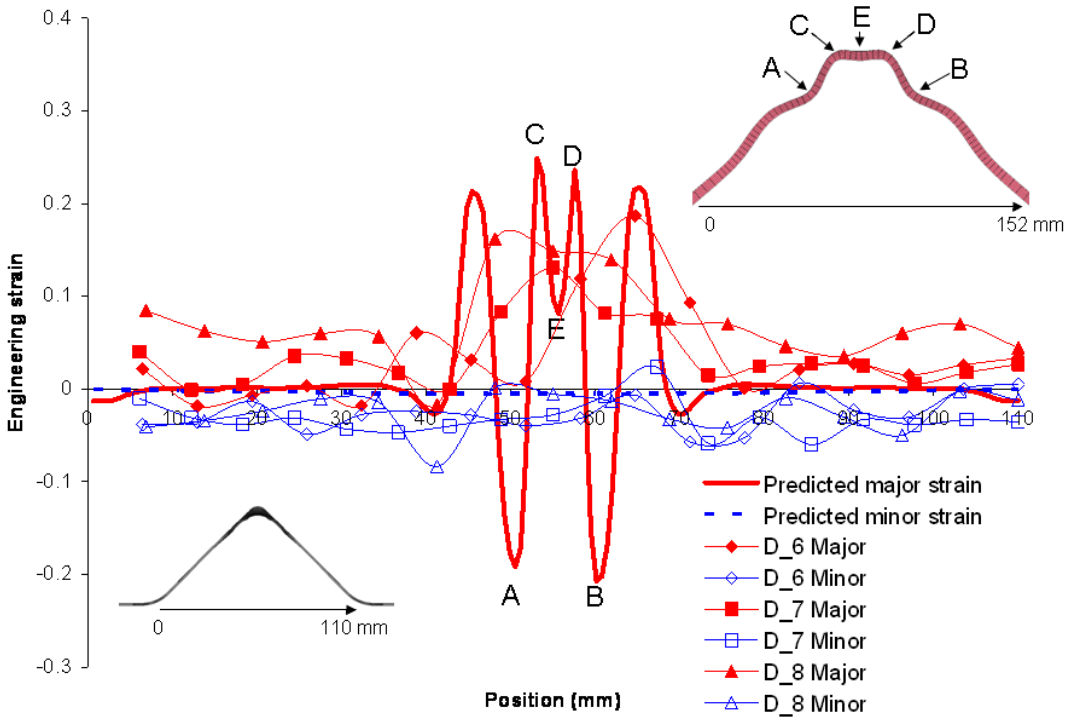

Figure 160: Predicted and measured engineering strains for the longitudinal direction.

To attempt to obtain a better comparison with the measurements, the average of the predicted strains in transverse direction the average of three elements, one each from areas C, E and D as shown in Figure 160 was calculated and the results are shown in Figure 161. Using this approach, the averaged strains cover an area comparable to the grids used to measure the strains. The "averaged" strains in the transverse direction agree relatively well with the measured ones. The low strains predicted on either end of the sample are due to the reduced height presented by the samples.

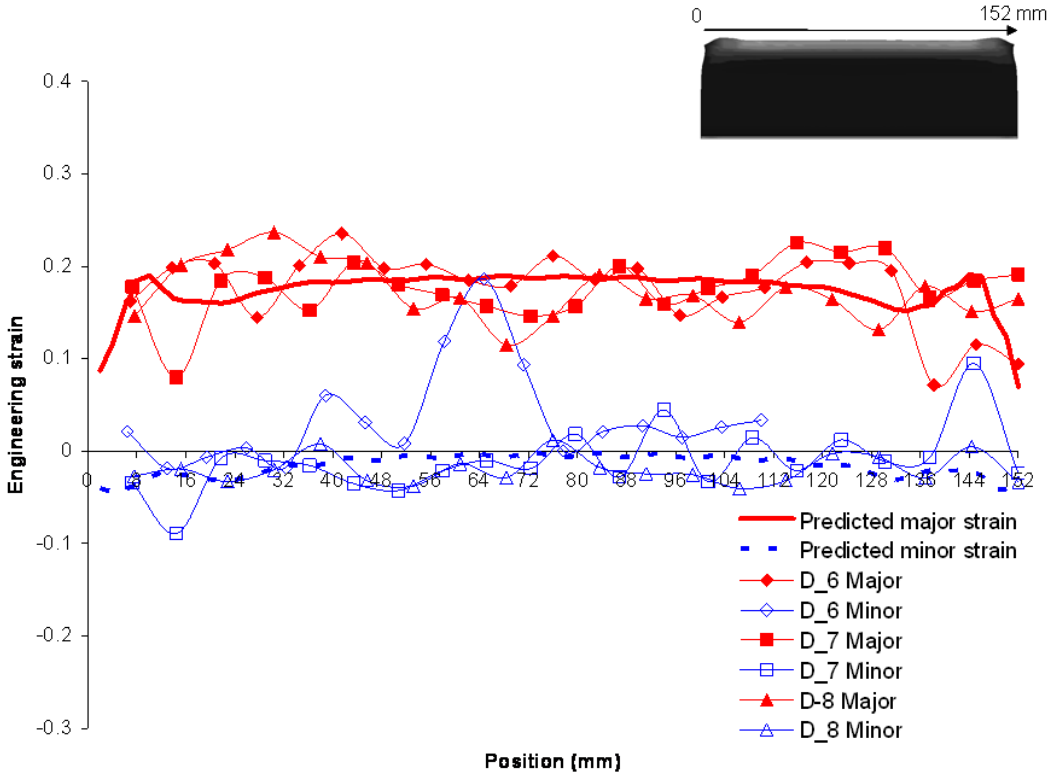

Figure 161: Predicted and measured engineering strains for the transverse direction.

5.3.1 Stress and Strain Histories from the Corner Fill Operation

The histories of the stresses and strains are a very important consideration since they can lead to an understanding of possible damage generation and suppression mechanisms, they can show whether or not the strain paths are linear and they can illustrate whether the process can be considered to be plane stress. The latter is particularly important in numerical simulations since it can lead to decisions on whether a particular process can be modeled with

shell elements, which are plane stress elements, or if the process has to be modeled with brick elements or "thick-shell" elements.

To examine the stress and strain histories of the EM corner fill operation, the histories of elements in three representative zones of the formed area were extracted from the models. Figure 162 shows the zones selected for study and their position as each impact the die. The outside (in contact with the die) and inside elements of each zone were chosen. The models used for this study were those with the flow stress and current input described in Section 3.2.2. The stress and strain histories presented will be for the first 100 μs of the process, which includes the impact with the tool. Figure 163 and Figure 164 shown the directions and labels used for the stresses and strains in the normal and shear directions.

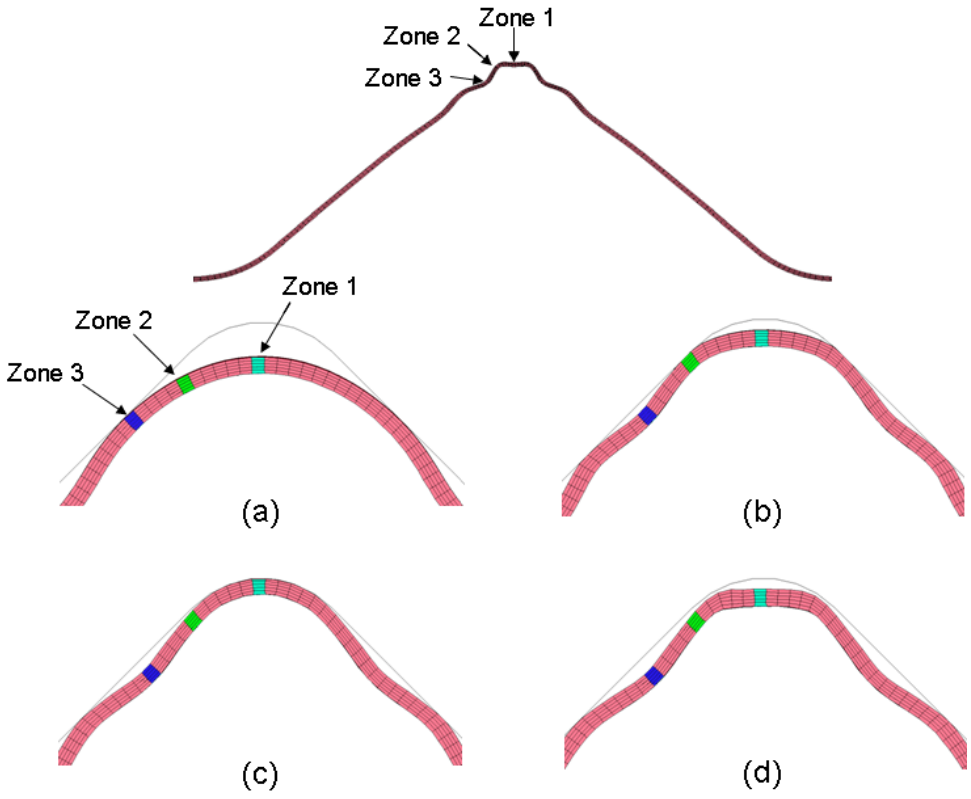

Figure 162: The three zones that were chosen for stress/strain history analysis. The impact of zone 3 is presented in a), of zone 2 in b) and of zone 1 in c). Image d) shows the sample after it has rebounded.

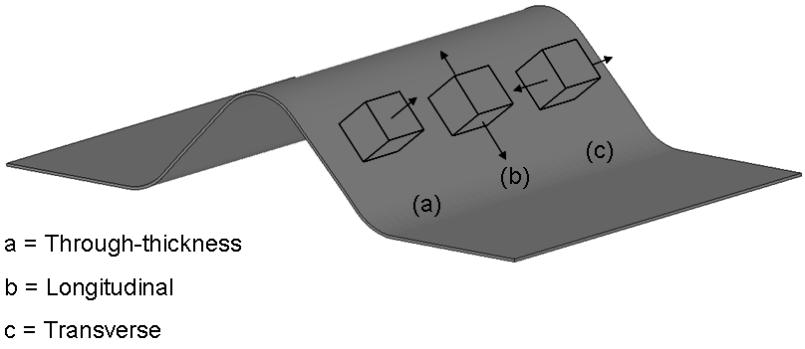

Figure 163: Normal stress directions and designations for the stresses presented in the stress histories.

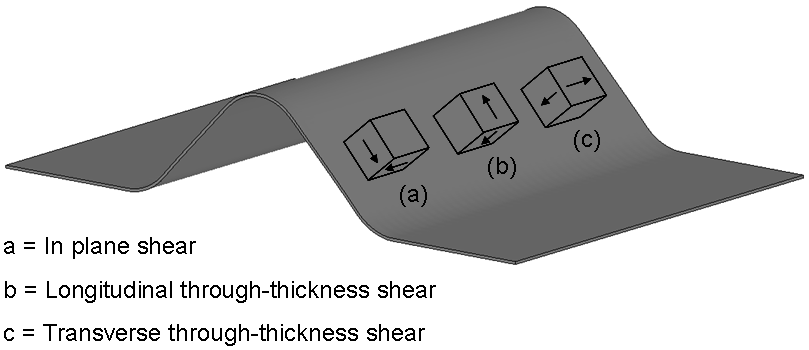

Figure 164: Shear stress directions and designations for the stresses presented in the stress histories.

5.3.1.1 Stress Histories

The normal stress histories are shown in Figure 165 to Figure 167, with the time of impact for each zone marked with a straight line. The non-zero values observed at time zero are due to the stresses that were transferred from the pre-form model and are consistent with material that has been bent. The largest normal stresses were predicted for elements on the outside of zone 1 at the time of impact (Figure 165). The highest stress was the through-thickness stress which reached a value of 1,630 MPa in compression, a value that is approximately 17 times the value of the material yield stress (97 MPa). The peak transverse and longitudinal stresses for the same element were 1,490 and 1,290 MPa in compression, respectively. These high stresses were not long lived. The highest stresses on the inner elements were less than half of those on the outer elements.

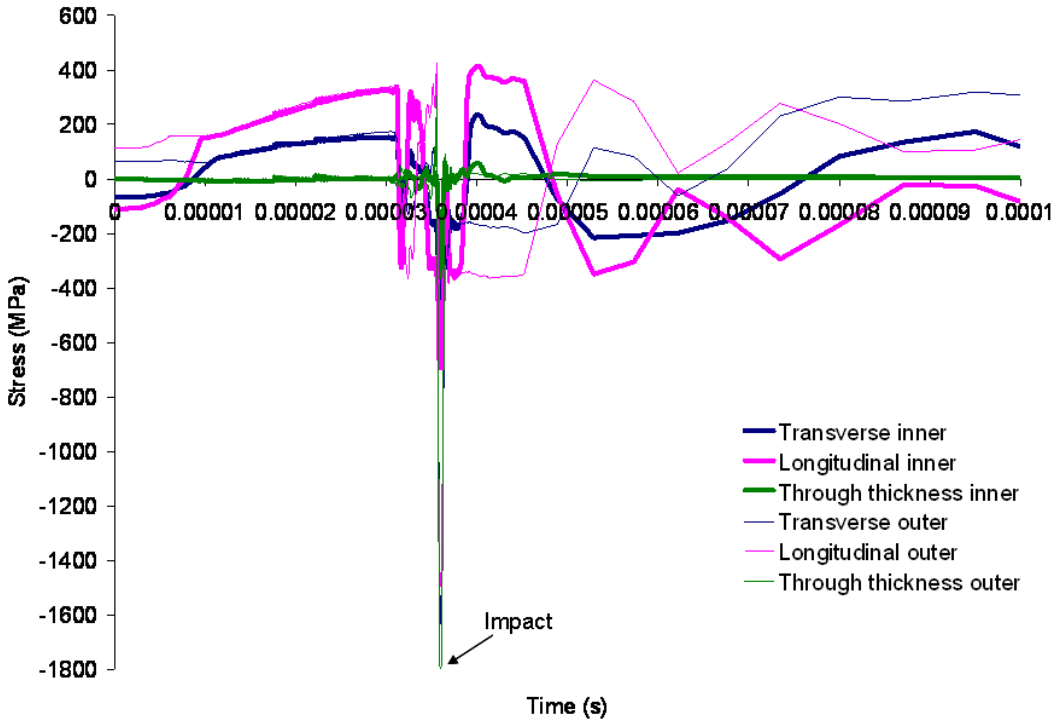

Figure 165: Normal stress histories for zone 1 elements.

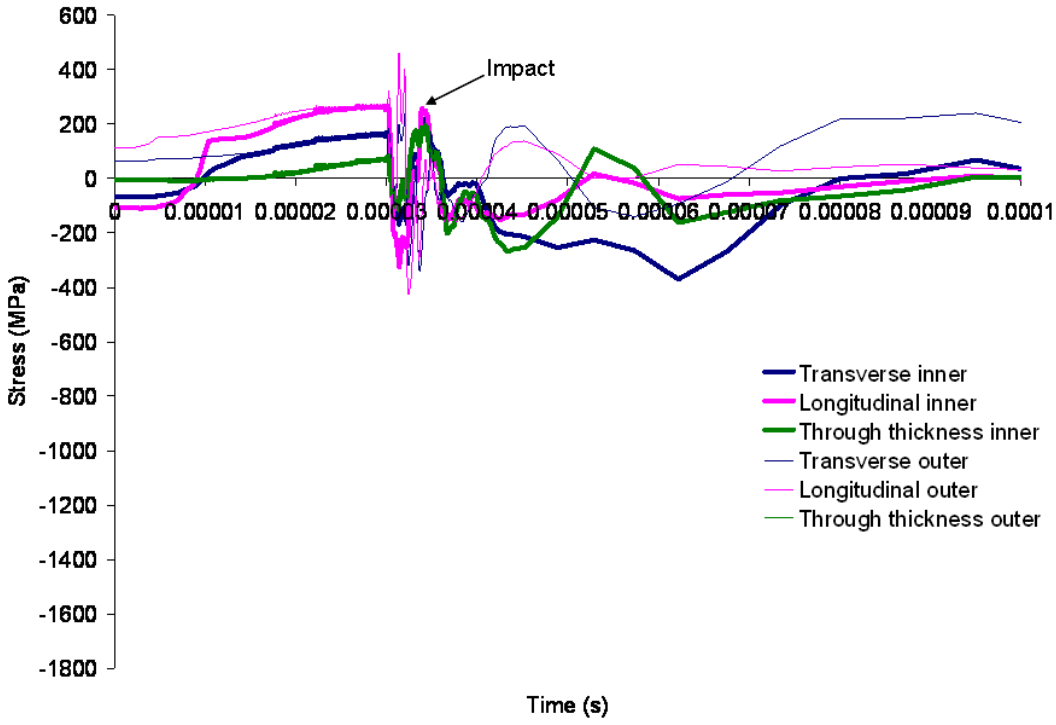

Figure 166: Normal stress histories for zone 2 elements.

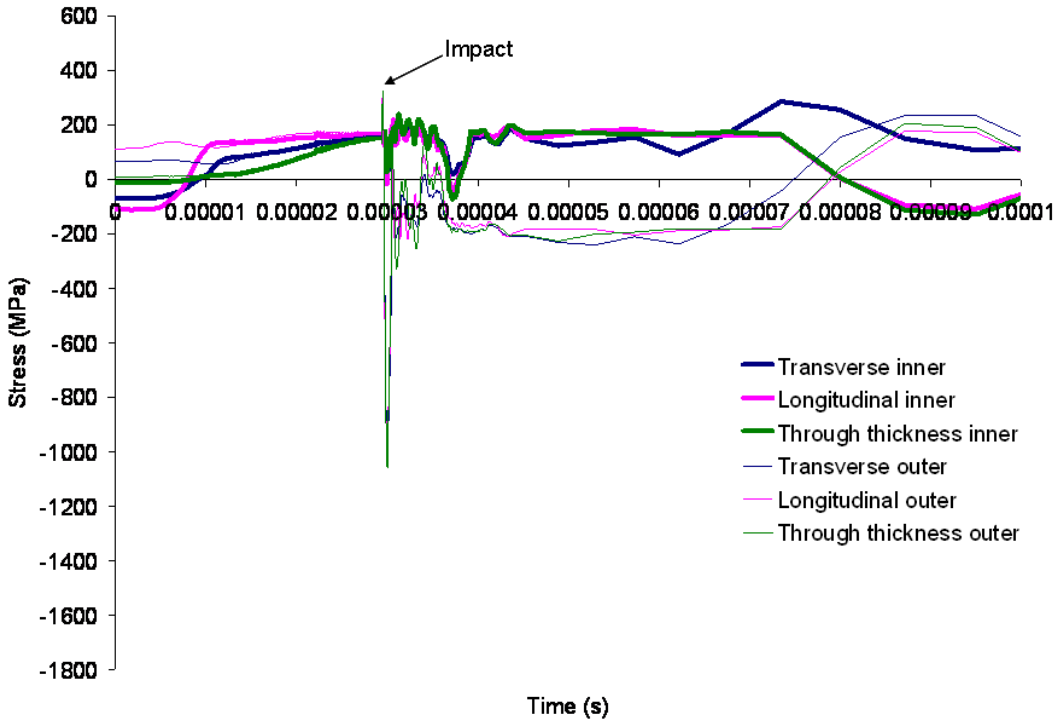

Figure 167: Normal stress histories for zone 3 elements.

The normal stresses for the elements in zones 2 and 3 did not achieve the magnitudes observed for zone 1, as can be seen in Figure 166 and Figure 167. The stresses were significantly affected by the impact and the highest stresses recorded were at least twice the value of the yield stress. The lower values of the stress are likely due to the reduced kinetic energy imparted to the material before impact in zones 2 and 3, when compared to zone 1. The predicted through-thickness stresses were higher for zone 3 than for zone 2; this is the result of zone 3 making impact with the die first (Figure 162) and then zone 2 contacting the die in more of a rolling fashion. Up until the point of impact all zones exhibit a stress state that is consistent with biaxial expansion and the plane stress assumption. However, the through-thickness stresses for zones 2 and 3 started to increase before impact, but they were always smaller than the in-plane stresses. At the moment of impact the predicted stress state is highly three dimensional.

The shear stress histories present an opposite trend to the normal stress, with zone 1 showing the lowest shear stresses and zones 2 and 3 the highest. This behaviour reflects the angle of impact that zones 2 and 3 since they experience a more oblique impact. The histories are shown in Figure 168, Figure 169 and Figure 170. For zone 1 no shear stresses above the

yield stress were predicted, which is consistent with material that has undergone stretching and then compression at impact. For zones 2 and 3, the shear stresses reached magnitudes above 170 MPa, higher than the yield stress of the material. The impact is the event that affects the shear stresses most significantly, with the shear stress being significantly affected just before, during and just after impact. The most significant change was predicted for the longitudinal shear stresses for zones 2 and 3. For zone 2, impact resulted in the longitudinal shear stress changing by 344 MPa, with the stress going from -173 to 171 MPa immediately after impact. For zone 3 the change was 319 MPa, with the impact resulting in the stress going from -162 MPa to 157 MPa. The magnitudes of these changes in shear stress are significant given that the yield stress of the material is 97 MPa.

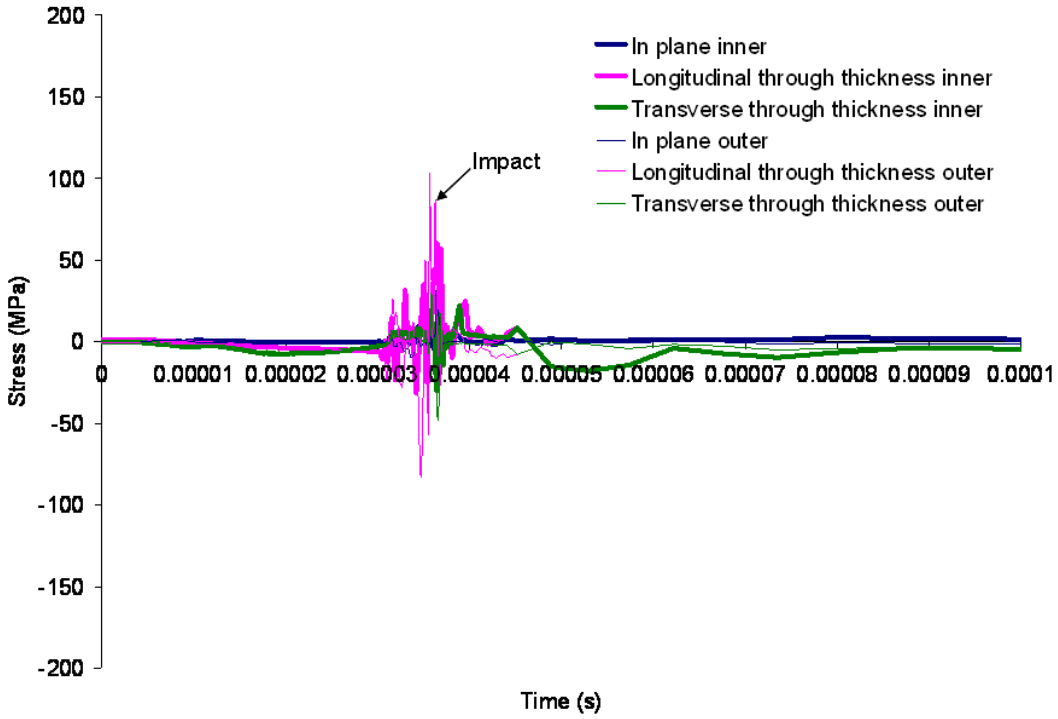

Figure 168: Shear stress histories for zone 1 elements.

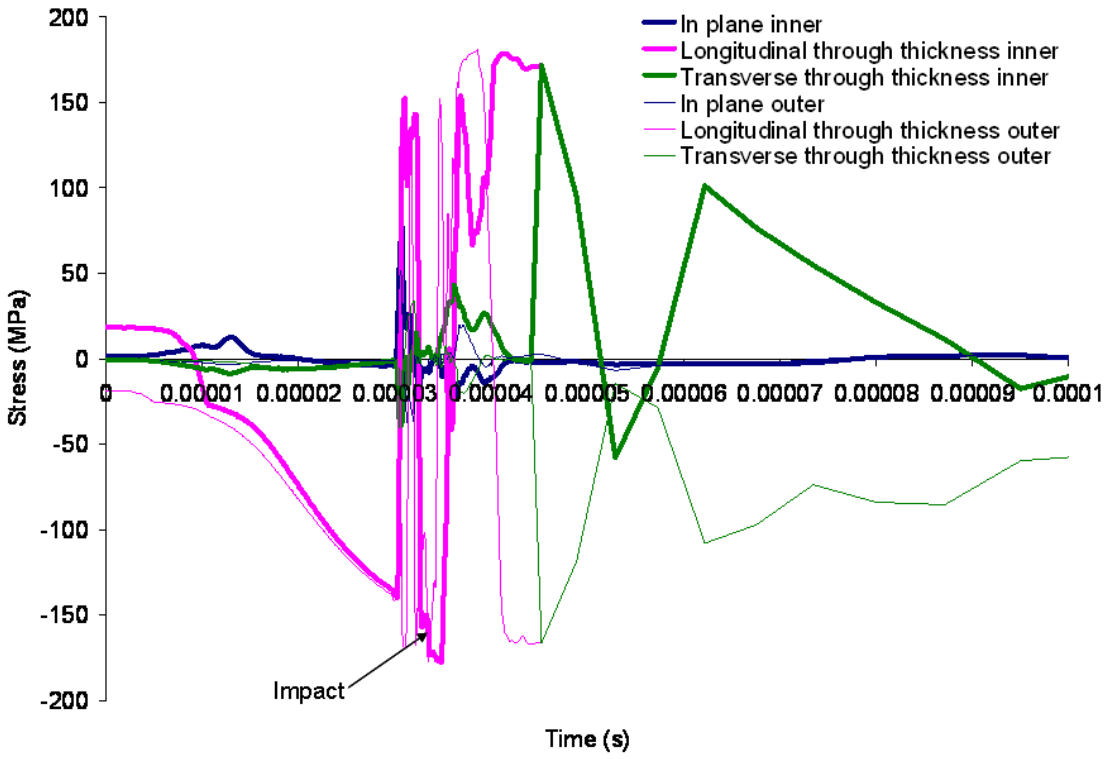

Figure 169: Shear stress histories for zone 2 elements.

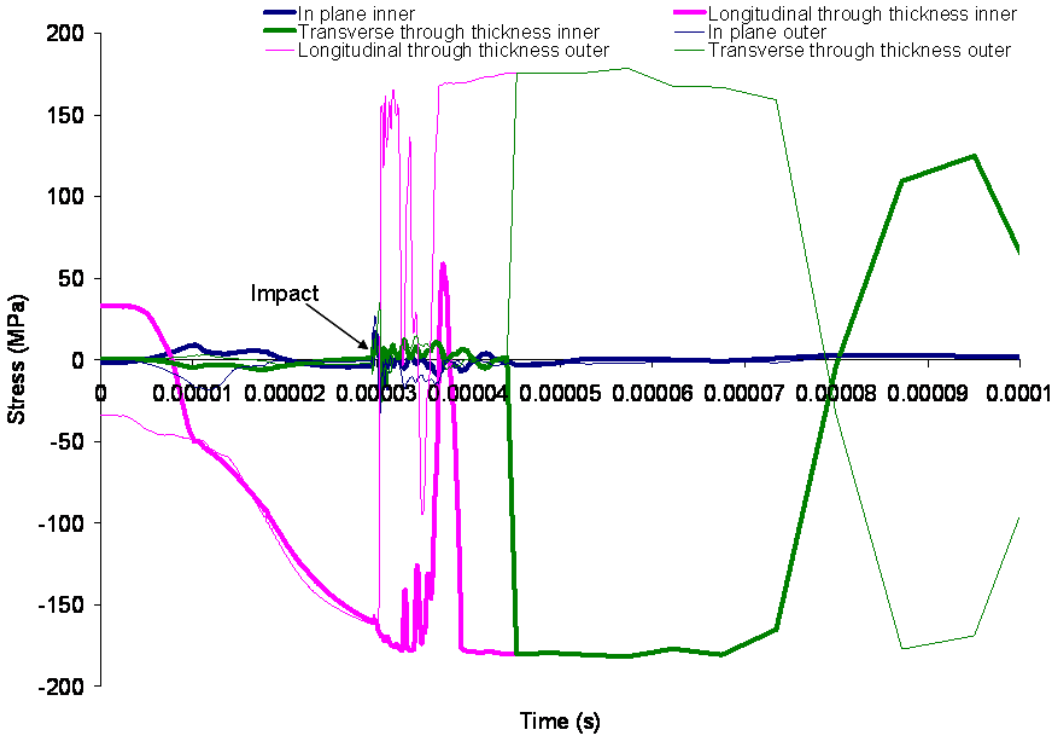

Figure 170: Shear stress histories for zone 3 elements.

In all zones the highest shear stresses are the longitudinal through-thickness stresses, with the stresses for the outer and inner elements showing opposite signs after impact. The presence of these high shear strains indicates that additional deformation is being achieved through shear strain, which can be observed in zone 2 of Figure 162-c and is confirmed by the prediction of large shear strains in the longitudinal through-thickness direction, which are described in Section 5.3.1.2. A similar finding was reported in [17].

The formability of ductile materials is affected by the formation of micro-voids in the material, which can grow under positive hydrostatic stresses until they merge with other voids and eventually form a fracture. This growth and coalescence of voids is significantly affected by the hydrostatic stresses, as was discusses in Section 1.5.1. Positive hydrostatic stresses promote growth and coalescence of voids, while negative ones can suppress growth and coalescence. The predicted hydrostatic stresses for the three zones of interest are shown in Figure 171. The highest stresses are compressive and are predicted for the zone 1 outer element which is consistent with very high normal stresses predicted for this element. These high compressive hydrostatic stresses could help reduce the amount of damage present at the top of the part, which is the area where the material would typically fail during conventional forming.

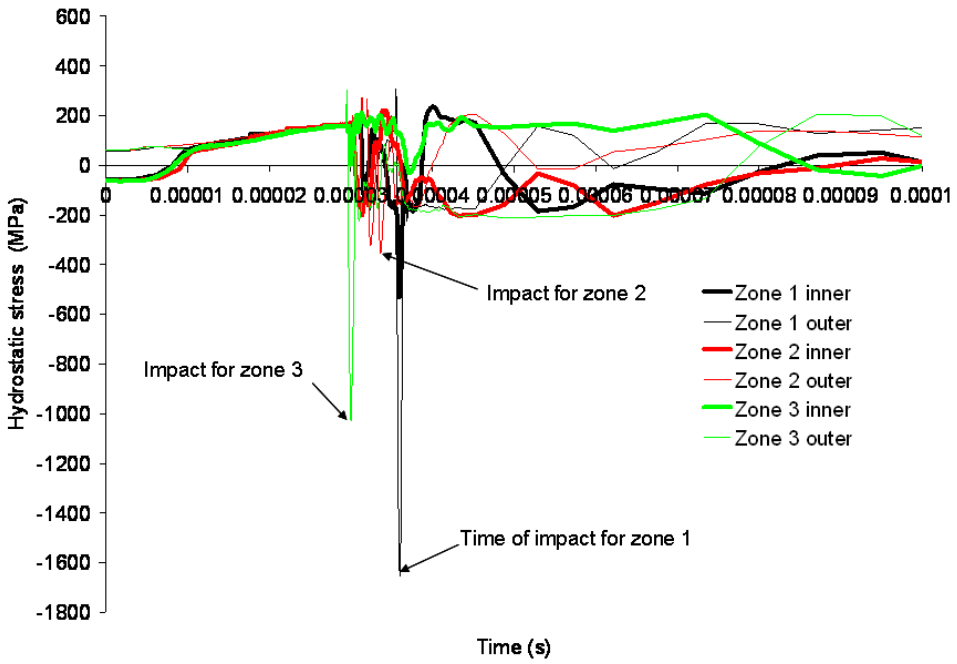

Figure 171: Triaxiality histories for the elements of all three zones.

5.3.1.2 Strain Histories

The normal strain histories for the three zones are shown in Figure 172 to Figure 174. As for the normal stress histories, non-zero strain values are present at the beginning of the simulation, which are the strains carried over from the pre-form model and are consistent with a material that has been pre-bent. The highest strains are predicted for the zone 1 elements at the time of impact. After impact the magnitude of the strains is reduced, which is due to the rebound of the sheet. The strain histories for zone 2 (Figure 173) also show the significant effect of the impact on the strain, with the longitudinal and through-thickness strains changing signs abruptly. This is the result of the bi-axial expansion of the sheet being suddenly interrupted by the impact. The lowest strains were predicted for zone 3, which is consistent with these elements being closest to the die and thus not having to deform as much prior to or after impact.

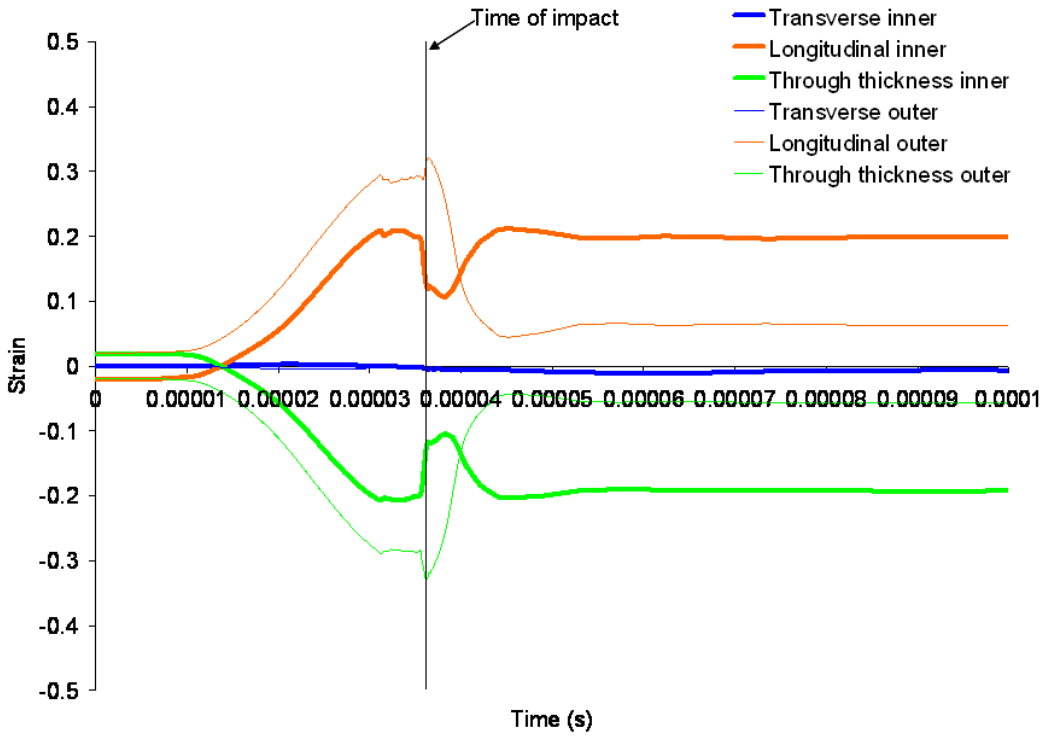

Figure 172: Normal strain histories for zone 1 elements.

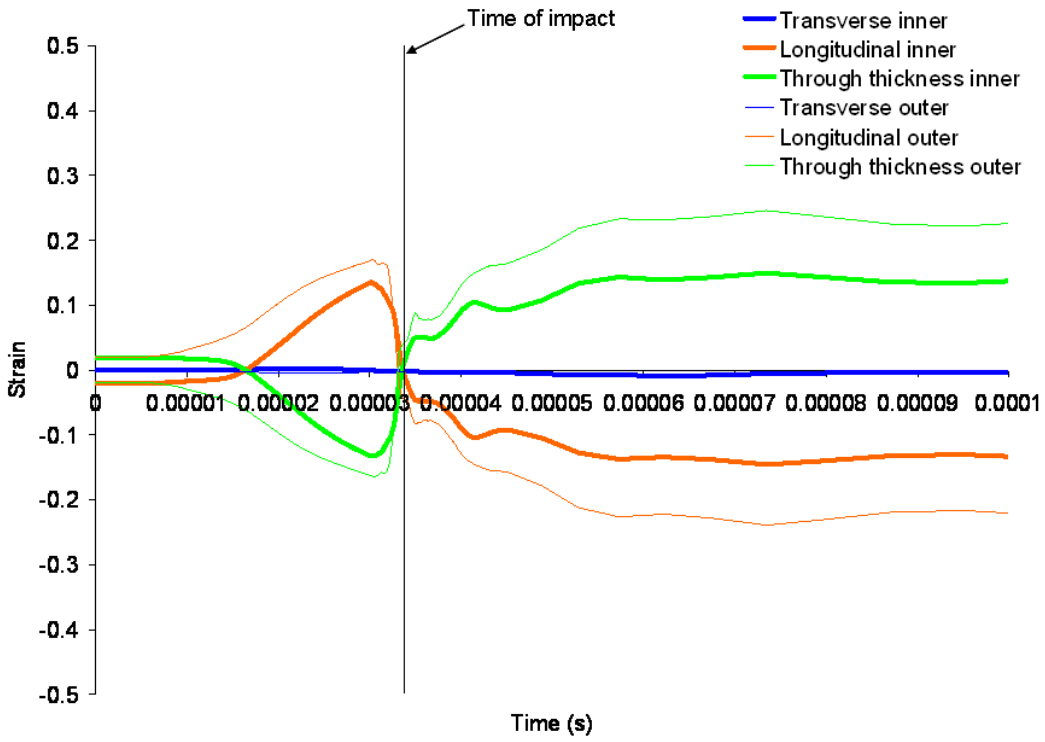

Figure 173: Normal strain histories for zone 2 elements.

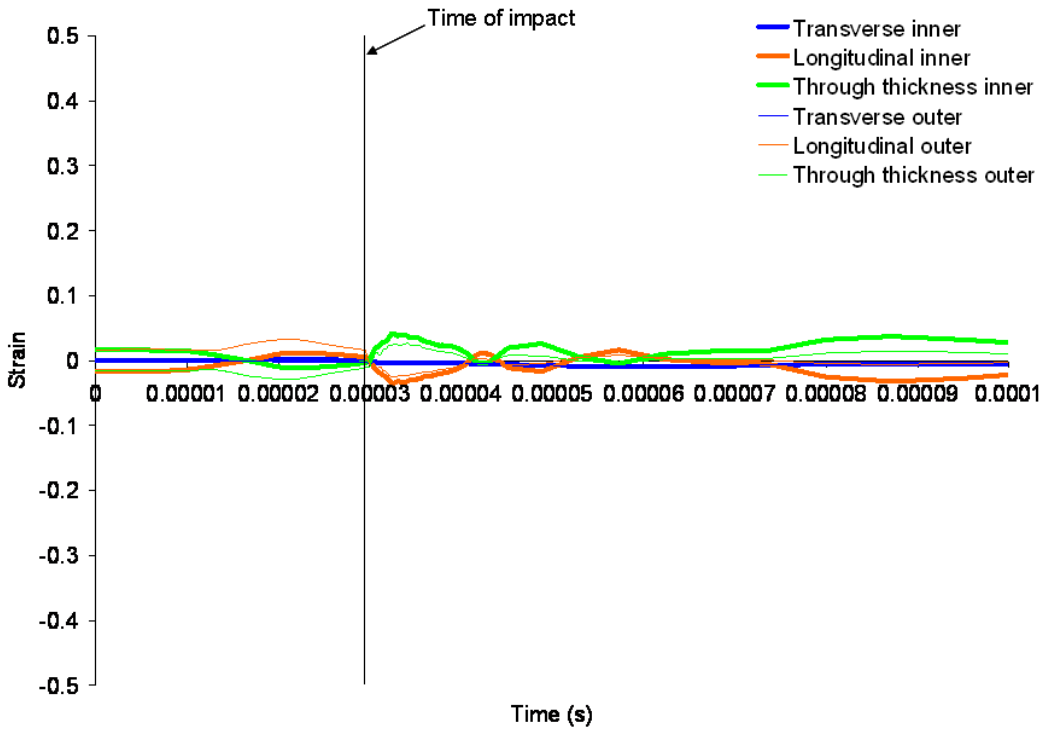

Figure 174: Normal strain histories for zone 3 elements.

The predicted shear strain histories are shown in Figure 175, Figure 176 and Figure 177. Low shear strains are predicted for zone 1 and the highest strains for these elements are predicted after impact as the sheet rebounds. In contrast, very high shear strains are predicted for zones 2 and 3. In all cases the longitudinal through-thickness shear strains (Figure 164) are the only ones that are predicted to increase, with the in-plane and transverse through-thickness strains showing negligible changes. This behaviour is consistent with the shear stress predictions. The highest shear strains are reached at or just after impact, with the strains increasing or decreasing during the rebound. The shear strains add an additional deformation mode that could be contributing to the increased formability that has been observed in the EM corner fill.

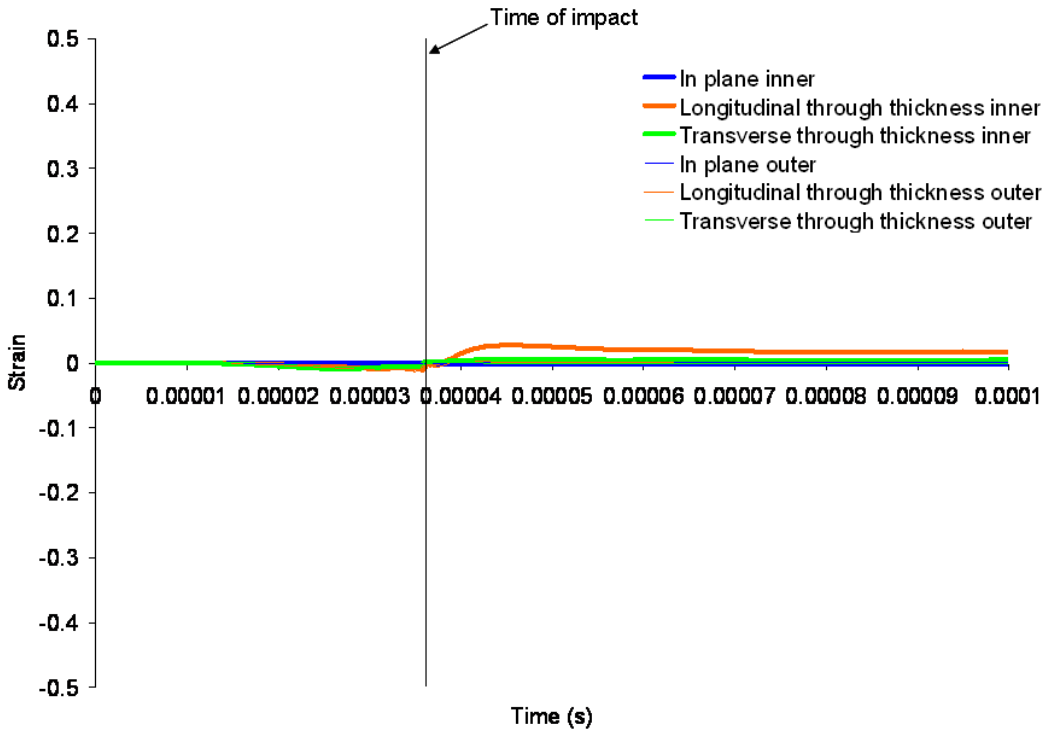

Figure 175: Shear strain histories for zone 1 elements.

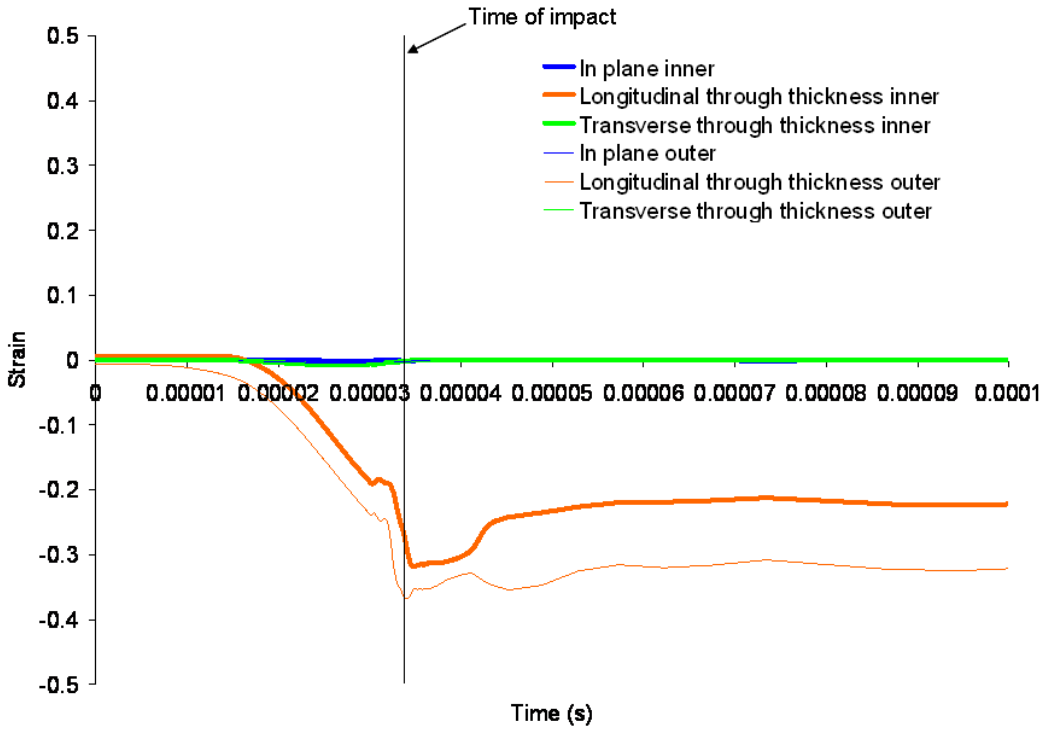

Figure 176: Shear strain histories for zone 2 elements.

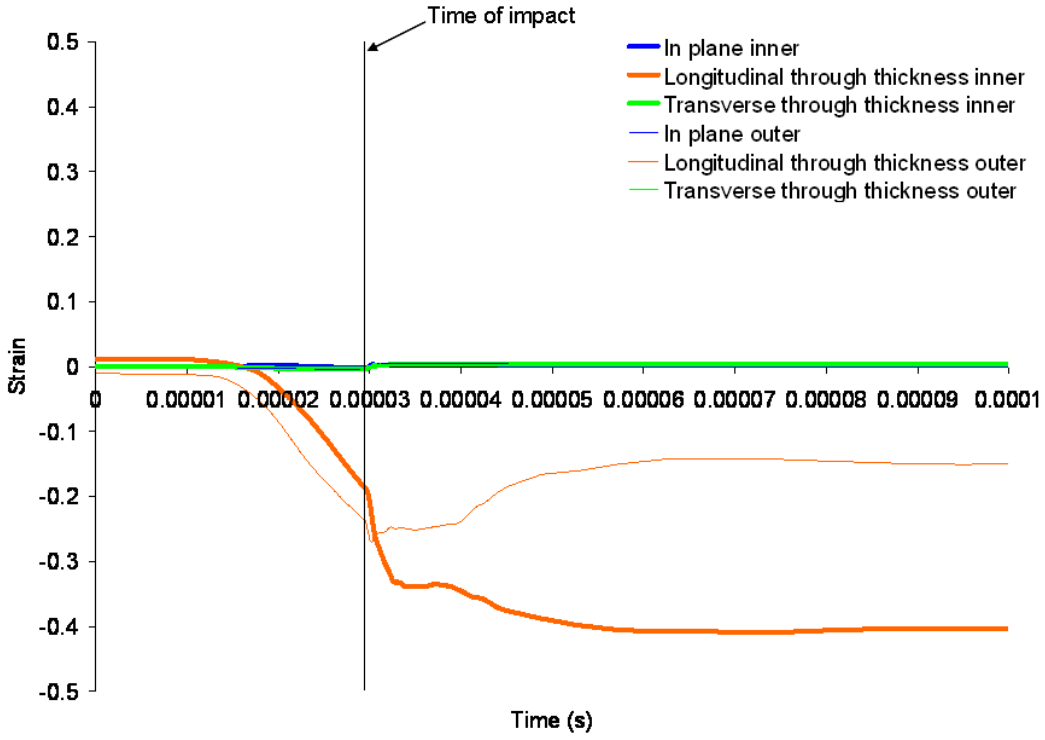

Figure 177: Shear strain histories for zone 3 elements.

5.3.2 Strain Rates

The strain rates to which materials are subjected to during EM forming, remain an open question in the literature. There are significant technical difficulties that impede the direct measurement of strain rate during these processes and numerical models offer one way, sometimes the only one, of getting insight into the operative strain rates. To determine the predicted strain rates for the corner fill application the effective plastic strain histories for the elements in the three previously described zones were obtained from the model. The histories are shown in Figure 178, from which it can be seen that the strain does not increase uniformly. The impact times are indicated in the figure and it is clear that the strains keep increasing after the impact, which is due to the rebound of the sheet.

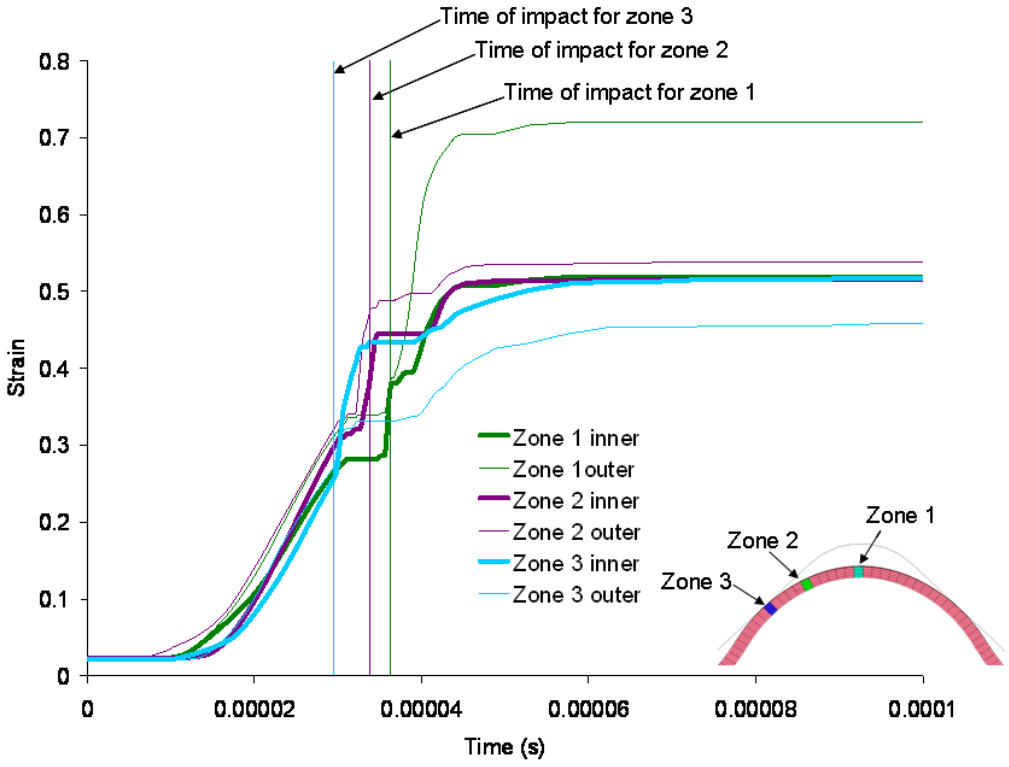

Figure 178: Effective plastic strain histories. Inset indicates the locations of the zones.

It is apparent from Figure 178 that the strain rates are changing with time and that local values might differ significantly from the averaged values show in Table 6. The instantaneous strain rates (ISR) for each of the elements being studied was determined from the data in Figure 178, by using;

$$ISR = \frac{\Delta\varepsilon}{\Delta t}$$ **Equation 5-1**

Where, ε is the strain rate and *t* is time. The results are shown in Figure 179.

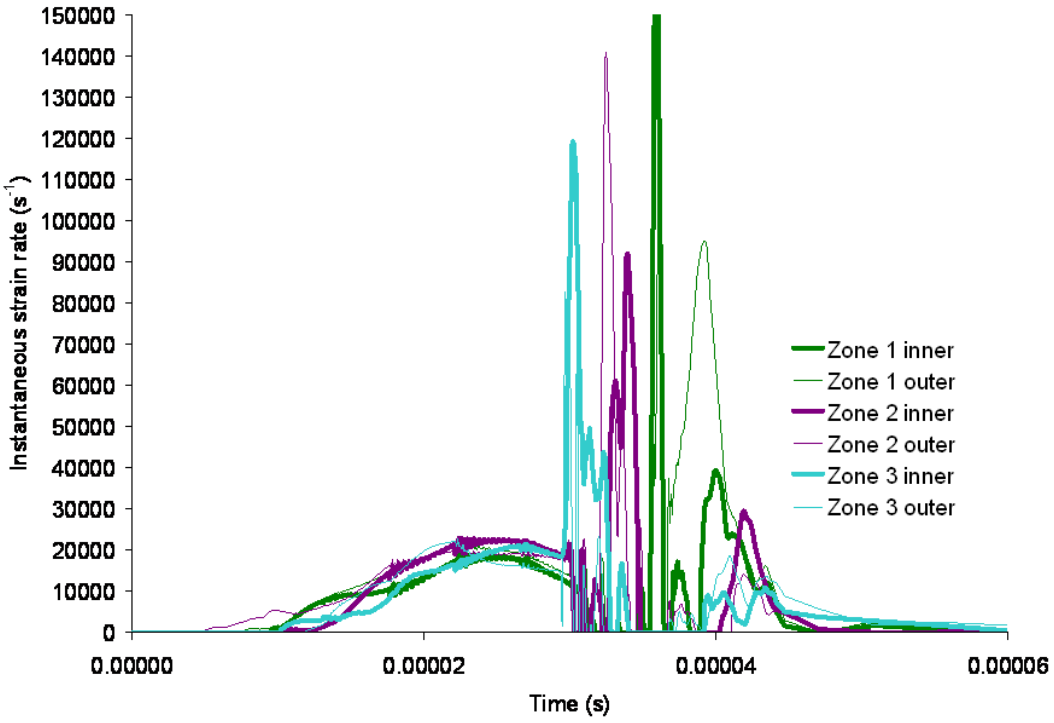

Figure 179: Instantaneous strain rates calculated for the inner and outer elements of zone's 1, 2 and 3.

It can be seen from Figure 179 that the strain rates vary significantly throughout the process and that very high values are reached. The three largest instantaneous strain rate values are presented in Table 5. The highest strain rates for zone 2 are predicted for the outer element, which is an intuitive result since this the element that makes impact with the die. In contrast, for zones 1 and 3 the highest strain rate is predicted for the inner element. For zone 3, this is the result of the area being close to the die from the beginning of the process and thus not being accelerated to as high a speed as the other areas of the part prior to impact. This is also the area where the sheet encounters the most significant and abrupt bending, which leads to the inner element presenting the highest strain rate. It is believed that for zone 1, the inner elements exhibit the highest strain rates due to the deformation produced by the excessive rebound that will be discussed in Section 5.4.

Table 5: The three highest strain rates and the elements where they where predicted.

Element	Strain Rate (s^{-1})
Zone 1 inner	149,000
Zone 2 outer	141,000
Zone 3 inner	119,000

To calculate an average strain rate, the segment of the strain history in Figure 178 between the first increase in strain and impact was considered. This gave an average strain rate for the period. The first instance of predicted increase in strain was recorded and was used together with the strain and time at the time of impact. The resultant strain rates are shown in Table 6. It can be seen that the strain rates are an order of magnitude higher than the 1,500 s^{-1} for which the adopted material data has been published. The strains rates in Table 5 are over three times higher than the average strains rates shown in Table 6.

Table 6: Strain rates calculated from the time of the first change in strain of the element to the time of impact.

Element	Strain Rate (s^{-1})
Zone 1 inner	12,779
Zone 1 outer	11,731
Zone 2 inner	15,077
Zone 2 outer	15,503
Zone 3 inner	12,141
Zone 3 outer	14,218

The predicted strain rates are significantly higher than those observed in conventional metal forming and those used for the published high-rate testing of the aluminum alloys used. Despite the acknowledged limitations of the numerical models, the predictions indicate that the materials in this EM forming operations can reach levels at which the high-rate behaviour of the material is not known. The properties of these alloys at these strain rates should be determined to better understand EM forming operations.

5.4 Possible Causes of the Deviation of the Predicted Final Shape from the Experimentally Observed Profile

The final predicted shape differs from that observed in the experiments due to the predicted rebound being higher than the observed behaviour. The numerical models are significantly over-predicting the rebound effect. Several factors were identified as possible causes for the over-prediction:

1. The adopted constitutive response in the model led to a flow stress that is lower than the actual material flow stress during the process.
2. The air between the sheet and the die could be providing a cushioning effect that reduces the energy at impact and is not captured in the numerical models.
3. Additional forces generated by the multiple current pulses produced by the actual process (Figure 101), only one of which was included in the models.
4. An over-prediction of the energy being transmitted to the sheet, and thus the induced forces.
5. Damping effect produced by the movement of the die generated during impact.
6. The inability of the contact algorithm to properly handle the contact between the sheet and the die during impact.

Of the six possible causes listed all but the possibility of the air providing a damping effect were studied numerically to determine the possible effects they may have on the numerical models. The possibility of air damping was not studied since it would require a different simulation approach which was beyond the scope of this research.

A possible source of the over prediction of the rebound could stem from the contact algorithm. The current model utilizes a penalty function-based contact treatment that may be too stiff and also too elastic resulting in an artificially large rebound. Models with decreased contact stiffness were attempted with little or no effect on the final shape. A more detailed study of the effects of the contact algorithm should be performed in the future.

5.4.1 Effect of the Material Flow Stress

The high strain rate properties of this material as it is formed at high speeds remain a source of uncertainty, particularly for strain rates above 1,000 s^{-1}. The quasi-static material properties used for this model were adopted since aluminum alloys show very little or no strain rate sensitivity at least up to the strain rates (1,000-1,500 s^{-1}) that can be accessed using Hopkinson bar techniques (a review of the subject is presented in [17]). Smerd *et al.* [28] studied AA 5754 sheet and found relatively mild rate effects on flow stress up to the strain rates of 1,500 s^{-1}. However, in the current work, the models predicted maximum effective plastic strain rates as high as 62,200 s^{-1}, which is an order of magnitude higher than the strain rates studied to date in constitutive characterization of this material. To the authors'

knowledge no data has been published for AA 5754 sheet at these rates. To investigate the potential effect of increasing flow stress through high strain rate sensitivity, models with flow curves that were scaled by 120, 130 and 140% of the current data were run. The corresponding flow curves are shown in Figure 180. The results of these models are shown in Figure 181. It can be seen that the model that gives the most accurate final shape is the one with the 140% flow curve.

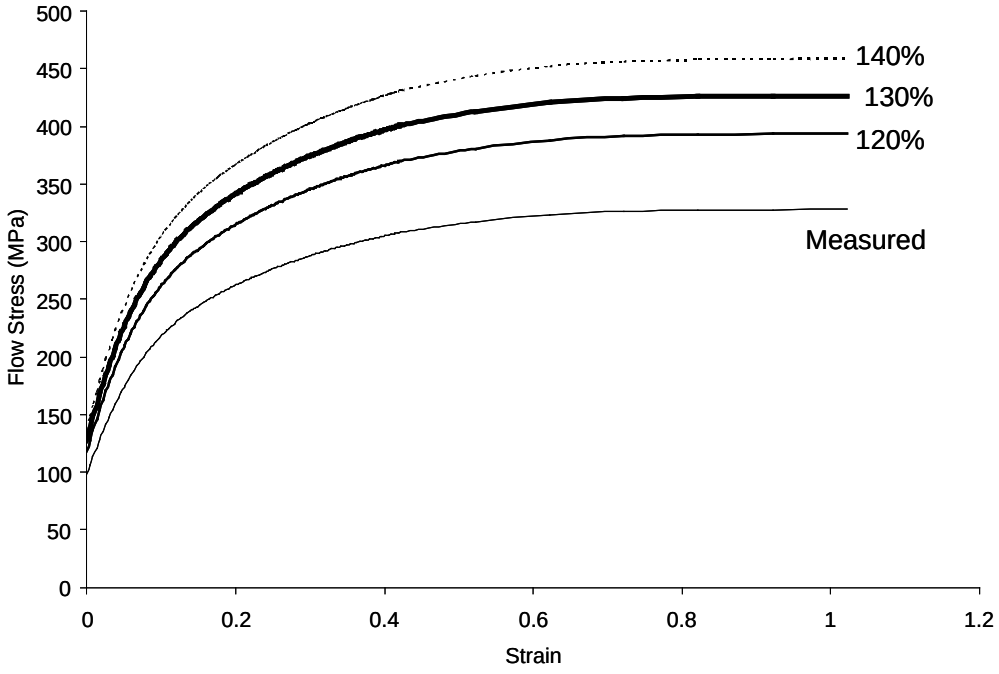

Figure 180: Flow stresses used for the numerical study.

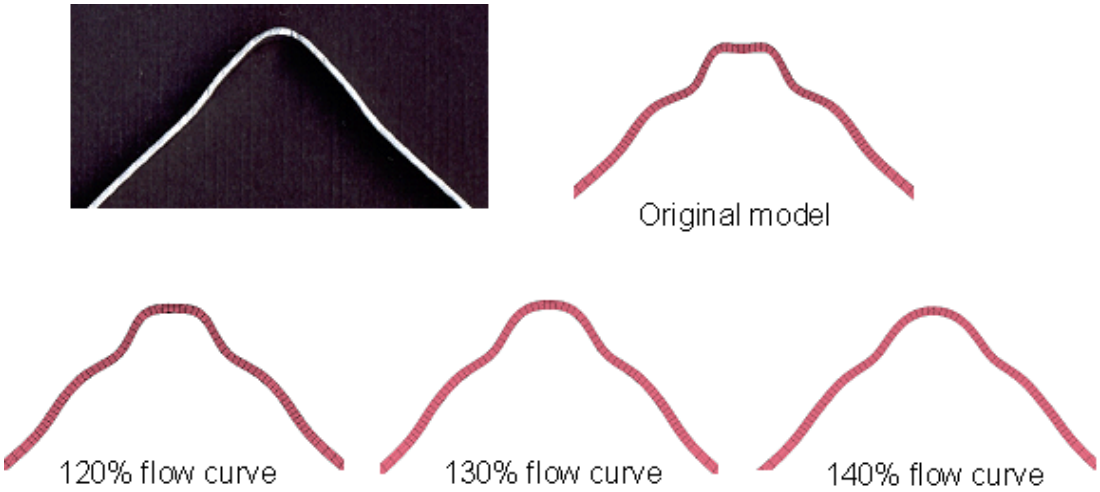

Figure 181: Predicted final shapes of the centre of the sample using flow curves scaled to 120, 130 and 140% as shown in Figure 180.

The final sample shape predicted using the 140% flow curve is shown in Figure 182 together with a picture of an actual sample from which it can be seen that there is good agreement between the experimental and numerical shapes. Figure 183 and Figure 184 show a comparison of the predicted and measured engineering strains. The predicted strains in the longitudinal direction agree better with the experimental data when compared to Figure 160. As with the predictions made with the original flow stress, there are two significant negative values (A and B in Figure 183) in the longitudinal strain measurements. The reason for these compressive peaks is the compressive state generated by the bending caused by the rebound. There is only one peak in the positive strain (point E in Figure 183), as opposed to the three observed in Figure 160. The absence of additional seen peaks in Figure 160 is the result of a reduction in the predicted rebound and bending in the radius region of the samples, so that the compressive bending stresses causing these peaks are eliminated.

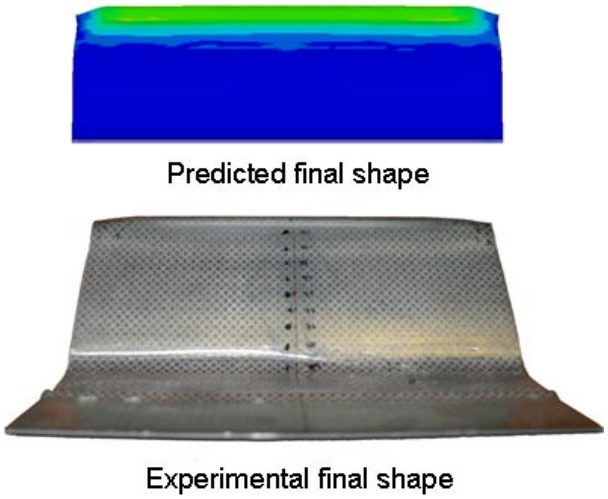

Figure 182: Predicted final shape using a flow stress scaled up by 140% together with a picture of an experimental sample. Note the closer agreement to the actual sample shape.

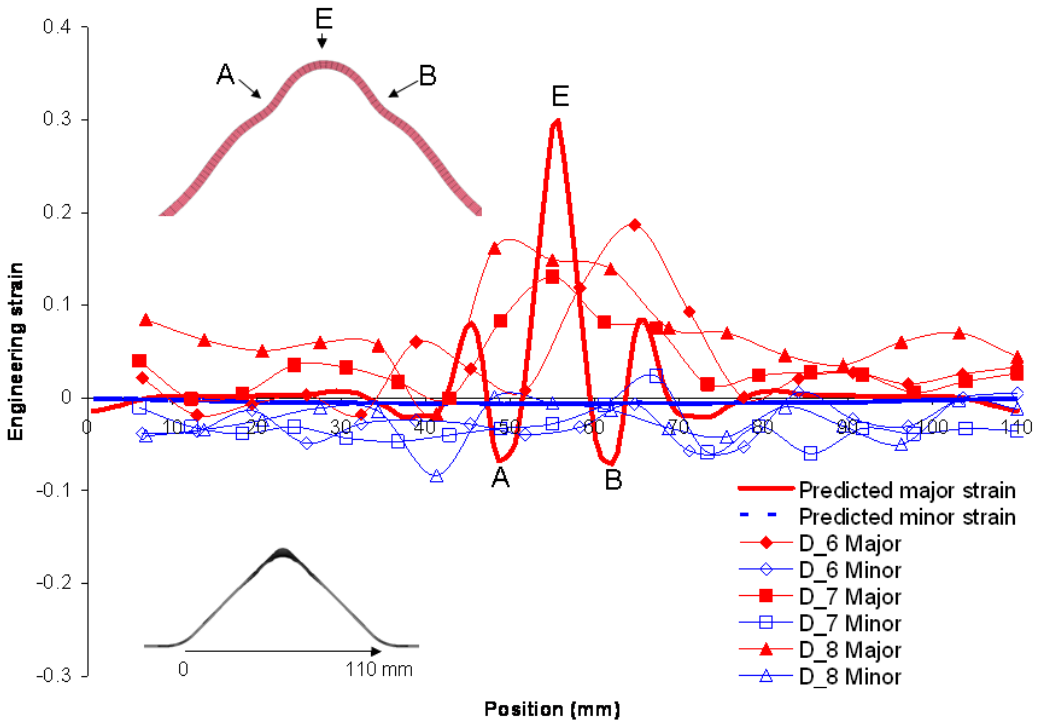

Figure 183: Predicted and measured engineering strains for the longitudinal direction for the model with the flow stress scaled by 140%.

For the strains in the transverse directions shown in Figure 184, the average of three elements was used. The approach used was the same one used to produce Figure 161. It can be seen that this approach results in a similar strain distribution to that obtained with the original flow stress curve

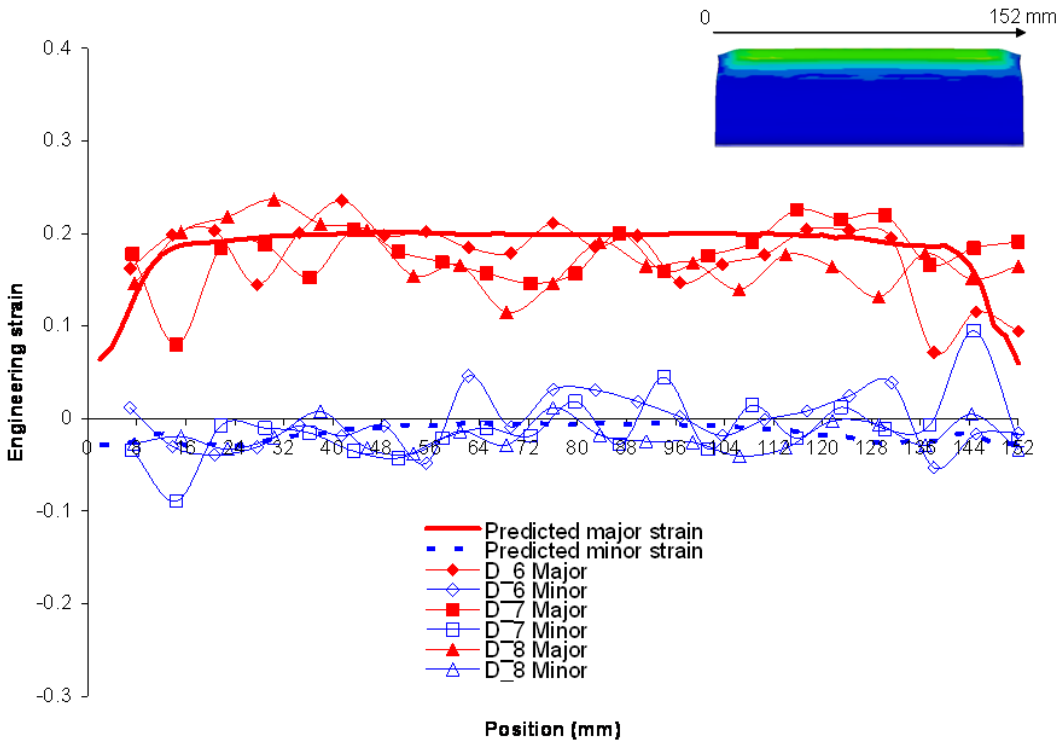

Figure 184: Predicted and measured engineering strains for the transverse direction for the model with the flow stress scaled by 140%.

It can be seen that the models that use the flow stress scaled by 140% agree better with the experimental results. This is an interesting outcome, since it indicates the possibility that there could be significant flow stress increases in the material. Hopefully, the material will be characterized at the strain rates encountered in EM forming in the near future.

5.4.2 Current Profile Effects

The numerical models used for this research considered only part of the actual current profile as an input, as indicated in Figure 185. This was done to save computational time under the assumption that the majority of the deformation occurred due to the first pulse. However, the actual current profiles contain more than one pulse which could also contribute to the deformation. Srinivasan *et al.* [91] present evidence that suggests that the additional pulses provide additional forces that can help achieve a part that is closer to the desired shape. To determine whether a current pulse with additional peaks would affect the final shape of the sample a model was generated that used a larger portion of the recorded experimental current profile. Figure 185 shows the profile used for these models, which has four peaks, or pulses,

as opposed to the single peak used in the original models. The resulting cross section from this model is shown in Figure 186 along with a cross section of an actual sample. It can be seen that the top of the part does not conform to the die, but that the sides of the parts are closer to the actual sample than in the models which used only one current pulse. This is due to the second pulse (the first negative peak), which produces sufficient forces to push the sides out to the final shape shown.

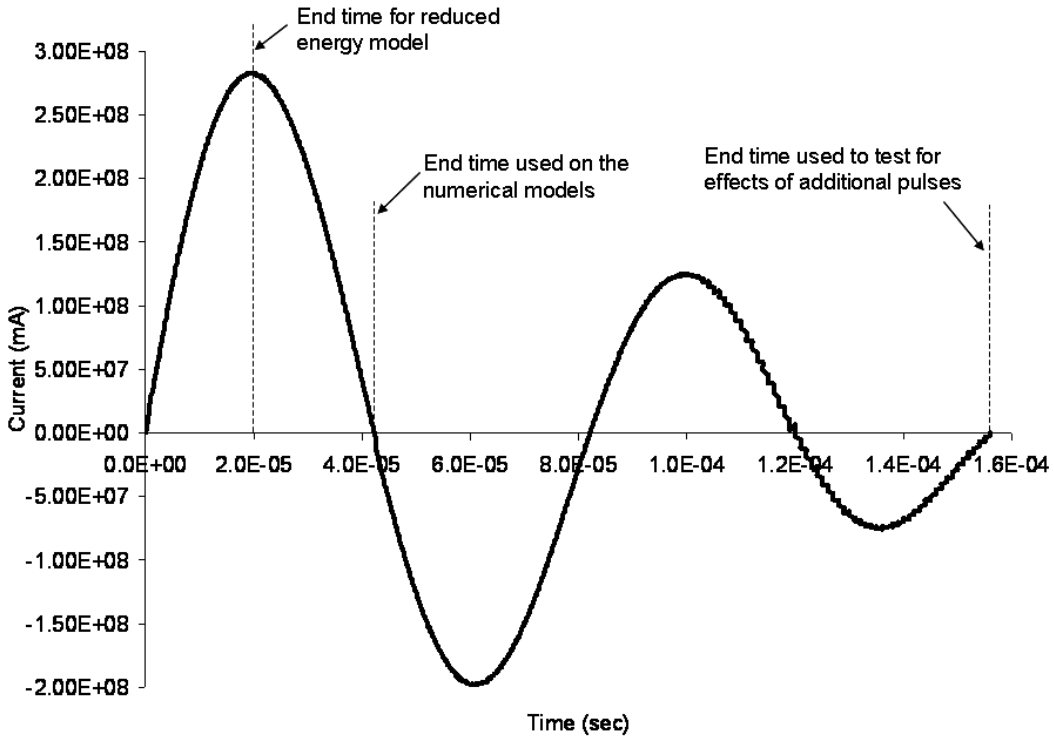

Figure 185: Current profile used to test the effects of additional EM pulses on the workpiece.

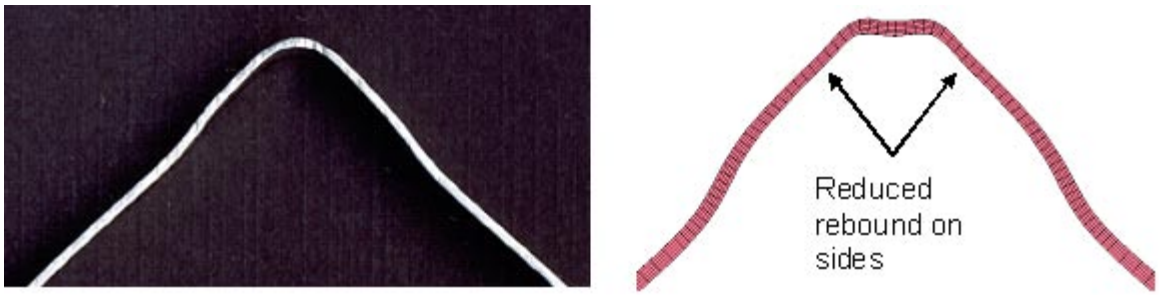

Figure 186: Section of the experimental sample compared to the numerical prediction using the current profile shown in Figure 185**.**

The tip of the sample still presents the results of rebound over-prediction. It was found that only the second pulse produced sufficient force to cause additional deformation of the

material. Figure 187 shows the model at different times during the multiple pulse simulation. The effect of the second pulse can be seen in Figure 187-e. The time image show in Figure 187-e is shown enlarged in Figure 188, where it can be seen that the highest forces are induced in the areas of the sheet that have the most significant rebound. This subsequent loading drives the sheet back towards the die, as seen on Figure 185 f-i. The additional pulses are not adequate to reverse the shape of the sheet at the top of the die and produce a part closer to the experimental samples. Whether this is what is actually occurring in the experiments or is a numerical effect caused by excessive rebound predictions remains an open question. Thus, as of the time of writing, the use of the larger current pulse in the models did not completely address the rebound over-prediction.

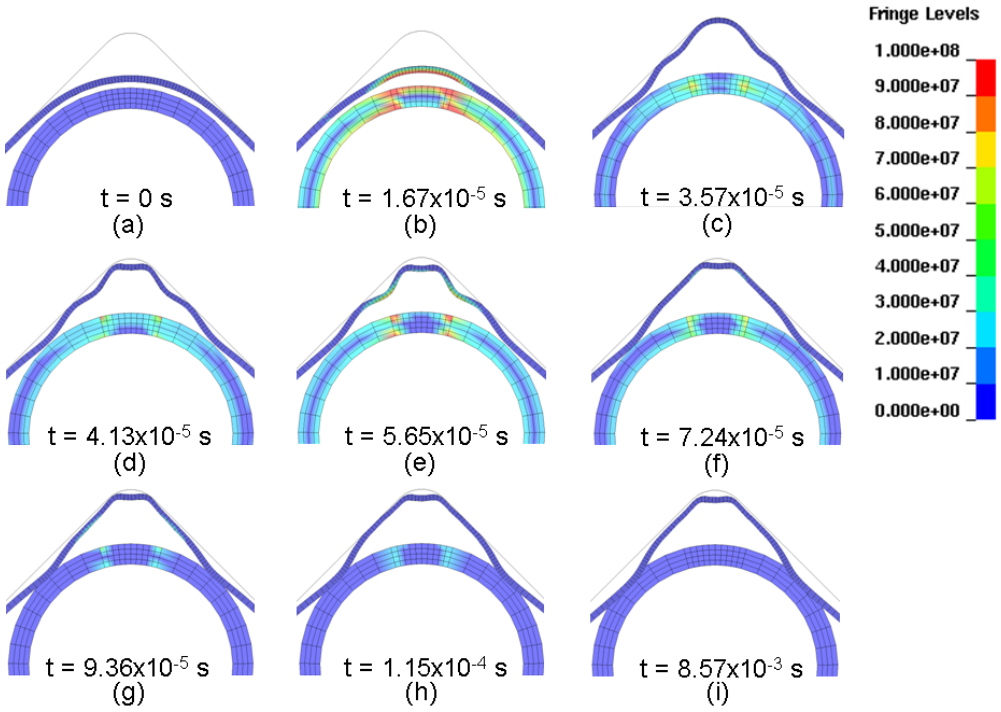

Figure 187: Deformation history of the sample with the multiple peak current pulse show in Figure 185. The forces induced by the second pulse can be seen on e). The contours are of Lorentz's forces in μN.

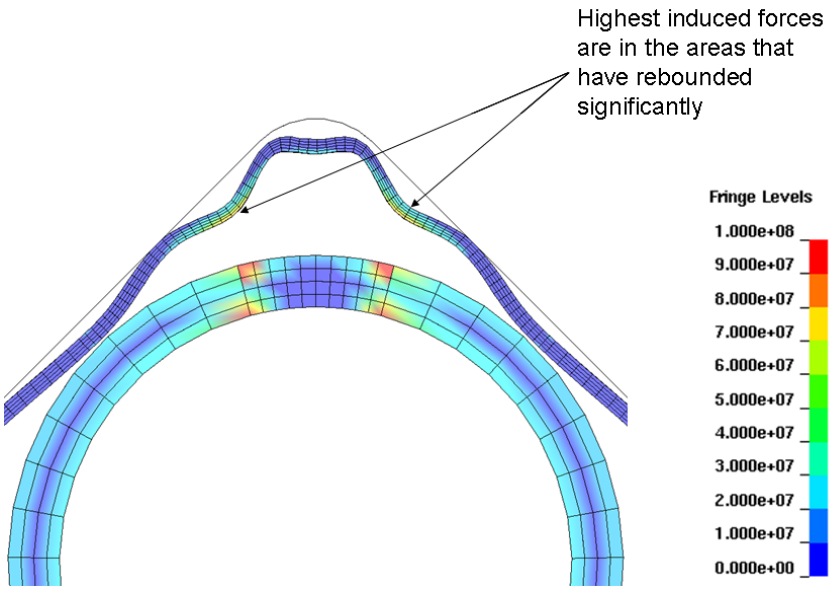

Figure 188: Image showing where the forces are induced on the second by the second current pulse. The contours are of μN.

5.4.3 Effects of Reducing the Amount of Energy

The numerical model could be over-predicting the amount of energy in the process, which could by producing the excessive rebound by generating excessive induced forces. A simple way of estimating the effect of providing less energy to the system is to "cut" the current supply to the coil at the peak of the pulse (20 μs) shown in Figure 84 and providing only half the current duration to the system, a shown in Figure 189. The profile is indicated in Figure 185 within the more complete current pulse. This is a simple numerical experiment that does not reproduce conditions that are likely to occur in an actual EM forming process; however, it is interesting to note that similar pulses have been reported experimentally in [93]. The results of doing this are shown in Figure 190 by comparing the predicted cross section of a segment at the centre of the part with a segment from the same general location of an actual sample. It can be seen that the predicted shape is close to the actual shape. An over-prediction of the energy transferred could be caused by using incorrect electrical properties for the materials, by not accounting for the change of electrical properties due to heating, by artificially high current densities produced at the sharp edges of the coil mesh, by the mesh being too coarse, for example. A more detailed numerical study could be undertaken to determine the effect, if any, of the possible causes listed.

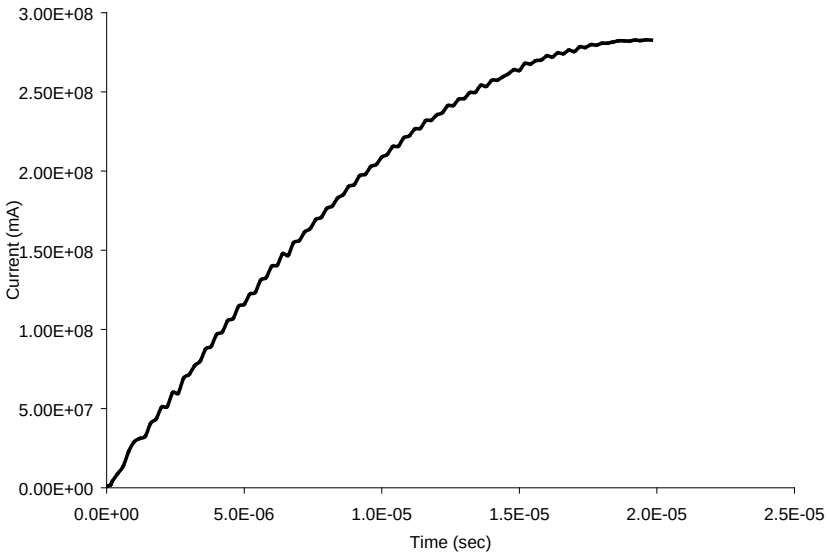

Figure 189: Current versus time profile used for the reduced energy simulations.

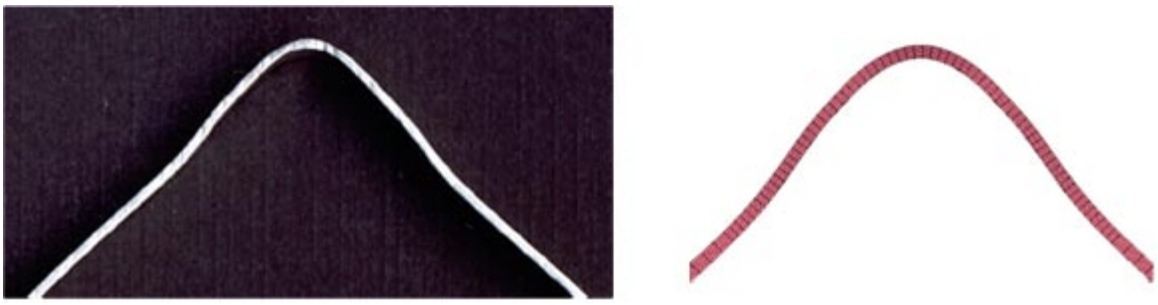

Figure 190: Section of an experimental sample compared to the numerical prediction using half the current profile shown in Figure 84.

5.4.4 Possible Damping Effects

Another explanation for the over-prediction of the rebound could be that the die/press combination used for the experiments is providing a compliance, or damping, effect. The die was held in place by a hydraulic cylinder and it is possible that when the material struck the die it compressed the hydraulic cylinder slightly and thus some of the energy of the impact was dissipated in the hydraulic cylinder. This compression of the cylinder was observed when testing the field shapers described in Section 2.8; however, the shapers were essentially in direct contact with the die and the Lorenz forces were generated over a much larger area in those experiments. This effect was not part of the original model, since the die was modeled

as a rigid body, thus allowing no energy absorption. Damping has been studied in the past and proposed as a way to reduce rebound effects by Risch *et al.* [69,94].

A simple model was developed to determine if compliance in the fixturing of the die could affect the final shape of the part. To create this effect numerically the die was allowed to accelerate after impact to a velocity of 10 m/s (Figure 188). Allowing the die to accelerate to higher velocities was considered, but higher velocities were deemed unrealistic and not pursued. The resulting final cross sections can be seen in Figure 192. Allowing the die to accelerate away from the material did not have any significant effect. Further experimental and numerical studies could be undertaken to investigate the effect of damping on the final shape of an EM formed part, but were deemed unnecessary.

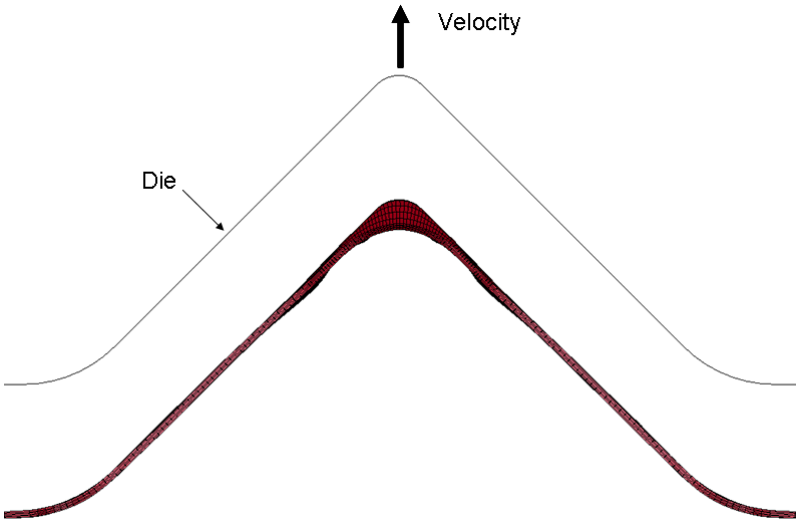

Figure 191: Allowed displacement of die used to simulate damping due to a moving tool.

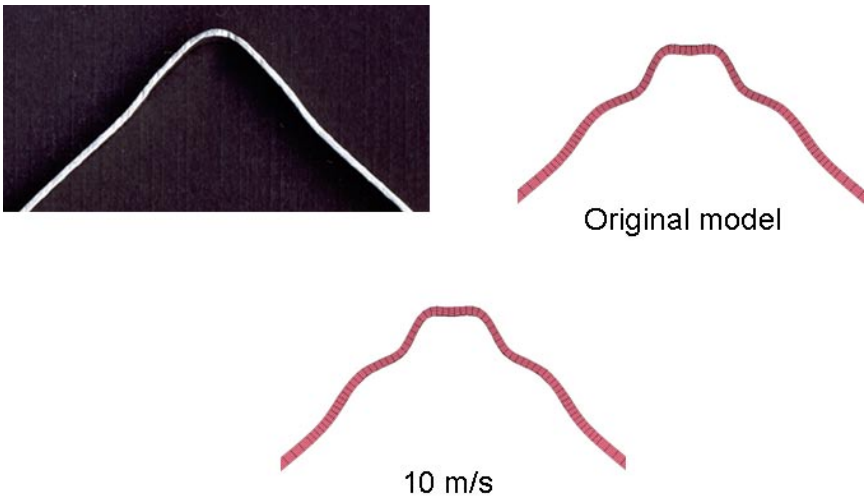

Figure 192: Effect of allowed die velocity on the final predicted shape.

The over-prediction of the rebound remained an unsolved issue as of the time of writing. The numerical studies performed showed that several effects could be causing these effects. It is possible that no one of the possible causes is entirely responsible; rather a combination of the factors could be at play.

5.5 Pre-Strained Sheet Simulations

Since the pre-straining process itself was not modeled, the blank thickness used for the pre-form models were reduced to match the measured thicknesses, which were for 0.96 mm for the 5% pre-strain, 0.90 mm for the 10% pre-strain and 0.91 mm 15% pre-strain. The values for the 10 and 15 % strains are essentially identical, which was unexpected. This could be due to slight differences in the stock material supplied and/or measurement error. The theoretical thickness after pre-straining were calculated using the average measured and minor strains and were: 0.97 mm for 5%, 0.94 for 10% and 0.93 for 15%. The flow stress curves were adjusted to account for the pre-straining, by shifting the curves so that they started at the level of work hardening corresponding to the pre-strain value, as shown in Figure 193. As with the previous model, the geometry of the pre-form, together with the predicted stresses and strains were used for the corner fill models.

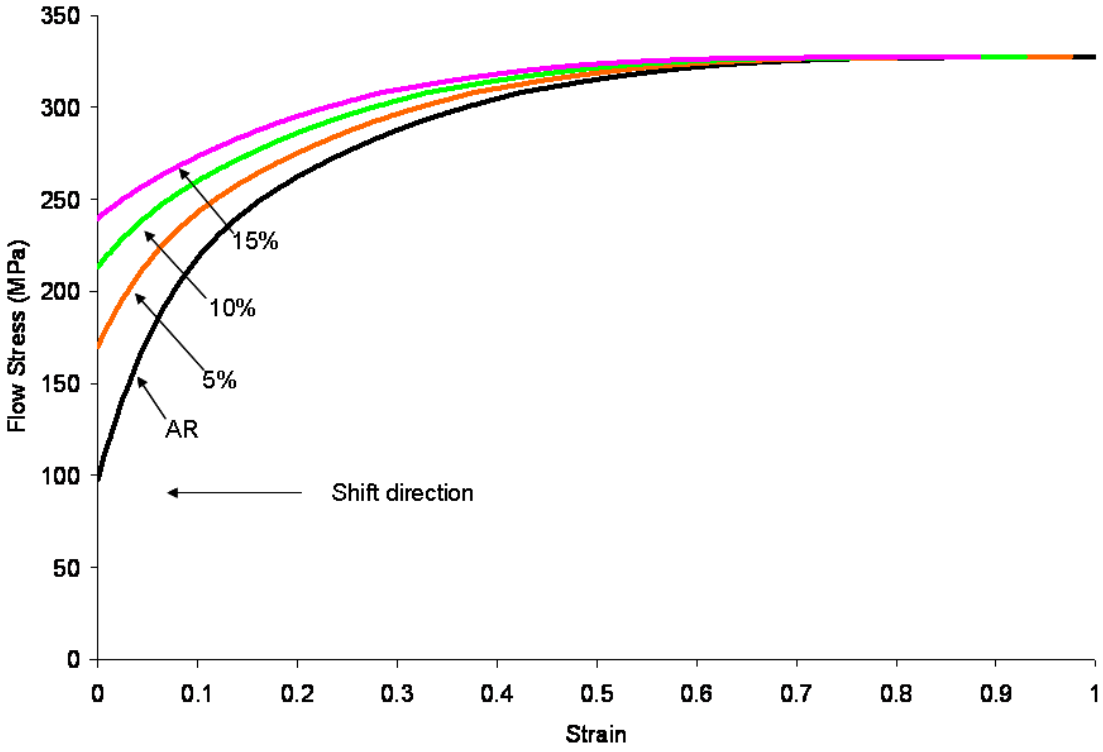

Figure 193: Flow stress used to simulate the effect of the pre-straining on the sheet.

The predicted final cross-sections at the specimen centre for the pre-strained sheet models are compared with the cross section of the non-pre-strained model and actual samples in Figure 194. It can be seen that there is no significant effect on the predicted cross section, the most noticeable effect showing for the 15% pre-strained sheet. The effect of the pre-straining is not as pronounced as the effect of scaling the flow stress curves (Section 5.4.1), which is expected since the pre-strain effect is seen primarily in the early yield response.

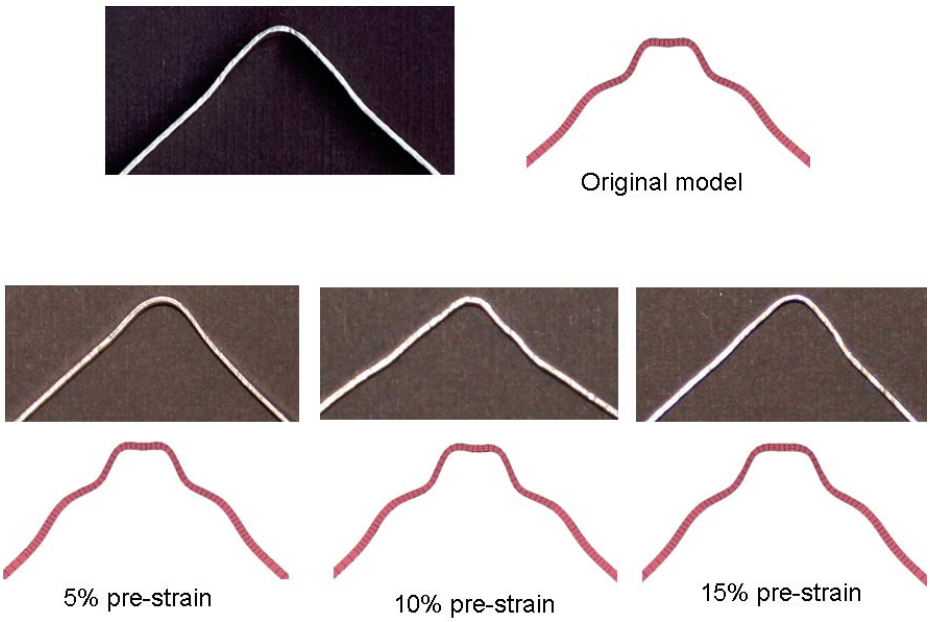

Figure 194: Cross sections of the predicted final shapes for t he original (0% pre-strain), 5, 10 and 15% pre-strain models, compared to a sections of the actual corresponding samples.

The predicted strains are compared to the measured distributions in Figure 195-Figure 200. Since the strains generated by the pre-form operation were not included in the model, the average measured major and minor strain for the sheets were added to the numerical results. As expected, the strains follow the same trends as the models with no pre-strain, with the exception that the strains are shifted up due to the pre-straining.

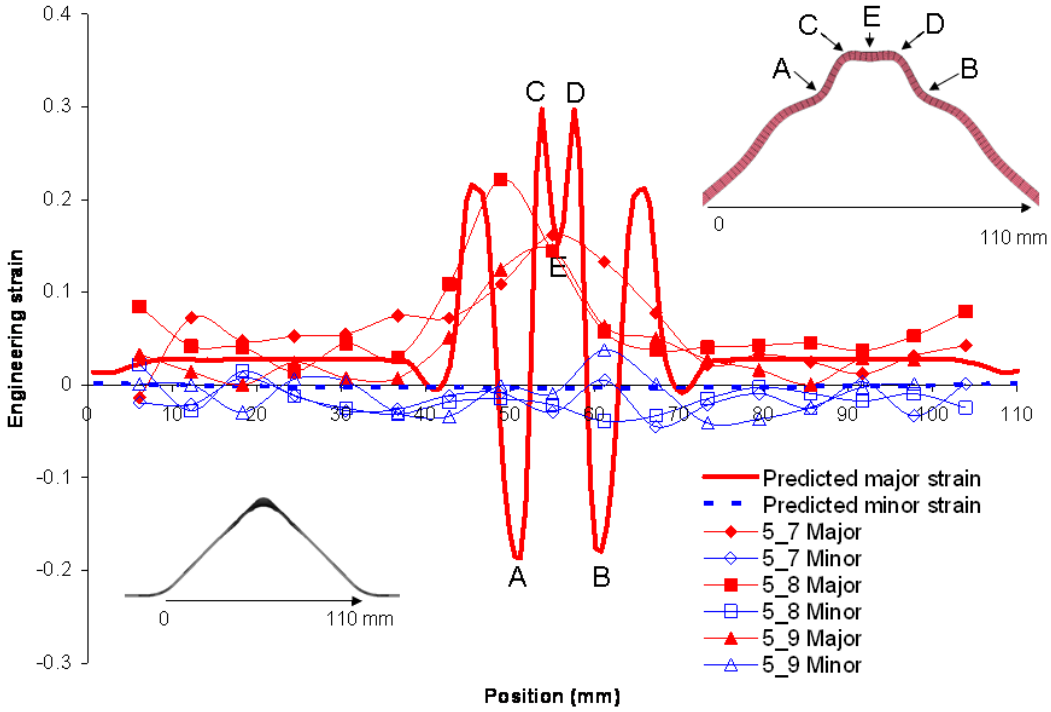

Figure 195: Predicted and measured engineering strains for the longitudinal direction for the model with the sheet pre-strained by 5%.

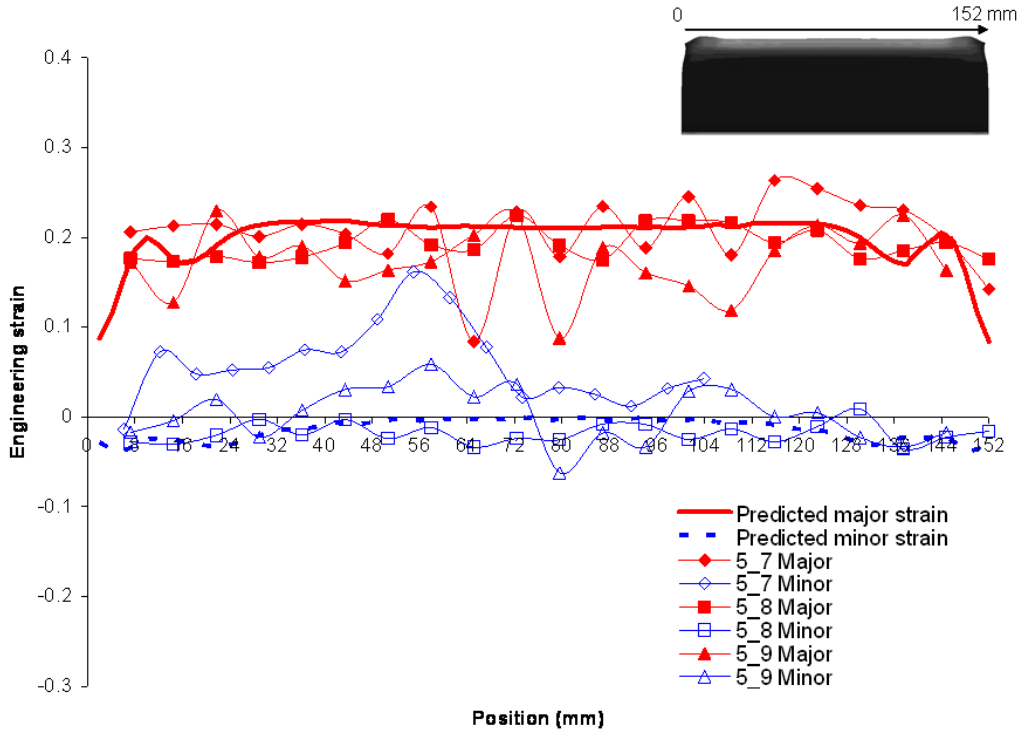

Figure 196: Predicted and measured engineering strains for the transverse direction for the model with the sheet pre-strained by 5%.

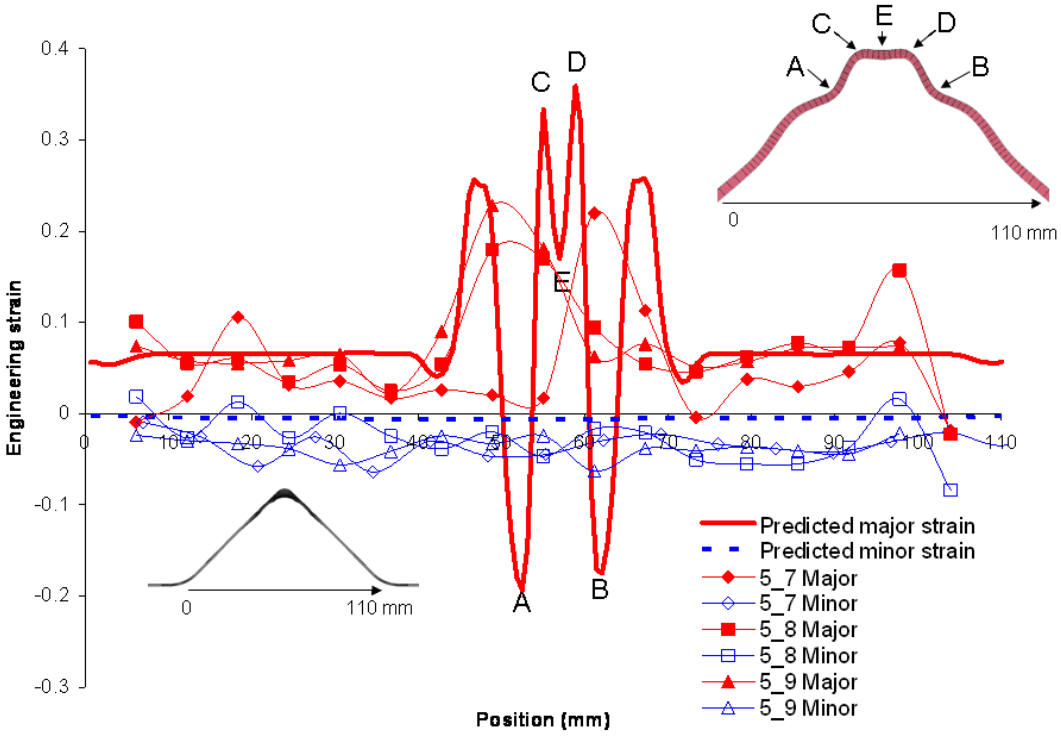

Figure 197: Predicted and measured engineering strains for the longitudinal direction for the model with the sheet pre-strained by 10%.

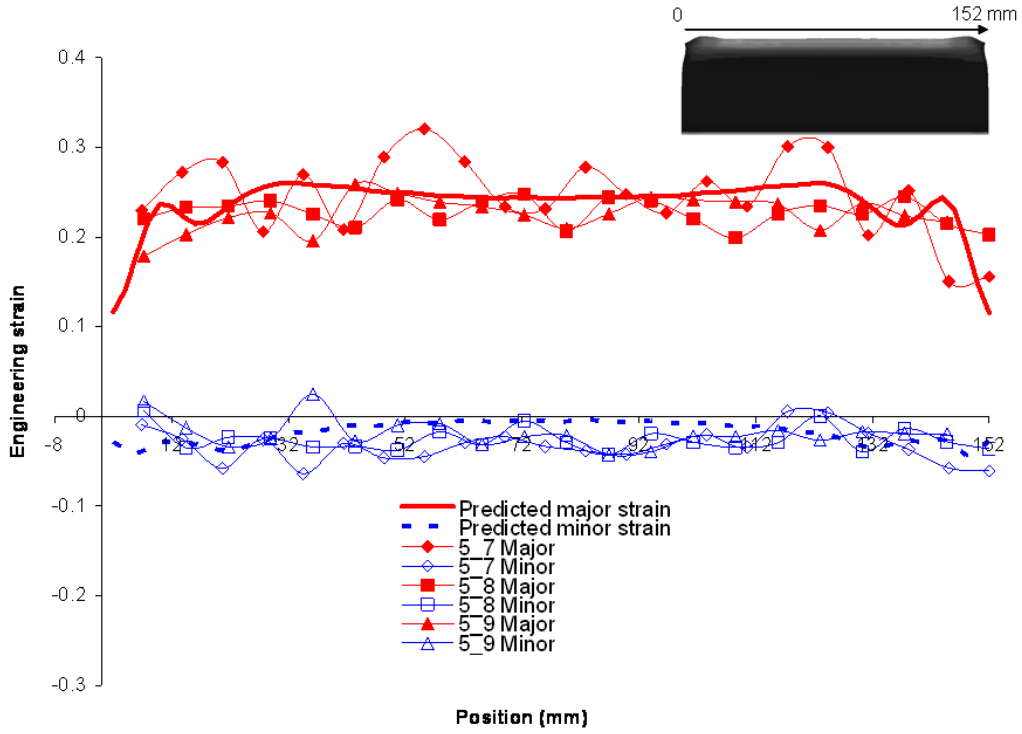

Figure 198: Predicted and measured engineering strains for the transverse direction for the model with the sheet pre-strained by 10%.

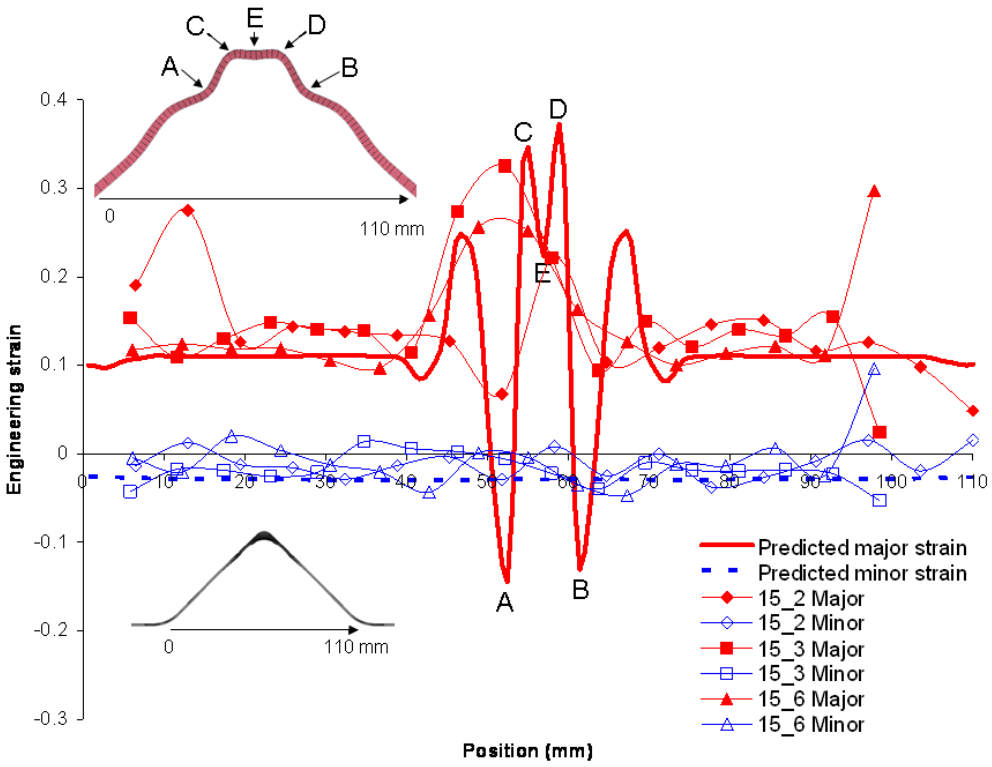

Figure 199: Predicted and measured engineering strains for the longitudinal direction for the model with the sheet pre-strained by 15%.

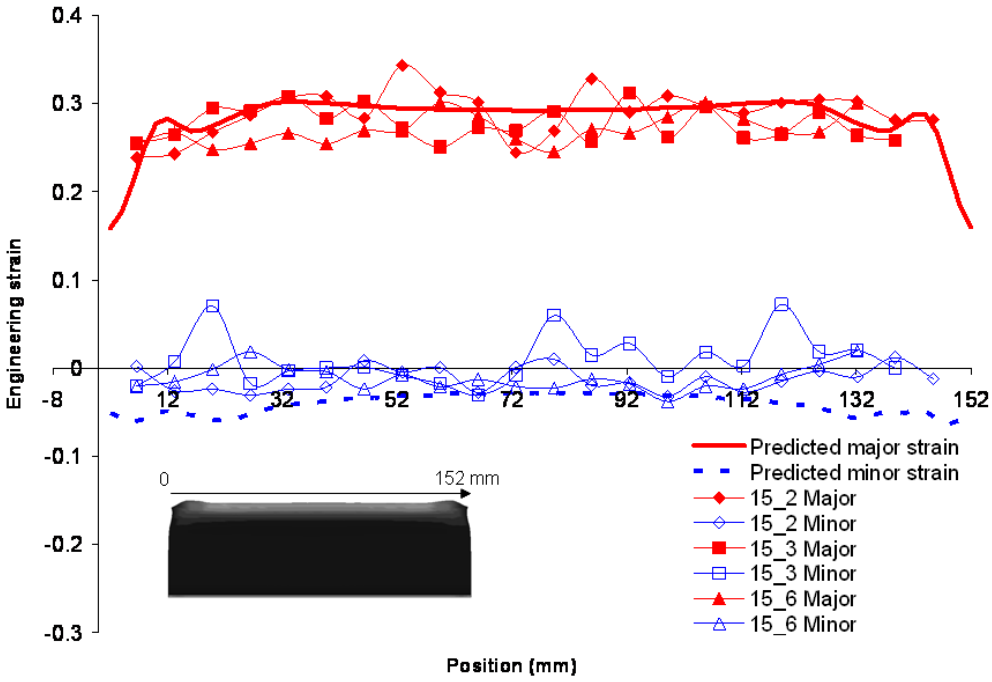

Figure 200: Predicted and measured engineering strains for the transverse direction for the model with the sheet pre-strained by 15%.

5.6 Efficiency of the Corner Fill Process

Moon [57] estimates that the average efficiency of an EM forming process is 15%, while Belyy *et al.* [14] state that for a sheet forming process the efficiency is 3 to 4%. The predicted plastic work consumed by the EM forming process was used to try to obtain an estimate of the efficiency of the corner fill process. The models with the current profile shown in Figure 185 were used since they provide a closer representation of the actual process than the case where only the first pulse of the current profile was used. The predicted internal plastic work was 372 J. To calculate the efficiency, the predicted plastic work was divided by the actual charge energy used for the process (15.1 kJ) and by the energy that was calculated from the current versus time profile for an actual experiment shown in Figure 24. To calculate the energy from the current profile, the well known instantaneous power equation was used [58],

$$P = i^2 R \qquad \textbf{Equation 5-2}$$

To obtain a value for the energy from the current time profile the equation was modified as follows;

$$\frac{\Delta E}{\Delta t} = i^2 R \qquad \textbf{Equation 5-3}$$

$$\Delta E = (t_2 - t_1)(i_{avg})^2 R \qquad \textbf{Equation 5-4}$$

$$i_{avg} = \frac{(i_2 - i_1)}{2} \qquad \textbf{Equation 5-5}$$

The current and time quantities used are illustrated in Figure 201. With this method the energy delivered was calculated as 11.47 kJ.

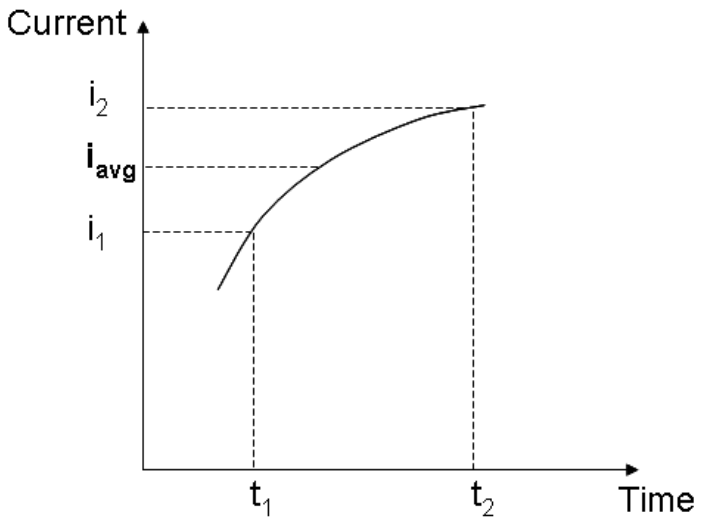

Figure 201: Illustration of the quantities used in equation 5-3.

To confirm the accuracy of the energy calculation, the energy was also calculated using

$$P = i_{rms}^2 R$$ **Equation 5-6**

The calculated i_{rms} was 99,809 A, which resulted in an energy value of 11.49 kJ, which agrees well with the previous value.

Using the stored energy of 15.1 kJ the efficiency was calculated at 2.46% and using the energy from the current versus time profile it is 3.24 %, which agrees well with the efficiency quoted in [14].

6 DISCUSSION

The research presented in this thesis has shown that a hybrid process consisting of a conventional (stamping) operation followed by an EM corner fill can be used to sharpen a radius on sample made from AA 5754 sheet that could not be formed using conventional stamping techniques. This outcome indicates that the formability of the material was increased through the use of the hybrid process. The increased formability is easily seen in Figure 202, which reproduces the results of the strain measurements for the corner filled samples formed with the sheet pre-strained to 15%. The pre-straining and pre-forming processes produce strains on the part that are close to the FLC, which in conventional forming would indicate that the material is on the verge of failure. The EM corner fill step formed the material into the corner resulting in strains that are significantly above the FLC, without any indication of failure in the material. Attempts to sharpen the corner with a conventional stamping operation resulted in failure of the sample for all pre-strain conditions. The experiments showed that some issues remain with the process, namely the deviation of the final shape from the nominal one and the challenges involved in the design and construction of the coils.

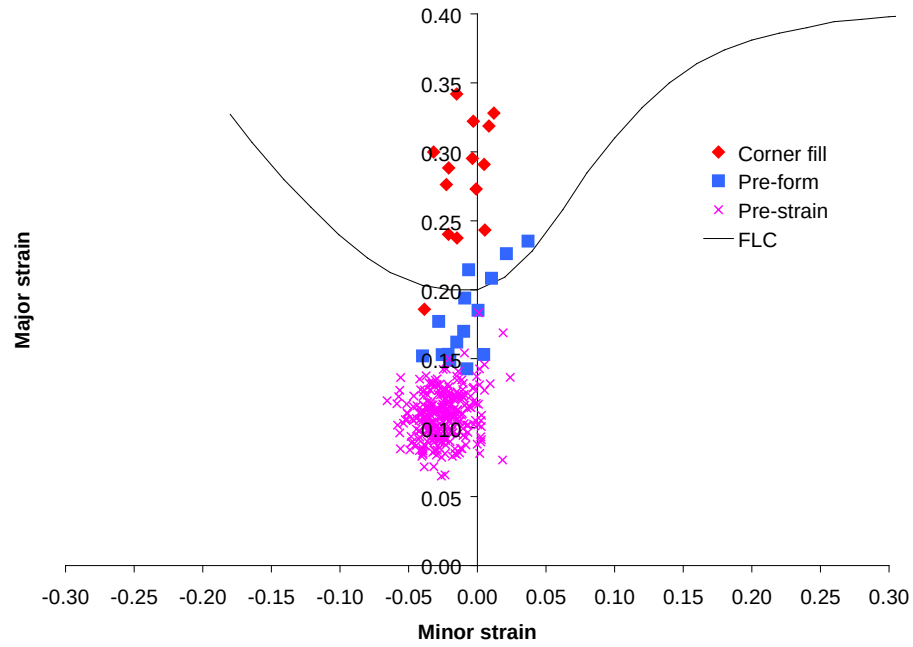

Figure 202: Forming limit diagram containing the largest strains measured on the final corner filled samples and the samples in the pre-formed state formed with the sheet pre-strained to 15%. Also shown are the strains measured on the pre-strained sheets.

The reasons for the increased formability are not completely understood; however high workpiece speeds are generated in the process and the increased formability reported here and in other studies has been attributed to the associated high strain rates (see Section 1.4). Numerical simulation of the current experiments has predicted strain rates in the range of 10,000 to 100,000 s^{-1}, which are significantly above the available data for the alloy studied. The predicted effective plastic strain, longitudinal strain and instantaneous strain rates are show in Figure 203 to Figure 208 for the elements analyzed in Section 5.3. It can be seen from the figures that very high strain rates are predicted for large parts of the deformation. Despite the fact that relatively low strain rate sensitivity has been observed in these alloys for strain rates up to 1000 s^{-1}, the much higher rates in this process could very well have an effect on the formability of these materials. Hopefully, high-strain rate data for the conditions experienced in EM forming will be available in the near future.

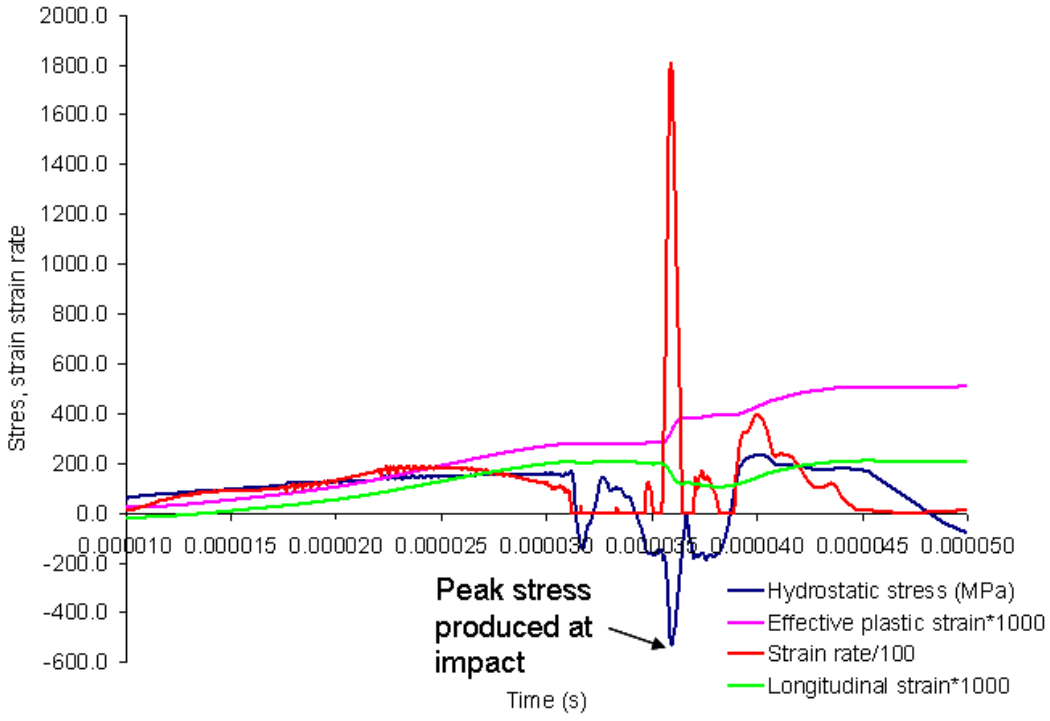

Figure 203: Figure showing the predicted hydrostatic stress, strain and instantaneous strain rate for the inside element of zone 1.

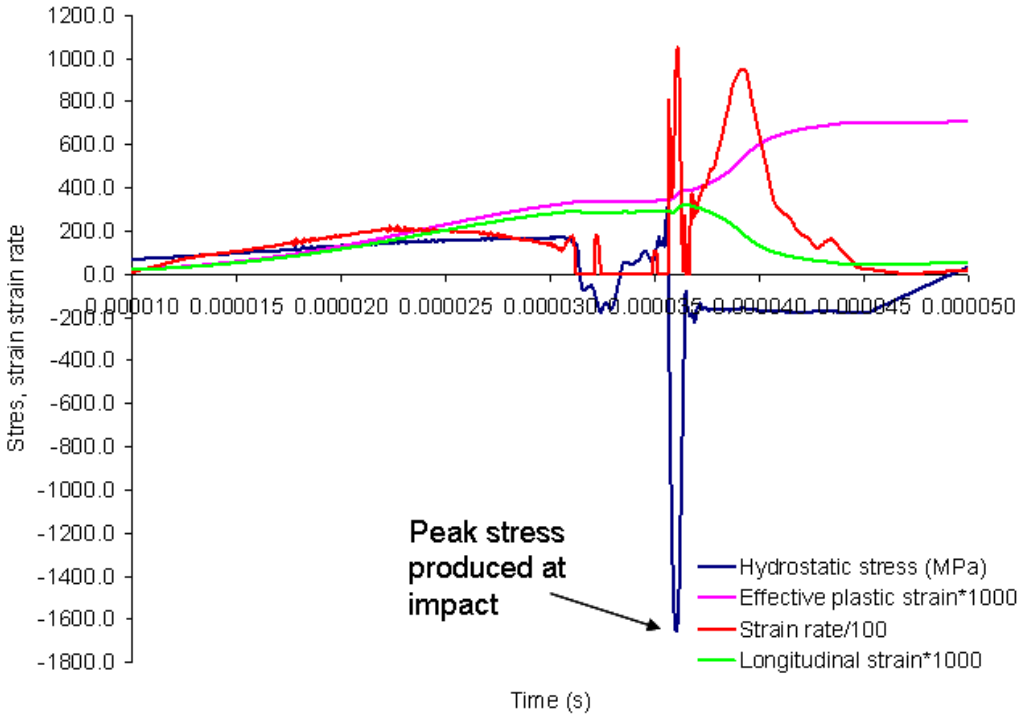

Figure 204: Figure showing the predicted hydrostatic stress, strain and instantaneous strain rate for the outside element of zone 1.

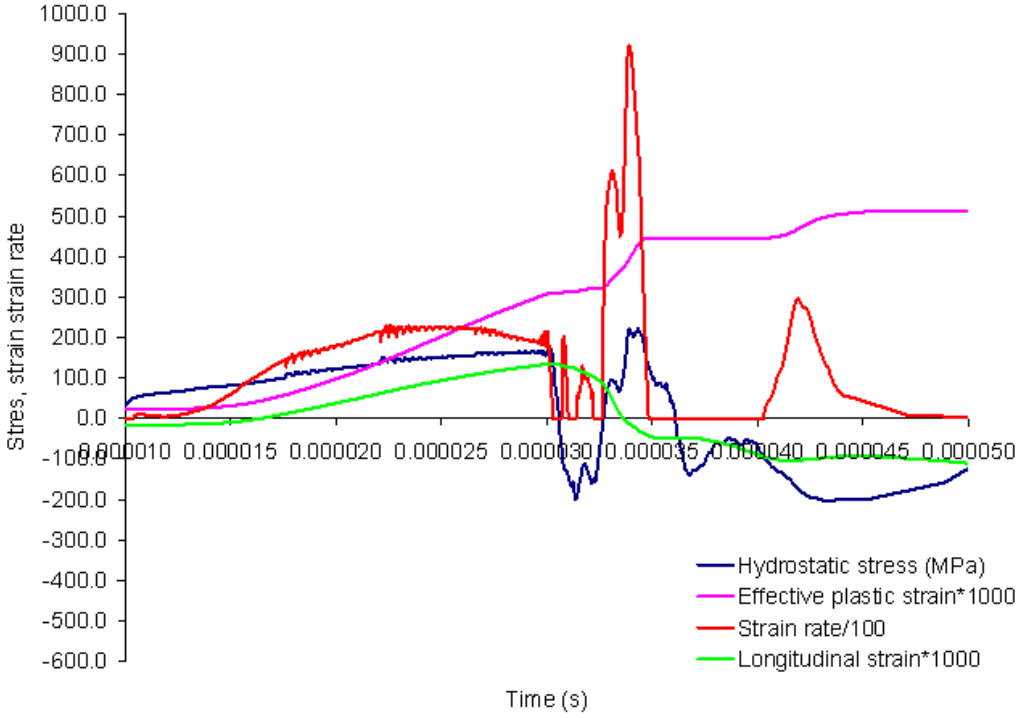

Figure 205: Figure showing the predicted hydrostatic stress, strain and instantaneous strain rate for the inside element of zone 2.

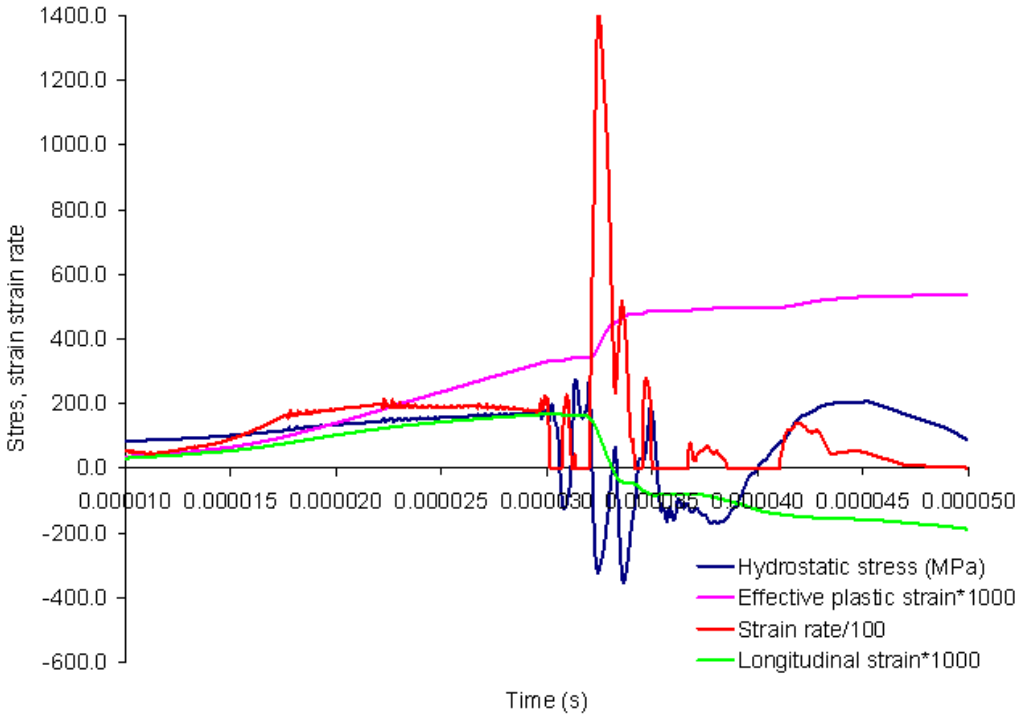

Figure 206: Figure showing the predicted hydrostatic stress, strain and instantaneous strain rate for the outside element of zone 2.

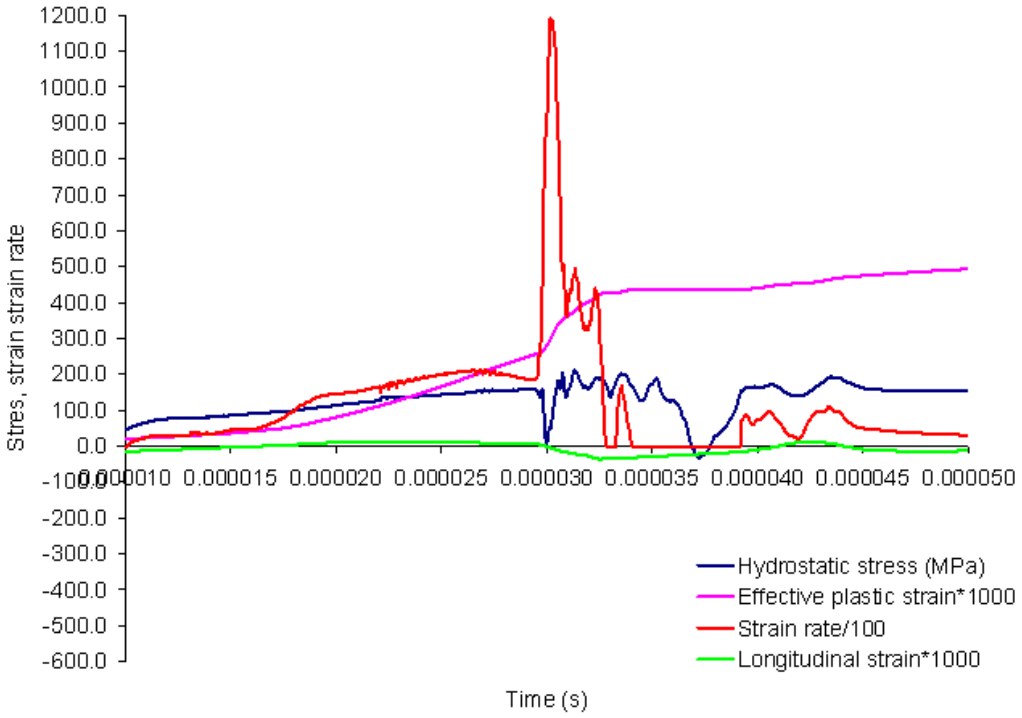

Figure 207: Figure showing the predicted hydrostatic stress, strain and instantaneous strain rate for the inside element of zone 3.

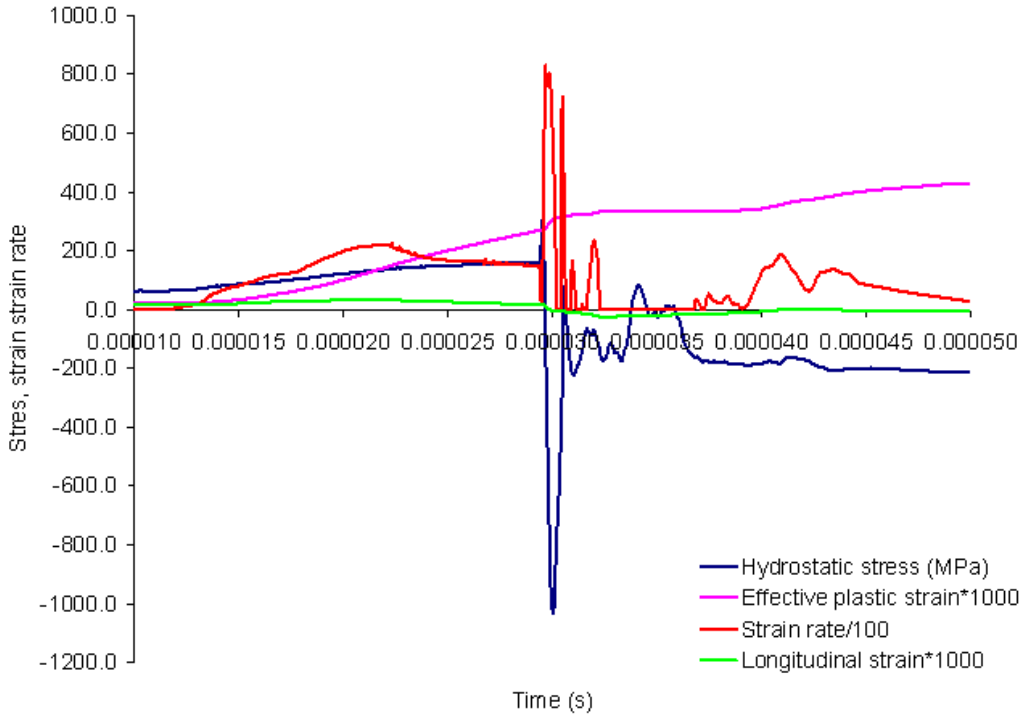

Figure 208: Figure showing the predicted hydrostatic stress, strain and instantaneous strain rate for the outside element of zone 3.

High strain rates are not the only factor in the observed increased formability. The interaction of the fast moving sheet with the tool produces stress and strain states that are very different from the plane-stress state that is typically attributed to conventional sheet forming process. The numerical predictions show that, at the time of impact, significant through-thickness compressive and hydrostatic stresses are generated (Figure 203 to Figure 208), which produce an inertial ironing condition favourable to damage reduction (evidence of this was found in the low damage values observed on the samples measured), which can contribute to increased formability. The largest negative hydrostatic stresses coincide with large increases in strain rates and effective plastic strain between 10 to 15% strain (Figure 204 and Figure 205). This indicates that a significant amount of deformation is occurring when conditions favourable to damage suppression are present. However, the predicted longitudinal strains do not show an increase in magnitude, which is due to the bending strain component generated by the rebound. As discussed in Section 5.4, the predicted rebound is thought to be excessive and unfortunately adds a measure of uncertainty to the conclusion that inertial ironing effects are contributing to the increased formability. As presented in Section 5.4 it is thought that improvements in the constitutive model will also help to better control rebound. Hopefully,

more accurate constitutive data for the material will become available in the near future that may eliminate the over-predictions in the rebound and produce more accurate strain states.

Another aspect of inertial ironing is seen in the through-thickness shear stresses generated, whose magnitude is above the yield stress of the material (Figure 168 to Figure 170). The corresponding shear strains (Figure 175 to Figure 177) contribute to the overall deformation of the material, providing an additional mode of deformation when compared to traditional stamping processes.

This change from a plane-stress forming process to one with a more complex stress state and the high strain rates is thought to combine to produce the observed increase in formability. This complex stress states also have important consequences for the numerical modeling of the process, since solid elements are required to properly resolve all the stress components, as opposed to the shell elements typically used to model sheet metal forming.

The final shape of the experimental samples differed from the nominal part shape. Although the differences observed may be considered minor for some applications, they were significant enough that production parts formed with this process could be rejected for being out of tolerance. The differences in geometry were produced by the force distribution and the rebound of the sheet. These effects were observed experimentally and in the numerical predictions. The coil and die design could, in principle, be adapted to remedy the geometry deviations in EM formed parts and should be further studied. Also, the possibility of additional discharges to obtain the final shape, in what would be the equivalent of a re-strike operation, could be considered to obtain samples with tighter tolerances.

The numerical simulations provided valuable insight into the process and good qualitative results were obtained. The models over-predicted the rebound of the sheet and the reasons for this are not known. Several causes were put forward as sources for this over-prediction, which are:

- Potential errors in the constitutive model, which is not calibrated for strain rates above 1000 s^{-1}.
- Damping provided by the air
- The additional forces generated by the multiple current pulses produced by the actual process.

All of these effects were explored numerically, with the exception of the possible air cushion. No one cause was found for the over-prediction, but it was determined that the scaling of the flow stress to account for possible rate effects resulted in final shapes that were closer to the nominal shape. Consideration of additional current pulses provided closer predictions to the nominal shape, indicating that the additional current pulses also could have an effect on the final sample shape. Despite the over-prediction of the rebound, the data obtained from the model provided valuable information on the stress and strain histories of the process, which helps in explaining the increased formability.

The research has shown that the hybrid process for corner fill can produce features that cannot be produced by conventional stamping operations. The results of this work indicate that hybrid EM processes like the one studied have potential industrial applications; however, several issues must be addressed before such a process becomes feasible in production. Probably the most challenging issue is the robustness of the process, specifically the durability of the coils. For a typical automotive application, the coils would have to resist hundreds of operations per day and coils that could resist those harsh conditions would have to be developed. Another key requirement is the availability of an accurate, reliable and fast predictive capability for EM forming processes. The two most important issues that must be addressed to gain this capability are: i) obtaining accurate material properties and ii) the availability of more efficient computational algorithms coupled with effective massively parallel implementation of the available simulation codes that would reduce the simulation times. Obtaining accurate material properties at the strain rates encountered in EM forming is possible, albeit very challenging, and hopefully this data will become available soon. The software used in the current work shows great promise for use as a predictive tool; however the computational costs are very high and more validation must be performed. Software improvements and the availability of increasingly powerful computers at affordable prices, will soon make numerical predictions for EM forming part of a typical part/tool design processes. The outlook for a feasible commercial EM forming process is positive; however further study is required. The next section will outline the conclusions reached, together with specific recommendations for further work.

7 CONCLUSIONS AND FUTURE WORK

7.1 Conclusions

The following conclusions were reached from the experiments:

- A hybrid operation consisting of a conventional (stamping) pre-form and EM corner fill of an AA 5754 proved successful in reducing the radius part from 20 mm to 5 mm without draw-in.
- All of the EM corner fill samples were formed to essentially the same shape regardless of the initial condition (pre-strain) of the sheet. In contrast, the samples that were corner filled conventionally to the 5 mm radius by stamping all fractured prior to reaching the final desired shape.
- The recorded strain data demonstrates that the hybrid process resulted in an increase in formability of AA 5754 when compared with conventional forming for the conditions studied.
- The final sample shape deviated from the nominal part geometry due to rebound and to the induced force EM distribution.
- Acceptable samples were not formed with the single step EM process, due to the significant rebound and distortion that was present in the samples. This indicates that significant difficulties could be encountered when trying gain significant deformation with a single EM step.
- Coil design is critical for corner fill operations, as it is for all EM forming processes.

The numerical models provided significant insight into the forming process and the following conclusions were reached from the numerical simulations:

- The numerical models for the hybrid process indicate that the EM stage is not a plane stress forming process due to the presence of significant through-thickness normal and shear stresses. This non-plane stress state has implications for modeling of EM forming process since it means that plane

stress shell elements may not provide accurate enough representation of the process.

- Conditions favourable for inertial ironing were predicted: large compressive through-thickness and hydrostatic stresses, effective plastic strain rates on the order of 10,000 to 60,0000 s^{-1}, and large through-thickness shear stresses and strains.
- The predictions indicate that the process has an efficiency of 3%, which is low, but in line with the values from the literature.

7.2 Future Work

This work has provided new insight into the process of the EM corner fill. Still, there remain questions that need to be addressed before this process can be implemented. The following are suggestions for future work:

- High strain rate data for the sheet alloys at operative strain rates of 10,000 s^{-1} or higher must be obtained and used in the future modeling of this process.
- A detailed study should be undertaken on the use of EM corner fill in corners where three planes intersect, e.g. the corners of a deep drawn rectangular pan. As was discussed in Chapter 1, studies have shown that these corners are difficult to realize with EM forming.
- High speed video of the sheet as it interacts with the die should be obtained to measure the impact conditions that are generated during the process.
- The coil design should be tested and modeled to determine whether it can withstand the rigors of mass production.
- The use of coil and die design to reduce the deviations in geometry of the final part should be further studied.
- The over-prediction of the rebound by the numerical models should be further investigated by incorporating the air in the simulations or by performing the experiments in a vacuum to determine the effects of the air on the process. Also, the effects of the contact algorithms used should be investigated.

- Material models that incorporate damage should be used to see how the generation of damage is affected by the EM process.

REFERENCES

1 Wilson, D.V., "Aluminium versus steel in the family car-The formability factor", *Journal of Mechanical. Working Technology*, v.16, 1988, pp. 257-277.

2 Miller, W.S., *et al*, "Recent development in aluminium alloys for the automotive industry", *Materials Science and Engineering A*, v.A280, 2000, pp. 37-49.

3 Mori, T.; Hino, M,; Iwaya, J. and Miyahara, M., "Press formability of aluminum alloy sheets for automobile parts", *KOBELCO Technology Review*, n.14, July 1992, 49-53.

4 Wagner, H.J. and Boulger, F.W. "High velocity metalworking processes based on the sudden release of electrical of electrical energy" memorandum prepared by the Battle Memorial Institute for the Defense Metals Information Center, 1960.

5 *High Velocity Forming of Metals- Revised Edition* edited by Bruno E.J. American Society of Tool and Manufacturing Engineers, Dearborn, MI 1968.

6 Daehn, G.S.; Vohnout, V.J. and DuBois, L., "Improved Formability with Electromagnetic Forming: Fundamentals and Practical Example", *http://www.ecr6.ohio-state.edu/~daehn/overview/index.htm*, Ohio State University, date not available.

7 Google Images. http://images.google.com/imgres?imgurl=http://zo-d.com/stuff/images/Mercedes-SL500-11-99-license-plate-frame.jpg&imgrefurl=http://zo-d.com/stuff/automotive.html&h=304&w=480&sz=18&hl=en&start=3&tbnid=2hI4B8KQ9-TUYM:&tbnh=82&tbnw=129&prev=/images%3Fq%3Dlicense%2Bplate%2Bpocket%26svnum%3D10%26hl%3Den%26rls%3DGGLD,GGLD:2005-19,GGLD:en%26sa%3DN

8 Autoblog.com. http://www.autoblog.com/media/2006/05/GV-Door-handle-resized.JPG

9 Schey, J.A., "Introduction to Manufacturing Processes", 3rd ed., McGraw-Hill, Toronto, 2000.

10 Altan, T., "Design Rules for Forming Aluminum Stampings. Parts 1 and 2", *The Fabricator.com*,

http://www.thefabricator.com/ToolandDie/ToolandDie_Article.cfm?ID=179. , February 2, 2002.

11 Oliveira, D.A. *Electromagnetic Forming of Aluminum Alloy Sheet: Experiment and Model*. Masters of Applied Science thesis, University of Waterloo, 2002.

12 Lal, G.K. *The Plastomagnetodynamics of Electromagnetic Metal Forming*. PhD thesis, University of Waterloo, 1969.

13 "Electromagnetic Forming", Edited by Plum, M.M. Part of Forming Processes for Sheet, Strip and Plate. ASM, Materials Park OH, 1995.

14 Belyy, I.V.; S.M. Fertik and Khimenko, L.T., "Electromagnetic Metal Forming Handbook". Translation by Altynova, M.M. Available from the Hyperplastic Forming Consortium at the Ohio State University. Original published in 1977, translated in 1996

15 Al-Hassani, S.T.S. " Magnetic Pressure Distributions in Sheet Metal Forming". Electrical Methods of Machining, Forming and Coating. Institute of Electrical Engineers Conference Publication No. 1975, pp. 1-10.

16 Golowin, S.; Kamal, M.; Shang, J.; Portier, J.; Din, A: Daehn, G.S.; Bradley, J.R.; Newman, K.E. and Hatkevich, S. "Application of a Uniform Pressure Actuator for Electromagnetic Processing of Sheet Metal", *Journal of Materials Engineering and Performance* , v. 16, n. 4, 2007, pp. 455-460.

17 Imbert, J. M. *Increased Formability and the Effects of the Tool/Sheet Interaction in Electromagnetic Forming of Aluminum Alloy Sheet.* Masters of Applied Science thesis, University of Waterloo, 2005.

18 Yudaev, V.B. "Manufacture of large sheet-metal parts by incremental electromagnetic forming" *kuznechno-Shtampovochnoe Proizvodstvo,* n. 7, 1989, pp. 1-2.

19 Balanethiram, V.S and Daehn, G.S. "Hyperplasticity: Increased forming limits at high workpiece velocity" *Scripta Metal.lurgica at Materialia,* v. 30, 1994, pp. 515-520.

20 Balanethiram, V.S. Hyperplasticity: Enhanced Formability of Sheet Metals at High Workpiece Velocities. Ph.D. Thesis, Ohio State University, 1996.

21 Golovashchenko, S.F.; Mamutov, V.S.; Dmitriev, V.V. and Sherman, A.M., "Formability of sheet metal with pulsed electromagnetic and electrohydraulic technologies", Proceedings of the *al.uminum 2003, Proceedings of the TMS annual meeting*, edited by S.K. Das, San Diego, Ca., TMS, 2003, pp. 99-110.

22 Tobe, T.; Kata, M. and Obara, H. " Metal forming by underwater wire explosion 1. An analysis of plastic deformation of circular membranes under impulsive loading" *Bulletin of the JSME* , v. 22, n. 164, February 1979, pp. 271-278.

23 Vohnout, V.J. and Daehn, G.S., "Effect of quasi-static prestrain and eddy currents on limit strains in electromagnetic pulse forming of two aluminum alloys", Proceedings of the *al.uminum 2002, Proceedings of the TMS 2002 annual meeting*, edited by S.K. Das and M.H. Skillingberg, TMS, 2002, pp. 19-25.

24 Takatsu, N.; Kato, M.; Sato, K. and Tobe, T., "High-Speed Forming of Metal Sheets by Electromagnetic Force", *JSME International Journal-Series III*, v. 31, n.1, 1988, pp. 142-148.

25 Personal comunictaion with D. Lloyd, ALCAN Internatinal, Kingston, ON, Canada, 2004.

26 Dieter, G., "Mechanical Metallurgy", 2nd edition, Mcgraw-Hill, Toronto, 1976, pp. 350-353.

27 Lindholm, U.S., Bessey, R.L and Smith, G.V., "Effect of strain rate on yield strength, tensile strength, and elongation of three aluminum alloys", *Journal of Materials*, JMLAS, v.6, n.1, 1971, pp. 119-133.

28 Smerd, R.; Winkler, S; Salisbury, C; Worswick, M.; Lloyd, D; and Finn, M., "High Strain Rate Tensile Testing Of Automotive Aluminum Alloy Sheet", submitted for publication to the *International Journal of Impact Engineering*, November 2004.

29 Tanaka, K and Nojima, T "Strain rate tests of aluminium alloys under high strain rate" The 19th Japan congress of Materials Research-Metallic Materials, March 1976, pp. 48-52.

30 Mukai, T; Masataka, K; and Kenji, H., "Strain-rate dependence of mechanical properties in AA 5056 Al-Mg alloy processed by equal-channel-angular-extrusion", *Materials Science and Engineering: A*, v.247, 1998, pp 270-274.

31 Higashi, K. *et al.*, "Strain rate dependence on mechanical properties in some commercial aluminum alloys", *Journal de Physique IV, Colloque C3, supplement au Journal de Physique III*, v. 1, oct. 1991, pp. 341-346.

32 Oosterkamp, L.; Ivankovic, A. and Venizelos, G., "High strain rate properties of selected aluminium alloys", *Materials Science and Engineering: A*, v.278, 2000, pp 225-235.

33 Rajendran, A.M. and Fyfe, I.M. "Inertia effects on the ductile failure of thin rings" *Transactions of the ASME - Journal of Applied Mechanics*, v. 49, 1982, pp. 31-36

34 Fressengeas, C. and Molinari, A. "Inertia and thermal effects on the localization of plastic flow", *Acta Metallurgica*, v. 33, n.3, 1985, pp. 387-396.

35 Regazzoni, G, Johnson, J.N. and Follansbee, P.S. "Theoretical Study of the Dynamic Tensile Test" *Transactions of the ASME - Journal of Applied Mechanics*, v. 53, 1986, pp. 519-528

36 Hu, X.; Wagoner, H.; Daehn, G.S. and Gosh, S., "The effect of inertia on tensile ductility" *Metallurgical and Material Transactions A*, v. 25A, December 1994, pp. 2723-2735.

37 Balanethiram, V.S *et al.*. "Hyperplasticity: Enhanced formability at high rates" *Journal of Materials Processing Technology*, v. 45, 1994, pp. 595-600.

38 Hu, X. and Daehn, G.S. "Effect of velocity on Flow localization in tension", *Acta Materialia*, v. 44, n. 3, 1996, pp. 1021-1033.

39 Altynova, M; Hu, X and Daehn, G.S., "Increased ductility in high velocity electromagnetic ring expansion", *Metallurgical and Materials Transactions A*, v. 27A, July 1996, pp 1837-1844.

40 Golovashchenko, S., "Numerical and experimental results on pulsed tube calibration," Proceedings of the *TMS annual meeting: Sheet metal forming technology-1999*, M. Demeri ed., San Diego, Ca., TMS, 1999, pp. 117-127.

41 Fenton, G.K. and Daehn, G.S., "Modeling of electromagnetically formed sheet metal", *Journal of Materials Processing Technology*, v.75, 1998, pp. 6-16.

42 J. Hallquist, *LS-DYNA Theoretical Manual*, Livermore Software Technology Corporation, 1998.

43 Gurson, A.L., "Continuum Theory of Ductile Rupture by Void Nucleation and Growth: Part 1 – Yield Criteria and Flow Rules for Porous Ductile Media," *Journal of Engineering Materials Technology*, v. 99, 1977, pp. 2-15

44 Tvergaard, V., "Influence of Voids on Shear Band Instabilities Under Plane Strain Conditions," *International Journal of Fracture*, v.37, n.4, 1981, pp. 389-407.

45 Tvergaard, V. and Needleman, A., "Analysis of the Cup-one Fracture in a Round Tensile Bar", *Acta. Metallurgica*, v. 32**,** 1984, pp. 157.

46 Worswick, M.J. and Pick, R.J., "Void growth and coalescence during high velocity impact", *Mechanics of Materials*, v. 19, pp. 293-309, 1995.

47 Lewandowski, J.J. and Lowhaphandu, P., "Effects of hydrostatic pressure on mechanical behaviour and deformation processing of materials", *International Materials Reviews*, v.43, n.4, 1998, pp.145-187.

48 Spitzig, W.A., "Effect of hydrostatic pressure on deformation, damage evolution, and fracture of iron with various initial porosities", *Acta Metallurgica et Materialia*, v.38, n.8, 1990, pp. 1445-1453.

49 Zok, F. and Embury, J.D., "Forming of low-ductility materials under hydrostatic pressure", *Journal of Material. Shaping Technology*, v.8, 1990, pp. 77-81.

50 Brownrigg, A.; Spitzig, W.A.; Richmond, O.; Teirlinck, D. and Embury, J.D., "The influence of hydrostatic pressure on the flow stress and ductility of a spherodized 1045 steel", *Acta Metal.lurgica*, v.31, n.8, 1983, pp.1141-1150.

51 French, I.E. and Weinrich, P.F., "The effects of hydrostatic pressure on the mechanism of tensile fracture of aluminum", *Metallurgical Transactions A*, v.6A, 1975, pp. 1165-1169.

52 Imbert, J.M.; Worswick, M.J. and Golovashchenko, S., "Contributing Factors to the Increased Formability Observed in Electromagnetically Formed Aluminum Alloy Sheet",

Proceedings of the 2nd International Conference on High Speed Forming, Dortmund, Gremany, March 20th-21st, 2006, pp. 3-12.

53 Graf, A. and Hosford, W., "The Influence of strain-path changes on forming limit diagrams of AA6111 T4", *International Journal of Mechanical Sciences*, v. 36, n. 10, 1994, pp. 897-910.

54 Sang, H. and Lloyd, D.J., "The influence of biaxial prestrain on the tensile properties of three aluminum alloys", *Metallurgical Transactions A*, v. 10A, 1979, pp. 1771-1776.

55 Kohara, S., "Forming-limit curves of aluminum and aluminum alloy sheets and effects of strain path on the curves", *Journal of Materials Processing Technology*, v.38, 1993, pp. 723-735.

56 Belyy, I.V.; S.M. Fertik and Khimenko, L.T., "Electromagnetic Metal Forming Handbook". Translation by Altynova, M.M. Available from the Hyperplastic Forming Consortium at the Ohio State University. Original published in 1977, translated in 1996

57 Moon, F., "Magneto-Solid Mechanics", John Wiley & Sons, Toronto, 1984.

58 Serway, R.A., "Physics for Scientists and Engineers with Modern Physics", 3rd ed., Saunders College Publishing, Toronto, 1990.

59 Al-Hassani, S.T.S.; Duncan, J.L. and Johnson, W., "On the Parameters of the Magnetic Forming Process", *Journal of Mechanical Engineering Science*, v. 16, n.1, 1974, pp. 1-9.

60 L'Eplattenier, P.; Cook, G.; Ashcraft, C.; Burger, M.; Imbert, J. and Worswick, M. " Introduction of an Electromagnetism Module in LS-DYNA for Coupled Mechanical-Thermal-Electromagnetic Simulations", *Steel Research InternationalI*, v. 80, n. 5, 2009, pp. 351-358.

61 Tai, C.T., "A Study of Electrodynamics of Moving Media", *Proceedings of the IEEE*, June 1964 pp.685-689,

62 Pao, Y. and Hutter, K., " Electrodynamics of Moving Elastic Solids and Viscous Fluids", *Proceedings of the IEEE*, v.63, n.7, July 1975, pp. 1011-1021.

63 Zhang, H.; Murata, M. and Suzuki, H., “Effects of various working conditions on tube bulging by electromagnetic forming”. *Journal of Materials Processing Technology*, v. 48, 1995, pp 113-121.

64 Lee, S.H. and Lee, D.N., “A finite element analysis of electromagnetic forming for tube expansion”, *Journal of Engineering Materials Technology*, v.116, 1994, pp. 250-254.

65 Mahanian, S. and Blackwell, D., ”Finite element analysis of electromagnetic forming of tubes with fittings”, *Manufacturing Science and Engineering*, MED-V. 4, 1996, pp. 323-329.

66 Shangyu, H.; Zhihua, C.; Zhongren, W.; Lifeng, W. and Mei, Y., “A finite-element analysis of electromagnetic sheet metal-expansion process” (sic), *Transactions of the Nonferrous Metals Society of China*, v.8, n.3, 1998, pp. 490-495.

67 Oliveira, D.A.; Worswick, M.J. and Finn, M., “Finite Element Modeling of the Electromagnetic Forming of Aluminum Alloy Sheet,” Proceedings of The 4th International ESAFORM Conference on Material Forming V. II, Liege, Belgium, 2001, pp. 773-776.

68 Oliveira, D.A. and Worswick, M.J., “Electromagnetic forming of aluminum alloy sheet”, *Journal de Physique IV France*, v.110, 293-298 (2003).

69 Risch, D.; Beerwald, C.; Brosius, A. and Kleiner, M., “On the significance of the die design for electromagnetic sheet metal forming” Proceedings of the *1st International Conference on High Speed Forming*, Lerhstuhl fur Umformtechnik, University of Dortmund, M. Kleiner ed., March 31-April 2004, Dortmund, Germany, pp. 191-200.

70 Oliveira, D.A. and Worswick, M.J., “Electromagnetic forming of aluminum alloy sheet”, *Journal. de Physique IV France*, v.110, EDP Sciences, Les Ulis, DOI: 10.1051/jp4:20030709, 293-298 (2003).

71 El-Azab, A.; Garnich, M. and Kapoor, A., “Modeling of the electromagnetic forming of sheet metals: state-of-the-art and future needs”, *Journal of Materials Processing Technology*, v.142, 2003, pp. 744-754.

72 Bendjima, B. and Féliachi, M.; "Finite element analysis of transient phenomena in electromagnetic forming system", Proceedings of the *IEE 3rd International Conference on Computation in Electromagnetics*, 10-12 April 1996, Bath, UK, pp.113-116.

73 Bendjima, B.; Srairi, K. and Féliachi, M., "A coupling model for analysing dynamical behaviours of an electromagnetic forming system", IEEE Transactions on Magnetics, v. 33, n. 2, March 1997, pp.1638-1641.

74 Bessonov, N. and Golovashschnenko, S., "Numerical simulation f pulsed electromagnetic stamping processes", Proceedings of the *1st International Conference on High Speed Forming*, Lerhstuhl fur Umformtechnik, University of Dortmund, M. Kleiner ed., March 31-April 2004, Dortmund, Germany, pp. 83-91.

75 Stiemer, M.; Svendsen, B.; Unger, J.; Suttmeier, F.T. and Blum, H., "Development of multi field software solutions and their applications for the optimization of electromagnetic high speed forming processes" Proceedings of the *1st International Conference on High Speed Forming*, Lerhstuhl fur Umformtechnik, University of Dortmund, M. Kleiner ed., March 31-April 2004, Dortmund, Germany, pp. 93-104.

76 Stiemer, M.; Klocke, M.; Suttmeier, F.T.; Blum, H.; Joswig, A. and Kulig, S., "Validation of different approaches to coupled electrodynamic-structural mechanical simulation of electromagnetic forming", Proceedings of the *1st International Conference on High Speed Forming*, Lerhstuhl fur Umformtechnik, University of Dortmund, M. Kleiner ed., March 31-April 2004, Dortmund, Germany, pp. 105-118.

77 Shang, J., "Electromagnetically Assisted Sheet Metal Stamping", Ph.D. Thesis, Ohio State University, 2006.

78 Woodward, S.; Weddeling, C.; Daehn, G.; Psyk, V.; Carson, B. and Tekkaya, A.E., "Agile Production of Sheet Metal Aviation Components Using Disposable Electromagnetic Actuatrors", Proceedings of the *4th International Conference on High Speed Forming*, Ohio State University, G. Daehn ed., March 9-10 2010, Columbus, Ohio.

79 Psyk, V.; Beerwald, C.; Homberg, W.; Kleiner, M.; Beerewald, M. and Henselek. A., " Investigation of the Process Chain Bending-Electromagnetic Compression –

Hydroforming on the Basis of an Industrial Demonstrator Part", Proceedings of the *2nd International Conference on High Speed Forming*, Lerhstuhl fur Umformtechnik, University of Dortmund, M. Kleiner ed., March 20-21, 2006, Dortmund, Germany, pp. 117-127.

80 Psyk, V.; Beerwald, C.; Henselek, A.; Homberg, W.; Brosius, A. and Kleiner, M., " Intergration of Electromagnetic Calibration into the Deep Drawing Process of an Industrial Demonstrator Part", *Key Engineering Materials*, v. 344, 2007, pp. 435-442.

81 Psyk, V.; Risch ,D.; Beerwald, C.; and Tekkaya, A.E., "Investigation of Combined Electromagnetic and Conventional Forming", Proceedings of the *International Deep Drawing Research Groupt (IDDRG) 2008 International Research Conference*, Olofstrom, Sweeden, Asnafi, N. ed., 2008, pp. 487-498.

82 Liu, D.; Li, C. and Yu, H., "Numerical Modeling and Deformation Analysis for Electromagnetically Assisted Deep Drawing of AA 5052 Sheet", *Transactions of the Nonferrous Metals Society of China*, v. 19, 2009, pp. 1294-1302.

83 Golovashchenko, S.F., "Electrohydraulic Forming for Automotive Applications", Proceedings of the *4th International Conference on High Speed Forming*, Ohio State University, G. Daehn ed., March 9-10 2010, Columbus, Ohio.

84 Pulsar. http://www.pulsar.co.il/

85 www.matweb.com

86 Golovashchenko, S., "Electromagnetic Forming and Joining for Automotive Applications", Proceedings of the *2nd International Conference on High Speed Forming*, Lerhstuhl fur Umformtechnik, University of Dortmund, M. Kleiner ed., March 20-21, 2006, Dortmund, Germany, pp. 201-206.

87 Q Imaging, www.qimaging.com.

88 MediCybernetics, Newburyport, MA, USA, www.mediacy.com.

89 ASM Handbook, Volume 2, Properties and Selection: Nonferrous Alloys and Special-Purpose Materials. Online Edition. 2010.

90 Srinivasan. S.; Wang, H; Taber, G. and Daehn, G., "Dimensional Control and Formability in Impact Forming", Proceedings of the *4th International Conference on High Speed Forming*, Ohio State University, G. Daehn ed., March 9-10 2010, Columbus, Ohio. Pp. 239-249.

91 Personal communication with Dr. Sooky Winkler, Research Assistant Professor, Department of Mechanical and Mechatronics Engineering, University of Waterloo, 2004.

92 Winkler, S. Personal communication. June 2010.

93 Cenanovic, M.B., "Magnetic Metal Forming by Reversed Electromagnetic Forcess", *Proceedings of the 4th IEEE Pulsed Power Conference*, Albuquerque, NM, June 6-8, pp. 83-86, 1983.

94 Risch, D.; Vogli, E.; Bauman, I; Brosius, A.; Beerwald, C.; Tillman, W.; and Kleiner, M., Aspects of Die Design for the Electromagnetic Sheet Metal Forming Process" *Proceedings of the 2nd International Conference on High Speed Forming*, Dortmund, Kleiner, M ed. Germany, pp. 189-199, 2006.